Thèse

Présentée pour obtenir le grade de

Docteur de l'Université de Savoie

Spécialité: Matériaux Polymères et Composites

Par

Sudharsan Pandiyan

Modélisation moléculaire de la perméabilité du CO_2 dans les membranes polymères

A molecular-level understanding of CO_2 permeability in polymer membranes

Soutenance le 11 Décembre 2009

Jury :

D. Brown	Professeur, Université de Savoie	Co-directeur de thèse
M. Johnson	Professeur, Université de Nottingham	Examinateur
S. Neyertz	Maître de conférences, Université de Savoie	Directeur de thèse
A. Padua	Professeur, Université Blaise Pascal	Rapporteur
N.F.A. van der Vegt	Professeur, Université Technique de Darmstadt	Co-directeur de thèse
M. Wessling	Professeur, Université de Twente	Rapporteur

Thèse préparée en collaboration au Laboratoire des Matériaux Organiques à Propriétés Spécifiques (LMOPS), UMR CNRS 5041 à l'Université de Savoie, France sous la direction de Dr. S. Neyertz et Prof. D. Brown et à l'Institut Max-Planck pour les Polymères (MPIP), Mayence, Allemagne sous la direction de Prof. Dr. N.F.A. van der Vegt.

Modélisation moléculaire de la perméabilité du CO_2 dans les membranes polymères

A molecular-level understanding of CO_2 permeability in polymer membranes

Sudharsan Pandiyan

Acknowledgments

This project was made possible by the award of a doctoral grant co-financed by the MPIP (Max Planck Institute for Polymer Research, Mainz, Germany) and the APS (Assemblée des Pays de Savoie, France). The CCRT, IDRIS, CINES national supercomputing centres in France, the MUST cluster at the University of Savoie (France) and the MPIP (Germany) are also acknowledged for their generous provision of computer time.

Introduction

Gas separation using polymer membranes

The basic foundations for gas separation were established by the gas diffusion laws of Graham and Fick in the mid-19th century.[1-3] Graham gave the first description of gas transport inside a membrane material in the form of a solution-diffusion model. Later in the mid-20th century, researchers like Barrer,[4] Stern[5] and Meares[6] laid the foundations for modern theories of gas permeation in dense polymer membranes, in which the solution-diffusion framework is still the accepted model for gas transport. However it was only three decades ago that the use of polymeric materials for gas separation went from laboratory to commercial ventures.[7,8] Since then, polymer membrane-based gas separation has emerged substantially as an important process in chemical industries.

Glassy polymers are promising membrane materials for carbon dioxide (CO_2) separation applications because of their effective gas selectivity behaviour.[3,7,8] Polymer membranes are economically and environmentally attractive alternatives to traditional gas separation methods such as amine scrubbing technology[9], physical adsorption,[10-16] chemical adsorption[17-24] and low-temperature distillation.[25,26] In their simplest ideal form, membranes act as molecular scale filters. The portable and compact nature of polymer membranes makes them more popular than other gas separation methods and they also can be combined with other gas separation techniques to increase the efficiency.[7,8]

The development of robust polymer membranes should make membrane gas separation a superior technique over other available methods. However, the continuous commercial development of this field depends upon achieving clear ideas of relationships between polymer structure and gas transport as well as gas selectivities.[7,8] The vast amount of

work available in the literature is mostly based on experimental results,[3,5,8,27-65] although a few basic molecular simulations have been reported.[66-70]

Importance of carbon dioxide (CO_2) separation

Global warming has been identified as one the world's major environmental issues in the 21st century.[71] It is possible to mitigate this effect and reduce the release of greenhouse gases such as carbon dioxide in to the atmosphere by separating them from gas streams in e.g. cement industry and oil recovery plants.[71] It is generally accepted that the increased concentration of CO_2 in the atmosphere is an important reason for global warming. The larger sources of CO_2 emission are fuel and biomass energy facilities, natural gas production, synthetic fuel plants, fossil fuel-based hydrogen production plants and major industries.[71] The current levels of CO_2 are considerably higher than over the last 65,000 years.[72] In this context, CO_2 separation and storage (CSS) is an absolute necessity at this moment to preserve the ecology of our planet.

In most power stations, amine sorption technology[73] is used to separate CO_2 from high-pressure gas streams. More occasionally, the physical swing adsorption[10-16] or temperature swing adsorption method[74-79] have been adopted to separate CO_2. The recent developments in the field of polymer membranes, and especially the preparation of high-performance gas separation membranes, are a vital alternative for CO_2 separation applications. They can achieve a large difference in permeation rates (>100 times) between different gases in a stream. Such membranes can be used to separate a wide spectrum of gases.[8]

Potential applications of CO_2 separation

Initial efforts of CO_2 separation were addressed with respect to its industrial uses. There are lot of potential applications of CO_2 in its liquid, gas and super-critical states.[48,58,80-86]

i) It is used as a solvent in chemical syntheses because of its non-toxic and easy processing nature.[87-92]

ii) A very important application is its use in oil recovery plants,[71] where high-pressure CO_2 reduces the viscosity of crude oil and forces it through the fuel pipes.[93-97]

iii) It enhances the hardness of the steel in the moulding process.[98]

iv) It is also used as a refrigerant in its solid form ("dry ice").[99]

v) Another well-known application is the preparation of carbonated drinks.[100]

vi) It is employed as a fire extinguisher because of its non-flammable character and its lack of assistance to combustion.[101]

vii) It can be combined with limonene oxide or other epoxides to make plastics.[102]

viii) It is an important ingredient in the photosynthesis process. [103]

The popularity of CO_2 as an industrial solvent is increasing day-by-day because of its tunable properties near its critical temperature of 304 K.[104] So it is important to develop an economically-favourable CO_2 separation technique, such as high-performance polymer membranes, in order to reduce the production costs.

Molecular simulations of CO_2 transport

In general, CO_2 is treated in the same way than all other small gas molecules in most molecular simulation studies.[105] However CO_2 has a specific tendency to plasticize polymer membranes at high concentrations and the performance of the membrane can be significantly altered. For example, in CO_2/CH_4 gas separation, the polymer swells upon sorption of CO_2 accelerating the permeation of CH_4 and decreasing the selectivity of the polymer membrane.[67,69]

Earlier attempts to model CO_2 transport in polymer membranes using molecular simulations are quite unsatisfactory. In the Gusev-Suter transition state theory[67,69] (GSTST), the pressure dependence of the solute concentration at elevated pressures is calculated from the statistical equilibrium between the solute in the static matrix and the ideal-gas phase. However, the assumption that the polymer packing does not undergo any structural relaxations due to the presence of the penetrant molecules is not exactly valid for CO_2 sorption. As a consequence, GSTST always predicts much higher solubility coefficients for CO_2 than those reported experimentally.[106] The fairly-common use of spherical united-atom models for linear CO_2 molecules is also highly suspect.[67,69,70,107] Indeed, it helps to artificially slow down the diffusion of CO_2 molecules in the polymer membranes and increases the solubility, an artifact which is solely due to the "large-bead" character of the model penetrant. There have also been attempts to use a flexible CO_2 model.[108-110] However, in classical MD simulations, the use of flexible bending angles for CO_2 leads to non-equipartition of kinetic energy, because of the associated two extra degrees of freedom, i.e. an angle bend and the rotation around the O-C-O axis. In particular, the latter has a very small moment of inertia and couples very poorly with the other degrees of freedom.

In this work, we intend to build atomistic models for some glassy polymers and study CO_2 transport in these models using molecular dynamics (MD) simulations[111] without any pre-assumptions about the polymer relaxations in the presence of CO_2 molecules. This will eventually help to understand the plasticization phenomenon at the atomistic level and the actual factors affecting CO_2 transport in polymer membranes.

Chapter 1.

Background and Theory

1.1) Gas permeation

The solution-diffusion mechanism was proposed in 1866 by Thomas Graham, and is widely accepted for gas transport in polymer membranes.[62,64,112-115] According to this mechanism, gas transport occurs when the gas molecules enter the membrane at its high-pressure side, then diffuse across the membrane and re-emerge at its low-pressure side. Gas permeability *P* is defined as a measure of the ease of transport of the gas through the polymer membrane, which is given by the thickness-normalized flux divided by the pressure difference across the membrane (Eq. 1):[3,116]

$$P = J\frac{l}{\Delta p} \tag{1}$$

where *J* is the gas flux through a membrane of thickness *l* and Δp is the pressure difference across the membrane. The flux *J* of a gas through a polymer membrane is itself given by Fick's first law (Eq. 2):[3]

$$J = -D\frac{\partial C}{\partial x} \tag{2}$$

where *D* is called the diffusion coefficient and $\left(\frac{\partial C}{\partial x}\right)$ is the penetrant concentration as a function of the distance *x* across the film. By combining Eq. 1 and Eq. 2 and assuming that the downstream pressure is negligible,[3] one obtains Eq. 3:

$$P = DS \tag{3}$$

where *S* is called the solubility coefficient. It is difficult to calculate gas permeabilities directly using molecular dynamics simulations in glassy long-chain polymers because of the current limitations of computational times and system sizes.[117] Fortunately, the problem can

be circumvented by Eq. 3. Both diffusion coefficient *D* and solubility coefficient *S* are bulk properties and can be calculated separately in MD simulations.

When applied to gas mixtures, the separation factor $\alpha^*_{A/B}$ defines the ability of a membrane to separate gas *A* from gas *B* (Eq. 4):

$$\alpha^*_{A/B} = \frac{y_A / y_B}{x_A / x_B} \tag{4}$$

with *x* and *y* being the upstream and downstream mole fractions of *A* and *B*, respectively. In most cases, the downstream pressure is negligible with respect to the upstream pressure, and Eq. 4 reduces to Eq. 5:

$$\alpha^*_{A/B} = \alpha_{A/B} = \frac{P_A}{P_B} \tag{5}$$

where $\alpha_{A/B}$ is known as the permselectivity of the membrane. It can be further split into two parts (Eq. 6):

$$\alpha_{A/B} = \left(\frac{D_A}{D_B}\right)\left(\frac{S_A}{S_B}\right) \tag{6}$$

$\frac{D_A}{D_B}$ is called the diffusivity selectivity and $\frac{S_A}{S_B}$ is called the solubility selectivity.

1.2) Gas sorption

The solubility of a gas in a polymer membrane is related to the concentration *C* of gas in the polymer phase at certain partial pressure *p* of the gas.[107] Several models have been proposed to describe the gas sorption isotherms as a function of feed pressure,[27,62,64,112-114,118] among which the so-called dual-mode sorption (DMS) model has been the most popular over the last three decades.[8,27,65,118]

In the dual-mode sorption model, the penetrant concentration C can be defined as a sum of two different concentrations, C_D and C_H, which represent Henry's law sorption and Langmuir sorption respectively (Eq. 7):

$$C = C_D + C_H \tag{7}$$

These two quantities can be further characterised by various parameters as shown in Eq. 8:

$$C = C_D + C_H = k_d p + \frac{C_H' bp}{1+bp} \tag{8}$$

where k_d is Henry's law solubility coefficient (cm^3(STP)/cm^3(polymer) atm), p is the pressure (atm), C_H' is the Langmuir sorption capacity (cm^3(STP)/cm^3(polymer)) and b is the Langmuir affinity parameter (atm^{-1}). A schematic graph is shown in Figure 1.

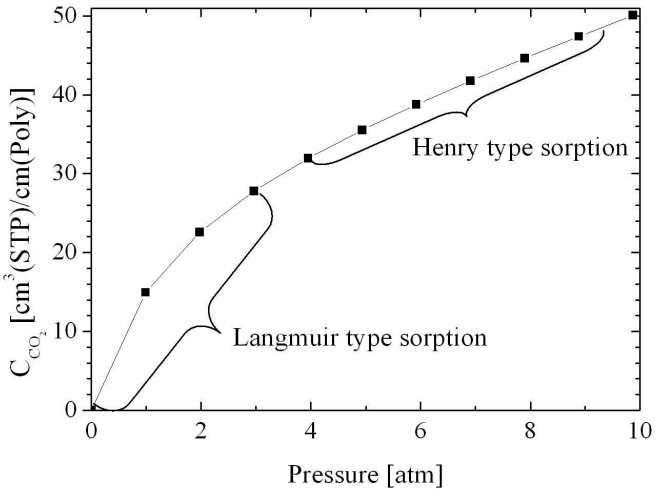

Figure 1. General shape of dual-mode sorption isotherms.[118] The example shown is that of CO_2 in 6FDA-6FpDA at 35°C.[118]

Langmuir-type sorption is assumed to be linked to packing defects or microvoids with the size of penetrating gas molecule. This type of sorption thus decreases sharply with the pressure and reaches a plateau once the microvoids are saturated. In Henry's type sorption,

the sorbed gas molecules go into dense packed regions within the polymer similar to sorption environments in liquids (Figure 1).

Figure 2 gives the relationship between the specific volume of the polymer and the temperature.[119] The amount of microvoids increases as the relative distance between the polymer glass-transition temperature T_g and the actual temperature T increases.[119] V_0 is the volume occupied by polymer atoms, V_l is the expected liquid-like specific volume (i.e. the equilibrium specific volume with infinitely slow cooling rates) and V_g is the actual specific volume of the glassy state. During the sorption phase, all gas molecules first fill the available non-equilibrium free volume (*i.e.* microvoids) at *T*. The value of the Langmuir sorption capacity ($C_H^{'}$) is thus directly proportional to the amount of microvoids available in the polymer matrix.[119] Once all the available microvoids are filled, CO_2 enters the densely packed regions of the polymer (i.e. Henry's type sorption) which lead to its swelling.

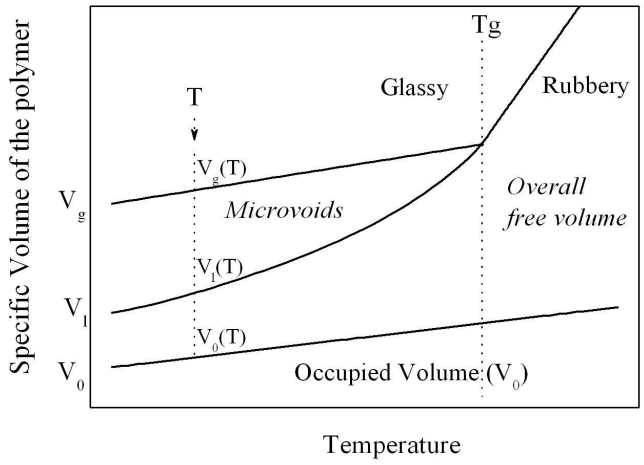

Figure 2. Schematic representation of the relationship between the specific volume of an amorphous polymer and the temperature.[119]

The DMS sorption model is very popular because it correlates with many features such as T_g, fractional free volume and d-spacing.[118,120] However there are also drawbacks to

that model. It lacks a solid molecular foundation and it does not have any information about volume dilation induced by gas molecules such as CO_2. In addition, Bondar *et al* [117] reported that the DMS parameters are sensitive to the pressure range under consideration, so that they cannot be considered as reliable predictors of what happens beyond the range of pressure fitted.

The other well-known model related to gas sorption in glassy polymers is the site-distribution (SD) model.[107] This model assumes that the sorption of gas molecules occur within a variety of sites distributed inside the polymer matrices. The free energy of gas molecule dissolution in the polymer should vary according to the size of the hole available for the insertion. By assuming the distribution of the hole volumes to be Gaussian, the free energy *G* of dissolution of gas molecules into the holes is also described by a Gaussian function (Eq. 9):

$$n(G) = n_o \exp\left(-\frac{(G - G_0)^2}{\sigma^2} \right) \tag{9}$$

with n being the number of sites and σ being the width of the distribution, which can be obtained from the volume of the penetrant V_g , the average hole volume V_{h0} , the shear modulus μ_s , the gas constant R, the temperature T_g where the free volume is frozen in and the bulk modulus B in the liquid state at temperature $T = T_g$ (Eq. 10):

$$\sigma = \frac{2\left(V_g^2 - V_{h0}^2\right)\mu_s}{3V_{h0}} \sqrt{\frac{2RT_g}{BV_{h0}}} \tag{10}$$

In Eq. 9, n_0 is a prefactor related to the number of holes (Eq. 11):

$$n_0 = \frac{1}{\sigma\sqrt{\pi}} \tag{11}$$

and G_0 is the free energy change caused by the dissolution of a gas molecule in an average hole of the polymer. The total concentration C of gas molecules inside the polymer matrix is given by the integration of the product over all energies of the number of sites and the thermal occupancy (Eq. 12):

$$C = \frac{1}{\sigma\sqrt{\pi}} \int_{-\infty}^{+\infty} \frac{\exp\left\{-(G-G_0)^2/\sigma^2\right\}}{1+\exp[(G-\mu)/RT]} dG \qquad (12)$$

where μ is the chemical potential of the dissolved gas, which is related to the pressure p by $\mu = \mu_0 + RT \ln p$. Eq. 12 can thus be considered as an implicit equation between the chemical potential μ (or the pressure p) and the total concentration C. Instead of the two different types of sorption assumed by the dual-mode sorption model, the SD model describes a single continuous distribution of sorption energies.

It should be noted that there are other much less-commonly used models such as Sanchez-Lacombe theory,[121] non-equilibrium lattice fluid (NELF) models,[122] free volume descriptions[123] which attempt to describe gas sorption in glassy polymers.

In experiments, the solubility is calculated directly from isotherms of the mass uptake vs the pressure.[27,28,118,124] Both DMS and SD models are able fit pressure-composition isotherms equally well.[62,64,112-114] In molecular simulations, there are several techniques available to calculate the solubility of a gas. They include thermodynamic integration,[125] umbrella sampling,[126] self-consistent histogram method[127,128] and the most-commonly used one which is called the Widom test-particle-insertion (TPI) method.[29,129-131]

1.2) Gas diffusion

The diffusion of gas molecules occurs inside the polymer membrane because of its chemical potential gradient inside the membrane. Consistent with Fick's first law, the flux goes from the highest to the lowest concentration region. In computer simulations, the well-known Einstein's equation of diffusion is usually used to calculate the self-diffusion coefficient *D* (Eq. 13).[132]

$$\left\langle \left| \mathbf{R_i}(t+t_0) - \mathbf{R_i}(t_0) \right|^2 \right\rangle = 6Dt \tag{13}$$

with the term on the left-hand side of Eq. 13 being the average mean-square displacement (MSD), *i.e.* the square of the distance over which the gas molecule has travelled between time-origin t_0 and time $t+t_0$. This equation is only really valid over long timescales, when gas molecules follow a random walk and have no memory of the previous steps. Gas diffusion can be classified into three different regimes based on the relationship between MSD and time. At very short times, the MSD is quadratic in time, ($\left\langle \left| \mathbf{R_i}(t+t_0) - \mathbf{R_i}(t_0) \right|^2 \right\rangle \propto t^2$). The gas molecules move freely until they hit the polymer atoms or walls of the microvoids. Following this initial very fast step, the gas molecules go through a slower diffusion regime called "anomalous regime", in which ($\left\langle \left| \mathbf{R_i}(t+t_0) - \mathbf{R_i}(t_0) \right|^2 \right\rangle \propto t^n ; n < 1$). Anomalous diffusion is caused by the polymer environment which prevents the gas molecules from following a random walk. However, over longer time intervals, the gas molecules can be considered as resuming a random walk, ($\left\langle \left| \mathbf{R_i}(t+t_0) - \mathbf{R_i}(t_0) \right|^2 \right\rangle \propto t$), and this is referred to as the "Fickian diffusion regime". In that case, Eq. 10 can be used to estimate *D* (Figure 3).

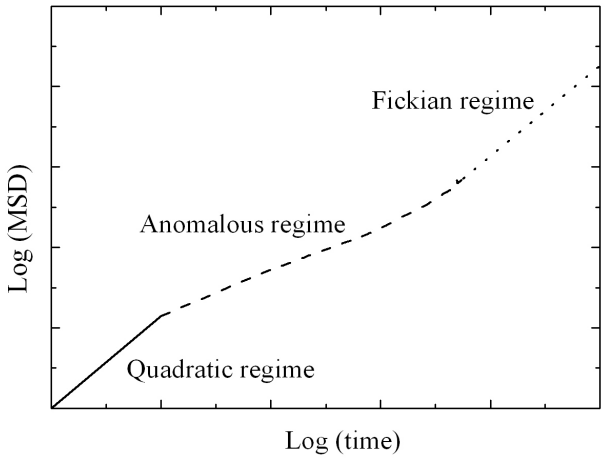

Figure 3. A schematic representation of the time dependence of the mean-square displacement (MSD) of a diffusing gas.[107]

In experiments, diffusion coefficients are calculated either by using the time-lag method or from the respective permeability and solubility data (Eq. 3).[34] The time-lag method[133] assumes that the equilibrium sorption of gases follows Henry's law and that the diffusion coefficient only depends on the temperature (Eq. 14):

$$D = \frac{l^2}{6\theta} \tag{14}$$

with l being the thickness of the membrane and θ being the diffusion time-lag constant obtained in uptake *vs* time plots by extrapolating the steady state part of the curve to the time *x* axis.

1.3) Plasticization

It is difficult to give an exact definition of plasticization but its existence is based on the observation of the increase in CO_2 permeability as a function of feed pressure.[132] This

occurs only when some critical level of CO_2-concentration is sorbed inside the polymer.[134] An increase in permeability enhances segmental mobilities, which decreases the diffusivity selectivity by opening gaps between the polymer chains. As a consequence, the polymer looses its gas selectivity.[27,28,31,65]

The pressure at which the increasing diffusivity compensates the decreasing solubility is usually called the plasticization pressure.[34,135] Bos *et al*[62,64,112-114] reported that there are no direct relationships between the plasticization pressure and the glass-transition temperature or the fractional free-volume of the polymer. Interestingly, all glassy polymers considered in their study were found to be plasticized by CO_2 at the same critical concentration of 38±7 cm^3(STP)/cm^3(polymer). There are several other works in the literature on the same subject. Ismail *et al*[134] presented a detailed review of plasticization effects in gas separation membranes and concluded that the investigation of correlations between molecular structure and plasticization will further enhance the fundamental knowledge in membrane separation technology.

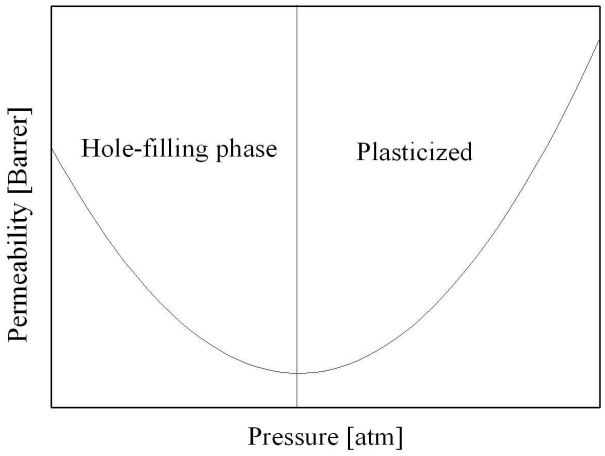

Figure 4. Behaviour of CO_2-induced plasticization in glassy polymers.[34]

In general, volume swelling is calculated experimentally as a change in length of the polymer sample as a function of the gas pressure by assuming that the swelling is isotropic. Methods such as dilatometry and optical interferometry are most commonly used to estimate volume swelling. [27,28,34,65,130, 32,124] It is also possible to measure the length change with the help of a high resolution video camera.[136] In simulations, volume-swelling can be calculated directly from the volume difference between a pure polymer matrix box and this same simulation box containing a known quantity of CO_2.

There are three main theories reported in the literature in order to explain plasticization: [62,64,112-114, 27,28,31,65,118,124, 135]

1) Volume swelling starts immediately after the first molecule of CO_2 enters the polymer membrane, *i.e.* each CO_2 molecule entering the polymer matrix actually contributes to the volume swelling, and there are also secondary volume relaxations at longer time scales. The delay in dilation kinetics is not related to the unrelaxed free volume of the glassy polymers but rather to the mass transport inside the polymer membrane of a certain thickness. This hypothesis is based on the results obtained for the polyimide PIXU218 by Wessling *et al.*[27,28,31,65,118,124]

2) With respect to the site distribution model,[62,64,112-114] a gas molecule of volume V_g (considered as a stiff sphere, which cannot be the case for CO_2) has to be inserted into a hole of volume V_h in the polymer matrix and the partial molar volume of the gas in the polymer V_p is given by Eq. 15a, where γ is related to Poisson's ratio v by Eq. 15b:[124]

$$V_p = \gamma\left(V_g - V_h\right) \tag{15a}$$

$$\gamma = 3\frac{1-v}{1+v} \tag{15b}$$

There are two situations to be considered here. If $V_g \leq V_h$, the molecule dissolves into the hole without any strain on the polymer. On the other hand, if $V_g > V_h$, the gas molecule has to be squeezed into the hole and hence the polymer has to adjust to dissolve the molecule, *i.e.* the polymer has to swell to accept the penetrant. In this model, the volume of the site occupied by a small molecule is related via elastic distortions to the dissolution energy into this site. The overall volume change ΔV for a glassy polymer is then obtained by averaging over the partial molar volumes of the dissolved molecules in the various sites (Eq. 16):

$$\Delta V = \int_{-\infty}^{+\infty} V_P(G) c_G dG \tag{16}$$

where G is the free energy of dissolution (see Eq. 9) and c_G is the partial concentration of molecules in sites lying within a free energy window $(G, G+dG)$.

3) In the DMS model at low gas pressures, the solubility of CO_2 is dominated by Langmuir-type sorption (Figure 1 & 2). When all the microvoids have been filled, the polymer has to swell to adopt more CO_2 molecules, similar to the volume change ΔV needed for dissolving a gas molecule in a rubbery polymer. ΔV is then directly proportional to the concentration of CO_2 in the densely packed regions of the matrix.[27,28]

In the DMS[27,28] and SD models, [62,64,112-114] volume swelling starts only after all the microvoids which are bigger than the size of the penetrant have been filled. However for Wessling *et al.*[27,28,31,65,118,124], there is no relationship between the microvoids available in the polymer and volume swelling.

The present work concentrates on trying to better understand the plasticization phenomena at the molecular level by measuring sorption, diffusion and CO_2-induced volume swelling in some glassy polymer matrices.

Chapter 2.

Materials and Methods

2.1) Materials selection

Some interesting candidates with a good CO_2 solubility are known to be fluorinated polyimides,[27,28,34,65,130] polycarbonate and ether-based polymers.[3] In this context, fluorinated polyimides have attracted plenty of attention because of their excellent mechanical, chemical, thermal and gas transport properties.[51] Fluorinated polyimides are used in industries because of their low dielectric constants, low thermal expansions and high glass transition temperatures.[3] The low polarity of fluorine atoms reduces the refractive index and electrical permittivity.[137] These attractive features mean that fluorinated polyimides are used in a wide range of applications ranging from electronics,[138,139] electrical insulations,[140] optical engineering,[141] radiation resistance[27,52] and aviation[3] to gas filtration membranes.[7,8] Their gas permeation properties are enhanced by the fluorine atoms, which disrupt the effective packing of the polymer and hence increase the free volume inside the polymer matrices.

Fluorinated polyimides can be synthesised either by solution or by melt polymerization.[142] Melt polymerization has the advantage of shortening the synthesis process but it is limited to fusible diamines and dianhydrides. On the other hand, solution polymerization can be used to synthesize a whole range of polyimides. In the middle of the 1980s, polyimides based on the 2,2-bis(3,4-dicarboxyphenyl) hexafluoropropane dianhydride (6FDA) were prepared at room temperature using solution polymerization in dimethyl acetamide (DMAc) as a solvent (Figure 5).[137-139] The characteristics of these polyimides were analysed and their densities, thermal, mechanical and permeation properties were reported in the literature.[3]

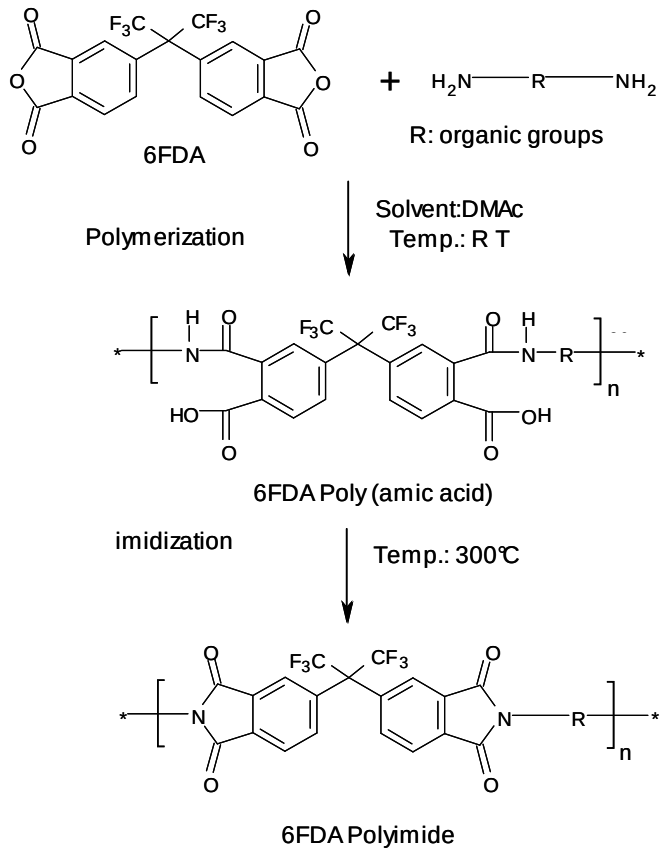

Figure 5. Synthesis scheme for 6FDA polyimides using solution polymerization.[3]

Following their synthesis, many researchers investigated their applications in microelectronics,[141] dosimetry measurements, [140] optical engineering[27,52] and gas separation membranes.[29,44,55,61,67] We have selected three fluorinated homopolyimides from the 6FDA family, namely 6FDA-6FpDA, 6FDA-6FmDA and 6FDA-DAM for our studies. Their actual names are poly((4,4'-[2,2,2-trifluoro-1-(trifluoromethyl)ethane-1,1-diyl]dianiline}-alt-{5,5'-[2,2,2-trifluoro-1-(trifluoromethyl)ethane-1,1-diyl]bis(isobenzofuran-1,3-dione)}) (6FDA-6FpDA), poly((3,3'-[2,2,2-trifluoro-1-(trifluoromethyl)ethane-1,1-diyl]dianiline}-alt-{5,5'-[2,2,2-trifluoro-1-(trifluoromethyl)ethane-1,1-diyl]bis(isobenzofuran-1,3-dione)}) (6FDA-6FmDA) and poly((2,4,6-trimethyl-m-phenylenediamine)-alt-{5,5'-[2,2,2-trifluoro-1-

(trifluoromethyl)ethane-1,1-diyl]bis(isobenzofuran-1,3-dione)}) (6FDA-DAM). The chemical structures of these three polyimides are shown in Figure 6. It should be noted that these polyimides are sometimes called with different names: 6FpDA is also known as BAAF,[37,38] 6FAP,[143] 4APF[46] or BAHF[35] , DAM can be referred to as TrMPD[54,59,63,144] or 3MPDA[143] and 6FmDA corresponds to 3APF. [32,33,57]

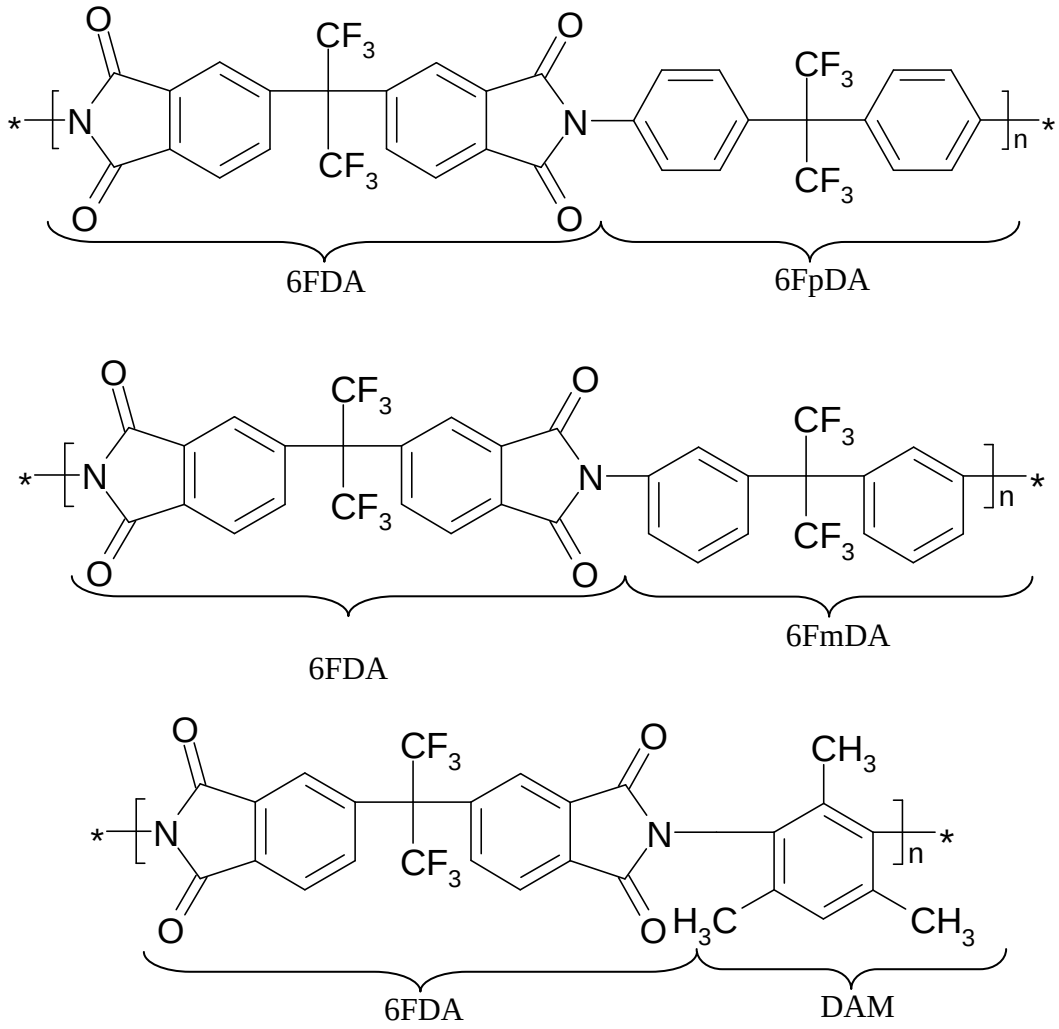

Figure 6. Chemical structures of the 6FDA-6FpDA, 6FDA-6FmDA and 6FDA-DAM.

These fluorinated polyimides have already been synthesised and characterised. There are consistent experimental results on their gas transport properties which are reported in the literature,[27,28,31-33,35,53,57,65,118,130,139] and which will be presented in more detail in the next section.

2.2) Bibliographic information

2.2.1. 6FDA-6FpDA

2.2.1.1. Density

The density of polymer samples can be measured using several techniques.[45,54,36,63,61,29,52,42,145,39,38,70,32] The flotation method[146] requires a liquid of known and adjustable density in which the sample is placed. The density of the liquid is adjusted by adding an aqueous solution such as potassium iodide until the sample either begins to sink, to float or is suspended in the liquid. In the latter case, the density of the object is then equal to that of the liquid. Alternatively, the density can be calculated by the buoyancy method from the weight difference of the polymer sample in air and in a fluid of known density. Another approach is that of the density gradient column method,[147] in which a column of liquid varying in density with height is used. A sample is placed in the liquid and observed in order to determine at which vertical level the sample remains suspended. The density of the liquid at that level is equal to the density of the sample, and that value is determined using pre-calibrated standards of known density.[148]

Table 1 gives the various densities and methods reported in the literature for 6FDA-6FpDA. In most cases, the density is measured around 25°C. The average value of the density at room temperature is 1.477±0.003 g cm^{-3}

Density (g/cm^3)	Temperature (°C)	Method	Reference
1.466	-	Density gradient column	[45]
1.48	-	-	[54]
1.478	25	-	[36]
1.480	-	Flotation with KI	[63]
1.474	25	Flotation with ZnNO3	[61]
1.480	-	-	[29]
1.471	-	-	[52]
1.477	-	-	[42]
1.477	-	Buoyancy method	[145]
1.472	25	Density gradient column	[39]
1.47	25	Density gradient column	[38]
1.466	25	Density gradient column	[70]
1.504	-	Density gradient column	[32]

Table 1. Experimental densities reported in the literature for 6FDA-6FpDA.

Figure 7 shows the digitized values of the specific volume (1/density) as a function of temperature reported by Costello *et al.* for 6FDA-6FpDA.[118] The lines on the plot indicate the different regimes between the thermal transitions. 6FDA-6FpDA has sub-glass-transition temperatures around 25 °C, 118.5 °C and 216.5 °C (i.e. 298 K, 391.5 K and 489.5 K) and the glass transition temperature around 320°C (593 K).

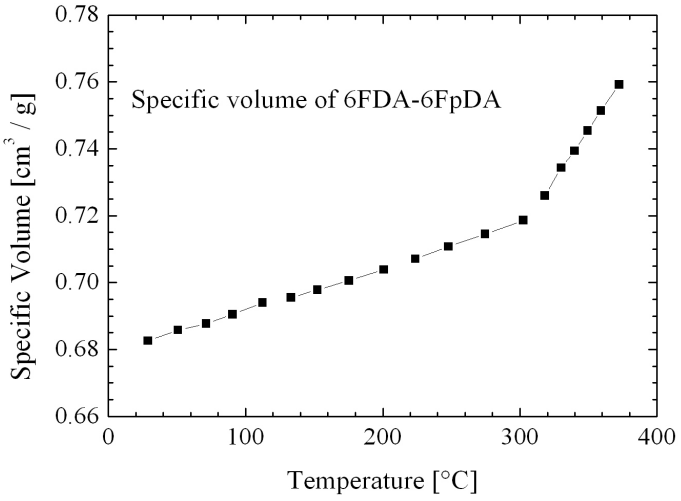

Figure 7. Temperature dependence of the specific volume for 6FDA-6FpDA.[118]

2.2.1.2. Glass-transition temperatures

The glass-transition temperature T_g is a very important parameter for polymers. Figure 2 showed the T_g-dependence of the amount of unrelaxed free volume in amorphous polymers.[119] Costello *et al.* report that the gas transport properties are closely related to the T_g and sub-T_g temperatures of the polymer.[118] There are different techniques such as differential scanning calorimetry (DSC), thermal mechanical analysis (TMA) and dynamic mechanical analysis (DMA) to estimate the T_g.[45,54,36,63,61,29,52,42,145,39,38,70,32] However, the measure of T_g relies on many parameters such as *e.g.* heating rate,[149] and the glass-transition temperature of the same polymer can vary between different studies.

A range of T_g, with an average value (± standard error) of 588±4 K, has been reported for 6FDA-6FpDA (Table 2).

T_g (K)	Method	Reference
593	DSC	45
578	DSC	54
615	TMA	36
578	DSC	63
593	DMTA	118
573	Bilayer bending technique	150
592	DSC	151
573	DSC	61
581	DSC	130
605	DSC	38
573	DSC	55
593	DSC	56
595	DMA	145

Table 2. Glass transition temperatures reported in the literature for 6FDA-6FpDA.

2.2.1.3. Fractional free-volume (FFV) and d-spacing

An empirical method introduced by Bondi is widely used to calculate the fractional free-volume in polymers.[152] According to Bondi, the zero point volume (volume at 0 K called V_0) is related to the Van der Waals volume V_W by the following approximation (Eq. 17):

$$\frac{V_0}{V_w} = 1.3 \tag{17}$$

V_W is defined as the total space occupied by the atoms constituting the molecule and is calculated from the atomic radii of the corresponding elements. Then the fractional free volume (*FFV*) is calculated from V_0 using Eq. 18:

$$FFV = \frac{V - V_0}{V} \tag{18}$$

with V being the actual volume of the polymer. Even though it is empirical, this unitless quantity gives a good measure of the amount of free volume available per unit volume of polymer. The calculated *FFV* for 6FDA-6FpDA reported in the literature range from 0.175 to 0.190,[31,45,56] depending on V and on the estimated V_0.

Costello *et al.*[118] extrapolated the density versus temperature plot to calculate the zero-point density and obtain V_0. They report the FFV of 6FDA-6FpDA as being 0.272. Heuchel *et al* [67] prepared bulk models of 6FDA-6FpDA using a low-density approach and calculated the *FFV* with a geometrical technique, reaching a value of 0.375. Both these values are not in agreement with the FFV calculated using Bondi's group contribution method. Wang *et al*[70] also prepared bulk models of 6FDA-6FpDA using a low-density approach and estimated the fractional cavity volume *(FCV),* which is equal to the *FFV* occupied only by spherical cavities, using another geometrical approach. They report a *FCV* of 0.110 and an average hole size of 6.76 Å.

The average interchain spacing for an amorphous polymer is estimated by its *d-spacing*. Experimentally, *d-spacings* are obtained using wide angle X-ray scattering (WAXS) or small angle X-ray diffraction (SAXD).[44,144] This is a measure of the packing of the polymer, since a polymer with tight packing has a small *d-spacing* and vice versa. The average *d-spacing* is calculated from the X-ray wavelength λ = 1.54 Å, corresponding to that of the CuK_α radiation, and from the mode of the large X-ray scattering peak using Bragg's law (Eq. 19), with θ being the angle between the incident ray and the scattering planes:

$$\lambda = 2(d - spacing)\sin\theta \tag{19}$$

The *d-spacing* for 6FDA-6FpDA using WAXS is found to be 5.9 Å.[44]

2.2.1.4. CO_2 transport properties

There is a large amount of experimental work which has been devoted to the study of CO_2 transport in 6FDA-6FpDA. Its high gas solubility, good selectivity for CO_2 and relatively high resistance with respect to plasticization attract the researchers. [28,32,36,130,39,42,118,54,40] Table 3 shows the various CO_2 transport data reported in the literature for 6FDA-6FpDA.

Table 3 shows that the experiments are done under different temperatures and pressures conditions and that a wide range of solvents have been used to cast the 6FDA-6FpDA membranes. The drying procedure can also very much vary. Hence the reported values depend strongly upon the sample preparation procedures and measurement conditions, as will be shown below. [118,27,28,31,40,32,33,56,57,130]

Authors	Experimental conditions	P_{CO_2}	D_{CO_2}	S_{CO_2}	Solvent
Coleman *et al.* [27]	10 atm 35°C	63.9	10.4	4.81	CH_2Cl_2
Kim *et al.* [32]	2 atm 35°C	70	-	-	NMP
Matsumato *et al.* [36]	4.87 atm 25°C	45	-	-	DMAc
Wang *et al.* [130]	10 atm 35°C	-	8.4	6	CH_2Cl_2
Hibshman *et al.* [39]	4 atm 35°C	20.3	2.09	7.36	DMAc
		77.3	5.83	10.1	
Cornelius *et al.* [42]	4 atm 35°C	49.2	4.08	9.02	DMAc
Costello *et al.* [118]	10 atm 35°C	-	-	5	CH_2Cl_2
Tanaka *et al.* [54]	10 atm 35°C	51.2	8.1	4.7	DMAc
Recio *et al.* [40]	1 bar 30°C	66.8	-	-	DMF
		68.4	-	-	DMAc
		76.5	-	-	THF
		81.4	-	-	DCM
		72.1	-	-	Ac

Table 3. CO_2 transport properties in 6FDA-6FpDA. Permeability P_{CO2} in Barrers, diffusion coefficient D_{CO2} in 10^{-8} cm^2/s, solubility coefficient S_{CO2} in $cm^3(STP)/cm^3(polymer)$ atm.

Costello *et al.*[118] studied the temperature dependence of CO_2 transport in 6FDA-6FpDA. This study reveals the effects of sub-T_g temperatures on gas permeabilities. As in other polymers, the permeability of CO_2 increases with increasing temperature in 6FDA-6FpDA but around 118.5°C (a sub-T_g temperature), a higher thermal expansivity presumably serves to increase the flux of CO_2 molecules inside the membrane. This is shown by an obvious change in the slope of the CO_2 permeability *vs* temperature plot. Once the chain motions begin to increase with the temperature, the polymer matrix starts relaxing at a higher rate. The Langmuir capacity is reduced dramatically and hence the solubility of CO_2 decreases with increasing temperature. The decrease in solubility is compensated by the increase in diffusivity. The increased thermal motion of the polymer and increased CO_2 flux inside the polymer matrix causes the CO_2 diffusion coefficient to increase with temperature thus leading to higher permeabilities. The same authors also reported dual-mode sorption parameters for 6FDA-6FpDA at different temperatures (Table 4):

Temperature (°C)	$k_d \left[\frac{cm^3(STP)}{cm^3 atm}\right]$	$C_H' \left[\frac{cm^3(STP)}{cm^3}\right]$	$b \left[\frac{1}{atm}\right]$
35	2.3	31	0.69
75	1.1	23	0.25
100	0.64	23	0.13
120	0.68	16	0.11

Table 4. Temperature dependence of the dual-mode sorption parameters for CO_2 in 6FDA-6FpDA within the pressure range of 0 to 10 atm.[118]

Coleman *et al.*[27,28] investigated the effect of high-pressure CO_2 exposure on gas transport in 6FDA-6FpDA. Figure 8 shows digitized plots of their sorption and desorption isotherms. The polymer membrane was exposed to 60 atm CO_2 for 2 to 3 weeks to get steady-state permeation before carrying out the desorption. They found that exposure to 60 atm results in significant plasticization and volume relaxations which eventually enhance the solubility during desorption.

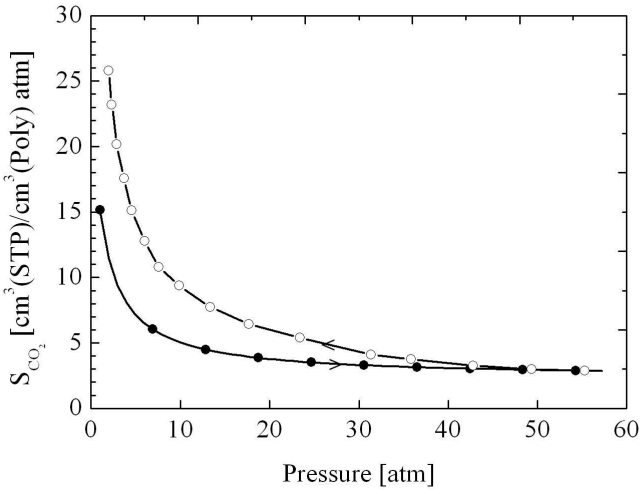

Figure 8. CO_2 sorption and desorption isotherms for 6FDA-6FpDA at 35°C. The line with full circles is the sorption isotherm, while that with white circles is the desorption isotherm following conditioning with CO_2 at 60 atm.[27]

Fuhrman *et al.*[31] reported the thermal hysteresis of gas permeation in 6FDA-6FpDA. Thermal quenching of polymer membranes from temperatures above T_g increases slightly the amount of free volume, and P_{CO2} increases with higher quenching temperatures compared to the annealed samples. These variations are attributed to the differences in the microstructures of the polymer membranes, when subjected to different thermal histories.

Kim *et al.*[32,33,56,57] analysed the effect of physical ageing and found that gas permeabilities decrease with increasing ageing time. On the other hand, even in the aged membranes, exposure to CO_2 increases gas permeabilities because of the induced plasticization.

Recio *et al.*[40] explained the effect of the solvent used to cast the polyimide films as being due to the difference between the casting temperature and the solvent boiling point. When a membrane is cast at a temperature far below the boiling point of the solvent, it needs a longer time to eliminate it, thus allowing the polymer chains to relax and to attain a state of lower fractional free volume. Consequently, the permeability is lower.

Some molecular simulations about gas transport in 6FDA-6FpDA have been reported in the literature but they were either restricted to very short simulation times (60 ps) or used low density approaches to create the models, *i.e*. methods which are known to lead to a bias in the chain conformations.[153] These simulations also used a simple spherical representation for CO_2, [67,69,70,154] which is far from its actual linear geometry.

Wang *et al*[130] reported diffusivity and solubility for various gases in 6FDA-6FpDA. The different forms of diffusion coefficients (D_{eff}, D_{avg}, D_{app} and D_D) have been calculated for

CO_2 and also for other gases. The effective diffusion coefficient D_{eff} is measured as a function of gas flux across the polymer membrane and the average diffusion coefficient D_{avg} is given by the average of the diffusivity over a concentration range. The apparent diffusion coefficient D_{app} is calculated using the time-lag method by extrapolating the steady-state part of the permeation to the time axis in the pressure *vs* time plot. Henry's mode diffusion coefficient D_D is estimated considering the Langmuir concentration inside the polymer matrix as being only partially mobilized. This coefficient is calculated both from the normalized flux of Henry's type sorption (D_D and from the time lag method ($D_{D,t}$). The values reported for CO_2 diffusion are as follows: D_{eff} = 17, D_{avg} = 8.4, D_{app}= 5.3, D_D = 26 and $D_{D,t}$ = 24 in the units of 10^{-8} cm^2/s.

These studies confirm that there are various factors such as solvent, drying conditions, temperature, thermal hysteresis, pressure, CO_2 exposure and physical ageing which affect CO_2 transport in 6FDA-6FpDA. So, it is important to consider each and every step from the synthesis to the gas transport measurements for the polymer membranes under study. It is actually really difficult to monitor all these parameters together under different experimental conditions. In this context, molecular simulations, where solvent, ageing, etc. can be controlled, can bring some useful insights in to the mechanisms underlying CO_2 transport in these systems.

2.2.2. 6FDA-6FmDA

2.2.2.1. Density

6FDA-6FmDA is a structural isomer of 6FDA-6FpDA (see Figure 6). 6FDA-6FmDA tends to pack better than its *para*-isomer and hence exhibit higher density.[27,28,31,118] However,

because of its poor gas transport properties,[27,28,31,118] there are not many experiments devoted to 6FDA-6FmDA. It is interesting to understand how two structural isomers can have such differences with respect to gas transport.

To our knowledge, only two experimental densities can be found in the literature for 6FDA-6FmDA. Husk *et al.*[155] report the value of 1.433 g/cm^3 and Coleman *et al.*[27] that of 1.493 g/cm^3. The latter is actually more often reported. Both experiments use the density gradient column method. In addition, Costello *et al.*[118] also report the specific volume (1/density) of 6FDA-6FmDA as a function of the temperature, which is shown in Figure 9. The lines on the plot indicate the different regimes between the thermal transitions. 6FDA-6FmDA has a sub-glass-transition temperature around 149°C (i.e. 422 K) and a glass-transition temperature around 257°C (530 K).

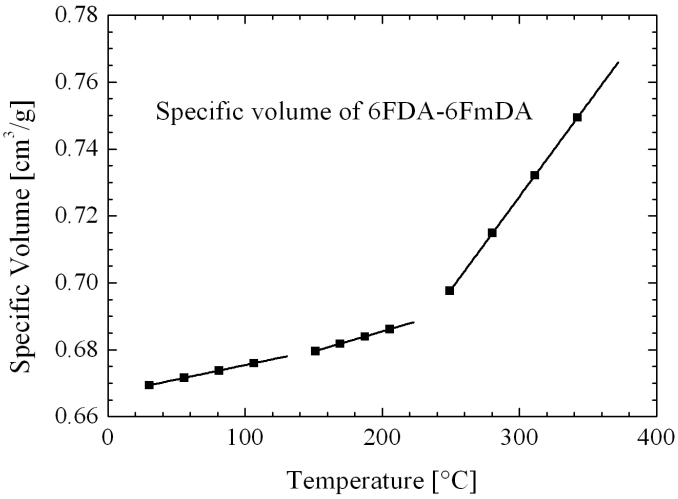

Figure 9. Temperature dependence of the specific volume for 6FDA-6FmDA.[118]

2.2.2.2. Glass-transition temperatures

There are individual experimental studies which report the T_g of 6FDA-6FmDA as ranging from 508 K to 603 K, with most of the results being around ~530 K.[45,150,151,155] As

noted above, Costello *et al.*[118] also show that 6FDA-6FmDA exhibits a sub-T_g temperature around 422 K, which they claim is difficult distinguish as it is "quite close to" the T_g, despite the over 100 K difference. This sub-T_g transition has an impact on transport properties when the polymer film is exposed to temperatures higher than 422 K.

2.2.2.3. Fractional free-volume and d-spacing

The effective packing of 6FDA-6FmDA reduces the amount of void space inside the polymer matrices, so it exhibits a lower fractional free volume.[27,28,31,118] In Bondi's group contribution method for calculating the *FFV*,[152] the value of V_0 is same for both the *para* 6FDA-6FpDA and *meta* 6FDA-6FmDA isomers, whereas the values of the actual volume V vary because of the different densities. The higher density of 6FDA-6FmDA will thus result in a lower FFV in this empirical calculation.

In the case of Costello *et al*[118], they prefer using the linear-fit extrapolation of the density to estimate V_0 (which is then different between both isomers) and which leads to a FFV of 0.225 for 6FDA-6FmDA. Wang *et al*[70] estimate the fractional cavity volume (*FCV*) as 0.103 and average hole size of 6.34 Å. It is important to note that, in all types of calculations reported in the literature, 6FDA-6FpDA has a higher *FFV* than its *meta*-isomer. The *d-spacing* value for 6FDA-6FmDA is 5.7 Å.[27,28,65,118]

2.2.2.4. CO_2 transport properties

Unlike its para-isomer, 6FDA-6FmDA has a very low permeability with respect to CO_2. [27,28,31,118] The major difference between both isomers comes from their diffusion coefficients, [27,28] since D_{CO2} for 6FDA-6FmDA is approximately 10% of D_{CO2} for 6FDA-6FpDA. The solubility values are comparable between both isomers:[65] (6FDA-6FpDA = 4.8 cm^3(STP)/cm^3(polymer) atm and 6FDA-6FmDA = 2.9 cm^3(STP)/cm^3(polymer) atm at 10 atm

and 35°C). The differences in diffusion are thought to be related to both effective packing and sub-T_g motions. 6FDA-6FpDA has a sub-*Tg* temperature around 300 K, which is close to the experimental temperature and it is likely that the subtle segmental motions of individual groups enhance the diffusion of gas molecules.[118]

Compared to 6FDA-6FpDA, there has been quite a limited amount of interest devoted to 6FDA-6FmDA because of its low permeability. However, Coleman *et al*[27,28] have also studied the conditioning effect of CO_2 in 6FDA-6FmDA. Figure 10 shows a digitized graph of the reduced permeability of CO_2 before and after conditioning with 60 atm of CO_2 for 2-3 weeks. The reduced permeability is the ratio of the permeability at a specific pressure with respect to the permeability of the unconditioned film at 10 atm pressure, which is 5.6 Barrers for 6FDA-6FmDA at 35°C. The solubility and diffusion coefficients are also reported under the same conditions as being 2.89 cm^3(STP)/cm^3(polymer) atm and 1.34 10^{-8} cm^2/s respectively. The decrease in permeability at lower pressures in the untreated membrane is due to the decrease in solubility (*i.e.* the saturation of microvoids). However, at pressures above 10 atm, the plasticization induced by CO_2 increases the diffusivity, compensates the effect of decreasing solubility and results in an overall increase in permeability. This conditioning effect (exposure to CO_2 at 60 bar for 2 to 3 weeks) substantially increases the permeability of 6FDA-6FmDA by a factor of 7 to 10.

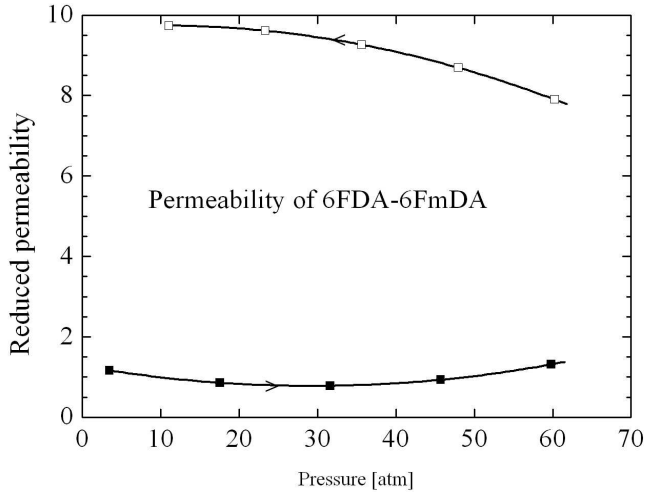

Figure 10. Reduced permeability of CO_2 in 6FDA-6FmDA at 35°C. Full squares refer to sorption and open squares to desorption following conditioning at 60 atm of CO_2.[27]

Costello *et al.*[118] studied the effect of temperature on gas transport in 6FDA-6FmDA and reported the dual-mode sorption parameters for CO_2 sorption at different experimental temperatures (Table 5):

Temperature [137]	$k_d \left[\frac{cm^3(STP)}{cm^3 atm}\right]$	$C_H' \left[\frac{cm^3(STP)}{cm^3}\right]$	$b \left[\frac{1}{atm}\right]$
35	1.4	22	0.60
75	0.70	16	0.23
100	0.75	5.8	0.31
120	0.67	3.2	0.33

Table 5. Temperature dependence of the dual-mode sorption parameters for CO_2 sorption in 6FDA-6FmDA within the pressure range of 0 to 10 atm.[118]

Permeability is also found to increase with increasing temperature. The slope of the permeability vs. temperature plot increases after the sub-T_g temperature of 422 K, which is assumed to be related to motions in 6FDA-6FmDA side-chains.

Fuhrmam *et al.*[31] investigated the effect of thermal history on gas permeation in 6FDA-6FmDA. They found that the systems quenched from temperatures above T_g, i.e. T_g + 15°C exhibit higher permeabilities and slightly higher *FFV* than the annealed system. The substantial change in permeability is much higher in 6FDA-6FmDA than for its *para*-isomer, because of the reduced restrictions in intersegmental motions in the quenched samples. However, these effects are mitigated over longer timescales (> 3 months duration).

CO_2 permeability is thus higher in 6FDA-6FpDA than in 6FDA-6FmDA under all circumstances. The solubility of CO_2 is not very different, but the diffusion is much faster in the *para*-isomer than in the *meta*-isomer. Due to its effective packing and restricted intersegmental motions, 6FDA-6FmDA has poorer gas transport properties. This is consistent with the fact that in 6FDA-6FpDA, the excess free volume and subtle side-chain motions at lower temperatures are thought to be related to the enhancement of gas transport.

2.2.3. 6FDA-DAM

2.2.3.1. Density

The density of 6FDA-DAM is comparatively lower than the other two fluorinated polyimides under study since the three methyl substitutions in the smaller diamine structure inhibit the effective packing of the polymer.[30] There are several experimentally-reported densities for 6FDA-DAM, ranging from 1.300 g/cm^3 to 1.353 g/cm^3 with an average of

1.339±0.007 g/cm^3.[35,49,54,56,57,63,156] Most of them[35,49,54,63,156] have been measured using the flotation method.

Kim *et al.*[56,57] studied the ageing-dependence of bulk density in 6FDA-DAM using refractive index as a monitor. The plot shown in Figure 11 shows the effect of ageing on density. It tends to increase the density more rapidly in thin films than in thick films.[157]

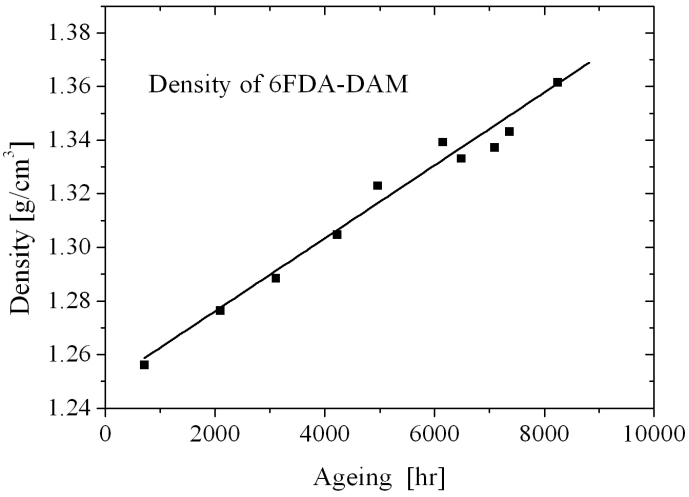

Figure 11. Ageing time dependence of density of 6FDA-DAM at 35°C.[57]

2.2.3.2. Glass-transition temperatures

The glass transition temperature of 6FDA-DAM is reported as spanning a range between 650 K to 669 K with an average of 656±4 K.[32,35,49,54,56,63,156] The higher T_g of 6FDA-DAM is due to the reduction in the number of flexible bonds in its backbone compared to both other polymers under study. The smaller DAM diamine has a rigid phenyl ring with methyl substitutions, but the rotations of side-chain methyl groups apparently do not affect the rigid polymer backbone.[30,54]

2.2.3.3. Fractional free-volume and d-spacing

The steric hindrance of substituted methyl groups increases the *FFV* of the 6FDA-DAM matrix compared to 6FDA-6FpDA and 6FDA-6FmDA.[56] The fractional free volume

estimated using Bondi's group contribution method is reported as being 0.190 in the literature.[27,28,54,56,70,118] The *d-spacing* is equal to 6.5 Å,[144] which means that the average interchain distance is larger than for the other two polyimides.

2.2.3.4. CO_2 transport properties

Due to its high gas transport ability combined with an acceptable selectivity for various gas mixtures, 6FDA-DAM is a good material for gas separation. Table 6 reports all published data for CO_2 transport in 6FDA-DAM:

Author	Experimental conditions	P_{CO_2}	D_{CO_2}	S_{CO_2}	Solvent
Yeom *et al.* [156]	10 atm 35°C	467	26	180	DMAc
Tanaka *et al.* [30]	10 atm 35°C	431	54	80	DMAc
Fritsch *et al.* [49]	1 atm RT	637	23	277	NMP/THF
Islam *et al.* [59]	2 atm 50°C	570	-	-	m-cresol
Matsui *et al.* [144]	0.26 atm 60°C	870	-	-	DMAc/THF
		900	-	-	
Kim *et al.* [32]	2 atm 35° C	299	-	-	NMP

Table 6. CO_2 transport properties in 6FDA-DAM. Permeability P_{CO2} in Barrers, diffusion coefficient D_{CO2} in 10^{-8} cm^2/s, solubility coefficient S_{CO2} in cm3(STP)/cm^3(polymer) atm.

The larger *d-spacing* value and the higher fractional free volume are the reasons for the higher solubility and diffusivity of gas molecules in 6FDA-DAM.[32,33,56,57] The methyl side chains prevent effective packing, which results in an enhancement of gas diffusion and the microvoids created because of the loose packing increase the solubility.

Wind *et al*[43,124] investigated the effect of chemical cross-linking on the gas transport properties of 6FDA-DAM. They reported the dual-mode sorption parameters for CO_2 transport at 35°C (Table 7). They also studied the effect of a thermal treatment on sorption and volume dilation in chemically cross-linked (6FDA-DAM:DABA 2:1) polymers and found

that the samples annealed at higher temperature have a lower volume dilation and higher gas solubility. The Langmuir sorption capacity (C_H') increases as well with the increasing annealing temperature.

Temperature (°C)	$k_d \left[\frac{cm^3(STP)}{cm^3 atm}\right]$	$C_H' \left[\frac{cm^3(STP)}{cm^3}\right]$	$b \left[\frac{1}{atm}\right]$
35	2.18	55	0.42

Table 7. Dual-mode sorption parameters for CO_2 sorption in 6FDA-DAM at 35°C within the pressure range of 0 to 25 atm.[43]

There is a computer simulation study by Hölck *et al.*[69] on CO_2 sorption induced volume dilation which includes 6FDA-DAM in addition to polysulfone. However, the authors use a low-density approach to prepare the polymer matrices, they study the sorption and volume-swelling isotherms under very short simulations (300 ps) and they also artificially swell the polymer samples by pre-inserting an estimated quantity of CO_2 inside the polymer matrix. Furthermore, it is likely (although the authors do not give any information about this specific point) that a spherical model is used for CO_2 in this study.

These three 6FDA-based polyimides have completely different CO_2 transport properties, and a detailed study at the molecular level would help to understand CO_2 sorption, volume dilation and plasticization phenomena. However Bos *et al*[132] already concluded that there is no relationship between any of the physical properties of the polymer and plasticization. Instead, all glassy polymers under consideration are plasticized at the same critical concentration of CO_2 equal to 36±7 cm^3 (STP)/cm^3.[132] It is worth checking whether the plasticization behaviour of our 6FDA-based polyimides is really independent of the polymer properties.

2.3) Molecular modelling

2.3.1. General principles and integration algorithm

Molecular modelling provides a picture of the systems under study at the atomistic level, in order to study their static and dynamic properties. Molecular dynamics (MD) simulation, which is based on assumptions of classical mechanics, is one of the important computational technique to model atomistic level systems.[111,158,159] These simulations are in many ways similar to real experiments as, in the same way, MD simulations also have sample preparations procedures, validation steps, analyses and statistical averaging.

To measure an observable macroscopic property using MD simulations, it is necessary to develop representative structures of the experimental conditions. In order to express the structures as a function of positions and velocities at time *t*, Newton's equations of motions are solved for all (*i*= 1,... N) atoms in a system (Eq. 20):

$$\mathbf{F}_i(t) = m_i \frac{\partial^2 \mathbf{r}_i(t)}{\partial t^2} \quad with\ i = 1....N. \tag{20}$$

with the forces ($\boldsymbol{F}_i(t)$) being the negative derivatives of the potential energy $U(\boldsymbol{r}_1(t),\boldsymbol{r}_2(t),\boldsymbol{r}_3(t),...,\boldsymbol{r}_N(t))$ (Eq. 21):

$$\mathbf{F}_i(t) = -\frac{\partial U(\mathbf{r}_1(t), \mathbf{r}_2(t), \mathbf{r}_3(t), ..., \mathbf{r}_N(t))}{\partial \mathbf{r}_i(t)} \tag{21}$$

The equations are solved simultaneously in successive discrete time-steps Δt for all the atoms in the system under a given set of conditions (*i.e.* constant temperature, pressure and number of atoms (*NPT*), constant temperature, isotropic pressure *p* and number of atoms (*NpT*), constant temperature, volume and number of atoms (*NVT*) or constant temperature, volume and energy (*NVE*)) and a given simulation time. Molecular configurations are stored

regularly over the total simulation time. The integration time-step Δt should be smaller than the fastest vibrational frequencies in the system under study. For this reason Δt is normally of the order of 10^{-15} s.

In order to solve Newton's equations of motion for a many-body system, some approximations are often made:-

1) In MD simulations, atoms are considered as point masses and the electrons are considered to be in their ground state. Electronic degrees of freedom are thus not taken into account.

2) Van der Waals interactions are generally ignored beyond a certain cut-off distance. Long-range Coulombic interactions are calculated using Ewald sums.

3) Periodic boundary conditions are generally used in order to avoid boundary artifacts.

4) High frequency vibrational modes are usually removed using rigid constraints in MD simulations in order to increase the time-step of the simulations and to avoid problems due to poor equipartition of kinetic energy.[160]

There are many computer simulation packages available on the market to carry out MD simulations. We have mainly used the well-established and documented *gmq* code[161] for our simulations. The general structure of the use of the *gmq* program in this work is presented in the following flowchart:

gmq suite of programs

Step 1. Initial data
(starting coordinates, force field parameters, partial charges)

-

Step 2. Generation of decorrelated chain structures
(PMC-MD single chain method)

-

Step 3. Preparation of bulk models
(Introduction of the full potential)

-

Step 4. Molecular dynamics simulations
(Newton's equations of motion)

-

Step 5. Output
(Analyses at required temperatures and pressures)

The *gmq* code uses the leap-frog form of the Verlet algorithm[162,163] to solve Newton's equations of motion numerically. The leap-frog algorithm (Eq. 22 and 23) uses positions $\boldsymbol{r}_i$ at time t and "velocities" $\boldsymbol{v}_i$ at time $t-\frac{\Delta t}{2}$; it updates positions and velocities using the forces $\boldsymbol{F}_i(t)$ determined at time t (see Eq. 21):

$$\mathbf{v}_i(t+\frac{\Delta t}{2}) \approx \mathbf{v}_i(t-\frac{\Delta t}{2})+\frac{\mathbf{F}_i(t)}{m_i}\Delta t \tag{22}$$

$$\mathbf{r}_i\left(t+\Delta t\right) \approx \mathbf{r}_i(t)+\mathbf{v}_i(t+\frac{\Delta t}{2})\Delta t \tag{23}$$

Figure 12 shows the leap-frog algorithm as a function of time. The velocities and positions are leaping "like frogs" over each others' back, thus explaining the name for this algorithm.

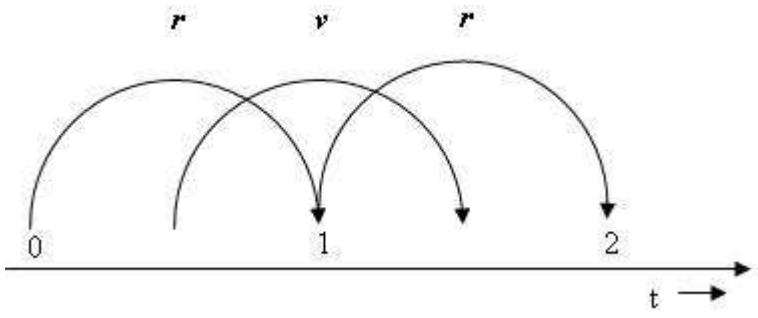

Figure 12. The leap-frog form of the Verlet algorithm.[159]

The leap-frog algorithm is computationally less expensive than other algorithms[159] and it requires less storage. This is an important advantage in the case of large-scale calculations.

The *gmq* program uses the SHAKE algorithm[160] to impose rigid constraints using an iterative scheme. This algorithm moves a set of unconstrained coordinates $\boldsymbol{r}'$ to a new set of coordinate positions $\boldsymbol{r}''$ with a list of distance constraints $\boldsymbol{r}$. It works within a tolerance value and will continue to iterate until all the constraints are satisfied. In order to control temperature and pressure, the *gmq* program incorporates loose-coupling techniques. [162,164]

2.3.1.1. Temperature control

The loose-coupling method of Berendsen *et al.*[164] is used to maintain the system at the required temperature ($T_{req}(t)$). The internally measured temperature, $T(t)$, is coupled to an external heat bath at $T_{req}(t)$ (Eq. 24):

$$\dot{T}(t) = \frac{-1}{\tau_T}(T(t) - T_{req}(t)) \tag{24}$$

with τ_T being the relaxation time determining the rate of heat flow. The temperature difference decays exponentially with the relaxation time. The temperature of the external heat

bath has a initial value of $T_{req}(0)$ and its rate of change is $\dot{T}_{req}$. So by controlling the rate of change, heating and cooling cycles are relatively easy to perform.

2.3.1.2. Pressure control

The six independent elements of the atomic pressure tensor[162] are controlled by rescaling the box size and shape, defined by the matrix **h** of basis vectors {**a**,**b**,**c**} (Eq. 25a) at every step using Eq. 25b:

$$\mathbf{h} = \begin{Bmatrix} a_x\ b_x\ c_x \\ a_y\ b_y\ c_y \\ a_z\ b_z\ c_z \end{Bmatrix} \tag{25a}$$

$$\dot{\mathbf{h}}(t) = \frac{\mathbf{P}(t) - \mathbf{P_{req}}(t)}{\tau_P\ \mu} \tag{25b}$$

where μ is a pre-defined constant, τ_P is the pressure relaxation time determining the rate at which the **h** matrix responds to the difference between the internal pressure tensor $\mathbf{P}(t)$ and the required pressure $\mathbf{P_{req}}(t)$. As for the temperature control, the rate of change in pressure, $\dot{P}_{req}$ can be controlled to obtain any pressure.

2.3.1.3. Temperature and scalar pressure control

In the case of an isotropic liquid system, the MD box will move from its initial cubic box shape because of the pressure fluctuations in the pressure tensor. This will eventually lead to a reduction of the box size below two times the non-bonded potential truncation radius. This problem can be avoided by a method that allows the box to fluctuate in response to differences between required and actual scalar pressure but maintains the shape of the original box. In that case, the former equation becomes:

$$\dot{\mathbf{h}}(t) = \frac{p(t) - p_{req}(t)}{\tau_P \ \mu}\mathbf{1} \tag{26}$$

with *p* being the scalar pressure and **1** the unit tensor.

The loose-coupling techniques suppress the kinetic energy fluctuations for the temperature. This will affect only second-order properties like specific heat, so all first-order properties, such as pressure, temperature, structure, and energy, are unaffected.

2.3.2) Potential

A very important part in a MD simulation is the calculation of the force acting on every particle. We have to consider the contributions of all its neighbours. In *gmq*, each atom interacts with the other atoms in the system through either bonded or non-bonded potentials and the total potential energy U_{pot} is given by (Eq. 27):

$$U_{pot} = \sum U_{bonded} + \sum U_{non-bonded} \tag{27}$$

2.3.2.1. Bonded potentials

In *gmq*, we use three different contributions to the bonded potential, namely the bending, torsional and out-of-plane potentials (Eq. 28):

$$\sum U_{bonded} = \sum_{\theta} U_{bend}(\theta) + \sum_{\tau} U_{tors}(\tau) + \sum_{i-sp^2} U_{oop}(i) \tag{28}$$

whilst the chemical bonds are kept at a fixed distance b_0 by a rigid constraint in order to avoid the use of shorter time steps during the integration (Eq. 29):

$$\left|\mathbf{r}_{ij}\right|^2 - b_0^2 = 0 \tag{29}$$

where *i* and *j* are the atoms forming the chemical bond, $\boldsymbol{r}_{ij}$ is to the bond vector and b_0 is the equilibrium bond length.

It is always possible to use *e.g.* an harmonic spring potential (Eq. 30) to define the stretching vibrations of a chemical bond, but this usually require shorter time-steps than 1 fs and it can also lead to difficulties in the equipartition of the energy:

$$U_{bond}(|\mathbf{r}_{ij}|) = \frac{1}{2}k_b(|\mathbf{r}_{ij}| - b_0)^2 \tag{30}$$

where k_b is a force constant. The other bonded potentials are described in more details below.

2.3.2.1.1. Bending potential U_{bend}

In order to keep bond angles θ close to their equilibrium values, the following bending potential (Figure 13) is employed in *gmq* (Eqs. 31 and 32):

$$U_{bend}(\theta) = \frac{1}{2}k_\theta(\cos\theta - \cos\theta_0)^2 \tag{31}$$

$$\cos\theta = \frac{(\mathbf{r}_{ij} \bullet \mathbf{r}_{kj})}{|\mathbf{r}_{ij}||\mathbf{r}_{kj}|} \tag{32}$$

where k_θ is a constant with energy units determining the flexibility of the angle and θ_0 is the equilibrium bond angle. The angle θ is a function of three atoms connected in a row, i.e. *i* bonded to *j* and *j* bonded *k* but *i* not bonded to *k*. $\boldsymbol{r}_{ij}$ (= $\mathbf{r}_i$-$\mathbf{r}_j$) and $\boldsymbol{r}_{jk}$ (= $\mathbf{r}_j$-$\mathbf{r}_k$) refer to the separation vectors between *i* and *j*, and between *j* and *k*, respectively. The same nomenclature will be adopted for all separation vectors used in the paragraphs related to the other potentials.

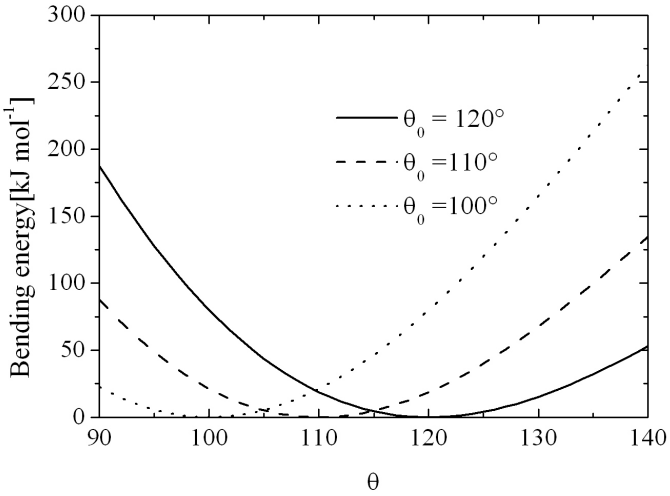

Figure 13. Behaviour of the bending potential (Eq. 31) as function of the bending angle θ.

Eq. 31 is well-behaved around $\theta \approx \pi$, but for $\theta_0 = \pi$, U_{bend} becomes flattened and close to zero. In order to avoid this flattening, an alternate bending potential is offered (Eq. 33):

$$U_{bend}(\theta) = k_\theta(1 - \cos(\theta - \theta_0)) \tag{33}$$

For $\theta_0 = \pi$, this potential simplifies to (Eq. 34):

$$U_{bend}(\theta) = -k_\theta(1 + \cos\theta) \tag{34}$$

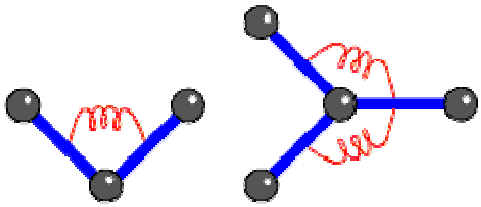

Figure 14. Some possible bending modes in a molecule.

The linear triatomic molecules like carbon dioxide have equipartition problems, if we consider all their degrees of freedom. Even if their bonds lengths are constrained, the rotation around the long molecular axis has a very low moment of inertia and does not couple well with the other degrees of freedom (three translations, two rotations and the C-O-C angle

bend). This causes problems of non-equipartition of the kinetic energy. In *gmq*, a vector constraint [165] is used to get a linear rigid rod like model for near-linear triatomic molecules.(Eq.35):

$$\mathbf{r}_k - (\mathbf{r}_j + \mathbf{r}_{ji} * d_{jk} / d_{ij}) = 0 \tag{35}$$

where d_{jk} and d_{ij} are the bond lengths between atoms *j* and *k*, *i* and *j*.

2.3.2.1.2. Torsional potential U_{tors}

The potential energy corresponding to the torsional rotations around the *j-k* bond in a *(i,j,k,l)* quadruplet is calculated using a 6th order polynomial function in the cosine of the dihedral angle τ with coefficients C_m (Eq. 36):

$$U_{tors}(\tau) = \sum_{m=0}^{6} C_m \cos^m \tau \tag{36}$$

where

$$\cos\tau = -\frac{(\mathbf{r}_{ij} \times \mathbf{r}_{jk}) \bullet (\mathbf{r}_{jk} \times \mathbf{r}_{kl})}{\left|\mathbf{r}_{ij} \times \mathbf{r}_{jk}\right| \bullet \left|\mathbf{r}_{jk} \times \mathbf{r}_{kl}\right|} \tag{37}$$

There are two possible cases available in *gmq*. If atoms separated by more than two bonds are considered as non-bonded, then U_{tors} describes only the part of the torsional energy in the 1...4 interaction. Otherwise, the coefficients for the equation have to be chosen to represent the whole torsional energy, *i.e.* atoms are considered as non-bonded if they are separated by more than three bonds. In *gmq*, the dihedral angle varies from -180° to +180° with τ = 0° being the trans conformation, *i.e.* all the four atoms are in the same plane but atoms *i* and *l* are at maximum distance apart from each other (Figure 15).

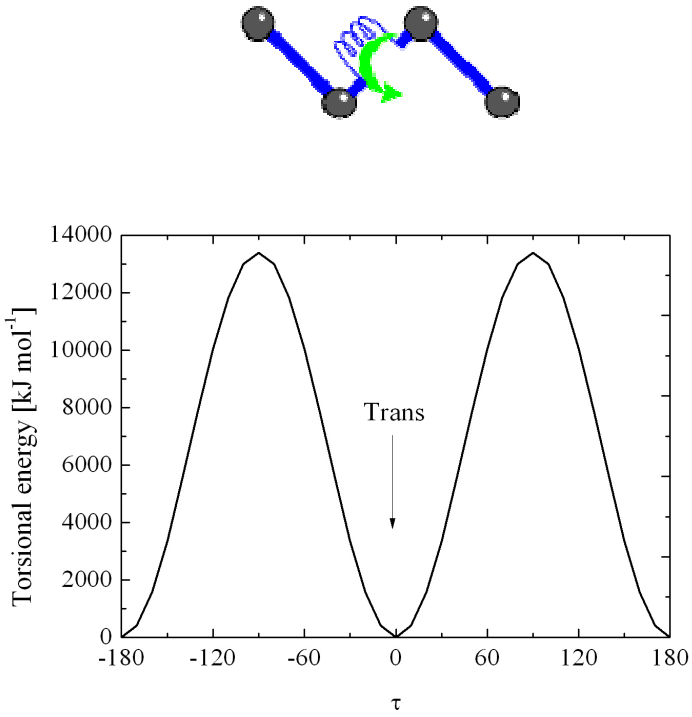

Figure 15. Examples of torsion angle and torsional potential.

2.3.2.1.3. Out-of-plane potential U_{oop}

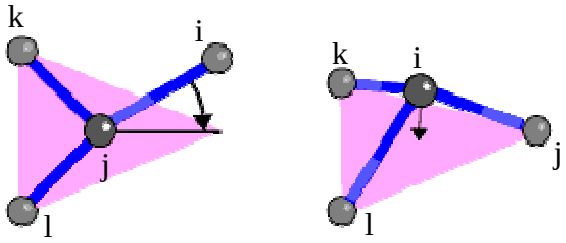

Figure 16. Some possible out-of-plane modes in a molecule.

The out-of-plane potential (Figure 17) restricts the motion of an atom *i* which is directly connected to atoms *j*, *k* and *l* to a single plane (Eq. 38):

$$U_{oop}(i) = \frac{1}{2} k_{oop}\, s^2 \tag{38}$$

where *s* is the perpendicular distance of atom *i* to the plane of atoms *j*, *k* and *l* (Eq. 39):

$$s = \mathbf{r}_{ji} \bullet \frac{(\mathbf{r}_{jk} \times \mathbf{r}_{jl})}{\left|\mathbf{r}_{jk} \times \mathbf{r}_{jl}\right|} \tag{39}$$

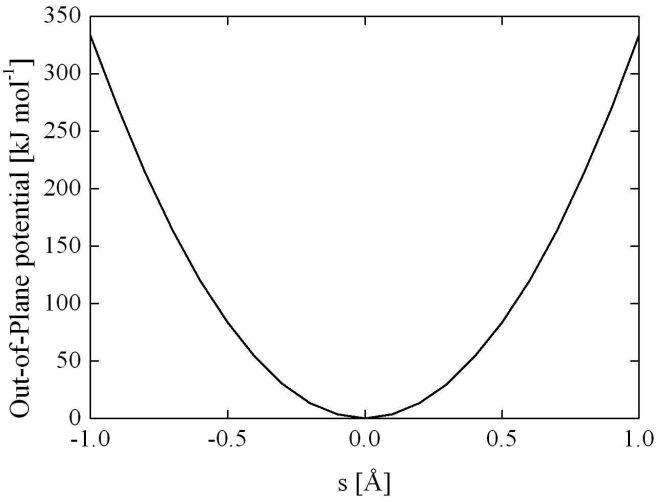

Figure 17. Behaviour of the out-of-plane potential as a function of the perpendicular distance ***s*** between the out-of-plane atom ***i*** and the plane of atoms ***j***, ***k*** and ***l***.

2.3.2.2. Non-bonded potentials

In *gmq*, atoms separated by more than two chemical bonds are usually considered to be interacting via non-bonded interactions (unless 1..4 non-bonded interactions are explicitely excluded, see torsional potential). The repulsive parts of the non-bonded potentials exclude two atoms from the same region of the space in the MD box, while the attractive interactions hold the molecular systems together in a preferred packing structure in the absence of containing walls. The non-bonded potential is divided into two components, the Coulombic interactions, which come from the partial charges on the atoms, and the Van der Waals interactions (Eq. 40):

$$U_{non-bonded} = \sum_{(i,j)nb} U_{vdw}(r) + \sum_{(i,j)nb} U_{coul}(r) \tag{40}$$

Both these interactions depend on the distance *r* between two interacting sites and consequently the calculation of all pair potentials at each step is computationally expensive.

2.3.2.2.1. Van der Waals interactions U_{vdw}

There are different forms of Van der Waals potentials available in *gmq*. The Lennard-Jones (LJ) 12-6 potential is the most commonly used one (Eq. 41):

$$U_{LJ}(|\mathbf{r}_{ij}|) = 4\varepsilon\left(\left(\frac{\sigma}{\mathbf{r}_{ij}}\right)^{12} - \left(\frac{\sigma}{\mathbf{r}_{ij}}\right)^{6}\right) \tag{41}$$

where ε is the well-depth of the potential and σ is the distance at which the potential is equal to zero. The $(1/\mathbf{r}_{ij})^{12}$ term describes Pauli repulsion at short ranges due to the overlap between the electronic orbitals of the interacting atoms and the $(1/\mathbf{r}_{ij})^{6}$ term describes the attraction between interacting atoms at longer distances (Figure 18).

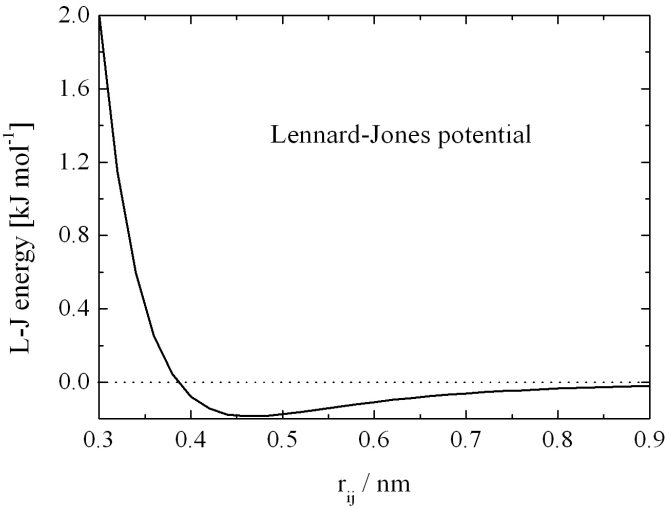

Figure 18. The Lennard-Jones 12-6 potential.

Another well-known potential is the Buckingham exp-6 form (Eq. 42):

$$U_{Buck}\left(\left|\mathbf{r}_{ij}\right|\right) = A\exp\left(-\frac{\left|\mathbf{r}_{ij}\right|}{B}\right) - \frac{C}{\left|\mathbf{r}_{ij}\right|^6} \tag{42}$$

where *A*, *B* and *C* are constants. This potential has the unphysical property of diverging to negative infinity at zero separation. There is also a short-range form with a completely repulsive potential, the Weeks-Chandler-Anderson (WCA) potential, which is available in *gmq* (Eq. 43):

$$\begin{aligned} U_{WCA}\left(\left|\mathbf{r}_{ij}\right|\right) &= 4\varepsilon\left(\left(\frac{\sigma}{\mathbf{r}_{ij}}\right)^{12} - \left(\frac{\sigma}{\mathbf{r}_{ij}}\right)^{6}\right) + \varepsilon \qquad for\ \left|\mathbf{r}_{ij}\right| \le 2^{1/6}\sigma \\ U_{WCA}\left(\left|\mathbf{r}_{ij}\right|\right) &= 0 \qquad\qquad\qquad\qquad\qquad\quad for\ \left|\mathbf{r}_{ij}\right| > 2^{1/6}\sigma \end{aligned} \tag{43}$$

From Figure 18, it is clear that the Van der Waals potential reaches relatively small values within short distances and hence the forces between atoms further apart than the cut-off distance (R_c) are less important. In *gmq*, long-range correction terms are estimated to account for the contributions of the Van der Waals potential to the potential energy and the pressure for interactions beyond R_c.[163]

2.3.2.2.2. Coulombic interactions U_{coul}

The Coulombic potential describes the electrostatic interactions between electrically charged particles (Eq. 44):

$$U_{coul}\left(\left|\mathbf{r}_{ij}\right|\right) = \frac{q_i q_j}{\left(4\pi\varepsilon_0\left|\mathbf{r}_{ij}\right|\right)} \tag{44}$$

where q_i and q_j are the partial charges on the interacting atoms and ε_0 is the vacuum permittivity. In periodic systems, the Coulombic interactions are calculated using the Ewald summation method (Eq. 45):[166]

$$U_{coul} = \sum_{n_x}\sum_{n_y}\sum_{n_z}{}^{*}\sum_{i}\sum_{j}\frac{q_i q_j}{r_{ij,n}} \tag{45}$$

where n_x , n_y and n_z are the MD box index vectors and the star indicates that the interactions between the same atoms (i.e. $i=j$) should be omitted. The distance $r_{ij,n}$ is the real distance between interacting atoms i and j. This potential diminishes slowly and decays as $1/r$. In order to converge the potential, the Ewald sum[163] divides the equation into two parts, that is a real space and a reciprocal space term.[161,166] In *gmq*, we have the option of specifying the real space cut-off distance R_c, the Ewald separation parameter α, and the upper bound for the number of reciprocal space vectors $K_{max.}$ All three parameters must be adjusted to get a good convergence.[167]

2.3.3) Periodic boundary conditions

The computational time required per time step increases inexorably with the number of atoms in the system. Simulation boxes can still only contain a number of atoms relatively small compared to macroscopic samples. This almost inevitably leads to edge effects. This problem is ameliorated by the use of periodic boundary conditions (PBC). In PBC, the simulation box is replicated in the three dimensions of the space in order to get an infinite lattice. If an atom moves from the primary simulation box to its periodic image, it reappears on the opposite side of the primary simulation box from the neighbouring periodic box, which conserves the number density in all the boxes. The errors produced by the unphysical vacuum boundaries are very much reduced by these systematic periodic boundaries. In *gmq*, the minimum-image convention is used, that is each atom interacts with the closest image of all other atoms in the system. A schematic representation of the PBC and the minimum image convention is presented in Figure 19.

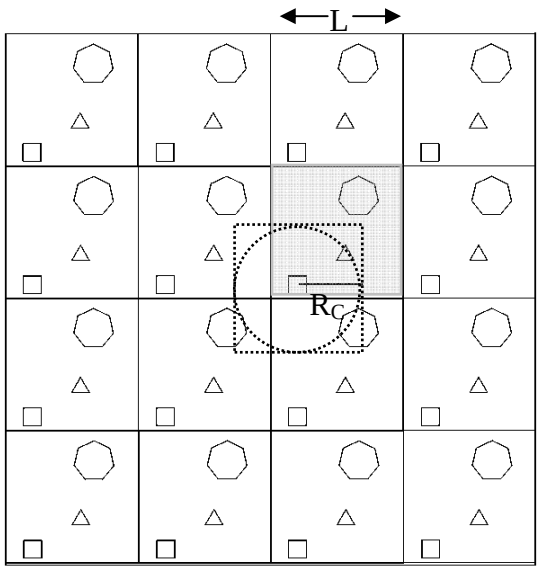

Figure 19. A schematic representation of periodic boundary conditions and the minimum image convention for a two-dimensional system.

Over the course of simulation, only the properties of the atoms situated in the primary simulation box are recorded. The cut-off distance for the real space part of the Ewald summation and the Van der Waals potential should be less than half the length of the box size in order to avoid interactions with different images of the same atom.

Chapter 3.

Preparation of polyimide and carbon dioxide molecular models

3.1) Force field parameters for polyimides

Force field parameters define the potential energy of a molecular system as a function of its atom types and atomic coordinates. Good-quality geometries can be obtained by selecting a suitable force field. In this work, we use the freely-available TRIPOS 5.2[168] force-field for the polyimides since it was optimized with respect to cyclic structures and has already proven successful to prepare molecular models of a variety of cyclic polymers.[169-182] Figure 20 shows the different atom-types (identified by a number from 1 to 15) which need to be considered in the set of force field parameters for our three polyimide structures. Atoms with the same chemical nature can be defined by the same atom-type even though their neighbouring atoms are different. For example, all the aromatic carbons in a 6FpDA, 6FmDA or DAM diamine structure can be grouped into the same atom type ("type 8"). A minimum number of atom types will reduce both the file-storage size during the analysis of molecular properties and possible errors in parameterization. The TRIPOS force-field provides parameters for all bonded and non-bonded potentials, except for the partial charges which are strongly dependent on the atomic position within the structure and have to be calculated separately. A letter can be added to the atom-type number to distinguish those atoms which have the same chemical nature, but different partial charges.

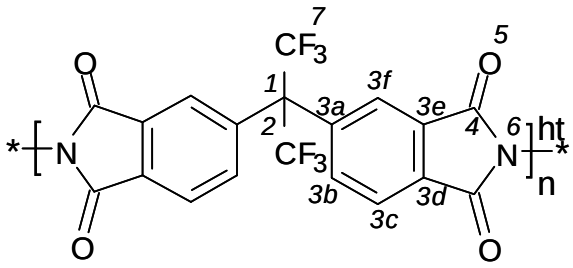

a) 6FDA

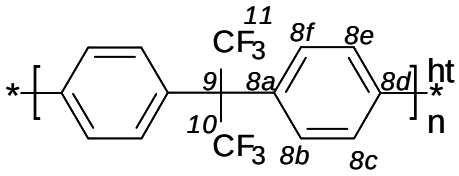

b) 6FpDA

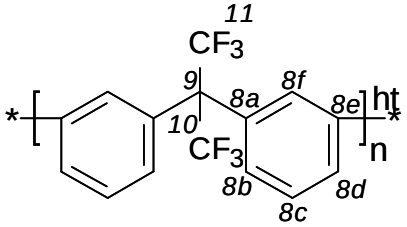

c) 6FmDA

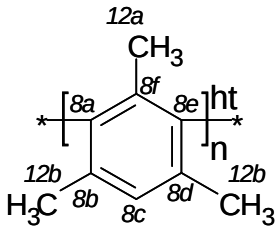

d) DAM

Figure 20. The different atom-types defined for the polyimides under study. For clarity, the hydrogen atoms (types 13 to 15) are not displayed. Type 13 refers to any H attached to a ring atom, type 14 to a methyl H and type 15 to a chain-end H.

Atom type number	Atom name in *gmq*	Symbol in TRIPOS 5.2
1	C_1	C_3
2	C_{F1}	C_3
3 (a to f)	C_{ar1}	C_{ar}
4	C_{ket}	C_2
5	O_{ket}	O_2
6	N	N_{am}
7	F_1	F
8 (a to f)	C_{ar2}	C_{ar}
9	C_2	C_3
10	C_{F2}	C_3
11	F_2	F
12	C_{CH3}	C_3
13	H_{all}	H
14	H_{CH3}	H
15	H_{term}	H

Table 8. Correspondence between the atom-type numbers (Figure 20), the names used in *gmq* and the symbols used in the TRIPOS 5.2 force-field.[168]

Table 8 gives the symbols used in TRIPOS 5.2 which correspond to the different atom-types of Figure 20. However the TRIPOS potential energies are expressed in a different analytical form than those in *gmq* (Table 9). In addition, the units of energies are *kcal* mol^{-1} in TRIPOS while they are *J* mol^{-1} in *gmq*.

Potential	TRIPOS 5.2	*gmq*
bending (U_{bend})	$k_{i,j,k} * (\theta - \theta_0)^2$ $k_{i,j,k}$ = bending force constant θ = actual bending angle θ_0 = equilibrium bending angle	$\frac{1}{2} k_\theta (\cos\theta - \cos\theta_0)^2$ (Equation 31)
torsion (U_{tors})	$k_{i,j,k,l} \times \left(1 + s/\lvert s\rvert \times \cos\left(\lvert s\rvert B_{i,j,k,l}\right)\right)$ $k_{i,j,k,l}$ = torsional force constant s = torsional coefficient $B_{i,j,k,l}$ = torsional angle	$\sum_{m=0}^{6} C_m \cos^m \tau$ (Equation 36)
out-of-plane (U_{oop})	$k * d^2$ k = out-of-plane bending force constant d = distance from the atom to the plane defined by its three attached atoms	$\frac{1}{2} k_{oop} s^2$ (Equation 38)
van der Waals (U_{vdw})	$k_{ij} * \left(\left(\frac{1}{\alpha^{12}}\right) - \left(\frac{2}{\alpha^6}\right)\right)$ k_{ij} = van der Waals constant α = distance between the two atoms divided by the sum of their radii	$4\varepsilon\left(\left(\frac{\sigma}{\mathbf{r}_{ij}}\right)^{12} - \left(\frac{\sigma}{\mathbf{r}_{ij}}\right)^6\right)$ (Equation 41)

Table 9. Analytical expressions for the different potentials in both TRIPOS 5.2 and *gmq*.

Consequently all the parameters given in TRIPOS must be converted into a form consistent with the analytical forms in *gmq*. The following conversions were used (Equation 46):

Bending potential :

$$k_\theta\left[Jmol^{-1}\right]=\frac{2k_{i,j,k}}{\sin^2\theta_0}\times 4184\times\left(\frac{180}{\pi}\right)^2 \tag{46a}$$

Torsional potential :

$$\begin{aligned}
&If\ s=-2,\ C_0=2k_{i,j,k,l}\times 4184;\ C_2=-2k_{i,j,k,l}\times 4184\left[Jmol^{-1}\right]\\
&If\ s=-3,\ C_0=k_{i,j,k,l}\times 4184;\ C_1=-3k_{i,j,k,l}\times 4184;\ C_3=4k_{i,j,k,l}\times 4184\left[Jmol^{-1}\right]\\
&If\ s=3,\ C_0=k_{i,j,k,l}\times 4184;\ C_1=3k_{i,j,k,l}\times 4184;\ C_3=-4k_{i,j,k,l}\times 4184\left[Jmol^{-1}\right]
\end{aligned} \tag{46b}$$

Out-of-plane potential :

$$k_{oop}\left[kgs^{-2}\right]=\left(\frac{2k\times 4184}{N_A}\right)\times\left(\frac{1}{10^{-20}}\right) \tag{46c}$$

where N_A is Avogadro's number.

Van der Waals potential :

$$\begin{aligned}
\frac{\varepsilon}{k}\left[K^{-1}\right]&=\frac{k_{ij}\times 4184}{8.31448}\\
\sigma\left[\mathring{A}\right]&=\frac{1}{2^{1/6}}\times\sum r_{vdw}
\end{aligned} \tag{46d}$$

where $\sum r_{vdw}$ is the sum of the van der Waals radii for the two interacting atoms (*i* and *j*) and *k* is Boltzmann constant

Figure 21 shows the comparison of a bending potential between TRIPOS 5.2 and *gmq*. It is clear that the different analytical forms do not really affect the energy, except at very distorted angles which are virtually never accessed in an MD calculation.

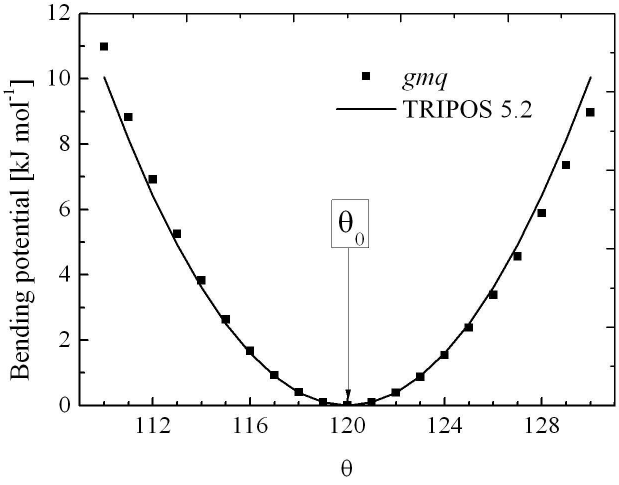

Figure 21. Comparison of the C_{ar}-C_{ar}-C_{ar} bending potential between TRIPOS 5.2 and *gmq*.

For the bonded potentials, there are in total 18 types of bonds, 28 types of bending angles, 39 types of torsional angles and 11 types of out-of-planes interactions, which have to be defined for the polyimides under study. The Van der Waals parameters for interactions between similar atom types (*i.e.* interactions between *i*---*i* and *j*---*j*) were also directly extracted from TRIPOS 5.2. The cross-term values for unlike atoms (*i.e.* interactions between *i*---*j*) were calculated using the well-known Lorentz-Berthelot rules, i.e. an arithmetic average was used for the distance σ at which the potential is equal to zero (Eq. 47) while a geometric average was used for the ε well-depth (Eq. 48):[183] The details of all parameters are given in the Annexes.

$$\sigma_{(i,j)} = \frac{\sigma_{(i,i)} + \sigma_{(j,j)}}{2} \tag{47}$$

$$\varepsilon_{(i,j)} = \sqrt{\left(\varepsilon_{(i,i)} \times \varepsilon_{(j,j)}\right)} \tag{48}$$

The partial charges on the atoms were calculated with an *ab initio* approach using representative structures for all three polyimides. Three or five basic moieties were used to extract the charges with Gaussian 03[184] at the B3LYP/6-31G** level (Figure 22). The electrostatic-potential fitted charges[185] on the central fragments, q_i/e, were kept for the calculation of the Coulombic potential (Equation 44). Table 10 gives the calculated partial charges. They are similar in both two structural isomers (6FDA-6FpDA and 6FDA-6FmDA), while for 6FDA-DAM, the different DAM diamine structure also affects the partial charges on the dianhydride 6FDA fragment.

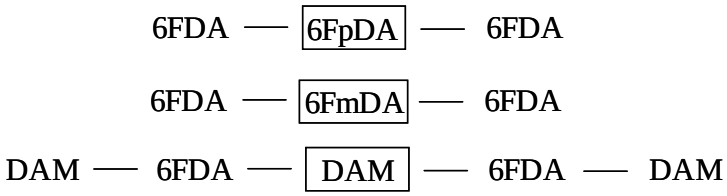

Figure 22. Representative fragments for calculating the partial charges.

Atom Type	Element Symbol	6FDA–6FpDA	6FDA– 6FmDA	6FDA- DAM
1	$C(C_1)$	-0.567	-0.559	-0.610
2	$C(C_{F1})$	0.441	0.429	0.427
3a	$C(C_{ar1})$	0.279	0.268	0.293
3b	$C(C_{ar1})$	-0.142	-0.141	-0.179
3c	$C(C_{ar1})$	-0.091	-0.102	-0.029
3d	$C(C_{ar1})$	-0.116	-0.091	-0.167
3e	$C(C_{ar1})$	-0.073	-0.099	-0.127
3f	$C(C_{ar1})$	-0.155	-0.125	-0.084
4	$C(C_{ket})$	0.583	0.553	0.463
5	$O(O_{ket})$	-0.447	-0.436	-0.427
6	N(N)	-0.410	-0.349	0.095
7	$F(F_1)$	-0.116	-0.115	-0.111
8a	$C(C_{ar2})$	0.092	0.263	-0.440
8b	$C(C_{ar2})$	-0.049	-0.272	0.406
8c	$C(C_{ar2})$	-0.321	-0.058	-0.457
8d	$C(C_{ar2})$	0.378	-0.272	0.406
8e	$C(C_{ar2})$	-0.321	0.331	-0.440
8f	$C(C_{ar2})$	-0.049	-0.315	0.419
9	$C(C_2)$	-0.405	-0.431	NA
10	$C(C_{F2})$	0.427	0.438	NA
11	$F(F_2)$	-0.123	-0.125	NA
12a	$C(C_{CH3})$	NA	NA	-0.389
12b	$C(C_{CH3})$	NA	NA	-0.383
H on 3b	H	0.137	0.138	0.138
H on 3c	H	0.139	0.141	0.128
H on 3f	H	0.135	0.126	0.122
H on 8b	H	0.129	0.173	NA
H on 8c	H	0.189	0.127	0.172
H on 8e	H	0.186	0.173	NA
H on 8f	H	0.129	0.177	NA
H on 12a	H	NA	NA	0.111
H on 12b	H	NA	NA	0.109

Table 10. Partial charges, q_i/e, on the different atoms for the polyimides under study.

3.2) Preparation of polymer molecular models

3.2.1) Hybrid Pivot Monte Carlo - Molecular Dynamics (PMC-MD) technique

Relaxed structures of amorphous polymers should be decorrelated from their initial positions. However, the current timescales of MD simulations (10^{-9} to 10^{-8} s) are not long enough compared with the relaxation times (~1 s) of high molecular-weight polymers.[186] There are a variety of approaches, such as modified rotational isomeric state (RIS),[187] reptation,[188] reverse,[189] end-bridging and other connectivity-altering Monte Carlo moves,[190,191] soft-core potentials[192], Gaussian lattice algorithms[193] and reverse mapping from coarse-grained polymer chains,[194-211] used to alleviate this problem in molecular simulations.

gmq offers a unique highly-efficient and fully-atomistic technique based on a hybrid Pivot Monte Carlo – Molecular Dynamics (PMC-MD) single-chain sampling method. This method has already been validated for different amorphous polymers.[169-177,212-214] It is based on Flory's hypothesis,[215] *i.e.* that the long-range interactions are completely screened in pure melts of homopolymers and that the configurations can be described by considering only a certain number of specific near-neighbour intramolecular interactions. This amounts to treating specific chains as isolated molecules.

Initially, an arbitrary configuration of the polymer chain is created with the equilibrium bond lengths and angles. A standard MD algorithm is used to explore the various oscillatory modes of the polymer chains, while pivot Monte Carlo moves[216] are attempted at fixed intervals between MD steps in order to sample more efficiently the polymer phase-space. The method is thus referred to as "hybrid PMC-MD". These PMC moves combined with MD steps help the polymer chain to decorrelate at a much faster rate. In order to increase

the number of energetically favourable configurations during PMC moves, a “smart table” is built for each type of pivotable torsion.[217,218]

When a new pivotable torsion angle is chosen, a PMC move is attempted. The potential energy difference between the pivoted and unpivoted chain ($\Delta\Phi = \Phi_{pivoted} - \Phi_{unpivoted}$) is calculated. $\Delta\Phi$ is then submitted to a standard Metropolis acceptance criteria,[219] where a random number R_n is chosen in the range $0 \leq R_n < 1$. The new pivoted configuration is accepted if $exp(-\Delta\Phi/k_BT) > R_n$. If this is not the case, the PMC move is refused and the original unpivoted chain is used again for additional MD steps and new PMC moves. If the pivoted configuration is accepted, then new randomized velocities are selected from a Boltzmann distribution corresponding to the required temperature. Although decorrelation of the chain with respect to its starting structure is usually obtained within a few hundred thousand PMC moves, the PMC-MD sampling procedure can be carried out for millions of steps in order to acquire good statistics. The degree of chain decorrelation can be assessed from the normalized autocorrelation functions $C_R(t)$ and $C_{RV}(t)$, which are calculated respectively for the square end-to-end distances $R_i^2(t)$ (Eq. 49) and the end-to-end vectors $\mathbf{R}_i(t)$ (Eq. 50):

$$C_R(t) = \frac{\left\langle R_i^2(0)R_i^2(t)\right\rangle - \left\langle R_i^2\right\rangle^2}{\left\langle R_i^4\right\rangle - \left\langle R_i^2\right\rangle^2} \tag{49}$$

$$C_{RV}(t) = \frac{\left\langle \mathbf{R}_i(0)\mathbf{R}_i(t)\right\rangle - \left\langle \mathbf{R}_i\right\rangle^2}{\left\langle \mathbf{R}_i^2\right\rangle - \left\langle \mathbf{R}_i\right\rangle^2} \tag{50}$$

Since the hybrid PMC-MD simulations are carried out within the framework of Flory’s local energy approximations (*i.e.* all the intermolecular interactions are switched off

and only the local interactions along the chain with a fixed number of backbone bonds are considered), the definition of a local energy parameter (*n-local*) has to be validated prior to longer-chain hybrid PMC-MD simulations. *n-local* represents the maximum number of bonds allowed between two non-pendant atoms which can interact through the non-bonded potentials (see Figure 23). The only drawback of the technique is the fact that the value of *n-local* value is not universal (Table 11), even if *n-local* = 4 was found in most cases where the hybrid PMC-MD method has already been validated.[178,220,221, 178,220,221, 171, 169, 222] The value of *n-local* depends primarily on the chemical structure of the macromolecule under study, more complicated structures such as cellulose having a tendency towards larger *n-local* values.

Polymer	Optimal *n-local*	References
n-alkanes and PE	4	178,220,221
PEO	4	178,220,221
PVC	5	174
BCDA-ODA	4	171
ODPA-PDB	4	171
PEEK	4	171
PBMA	4	223
Cellulose	7	224
PTFE	5	225
SBR	6	225
Kapton	4	169
PES	4	222
PPSU	4	222
PSU	4	222

Table 11. The optimal local energy parameter ***n-local*** validated for different polymers.

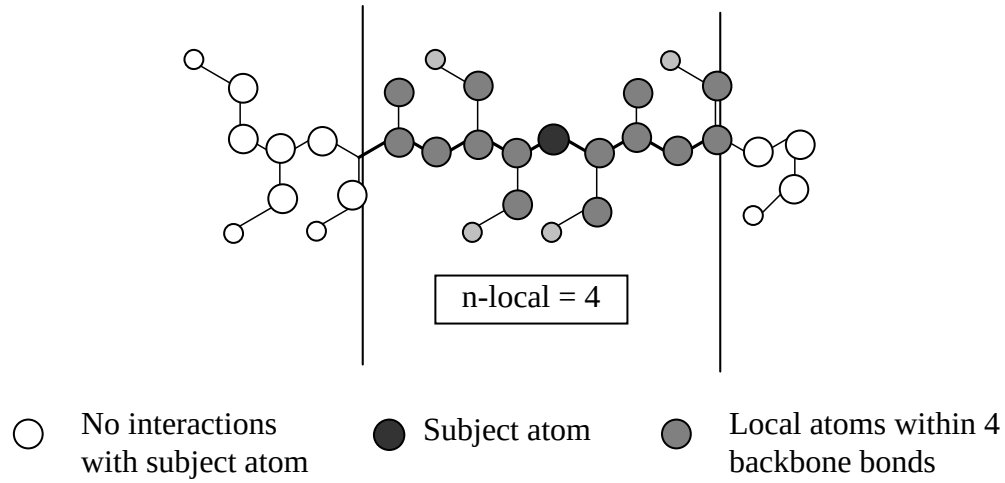

Figure 23. A schematic representation of the local energy approximation using n-local = 4.[225]

The *n-local* value can be validated by comparing the conformational and configurational properties of hybrid PMC-MD single-chains with those in bulk melts of short-homologue chains which are fully relaxed using MD. Indeed, short chains combined with high temperatures are the only cases where bulk melts can actually be decorrelated by using MD on its own. If the comparison is favourable, PMC-MD can then be used to generate longer chains, which cannot be relaxed using MD on its own with currently-available computational resources

For this purpose, various size of single-chain systems were prepared [four monomers (266 atoms for 6FDA-6FpDA and 6FDA-6FmDA, 226 atoms for 6FDA-DAM), five monomers (332 atoms for 6FDA-6FpDA and 6FDA-6FmDA, 282 atoms for 6FDA-DAM) and six monomers (398 atoms for 6FDA-6FpDA and 6FDA-6FmDA, 338 atoms for 6FDA-DAM]. They were then subjected to a series of PMC moves in between 100 MD steps at 1000 K. All the systems decorrelated within a time span of 200 ps, since PMC moves are very efficient in helping the single-chain systems to explore the whole possible torsional phase-space.

At the same time, separate bulk melts consisting of 20 four-monomer chains, 15 five-monomer chains and 12 six-monomers chains were also generated using hybrid PMC-MD sampling. The excluded-volume was introduced in a progressive way and the dense bulk melts were then decorrelated with MD on its own at 1000 K under *NpT* conditions. These bulk melts took much longer times to decorrelate from their initial positions, *i.e.* from 2000 ps up to 25000 ps depending on the chemical structure and the chain-length. Figure 24 shows some autocorrelation functions for the square end-to-end distance $C_R(t)$ (Eq. 49) and for the end-to-end vector $C_{RV}(t)$ (Eq. 50) as a function of time for the 20-chain four-monomer melts. The latter takes a lot longer to decorrelate than the former.

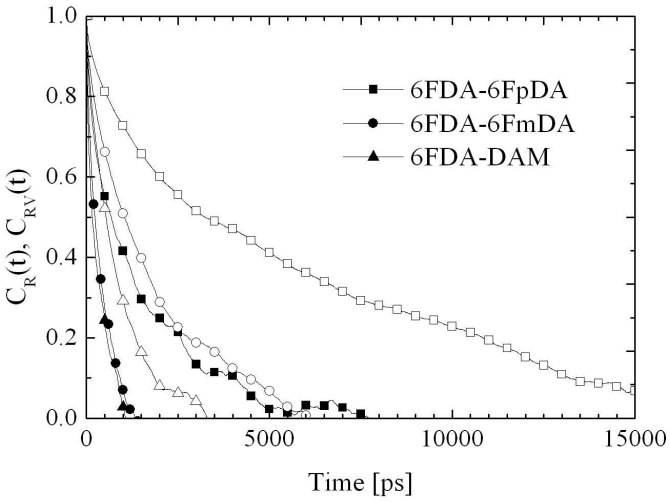

Figure 24. Normalized relaxation functions for the square end-to-end distances (closed symbols) and the end-to-end vectors (open symbols) at 1000 K in MD simulations of short 4-monomer homologue chains.

Once decorrelated, the torsional angle distributions, radii of gyration and end-to-end distances of bulk melts can be compared directly with the single-chain systems decorrelated using the hybrid PMC-MD technique. Figure 25 shows some distributions of different torsional angles in the 6FDA-6FpDA polyimide, which have been obtained both from the bulk melt and the single-chain sampled four-monomers with a *n-local* value of 4. A similar

level of agreement was found for the other two polyimides and for all the investigated chain lengths (four, five and six-monomers).

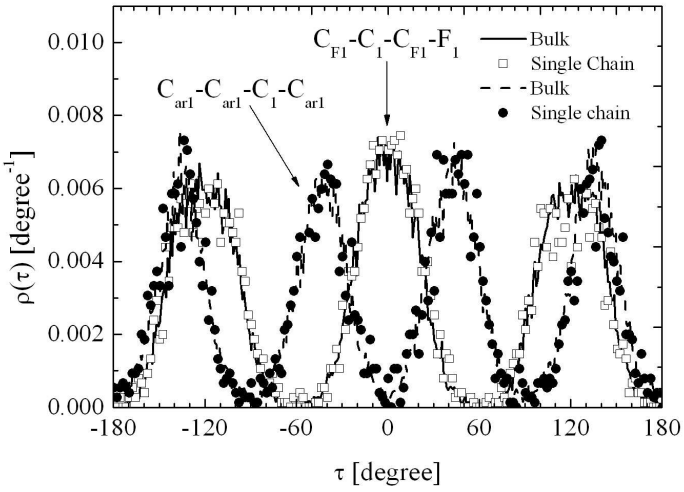

Figure 25. Probability densities of torsion angles in single-chain (sampled by PMC-MD) and bulk melts (sampled with MD) in 6FDA-6FpDA at 1000 K.

Figure 26 further confirms that the mean-square end-to-end distances $<R^2>$ and the mean-square radii of gyration $<S^2>$ are also in good agreement between bulk-melt and single-chain systems of similar sizes using a *n-local* value of 4. All polymers under study exhibit comparable results.

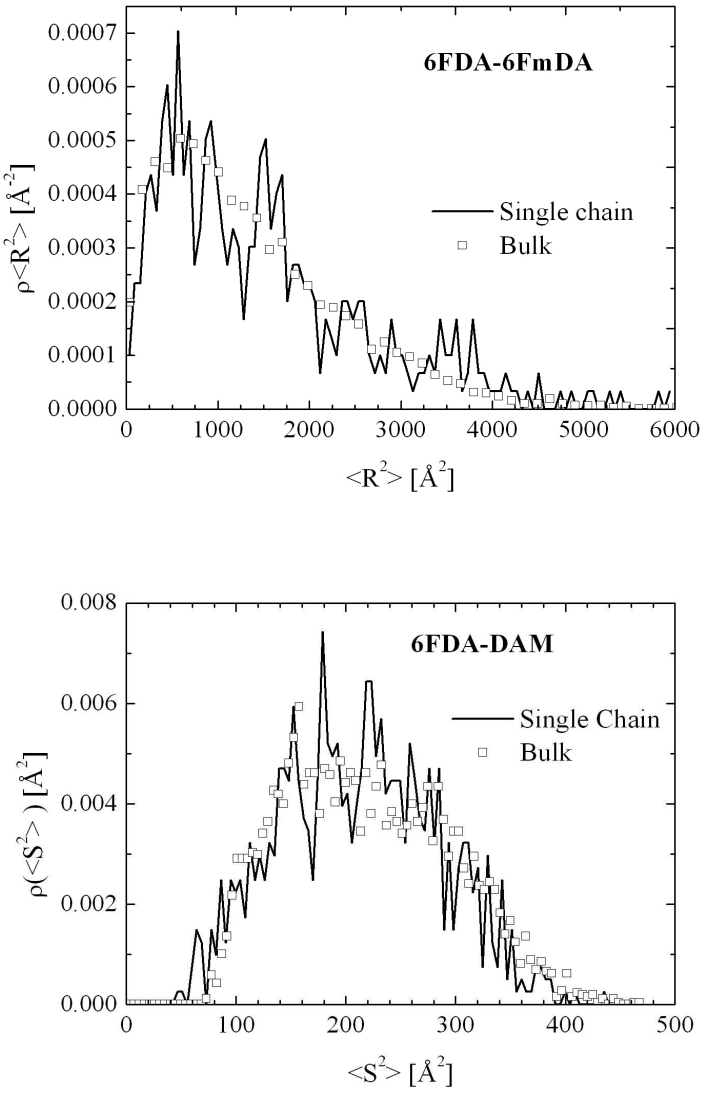

Figure 26. Probability densities for (a) the mean-square end-to-end distances $\langle \boldsymbol{R^2} \rangle$ and (b) the mean-square radii of gyration $\langle \boldsymbol{S^2} \rangle$ for the 4-monomer system in 6FDA-6FmDA and the 6-monomer system in 6FDA-DAM respectively at 1000K using ***n-local*** = 4.

The average percentage of dihedral angles in a *trans* state (i.e. between $-60° < \tau < 60°$) as well as the average mean-square radii of gyration and end-to-end distances are all in very good agreement (over ~95%) between the systems relaxed by the hybrid PMC-MD method

and those by pure MD (Figure 27). This shows that the hybrid PMC-MD technique is able, with a *n-local* value of 4, to decorrelate the polymer chains.

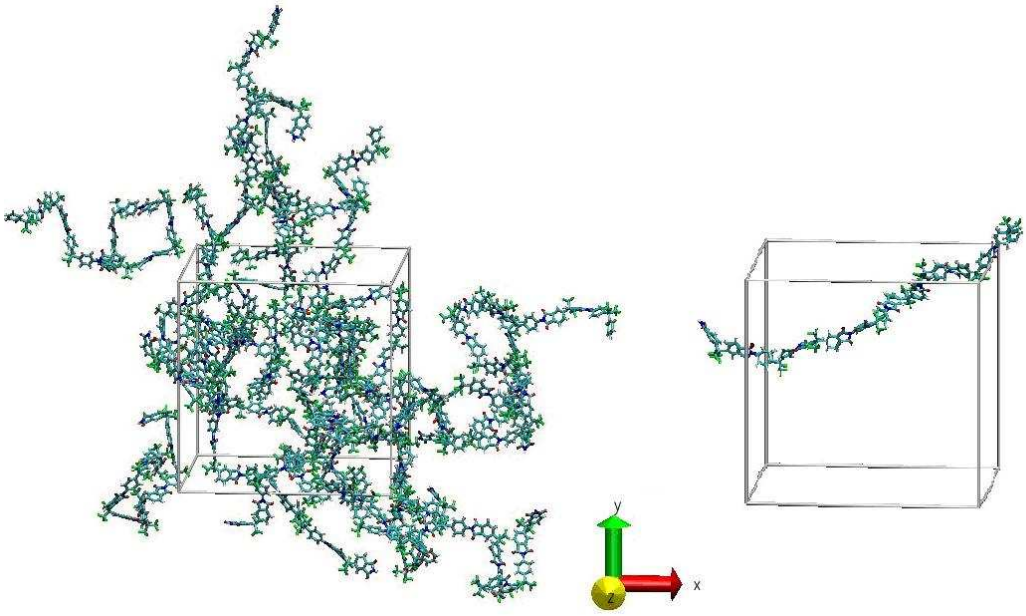

Figure 27. A schematic wire-frame representation of a bulk melt (20 chains of four-monomers) and the corresponding single-chain (four-monomers) simulation boxes for 6FDA-6FpDA. Single-chains were decorrelated by the hybrid PMC-MD technique and bulk melts of small homologues by pure MD simulations.

3.2.2. Polymer chain-lengths

Following the careful validation of the *n-local* parameter, it is important to decide on the length of the polymer chains which have to be used in the subsequent simulations in order to avoid end-effects. Many chain lengths for all three polyimides under study were prepared (from $n_{monomers}$ = 3 to 100 monomers) and decorrelated using the hybrid PMC-MD technique. The plots of $<R^2>/n_{monomers}$ as a function of the number of monomers $n_{monomers}$ show that there is no chain-length effect after 25 monomers (Figure 28).

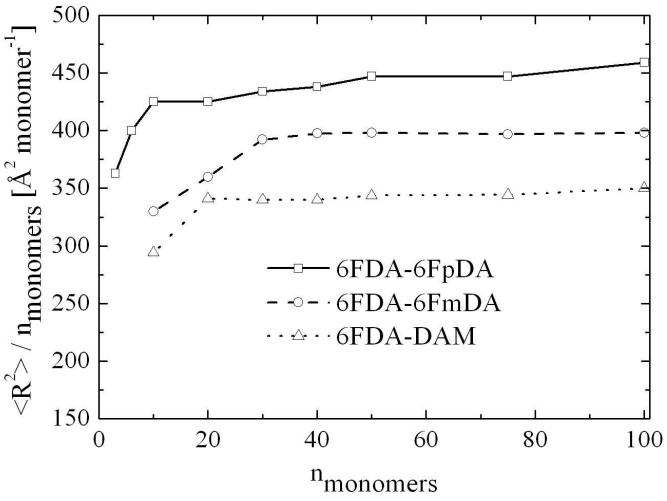

Figure 28. Mean-square end-to-end distances $\langle R^2 \rangle$ divided by the number of monomers as a function of number of monomers $n_{monomers}$ obtained following decorrelation by hybrid PMC-MD.

Consequently, chain-lengths of 50 monomers were used in the preparation of long-chain polymer molecular models. All the required hybrid PMC-MD runs were carried out at temperatures above the glass-transition temperatures (in the melt state), i.e. at 700 K for 6FDA-6FpDA and 6FDA-DAM and at 600 K for 6FDA-6FmDA.

3.2.3. Introduction of the excluded volume and MD production run

The polymer chains decorrelated by hybrid PMC-MD were placed in a cubic simulation box. In order to avoid any distortions following the introduction of the complete potential, the size of the MD simulation box was chosen such that it was close to the volume corresponding to the experimental density of the polymer (*see* Section 2.2). The excluded-volume potential was introduced in a systematic stepwise procedure by scaling the potential from 0 to 1. The heat produced during this process was removed at each time-step by

rescaling the velocities of the atoms. Unphysical spearings and polymer-chain interlockings are likely to occur during the progressive introduction of the excluded-volume. To avoid these artifacts, a phantom atom was placed at the center-of-mass of each five and six-membered ring in the polymer chain. These phantom atoms were removed immediately after the complete introduction of the excluded-volume potential.

For each fluorinated polyimide, a series of five three-chain systems (9906 atoms for 6FDA-6FpDA, 6FDA-6FmDA and 8406 atoms for 6FDA-DAM) along with five six-chain systems (19812 atoms for 6FDA-6FpDA, 6FDA-6FmDA and 16812 atoms for 6FDA-DAM) were prepared using PMC-MD (with *n-local* = 4) and then the excluded-volume potential was introduced. The total number of independent pure-polymer samples thus amounted to thirty.

Following the introduction of the excluded-volume, the complete potential was switched on and the Ewald summation[166] parameters were adjusted to get a satisfactory convergence. Table 12 shows the R_c (real space cut-off distance), the α (Ewald separation parameter) and K_{max} (upper bound for the number of reciprocal space vectors), which were used here in the calculations of the electrostatic interactions. The Van der Waals truncation radii were set to the same value than R_c and long-range corrections were included to the energy and pressure beyond the truncation radii.

Polymer	Three chain systems			Six chain systems		
	α [Å^{-1}]	K_{max}	R_c [Å]	α [Å^{-1}]	K_{max}	R_c [Å]
6FDA-6FpDA	0.27	13	9	0.29	17	9.5
6FDA-6FmDA	0.28	13	9	0.26	15	9.5
6FDA-DAM	0.28	14	9.5	0.27	15	9.5

Table 12. The Ewald summation parameters used for the different pure-polymer simulation boxes.

All the systems with the complete potential were further relaxed under *NVT* conditions for 500 ps at the same temperatures than those used for the PMC-MD decorrelations.

The introduction of the complete potential into an initially single-chain-based simulation box may lead to some moderate changes in the intrachain distances at intermediate length scales.[178,221,226] To check the importance of this effect, the mean square distances between two monomers separated by *n* others along the polymer chain ($<R^2(n)>$) were calculated, first directly following the decorrelation with hybrid PMC-MD and then right after the introduction and relaxation of the full potential. This value is sometimes referred to as the internal distance,[227] which is simply the mean square end-to-end distance when *n* is equal to the length of the polymer chain. Figure 29 shows the plot of $<R^2(n)>/nl^2$ as a function of number of *n*. The value of *l* has been defined as the average distance between the central carbons in the 6FDA fragments determined from the last configuration of the PMC-MD run (*i.e.* the "length" of a monomer). The values used for *l* were: 18.68 Å for 6FDA-6FpDA, 18.64 for Å 6FDA-6FmDA and 15.21 Å for 6FDA-DAM.

The differences in internal distances before and after the introduction of the full potential remain within 0.5%. This confirms that there are no real effects because of the introduction of the complete potential, which can be attributed to the highly rigid nature of the polyimides.

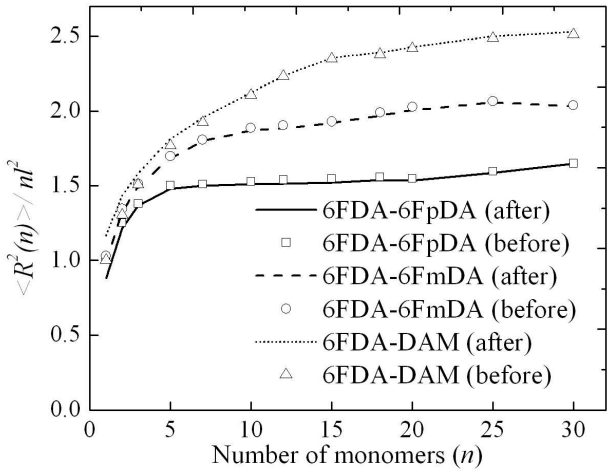

Figure 29. The average internal distances between monomers separated by ***n*** others along the chain divided by $\boldsymbol{nl^2}$ as a function of ***n*** and averaged over five three-chain systems. The open 'before' symbols refer to the last configuration of PMC-MD, while the lines show the same chains following the introduction of the full potential by MD at the same temperature.

After the preparation of the polymers in the melt, the simulation boxes were allowed to cool down to room temperature (298 K) at a rate of -1 K/ps under *NVT* conditions. At room temperature, systems were then relaxed for a short time (20 ps) under *NVT* conditions followed by *NPT* simulations for 3000 ps. This allowed the boxes to relax towards their natural density and shape. The pressure tensor was set to 1 bar for on-diagonal and 0 for off-diagonal components. The loose-coupling constants for the temperature and the pressure were set to 5 and 0.1 ps respectively. In the 3000 ps simulations under *NPT* conditions, the final 2000 ps were considered as the production run.

3.3. Validation of the polyimide bulk models

The atomistic models of the pure polymers were validated with respect to their experimental densities. Other bulk properties such as the Hildebrand solubility parameters and intermolecular potential energies were estimated. The values of fractional free volume and *d*-spacings were calculated and compared with the available data in the literature. Void-space and structural analyses were also carried out. The preparation and validation of bulk models of these amorphous polymers can be found in the affixed publication in *Journal of Polymer Science: Part B: Polymer Physics*.

Atomistic Models of Three Fluorinated Polyimides in the Amorphous State

S. PANDIYAN,[1,2] D. BROWN,[1] N. F. A. VAN DER VEGT,[2]* S. NEYERTZ[1]

[1]LMOPS, UMR CNRS 5041, University of Savoie, Bât. IUT, 73376 Le Bourget-du-Lac Cedex, France

[2]Max-Planck-Institute for Polymer Research, Ackermannweg 10, 55128 Mainz, Germany

Received 11 December 2008; revised 13 March 2009; accepted 26 March 2009
DOI: 10.1002/polb.21717
Published online in Wiley InterScience (www.interscience.wiley.com).

ABSTRACT: Molecular models of three fluorinated polyimides based on the 4,4′-(hexafluoroisopropylidene)diphthalic dianhydride (6FDA) have been studied using molecular dynamics (MD) simulations. The respective diamines were 4,4′-hexafluoroisopropylidene dianiline (6FpDA), 3,3′-hexafluoroisopropylidene dianiline (6FmDA), and 2,4,6-trimethyl-1,3phenylenediamine (DAM). Thirty independent samples were prepared using a hybrid pivot Monte Carlo-MD generation technique and average densities were found to be in very good agreement with experiment. Model structures also agreed with available wide-angle X-ray scattering data. Cohesive energies, Hildebrand solubility parameters, fractional free volumes (FFV), void space distributions and intermolecular as well as intramolecular interactions were analyzed. The differences in bulk properties between both 6FDA-6FpDA and 6FDA-6FmDA isomers remain fairly small, although the configurations of the former are more extended. 6FDA-DAM has a lower density, larger intermolecular distances, and higher free volume than the other two polyimides. Results are discussed with respect to their use as matrices for gas separation. © 2009 Wiley Periodicals, Inc. J Polym Sci Part B: Polym Phys 47: 1166–1180, 2009

Keywords: fluoropolymers; microstructure; molecular dynamics; molecular modeling; polyimides

INTRODUCTION

Fluorinated polyimides are highly strong as well as thermally and chemically-resistant polymers, with a large number of industrial applications.[1–5] They can be prepared either by melt or by solution polymerization from fluorinated fragments derived from diamines and dianhydrides.[6] The basic polyimide monomer is usually referred to as the -(dianhydride-diamine)- fragment. Melt polymerization has the advantage of shortening the synthesis path, but it is restricted to a narrow range of fusible diamines and dianhydrides. On the other hand, solution polymerization requires the use of solvents such as dipolar aprotic amides, but it can be applied to the whole range of polyimides.[6,7] In general, the low polarity of fluorine gives a low refractive index, a low dielectric constant, while free volume is increased.[6] Many fluorinated polyimides are based on the 4,4′-(hexafluoroisopropylidene)diphthalic dianhydride (6FDA) [refer Figs. 1 and 2(a)], which in addition to the aforementioned characteristics,

Present address: Center of Smart Interfaces, Technical University of Darmstadt, Petersenstrasse 32, 64287 Darmstadt, Germany.

Correspondence to: S. Neyertz (E-mail: sylvie.Neyertz@univ-savoie.fr)

Journal of Polymer Science: Part B: Polymer Physics, Vol. 47, 1166–1180 (2009)

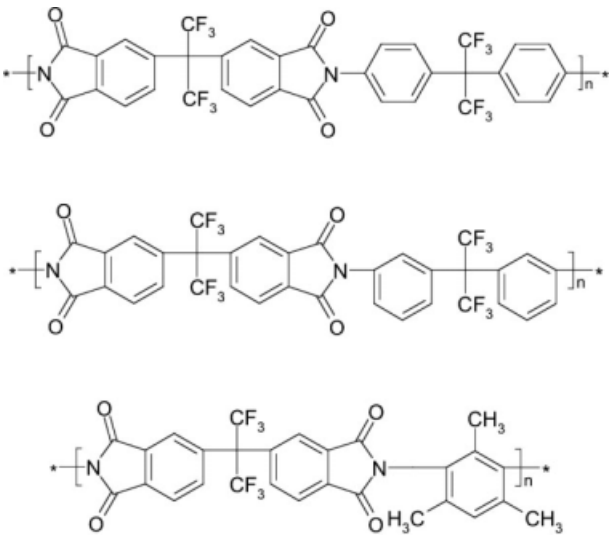

Figure 1. Chemical structures of the 6FDA-6FpDA, 6FDA-6FmDA, and 6FDA-DAM polyimides.

also leads to high glass-transition temperatures and high radiation resistances.[1–4]

The industrial applications of 6FDA-based polyimides are numerous and range from electronics,[8] electrical[9] and optical engineering,[10,11] radiation resistance,[12] and aviation[13] to filtration membranes.[3,4] For example, these polyimides are used in microelectronics to prepare the intermetal dielectric and passivation layers.[9] When they are used as an insulating material, the speed of the signal transmission in the electrical circuit increases.[6] They play a crucial role in the simultaneous counting of different radiations in dosimetry measurements,[12] as well as in preparing the optical waveguides in optical engineering.[10] Their gas separation properties are also well known.[3–5,14–27] Indeed, the fluorine linkages are thought to disrupt effective packing and increase free volume in the polymer matrices, which tends to enhance the permeability of gas molecules. Their increased permeability without much decrease in gas selectivity leads to high permselectivity as well, which makes these polyimides good membrane materials for such applications. Furthermore, they show acceptable plasticization resistance.[15,16,28]

Experimental characterizations for these macromolecules include density and solubility measurements as well as thermal, mechanical, and permeation analyses.[6,29] Polyimides can also be studied using UV-visible spectrophotometry,[30] wide-angle X-ray diffraction,[31] or positron annihilation.[32] Much effort has been devoted to understand molecular ordering and its influence on various properties.[33] This will potentially lead to new applications. Within this context, it is interesting to consider molecular dynamics (MD) simulations, which are able to provide a dynamic model of the polyimides at the atomic level. This information can be used to interpret the properties and the experimental behavior of the modeled polyimide structures.

MD simulations of several amorphous polyimides have already been reported in the literature.[34–48] In the present study, we have considered three 6FDA-based homopolyimides, namely 6FDA-6FpDA, 6FDA-6FmDA, and 6FDA-DAM. The actual names for the various polyimides are poly((4,4′-[2,2,2-trifluoro-1-(trifluoromethyl)ethane-

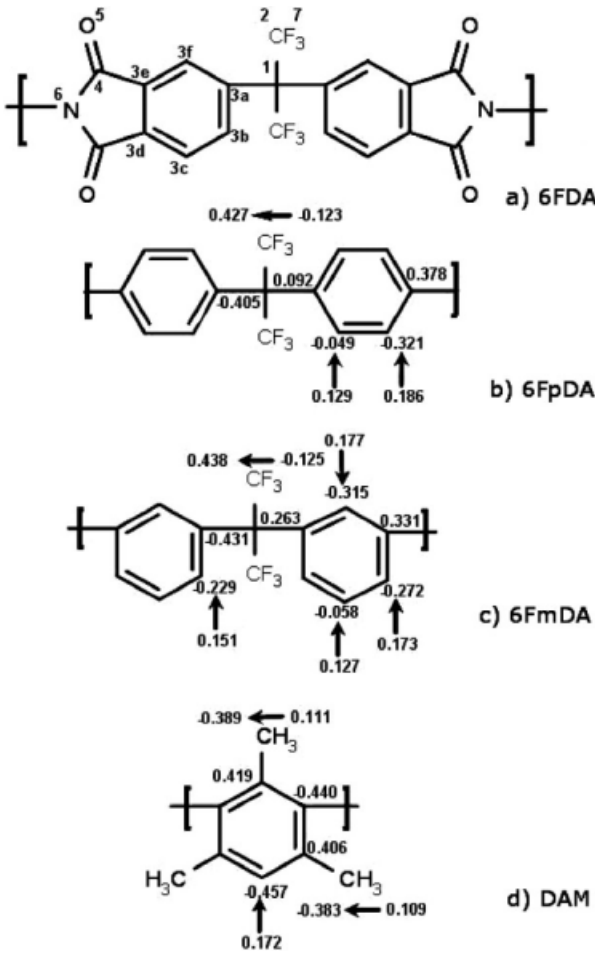

Figure 2. Partial charges q_i/e for the various basic fragments, i.e., 6FDA, 6FpDA, 6FmDA, and DAM. Since the charges on the 6FDA fragment depend on the adjacent diamine, they are given in Table 1. Charges placed at the start of an arrow are carried either by hydrogens or by fluorines for the 6FpDA, 6FmDA, and DAM structures. The arrows point towards the charges of the carbons carrying these hydrogens or fluorines.

Table 1. Partial Charges, q_i/e, on the 6FDA Fragment as a Function of the Adjacent Diamine

Atom Type	Element Symbol	6FDA with 6FpDA	6FDA with 6FmDA	6FDA with DAM
1	$C(C_1)$	−0.567	−0.559	−0.610
2	$C(C_{F1})$	0.441	0.429	0.427
3a	$C(C_{ar1})$	0.279	0.268	0.293
3b	$C(C_{ar1})$	−0.142	−0.141	−0.179
3c	$C(C_{ar1})$	−0.091	−0.102	−0.029
3d	$C(C_{ar1})$	−0.116	−0.091	−0.167
3e	$C(C_{ar1})$	−0.073	−0.099	−0.127
3f	$C(C_{ar1})$	−0.155	−0.125	−0.084
4	$C(C_{ket})$	0.583	0.553	0.463
5	$O(O_{ket})$	−0.447	−0.436	−0.427
6	N	−0.410	−0.349	0.095
7	$F(F_1)$	−0.116	−0.115	−0.111
H on 3b	H	0.137	0.138	0.138
H on 3c	H	0.139	0.141	0.128
H on 3f	H	0.135	0.126	0.122

1,1-diyl]dianiline}-alt-{5,5′-[2,2,2-trifluoro-1-(trifluoromethyl)ethane-1,1-diyl]bis(isobenzofuran-1,3-dione)}) (6FDA-6FpDA), poly((3,3′-[2,2,2-trifluoro-1-(trifluoromethyl)ethane-1,1-diyl]dianiline}-alt-{5,5′-[2,2,2-trifluoro-1-(trifluoromethyl)ethane-1,1-diyl]bis(isobenzofuran-1,3-dione)}) (6FDA-6FmDA), and poly((2,4,6-trimethyl-*m*-phenylenediamine)-alt-{5,5′-[2,2,2-trifluoro-1-(trifluoromethyl) ethane-1,1-diyl]bis(isobenzofuran-1,3-dione)}) (6FDA-DAM) and their chemical structures are shown in Figures 1 and 2. Note that 6FpDA is also sometimes referred to as BAAF,[23,31,32,38,49] 6FAP,[50,51] 4APF[52] or BAHF,[53] that DAM can be called TrMPD,[54–57] 3MPDA,[19] and that 6FmDA corresponds to 3APF.[52] In the present work, realistic atomistic models of long 6FDA-based polyimides have been prepared using well-established simulation techniques.[58] Their bulk densities, energies, voidspaces as well as their conformational and configurational properties are compared to available experimental data. Since all these polyimides have been synthesized and characterized, consistent experimental evidence[1–3,17,19,20,23,27,47,49,54–57,59–62] is available in the literature to be confronted to the MD simulations. Computational details are given in Section 2 and the long-chain models are analyzed in Section 3.

COMPUTATIONAL DETAILS

Force-Field

Molecular dynamics (MD) simulations were carried out using the scalar and parallel forms of the *gmq*[63,64] program. The force-field parameters for polyimides were taken from the freely-available TRIPOS 5.2 force field.[65] The reliability of the *gmq* program and the applicability of the force-field to polyimides have already been documented in the literature,[35–37,66–71] and only a brief review is presented here. We point out in passing that TRIPOS has also been used to model other types of polymers.[72–75] The functional form of the potential is divided into two categories, where the bending, torsional, and out-of-plane potentials are collectively called the "bonded" potentials. The van der Waals and electrostatic potential are referred to as the "nonbonded" potentials. The van der Waals interactions are represented by the Lennard-Jones (L-J) 12-6 form and electrostatic interactions are calculated using the Ewald[76] summation method. All atoms separated by more than two bonds interact through the nonbonded potentials. Rigid constraints are used for high frequency stretching modes,[77] and the timestep is set to 10^{-15} s. The partial charges q_i/e on the atoms were calculated on representative three- or five-fragment structures of the polyimides under study by using Gaussian 03[78] at the B3LYP/6-31G** level. Charges in the central moieties of the model fragments were extracted by an electrostatic-potential fitting procedure.[79] All q_i/e charges considered in this work are given in Figure 1 and Table 1. Lorentz-Berthelot combination rules[80] were used for all the cross-term parameters of the van der Waals potential.

Generation of the Starting Structures

The hybrid pivot Monte Carlo-molecular dynamics (PMC-MD) single-chain sampling procedure

was used to generate the initial configurations of polyimides.[35–37,66–71] In this method, a Monte Carlo pivot move of a randomly-selected rotatable torsion is attempted after a fixed number of standard MD steps. The change in energy is based on Flory's hypothesis of a "local energy approximation," i.e., conformations of polymer chains in the melt are governed by intramolecular interactions of a fixed number of near-neighbor atoms.[81] Only highly localized interactions, that is not more than those between atoms separated by a fixed number of backbone bonds (n_{bonds}), are considered for the local energy approximation. This method has been validated for a variety of polymers,[35–37,66–71] and in most cases, n_{bonds} has been found to be equal to 4. However, there were enough exceptions to prove that the n_{bonds} value is not universal,[70,82] and it should therefore be validated for all three new polyimide structures under study. The validation implies comparing the results obtained using PMC-MD single chain sampling under Flory's local energy approximation with those of a bulk melt decorrelated using MD on its own. It is clear that it can only be carried out for short homologues and, with such rigid chains as polyimides, at a fairly high temperature in order for the bulk melts to be totally decorrelated, i.e., independent of their starting structures, under the timescale available to MD simulations.

For each fluorinated polyimide, single chains of four monomers (266 atoms for 6FDA-6FpDA and 6FDA-6FmDA, 226 atoms for 6FDA-DAM), five monomers (332 atoms for 6FDA-6FpDA and 6FDA-6FmDA, 282 atoms for 6FDA-DAM), and six monomers (398 atoms for 6FDA-6FpDA and 6FDA-6FmDA, 338 atoms for 6FDA-DAM) were decorrelated and sampled using the hybrid PMC-MD technique with a variety of n_{bonds} values at 1000 K. Separate bulk melts (20 chains for the four-monomers, 15 chains for the five-monomers, and 12 chains for the six-monomers) were created with each chain being generated by PMC-MD and the excluded volume being introduced. The dense melts were decorrelated using MD on its own at 1000 K under NpT (constant number of atoms N, isotropic pressure p and temperature T) conditions. The respective number of atoms in the bulk-melt boxes were 5320 (four-monomers), 4980 (five-monomers), 4776 (six-monomers) for the 6FDA-6FpDA and 6FDA-6FmDA systems, and 4920 (four-monomers), 4605 (five-monomers) and 4416 (six-monomers) for the 6FDA-DAM bulks. Decorrelation was assessed using the normalized autocorrelation functions for the square end-to-end distances and end-to-end vector.[58] The latter took typically 8000 ps to decorrelate in the shorter four-monomer systems and as much as 25000 ps for the longer six-monomer systems. On the other hand, the PMC-MD-sampled chains were decorrelated in less than 200 ps. Following decorrelation of both single-chain-sampled and bulk melts chains, their structural characteristics for each set of the same structure and size were compared. As found before, they look very similar for an n_{bonds} value of 4. The average percentages of the pivot C—C—C—C τ angle in the middle of the 6FDA fragment which were calculated as being *trans* (i.e., defined as $-60^\circ < \tau < 60^\circ$), $\langle \%trans \rangle$, as well as the mean-square end-to-end distances $\langle R^2 \rangle$ and the mean-square radii of gyration $\langle S^2 \rangle$ are given in Table 2 for both PMC-MD single-chain-sampled and the corresponding MD bulk chains.

The underlying distributions show a similar level of agreement. For example, the distribution of $\langle S^2 \rangle$ for the four-monomer and for the six-monomer 6FDA-6FpDA is presented in Figure 3. It is clear that configurations created and sampled by PMC-MD are fully consistent with those of the decorrelated pure MD bulk melt, even if statistics are poorer in the latter case. There are similar levels of agreements in all 6FDA-6FmDA and 6FDA-DAM systems.

Using various chain lengths in the PMC-MD single-chain sampling procedure showed that a plateau is reached for $\langle R^2 \rangle / n_{\text{monomers}}$ after $\sim$25 monomers. A size of 50 monomers was consequently used in all our studies. For each polyimide simulation, the required number of uncorrelated chains, generated using PMC-MD at a temperature just above the glass transition T_g, were placed in a periodic cubic box of a size corresponding to the experimental density. The reason for using an initial simulation box that gives a density close to that expected from the experimental measurements warrants further explanation as it can be misinterpreted as being an attempt to guarantee good agreement between experimental and simulated densities. In fact, the reason is quite straightforward. The amorphous chain conformations are generated at a temperature consistent with the known glass transition temperature of the polymers. As the time scale for MD simulations is relatively short in comparison to the natural relaxation times for polymers, it is essential that there are no large scale changes in volume following the introduction of the chains

Table 2. Comparison of $\langle \%trans \rangle$ for the 6FDA Pivot Angle, $\langle R^2 \rangle$ and $\langle S^2 \rangle$ Between PMC-MD Sampled Single Chains with $n_{bonds} = 4$ ("Single Chain"), and the Corresponding Bulk Melt Chains Decorrelated Using MD on Its Own ("Bulk Melt") at 1000 K

Chemical Structure	Number of Monomers	Sampling	$\langle \%trans \rangle$	$\langle R^2 \rangle$ (Å^2)	$\langle S^2 \rangle$ (Å^2)
6FDA-6FpDA	4	Single chain	28.09 ± 0.03	1600 ± 50	240 ± 5
		Bulk melt	27.89 ± 0.02	1780 ± 250	260 ± 20
	5	Single chain	28.03 ± 0.03	2060 ± 80	320 ± 10
		Bulk melt	27.92 ± 0.01	1840 ± 330	300 ± 25
	6	Single chain	28.04 ± 0.03	2610 ± 130	400 ± 15
		Bulk melt	27.88 ± 0.01	2520 ± 490	370 ± 40
6FDA-6FmDA	4	Single chain	28.11 ± 0.04	1170 ± 60	190 ± 10
		Bulk melt	27.93 ± 0.04	1130 ± 180	180 ± 15
	5	Single chain	28.04 ± 0.04	1520 ± 100	245 ± 10
		Bulk melt	27.91 ± 0.03	1225 ± 220	260 ± 20
	6	Single chain	28.01 ± 0.03	1950 ± 100	315 ± 10
		Bulk melt	27.92 ± 0.03	1940 ± 440	315 ± 40
6FDA-DAM	4	Single chain	28.20 ± 0.04	1150 ± 60	170 ± 5
		Bulk melt	27.87 ± 0.02	1050 ± 150	160 ± 10
	5	Single chain	28.08 ± 0.04	1530 ± 70	230 ± 10
		Bulk melt	27.83 ± 0.02	1300 ± 240	210 ± 20
	6	Single chain	28.07 ± 0.03	1770 ± 70	270 ± 10
		Bulk melt	27.85 ± 0.02	1640 ± 320	250 ± 30

Analyses have been carried on a total of 4000 ps following decorrelation for both single-chain sampled and bulk melt chains. The averages are given with their standard errors.

and the switching on of the full interactions. Large volume variations will lead to distortion of the carefully prepared polymer conformations which will not have time to relax subsequently. It is thus necessary that the initial volume be as close as possible to the final one. Once the simulation is switched to constant pressure conditions at the required temperature, the volume is free to relax. Should the interaction parameters be poorly adapted to the system being simulated then the density can change significantly and, in our experience, differ by 10% or more from the experimental one.

Here, the generation temperature was 700 K for 6FDA-6FpDA and 6FDA-DAM, since experimental measurements of T_g are in the range 575–605 K for 6FDA-6FpDA[1,5,17,20,47,49,50,57,59–61,83–85] and 640–670 K for 6FDA-DAM.[1,19,27,55,57,84,86] The generation temperature was set to 600 K for 6FDA-6FmDA as it has a lower T_g of ~530 K.[15,47,83,87] For each fluorinated polyimide under study, a series of five three-chain systems (9906 atoms for 6FDA-6FpDA, 6FDA-6FmDA and 8406 atoms for 6FDA-DAM) was built as well as five larger six-chain systems (19812 atoms for 6FDA-6FpDA and 6FDA-6FmDA and 16812 atoms for 6FDA-DAM). The total number of independent samples generated thus amounted to thirty.

Following the single chain sampling procedure, the excluded volume was introduced gradually[58] by scaling the potential from 0 to 1. To remove the heat generated during this process, the velocities

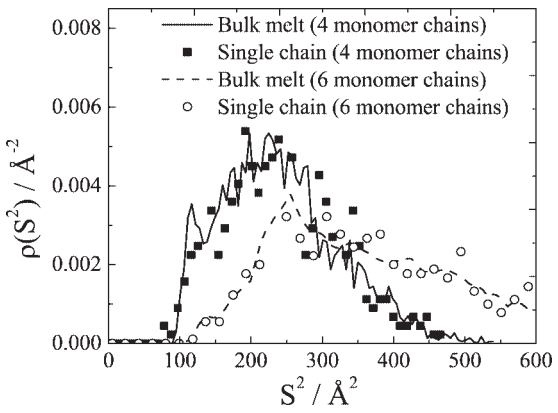

Figure 3. The probability densities for the square radii of gyration S^2 in 4-monomer and 6-monomer 6FDA-6FpDA chains at 1000 K using $n_{bonds} = 4$. Results obtained from single chain sampling are compared to those found in the bulk melt.

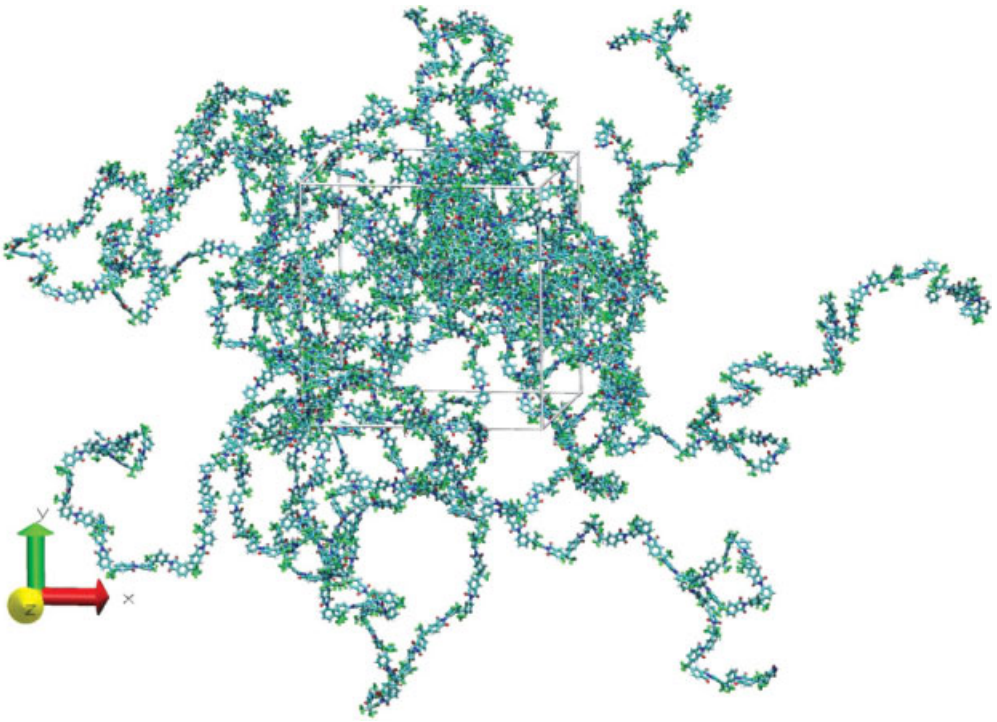

Figure 4. A schematic wire-frame representation of one of the 19812-atom 6FDA-6FmDA simulation boxes, showing the primary positions of the atoms. Simulations are carried out using three-dimensional periodic boundary conditions.

of the atoms were rescaled at each timestep. A phantom atom was placed at the center of mass of each five-atom and six-atom ring to avoid unphysical spearing and interlocking during this progressive introduction. Once the excluded volume had been introduced, the phantom atoms were removed and the electrostatic interactions were switched on. The Ewald summation[76,88] method was used to calculate the electrostatic interactions. For the three-chain systems, satisfactory convergence was obtained using the following parameters: $\alpha = 0.27$ Å^{-1} (6FpDA), 0.28 Å^{-1} (6FmDA and DAM); $K_{max} = 13$ (6FpDA and 6FmDA) and 14 (DAM); the real space truncation radius $R_c = 9$ Å (6FpDA and 6FmDA) and 9.5 Å (DAM). For the six-chain systems, the parameters used were: $\alpha = 0.29$ Å^{-1} (6FpDA), 0.26 Å^{-1} (6FmDA), 0.27 Å^{-1} (DAM); $K_{max} = 17$ (6FpDA), 15 (6FmDA and DAM); $R_c = 9.5$ Å (6FpDA, 6FmDA, and DAM). The van der Waals truncation radius was set to the same value than R_c and standard long-range corrections to the energy and the pressure were also made for interactions beyond the truncation radius. Systems were relaxed under constant-volume NVT conditions for 500 ps. The simulation boxes were then cooled down to room temperature (298 K) at a rate of −1 K/ps. Following a short NVT relaxation at room temperature, the systems were switched to NPT conditions, i.e., constant number of atoms, and controlled pressure and temperature. The required pressure tensor was set to 1 bar for on-diagonal and to 0 for off-diagonal components. The pressure[89] and temperature[90] of the systems were controlled by loose coupling using coupling constants of 5 ps and 0.1 ps, respectively. Under NPT conditions, each simulation was continued for up to 3000 ps, in which the final 2000 ps were considered as its production run. A schematic representation of a simulation box is shown in Figure 4.

It should be noted that the introduction of the full potential into an initially noninteracting ensemble of highly flexible chains such as alkanes[66,91] or bead-spring models[92] can lead to some moderate changes in the intrachain distances at intermediate length scales. To assess whether this is an important effect in these polyimide systems, the mean square distances between two monomers separated by n others along a polymer chain, $\langle R^2(n)\rangle$, have been calculated. This internal distance[93] tends towards the mean square end-to-end distance, $\langle R^2\rangle$, as n approaches the degree of polymerization of the polymer chain. A plot of $\langle R^2(n)\rangle/nl^2$ versus n should thus be similar

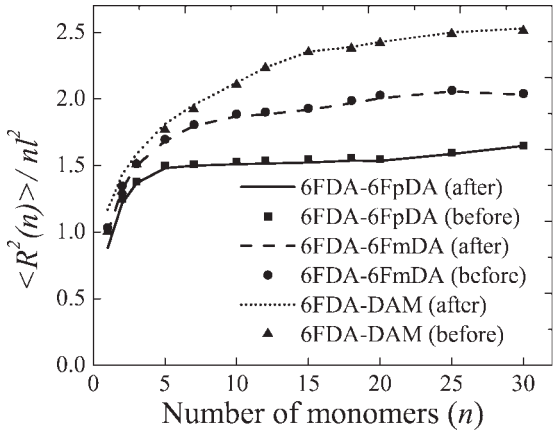

Figure 5. The average internal distances between monomers separated by n others along the chain divided by nl^2 as a function of n and averaged over 3-chain systems (5 systems of ~10000 atoms each per polyimide). Black "before" points were obtained from the last configuration of the PMC-MD runs in the melt. The "after" lines show the results for the same chains following the introduction of the full potential and NVT relaxation by MD at the same temperature.

to that for a characteristic ratio.[94] Such a plot is given in Figure 5, where the normalizing "length" of a monomer, l, has been defined to be the average distance between the central carbons of successive 6FDA fragments as determined from the last configurations of the PMC-MD runs. The values obtained for l for each polymer were: 18.68 Å for 6FDA-6FpDA, 18.64 Å for 6FDA-6FmDA, and 15.21 Å for 6FDA-DAM. Figure 5 compares the results obtained for the chains before the introduction of excluded volume with the same ones following relaxation by MD. Differences are typically less than 0.5%, i.e., of much the same order as found for some nonfluorinated polyimides.[58,93,95] These relatively small differences are attributed to the highly rigid nature of the polyimides and confirm that the effect of introducing the full potential remains very limited in such systems.

Figure 5 also shows that the three polyimides under study differ in terms of configurational properties. The trend is similar to the mean square end-to-end distances and radii of gyration displayed in Table 2, although the $\langle \%trans \rangle$ of 6FDA pivot angle, which is common to all three polymers, remains the same. Configurational differences are thus likely to stem mainly from the choice of the diamine. The order follows from the different values of l, i.e., the largest dimensions are found in 6FDA-6FpDA followed by 6FDA-6FmDA and then 6FDA-DAM.

RESULTS AND DISCUSSION

Bulk Properties

The bulk properties of the three polyimides were obtained from the production runs at 298 K of the 50-monomer multichain systems. The average values for the model densities, $\langle \rho_{\text{model}}^{298\text{K}} \rangle$, volumes of the MD cells, $\langle V \rangle$ and intermolecular potential energies, $\langle U_{\text{pot}}^{\text{inter}} \rangle$ are presented in Table 3.

The experimental density of 6FDA-6FpDA averaged over 12 literature values is 1477 ± 3 kg m^{-3}, that of 6FDA-6FmDA averaged over 3 literature values is 1493 ± 1 kg m^{-3} and that of 6FDA-DAM averaged over 7 literature values is 1339 ± 7 kg m^{-3}.[1,2,5,17,20,47,49,50,57,59–61,83,84] Our average model densities $\langle \rho_{\text{model}}^{298\text{K}} \rangle$ are clearly in very good agreement with the experimental densities available in the literature. The relative differences are only about 1% for 6FDA-6FpDA and less than 1.5% for both 6FDA-6FmDA and 6FDA-DAM. Considering the natural scatter in experimental results, our models reflect the accuracy of the force field and the quality of the preparation procedure. The decreasing order in densities follows the increasing order in wide-angle X-ray diffraction spacing, that is 6FDA-6FmDA (d-spacing = 5.7 Å)[4,47] < 6FDA-6FpDA (d-spacing = 5.9 Å)[4,31] < 6FDA-DAM (d-spacing = 6.5 Å).[55] The X-ray diffraction d-spacing is thought to be a useful measure of average interchain distances.[96,97]

It should be pointed out that the density difference between the symmetric 6FDA-6FpDA and asymmetric 6FDA-6FmDA polyimides is rather small, both from an experimental and from a modeling point of view. It has been noted in an experimental study that, although this could reflect small variations in intersegmental packing and void spaces, such a limited difference in density is not enough to fully explain the respective gas transport properties.[83] Indeed the permeability of CO_2 in the *para*-isomer has been measured to be about 10 times higher than that in the *meta*-isomer.[3,4,15,16,83] On the other hand, both isomers are known to differ markedly in glass transition (T_g) (575–605 K for 6FDA-6FpDA and ~530 K for 6FDA-6FmDA) and sub-T_g temperatures.[1–3,17,19,20,23,27,47,49,54–57,59–62] It has thus been suggested that the lower permeability of *meta*-linked aromatic polymers might be a result of hindered rotation about the *meta*-connected linkage.[98] This would imply that the dynamic properties are more important for gas diffusion in

Table 3. Average Densities $\langle \rho_{\text{model}}^{298\,\text{K}} \rangle$, Volumes of the MD Cells $\langle V \rangle$, Intermolecular Potential Energies $\langle U_{\text{pot}}^{\text{inter}} \rangle$, $\langle U_{\text{vdw}}^{\text{inter}} \rangle$, and $\langle U_{\text{coul}}^{\text{inter}} \rangle$, Hildebrand Solubility Parameters $\langle \delta \rangle$, and Fractional Free Volumes $\langle \text{FFV} \rangle$ Obtained from MD Simulations of the Three Polyimides Under Study

Properties	6FDA-6FpDA		6FDA-6FmDA		6FDA-DAM	
No. of atoms	9,906	19,812	9,906	19,812	8,406	16,812
No. of systems	5	5	5	5	5	5
$\langle \rho_{\text{model}}^{298\text{K}} \rangle$ (kg m^{-3})	1492 ± 3	1495 ± 3	1508 ± 3	1507 ± 2	1326 ± 10	1322 ± 4
$\langle V \rangle$ (nm^3)	124.0 ± 0.2	247.4 ± 0.4	122.7 ± 0.2	245.4 ± 0.4	104.7 ± 0.7	210.5 ± 0.7
$\langle U_{\text{pot}}^{\text{inter}} \rangle$ (kJ mol^{-1} monomer^{-1})	−141 ± 1	−140.6 ± 0.8	−138.4 ± 0.9	−138 ± 1	−102.7 ± 0.4	−103.7 ± 0.4
$\langle U_{\text{vdw}}^{\text{inter}} \rangle$ (kJ mol^{-1} monomer^{-1})	−133 ± 1	−132.9 ± 0.8	−131.6 ± 0.6	−131.0 ± 0.4	−96.0 ± 0.6	−97.2 ± 0.4
$\langle U_{\text{coul}}^{\text{inter}} \rangle$ (kJ mol^{-1} monomer^{-1})	−7.5 ± 0.3	−7.7 ± 0.1	−6.8 ± 0.3	−6.8 ± 0.1	−6.7 ± 0.3	−6.5 ± 0.2
$\langle \delta \rangle$ (J$^{1/2}$ cm$^{-3/2}$)	16.81 ± 0.07	16.80 ± 0.05	16.79 ± 0.05	16.64 ± 0.06	15.68 ± 0.04	15.67 ± 0.05
$\langle \text{FFV} \rangle$	0.176 ± 0.001	0.174 ± 0.001	0.167 ± 0.001	0.167 ± 0.001	0.178 ± 0.005	0.182 ± 0.003

The total number of simulations is 30, and for each size, five systems were averaged over their 2 ns production runs. Results are displayed with their associated standard errors.

these isomers rather than the static properties such as the density or solubility. In the case of 6FDA-DAM, $\langle \rho_{\text{model}}^{298\text{K}} \rangle$ is lower than for the other two polyimides as the three methyl groups carried by the DAM diamine tend to disrupt chain packing. This has been shown experimentally by Tanaka et al., in a study where they varied systematically the number of methyl groups and substitution positions.[57] Consequently, 6FDA-DAM exhibits high gas permeabilities and low selectivities.[1,27,55–57]

The average intermolecular potential energies of the systems $\langle U_{\text{pot}}^{\text{inter}} \rangle$ were very much comparable to those for other long-chain polyimide reported in the literature,[35,71,95] with the major part of the potential energy (>90%) coming from the van der Waals component $\langle U_{\text{vdw}}^{\text{inter}} \rangle$ (refer Table 3). Within the statistical errors, the van der Waals energies for both isomers are fairly similar whereas a slightly more important electrostatic contribution $\langle U_{\text{coul}}^{\text{inter}} \rangle$ is seen for 6FDA-6FpDA. This could be due to the differences in partial charges (refer Fig. 2 and Table 1). The presence of fluorine groups on the diamines does not seem to affect very much $\langle U_{\text{coul}}^{\text{inter}} \rangle$ despite the negative partial charges carried by fluorine atoms. Indeed, they can lead to attractive interactions with positively charged atoms, but this is counteracted by the steric repulsions due to the van der Waals volume (≈21.3 cm^3 mol^{-1} for a CF_3 group).[99] The effect of the DAM diamine is especially visible in $\langle U_{\text{vdw}}^{\text{inter}} \rangle$. It is consistent with a lower density and suggests a poorer stacking of the chains. However, it is difficult to compare it directly to the others as its geometry is fundamentally different.

The average Hildebrand solubility parameter $\langle \delta \rangle$, also shown in Table 3, is defined as the square root of the cohesive energy density,[99] that is:

$$\langle \delta \rangle = \sqrt{\frac{\left\langle U_{\text{pot}}^{\text{inter}} \right\rangle}{\langle V \rangle}} \tag{1}$$

with $\langle U_{\text{pot}}^{\text{inter}} \rangle$ being the average intermolecular energy of the system and $\langle V \rangle$ the average volume of the simulation box. It is generally assumed that if the Hildebrand δ parameters of a polymer and a solvent are similar, then the solubility of the polymer in the solvent should be favorable.[99] Solvents used to prepare fluorinated polyimide include dichloromethane (δ = 19.9 J$^{1/2}$ cm$^{-3/2}$), tetrahydrofuran (δ = 19.5 J$^{1/2}$ cm$^{-3/2}$), *N*,*N*-dimethylacetamide (δ = 22.1–22.8 J$^{1/2}$ cm$^{-3/2}$), *N*,*N*-dimethylformamide (δ = 24.9 J$^{1/2}$ cm$^{-3/2}$), and acetone (δ = 20.0–20.5 J$^{1/2}$ cm$^{-3/2}$).[7,99] Considering the empirical approach used to calculate these δ parameters for the solvents,[99] the calculated polymer δ reported in Table 3 are thus definitely in the right order of magnitude.

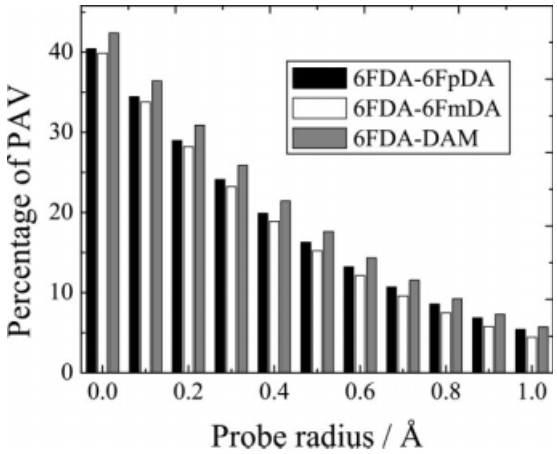

Figure 6. The mean percentage of probe accessible volume plotted as a function of the probe radius used in repeated trial insertions.

Void Space

The average fractional free volumes ($\langle FFV \rangle$) of the polymers were calculated by using $\langle FFV \rangle = (\langle V \rangle - V_0)/\langle V \rangle$ with $\langle V \rangle$ being the average volume of the simulation box and V_0 the volume at zero Kelvin (i.e., 1.3 times the Van der Waals volume),[99] as obtained using Bondi's group contribution method.[1,5,17,20,47,49,50,57,59–61,83–85] The model $\langle FFV \rangle$ for all three polyimides are also presented in Table 3. The values found are in excellent agreement with the reported values in the literature, that is 0.175–0.190 for 6FDA-6FpDA, 0.175 for 6FDA-6FmDA, and 0.182–0.190 for 6FDA-DAM.[3,54,62,83] This suggests that the polyimide with the lowest available free volume is 6FDA-6FmDA followed by 6FDA-6FpDA and 6FDA-DAM. This correlates directly with the order in permeabilities, solubilities, and diffusivities of small gas molecules in these polymer matrices.[1,14–16,20,27,47,57]

To further characterize the void space we have used a simple geometric technique to obtain the probe accessible volume (PAV). Full details of the method have been given elsewhere[95] but it is one of many similar methods which use a "phantom sphere approach" that are widely encountered in atomistic simulations.[40,41,100–102] In brief, the PAV is obtained by repeated trial insertions of virtual probes of preset radius into the dense polymer configurations without any preassumption on the actual form of the holes. An insertion is "accepted" when the probe does not overlap with the polymer atoms when represented by hard spheres with standard van der Waals radii: 1.20 Å for H, 1.47 Å for F, 1.50 Å for O, 1.55 Å for N, and 1.70 Å for C.[99,103] The percentage PAV is then just given by the average percentage of "accepted" insertions with respect to the total number of attempted insertions. It should be noted that the volume measured is just the volume of the system accessible to the centers of the probes. Figure 6 gives the percentage of probe accessible volume as a function of the probe size for all three systems under study.

As expected, the PAV decreases systematically as the probe radius increases. The experimental and model FFV values can be reproduced with probe radii of the order of 0.45 Å. Figure 6 shows that the *meta*-connected isomer tends to have a consistently smaller PAV than the *para*-connected isomer whatever the probe radius. Although not shown, this trend continues up to at least a probe radius of 2 Å. It has been reported elsewhere that the average cavity size in 6FDA-6FpDA should be larger than that in the 6FDA-6FmDA isomer,[47] although we are not aware of any experiments, e.g., positron annihilation, which actually tried to determine this directly. Our models suggest that the differences in accessible void volumes remain fairly minor. This is fully consistent with the small differences in densities seen both experimentally and in modeling, which have been discussed above.

In contrast, 6FDA-DAM exhibits clearly a larger PAV for all probe radii tested. This is obviously related to the lower density and poorer packing in this polyimide. Note that Figure 6 displays the percentage rather than the actual accessible void volume, i.e., the comparison is based on equal volumes of polymer. Comparisons based on equal masses, or moles, of polymer will be quite different for 6FDA-DAM since its density is much lower than the other two polymers (refer Table 3).

A visual inspection of the positions of accepted probes suggests strongly that void space is homogeneously distributed in all the polymer matrices considered. The distributions of hole sizes were then quantified for a range of probe radii corresponding roughly to the size of different gas molecules. The method used to obtain these distributions[64] is based on a standard cluster analysis of the positions of the centers of the accepted probes; all accepted probe centers less than 0.5 Å apart are considered to be in the same hole, i.e., they belong to the same cluster. The averages size of the cavities depends upon the probe radius used, of course, but in general, the average cavity size of 6FDA-6FpDA is larger than the 6FDA-6FmDA and interestingly 6FDA-DAM has smaller

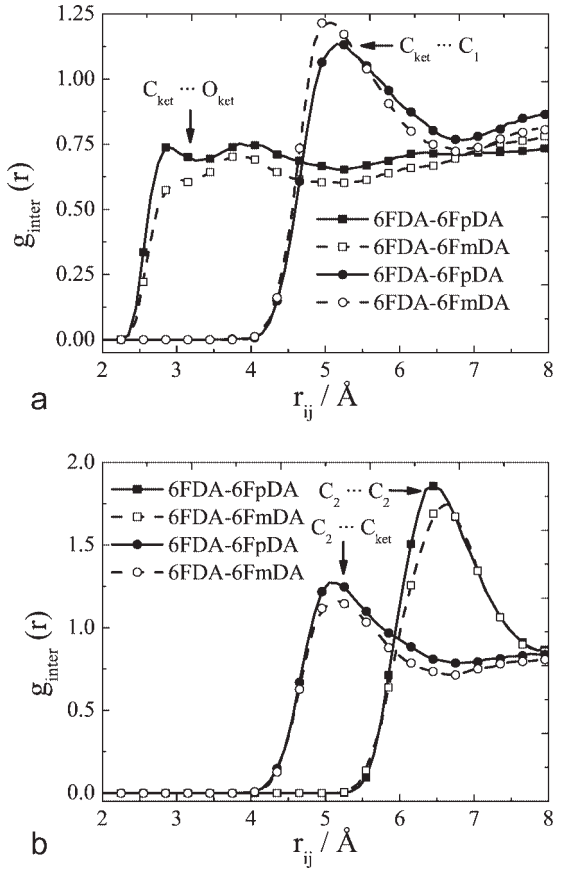

Figure 7. Selected intermolecular radial distributions functions $g_{inter}(r)$ for 6FDA-6FpDA and 6FDA-6FmDA. The upper plot (a) shows some interactions between dianhydride···dianhydride fragments (C_{ket}···O_{ket} and C_{ket}···C_1), and the lower one (b) shows some interactions between dianhydride···diamine and diamine···diamine fragments (C_2···C_{ket} and C_2···C_2). Refer text for definitions of atom types.

cavities. The high solubility and permeability of gas molecules in 6FDA-DAM can thus be explained by its larger total amount of void volume (Fig. 6) and also the resulting higher mobility of the atoms. The indiscriminate mean square amplitudes of motions in the polyimides for a time interval of 1 ns were found to be 0.59 Å^2 for 6FDA-6FpDA, 0.53 Å^2 for 6FDA-6FmDA, and 1.04 Å^2 for 6FDA-DAM. Such small values are typical of glassy polymers.

Structures

The intermolecular radial distribution functions, $g_{inter}(r)$, were extracted for all possible combinations of interactions between different atom types. Indiscriminate $g_{inter}(r)$ showed that there was no sign of crystallinity in our models. This seems consistent with experiment as none of the large number of DSC studies[1,4,15,17–19,27,50,55,60,62,83] reports a melting transition and no mention is made of crystallinity in the X-ray work.[4,32,47,55] As far as both 6FDA-6FpDA and 6FDA-6FmDA isomers are concerned, specific $g_{inter}(r)$ displayed slightly different behaviors depending on the location of the atoms on the respective monomers. In the case of dianhydride···dianhydride interactions, the fluorine 6FDA bridge tends to be somewhat more dominant in 6FDA-6FmDA, whereas interactions between the anhydride parts are favored in 6FDA-6FpDA. This can be seen in Figure 7(a), which displays the respective $g_{inter}(r)$ between ketone carbons (C_{ket}) and ketone oxygens (O_{ket}), as well as between C_{ket} and C_1 (i.e., the central carbon carrying both CF_3 groups in the 6FDA dianhydride).

In the case of dianhydride···diamine and diamine···diamine interactions, 6FDA-6FpDA almost systematically predominates with respect to its isomer. Figure 7(b) shows the $g_{inter}(r)$ for C_2 (i.e., the central carbon carrying both —CF_3 group on the diamine) with itself and with the dianhydride C_{ket}. The symmetric diamine finds it easier to stack than the asymmetric one but it should be stressed once again that the differences remain quite small. On the other hand, the corresponding $g_{inter}(r)$ are systematically found at significantly larger distances for 6FDA-DAM (Fig. 8), which agrees once again with its lower density and

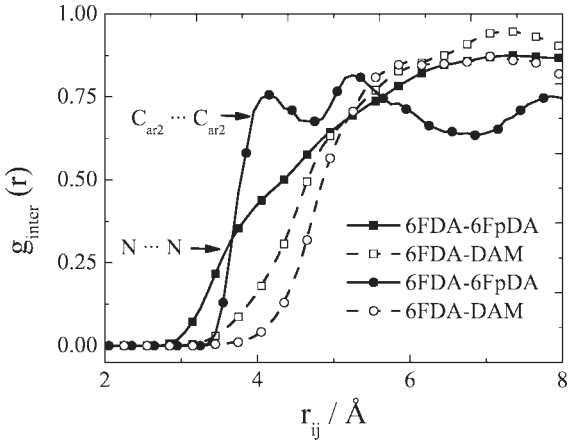

Figure 8. Selected intermolecular radial distributions functions $g_{inter}(r)$ for 6FDA-DAM compared to 6FDA-6FpDA. The interactions displayed are N···N in the 6FDA dianhydrides (squares) and C_{ar2}···C_{ar2} in the diamines (circles), with C_{ar2} being an aromatic diamine carbon.

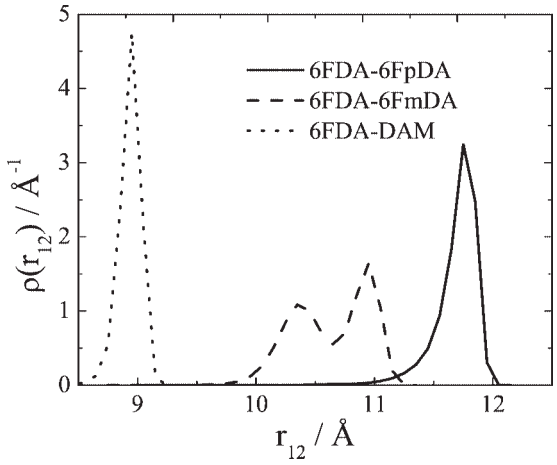

Figure 9. Probability density distributions for the distances, r_{12}, between C_1 (central carbon in the 6FDA dianhydride) and C_2 (central carbon in the diamine for 6FpDA and 6FmDA or center of mass for DAM) in all three polyimides under study.

higher *d*-spacing. The smaller DAM diamine has three substituted methyl groups and, as such, its stacking with another diamine or with a dianhydride is difficult. In turn, it also affects the 6FDA···6FDA $g_{inter}(r)$, which are found at larger distances than for the other polyimides. This poor stacking can be correlated to the larger accessible void volume in 6FDA-DAM (Fig. 6), and is certainly due to the specific geometry of the DAM diamine. Interestingly, $g_{inter}(r)$ for fluorine atoms with the other parts of the monomers are fairly similar in all three systems under study. The CF_3 bridges are very flexible compared to the cyclic motives and it seems that they can adapt easily to the changes in the polymer backbones.

Intramolecular radial distribution functions $g_{intra}(r)$ show mostly some differences for dianhydride···diamine interactions. This can be seen in Figure 9, which give the distributions of distances between C_1 (central carbon in the 6FDA dianhydride) and C_2 (central carbon in the 6FpDA and the 6FmDA diamine, or in the case of DAM, the center of mass of the diamine). If one compares 6FDA-6FpDA and 6FDA-6FmDA, the latter displays two peaks that are found at lower distances than the single peak of the symmetric isomer. The two peaks in 6FDA-6FmDA can be attributed to the two different positions of the C_2 atom with respect to C_1 that result from a rotation through 180° of the diamine ring around the N—C bond linking it to the dianhydride. Although the two peaks appear slightly different in Figure 9, the areas underneath the curves are in fact very close once the correct weighting for 3D space is taken into account. Both conformers are thus almost equally likely. The various combinations of successive conformers give rise to a fairly wide distribution (not shown) for the $C_1···C_2···C_1$ angles in 6FDA-6FmDA with one peak around 110° and another broader one at ~150°. In contrast, the $C_1···C_2···C_1$ angles in 6FDA-6FpDA are all close to 110°, as expected from the symmetry of the *para*-substitution and the single peak in Figure 9. As far as the torsional distributions are concerned, the nearest neighbors $C_1···C_2···C_1···C_2$ pseudotorsion angles are found to be fairly flat. This suggests that the intramolecular differences originate mainly from the very local interactions displayed in Figure 9. The larger distances between *para*-linked aromatic rings with respect to the *meta*-isomer support the aforementioned trend in end-to-end distances and radii of gyration (Table 2), with the 6FDA-6FpDA molecules being more extended than their structural isomers. In the case of 6FDA-DAM, dianhydride···dianhydride intramolecular interactions are fairly similar to those of the other two polyimides, but the smaller diamine leads to even less extended molecules for the same chain lengths (Fig. 9).

Experimental studies of the structure of these polyimides are limited to wide-angle X-ray scattering (WAXS) measurements but, to our knowledge, only two Intensity versus 2θ plots have been published, i.e., the work of Shimazu et al. for 6FDA-6FpDA[31] and of Matsui et al. for 6FDA-DAM.[55] In an attempt to make comparisons with experimental data, pseudo X-ray powder diffractograms (Debye formula) were generated using the DISCUS program[104] from the coordinates of the final configurations of all five samples of the MD-relaxed structures. The X-ray wavelength used in the calculations was $\lambda = 1.54$ Å, corresponding to that of Cu Kα radiation used in the experiments. The resulting average pseudodiffractograms are shown in Figure 10. The agreement with the raw Intensity versus 2θ experimental data is excellent for 6FDA-DAM. For 6FDA-6FpDA it appears less good but it should be noted that this is probably in part due to the experimental data not being published as a raw Intensity versus 2θ plot but in a rather more complex form which makes it difficult to reconstitute the original intensities.[31] Nevertheless the positions and the forms of the three major peaks that appear in the experimental curve are well reproduced by our models.

To characterize the distances and orientations between the rings, the centroid of each aromatic

and anhydride ring and the least-squares best-fit normal vector, $\boldsymbol{n}$, to the plane through the atoms constituting the rings were calculated. The ring···ring $g_{\text{inter}}(r)$ between the centroids were then obtained as well as the second-order Legendre polynomial functions.

$$P_2(\cos\ \theta) = \frac{3}{2}\langle \cos^2 \theta \rangle - \frac{1}{2} \qquad (2)$$

where θ is the angle between the vectors normal to the planes of the different rings. $P_2(\cos\ \theta)$ is 1 for a parallel orientation, 0 for a random orientation, and -0.5 for a perpendicular orientation. Figure 11 shows that the intermolecular diamine rings in 6FDA-6FpDA are close to being parallel at the shortest inter-ring separations but become randomly orientated at around 6 Å. In the corresponding $g_{\text{inter}}(r)$ functions for the centroids of the diamine rings, the tendency for parallel alignment is also restricted to the closest neighbors. Similar trends were found for the other two polyimides and the other ring types.

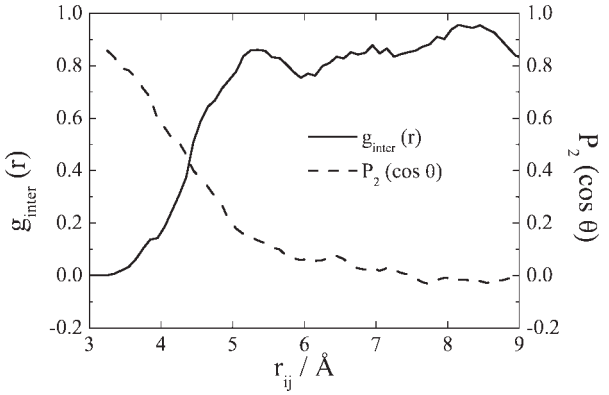

Figure 11. Intermolecular radial distribution function between the diamine aromatic carbons ($C_{ar2}\cdots C_{ar2}$) in 6FDA-6FpDA and the corresponding $P_2(\cos\ \theta)$, as defined in eq 2.

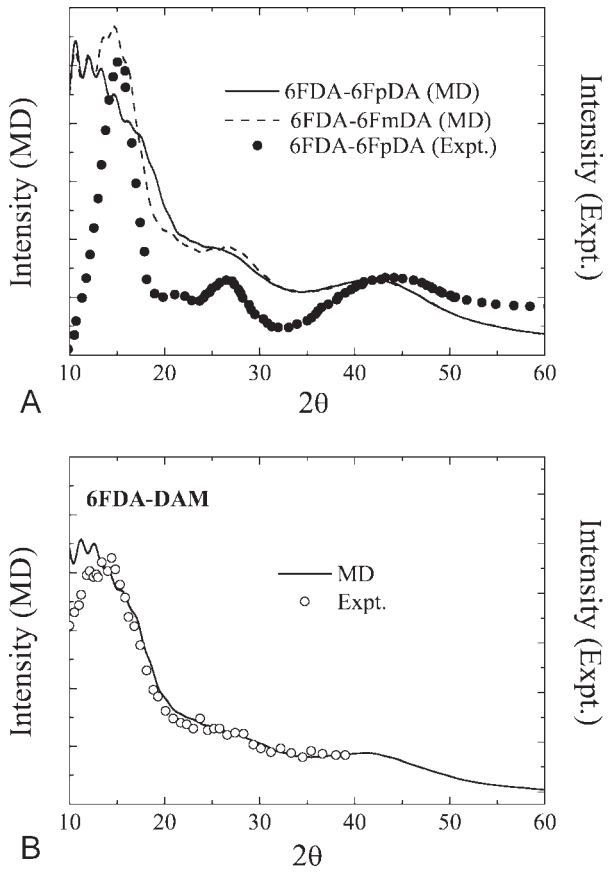

Figure 10. Pseudo X-ray diffractograms at 298 K for (A) 6FDA-6FmDA and 6FDA-6FpDA and (B) 6FDA-DAM; the left-hand MD intensity scales are the same in both plots. The experimental data for 6FDA-6FpDA were generated from Figure 3 of Shimazu et al.[31] by digitizing their data and dividing by the norm of the scattering vector. Data for 6FDA-DAM were taken directly from Figure 2, curve (a), of Matsui et al.[55]

This type of stacking is found in many polyimides and in the case of dianhydride···diamine interactions, it is thought to be related to their ability to form charge transfer complexes (CTC).[105] Classical MD simulations do not allow for such electron transfer but direct orbital interactions are only possible if rings come in close contact to each other. CTC have been found to occur in the 6FDA family, although the presence of fluorine bridges tends to reduce their occurrence compared to more planar dianhydrides such as PMDA-ODA.[105] However, it should be noted that there is as much stacking between dianhydride···dianhydride and diamine···diamine aromatic rings for obvious sterical reasons. This has been shown before for other polyimides.[35] In the present case, it can also be seen when integrating the $g_{\text{inter}}(r)$ to give $n_{\text{inter}}(r)$ between types i and j, i.e., the total number of atoms j belonging to a ring within a specified radius of an atom i belonging to another ring. There is very little difference in the $n_{\text{inter}}(r)$ between $C_{ar1}\cdots C_{ar1}$, $C_{ar1}\cdots C_{ar2}$, $C_{ar2}\cdots C_{ar1}$, and $C_{ar2}\cdots C_{ar2}$ for 6FDA-6FpDA and 6FDA-6FmDA. In the case of 6FDA-DAM, the $C_{ar1}\cdots C_{ar2}$ and $C_{ar2}\cdots C_{ar2}$ n_{inter} (r) are divided by 2 because the DAM diamine has only one aromatic ring. Stacking is thus possible between any kind of ring, irrespective of whether they belong to a dianhydride or a diamine fragment.

CONCLUSION

MD simulations of all-atom models of 6FDA-6FpDA, 6FDA-6FmDA, and 6FDA-DAM have been successfully carried out. In total, 30 independent long-chain samples were prepared using a well-established hybrid PMC-MD technique[58] after verification on short oligomers that a value of $n_{bonds} = 4$ was appropriate. No evidence was found to suggest that the introduction of excluded volume significantly distorts the carefully prepared polymer conformations. Average relaxed densities of the long-chain systems were found to be in very good agreement with experimental values. Model structures agreed also with available wide-angle X-ray scattering (WAXS) data.

The two isomers, 6FDA-6FpDA and 6FDA-6FmDA, show some differences that originate from intramolecular interactions which result in the 6FDA-6FpDA configurations being more extended than their 6FDA-6FmDA counterparts. There is also better stacking of the symmetric 6FpDA diamine and slight differences in the dianhydride interactions as seen in the intermolecular radial distribution functions. Globally, the isomers do not differ much in terms of densities, energies, free volume fractions, and probe-accessible volume distributions. The slight trend in the model free volumes (6FDA-6FpDA > 6FDA-6FmDA) is in agreement with the experimentally-determined gas diffusion and solubility coefficients being systematically larger in the 6FpDA isomer. However, as has been pointed out previously in the experimental studies of Coleman and Koros,[83] the differences in permeabilities between both isomers cannot be explained by such limited variations in bulk properties. It is more likely due to the different sub-T_g and T_g temperatures in the isomers.[14] We note in passing that it is our intention to perform simulations of CO_2 transport in these polymers to see whether we find the same difference as that reported by Koros and coworkers.[1,14–16]

6FDA-DAM has a lower density and higher energy than both other polyimides under study. It also exhibits higher fractional free volume which is in agreement with larger permeabilities and diffusivities for the gas molecules in this polymer matrix.[1,31,55–57] The 6FDA-DAM configurations are smaller for the same chain length than the other models but this is due to the fact that the diamine has only one ring. In addition, the DAM diamine finds it hard to stack with other fragments due to the presence of methyl groups, which increases the space available for penetrants. Indeed, the intermolecular interactions are systematically found at higher distances than for 6FDA-6FpDA and 6FDA-6FmDA.

In all cases, fluorine atoms do not really show any preferential interactions with specific atoms on the polymers. They have a general repulsive effect and limit close packing. In the present work, it is difficult to compare their effect to that of the methyl groups, as the DAM structure was chosen because of its high permeabilities to small gas molecules, rather than with respect to the geometry of its diamine. However, it has been shown experimentally that, providing the basic diamine structure is the same, fluorinated polyimides exhibit better permeabilities than nonfluorinated ones.[4] Whether the solubility of CO_2 in the pure polyimide matrices presented in this work can be linked to specific groups on the macromolecules will be the subject of a future publication.

The CCRT, IDRIS, and CINES national supercomputing centers in France, the MUST cluster at the University of Savoie (France), and the MPIP (Germany) are acknowledged for their generous provision of computer time. S. P. is deeply grateful to the Assemblée des Pays de Savoie and to the MPIP for the award of a doctoral research grant as well as to the Région Rhône-Alpes for the award of a travel grant. The authors acknowledge the helpful discussions with Yuri Andreev of the Chemistry Department of St. Andrew's University, Scotland, concerning experimental X-ray diffraction.

REFERENCES AND NOTES

1. Kim, J. H.; Koros, W. J.; Paul, D. R. J Membr Sci 2006, 282, 21–31.
2. Kim, J. H.; Koros, W. J.; Paul, D. R. J Membr Sci 2006, 282, 32–43.
3. Fuhrman, C.; Nutt, M.; Vichtovonga, K.; Coleman, M. R. J Appl Polym Sci 2004, 91, 1174–1182.
4. Coleman, M. R.; Koros, W. J. J Polym Sci Part B: Polym Phys 1994, 32, 1915–1926.
5. Staudt-Bickel, C.; Koros, W. J. J Membr Sci 2000, 170, 205–214.
6. Ghosh, M. K.; Mittal, K. L. Polyimides: Fundamentals and Applications; Marcel Dekker Inc.: New York, 1996.
7. Recio, R.; Palacio, L.; Pradanos, P.; Hernandez, A.; Lozano, A. E.; Marcos, A.; de la Campa, J. G.; de Abajo, J. J Membr Sci 2007, 293, 22–28.
8. Zhao, X.; Liu, J.; Yang, H.; Fan, L.; Yang, S. Eur Polym J 2008, 44, 808–820.

9. Yang, C.-Y.; Hsu, S. L.-C.; Chen, J. S. J Appl Polym Sci 2005, 98, 2064–2069.
10. Baek, S.; Kang, J.; Li, X.; Lee, M.; Kim, J. Opt Lett 2004, 29, 301–303.
11. Jiang, W.; Wang, D.; Guan, S.; Gao, H.; Zhao, Y.; Jiang, Z.; Gao, W.; Zhang, D.; Zhang, D. J Photochem Photobiol A Chem 2008, 197, 426–433.
12. Quaranta, A.; Vomiero, A.; Carturan, S.; Maggioni, G.; Della Mea, G. Synth Met 2003, 138, 275–279.
13. Synowki, R. A.; Hale, J. S.; Woollam, J. A. J Spacecr Rockets 1993, 30, 116–119.
14. Costello, L. M.; Koros, W. J. J Polym Sci Part B: Polym Phys 1995, 33, 135–146.
15. Coleman, M. R.; Koros, W. J. Macromolecules 1997, 30, 6899–6905.
16. Coleman, M. R.; Koros, W. J. Macromolecules 1999, 32, 3106–3113.
17. Wang, R.; Cao, C.; Chung, T.-S. J Membr Sci 2002, 198, 259–271.
18. Kim, J. H.; Koros, W. J.; Paul, D. R. Polymer 2006, 47, 3104–3111.
19. Liu, Y.; Pan, C.; Ding, M.; Xu, J. Polym Int 1999, 48, 832–836.
20. Hibshman, C.; Cornelius, C. J.; Marand, E. J Membr Sci 2003, 211, 25–40.
21. Pechar, T. W.; Kim, S.; Vaughan, B.; Marand, E.; Tsapatsis, M.; Jeong, H. K.; Cornelius, C. J. J Membr Sci 2006, 277, 195–202.
22. Wind, J. D.; Paul, D. R.; Koros, W. J. J Membr Sci 2004, 228, 227–236.
23. Yoshino, M.; Nakamura, S.; Kita, H.; Okamoto, K.-I.; Tanihara, N.; Kusuki, Y. J Membr Sci 2003, 212, 13–27.
24. Duthie, X.; Kentish, S.; Powell, C.; Nagai, K.; Qiao, G.; Stevens, G. J Membr Sci 2007, 294, 40–49.
25. Chung, T. S.; Cao, C.; Wang, R. J Polym Sci Part B: Polym Phys 2004, 42, 354–364.
26. Niwa, M.; Kawakami, H.; Kanamori, T.; Shinbo, T.; Kaito, A.; Nagaoka, S. Macromolecules 2001, 34, 9039–9044.
27. Yeom, C. K.; Lee, J. M.; Hong, Y. T.; Choi, K. Y.; Kim, S. C. J Membr Sci 2000, 166, 71–83.
28. Hibshman, C.; Mager, M.; Marand, E. J Membr Sci 2004, 229, 73–80.
29. Yampolskii, Y. P.; Paul, D. R. Polymeric Gas Separation Membranes; CRC Press: Boca Raton, FL, 1994.
30. LaFemina, J. P.; Arjavalingam, G.; Hougham, G. J Chem Phys 1989, 90, 5154–5160.
31. Shimazu, A.; Miyazaki, T.; Ikeda, K. J Membr Sci 2000, 166, 113–118.
32. Shimazu, A.; Miyazaki, T.; Shigeru, K.; Yasuo, I. J Polym Sci Part B: Polym Phys 2003, 41, 308–318.
33. Yampolskii, Y. P.; Pinnau, I.; Freeman, B. D. Materials Science of Membranes; John Wiley & Sons Ltd.: Chichester, 2006; p 445.
34. Heuchel, M.; Bohning, M.; Holck, O.; Siegert, M. R.; Hofmann, D. Desalination 2006, 199, 443–444.
35. Pinel, E.; Brown, D.; Bas, C.; Mercier, R.; Alberola, N. D.; Neyertz, S. Macromolecules 2002, 35, 10198–10209.
36. Neyertz, S.; Brown, D. J Chem Phys 2001, 115, 708–717.
37. Neyertz, S.; Douanne, A.; Brown, D. J Membr Sci 2006, 280, 517–529.
38. Heuchel, M.; Hofmann, D.; Pullumbi, P. Macromolecules 2004, 37, 201–214.
39. Heuchel, M.; Hofmann, D. Desalination 2002, 144, 67–72.
40. Nagel, C.; Schmidtke, E.; Gunther-Schade, K.; Hofmann, D.; Fritsch, D.; Strunskus, T.; Faupel, F. Macromolecules 2000, 33, 2242–2248.
41. Hofmann, D.; Heuchel, M.; Yampolskii, Y.; Khotimskii, V.; Shantarovich, V. Macromolecules 2002, 35, 2129–2140.
42. Hofmann, D.; Fritz, L.; Ulbrich, J.; Paul, D. Comput Theor Polym Sci 2000, 10, 419–436.
43. Hofmann, D.; Fritz, L.; Ulbrich, J.; Paul, D. Polymer 1997, 38, 6145–6155.
44. Hofmann, D.; Ulbrich, J.; Fritsch, D.; Paul, D. Polymer 1996, 37, 4773–4785.
45. Neyertz, S.; Brown, D. Macromolecules 2008, 41, 2711–2721.
46. De Angelis, M. G.; Doghieri, F.; Sarti, G. C.; Freeman, B. D. Desalination 2006, 193, 82–89.
47. Wang, X.-Y.; in 't Veld, P. J.; Lu, Y.; Freeman, B. D.; Sanchez, I. C. Polymer 2005, 46, 9155–9161.
48. Smith, S. W.; Hall, C. K.; Freeman, B. D. J Comput Phys 1997, 134, 16–30.
49. Tanaka, K.; Kawai, T.; Kita, H.; Okamoto, K.-I.; Ito, Y. Macromolecules 2000, 33, 5513–5517.
50. Kawakami, H.; Nakajima, K.; Shimizu, H.; Nagaoka, S. J Membr Sci 2003, 212, 195–203.
51. Iwase, M.; Sannomiya, A.; Nagaoka, S.; Suzuki, Y.; Iwaki, M.; Kawakami, H. Macromolecules 2004, 37, 6892–6897.
52. Koron, A. Kobunshi Ronchibunshu 1994, 51, 251–257.
53. Fried, J. R.; Hu, N. Polymer 2003, 44, 4363–4372.
54. Tanaka, K.; Taguchi, A.; Hao, J.; Kita, H.; Okamoto, K.-I. J Membr Sci 1996, 121, 197–207.
55. Matsui, S.; Sato, H.; Nakagawa, T. J Membr Sci 1998, 141, 31–43.
56. Islam, M. N.; Zhou, W.; Honda, T.; Tanaka, K.; Kita, H.; Okamoto, K.-I. J Membr Sci 2005, 261, 17–26.
57. Tanaka, K.; Kita, H.; Okano, M.; Okamoto, K.-I. Polymer 1992, 33, 585–592.
58. Neyertz, S. Soft Mater 2006, 4, 15–83.
59. Matsumoto, K.; Xu, P.; Nishikimi, T. J Membr Sci 1993, 81, 15–22.
60. Tanaka, K.; Kita, H.; Okamoto, K.-I. J Polym Sci Part B: Polym Phys 1993, 31, 1127–1133.
61. Cornelius, C. J.; Marand, E. J Membr Sci 2002, 202, 97–118.

62. Kim, J. H.; Koros, W. J.; Paul, D. R. Polymer 2006, 47, 3094–3103.
63. Brown, D.; Minoux, H.; Maigret, B. Comput Phys Commun 1997, 103, 170–186.
64. Brown, D. The *gmq* User Manual Version 4. 2008. Available at: http://www.lmops.univ-savoie.fr/brown/gmq.html.
65. Clark, M.; Cramer, R. D., III; Van Opdenbosch, N. J Comput Chem 1989, 10, 982–1012.
66. Brown, D.; Clarke, J. H. R.; Okuda, M.; Yamazaki, T. J Chem Phys 1994, 100, 6011–6018.
67. Neyertz, S.; Brown, D. J Chem Phys 1996, 104, 10063.
68. Neyertz, S.; Douanne, A.; Brown, D. Macromolecules 2005, 38, 10286–10298.
69. Neyertz, S.; Brown, D. J Chem Phys 1995, 102, 9725–9735.
70. Neyertz, S.; Brown, D.; Clarke, J. H. R. J Chem Phys 1996, 105, 2076–2088.
71. Neyertz, S.; Brown, D. Macromolecules 2004, 37, 10109–10122.
72. Chen, C. L.; Chen, H. L.; Lee, C. L.; Shih, J. H. Macromolecules 1994, 27, 2087–2091.
73. Chen, C. L.; Lee, C. L.; Chen, H. L.; Shih, J. H. Macromolecules 1994, 27, 7872–7876.
74. Shih, J. H.; Chen, C. L. Macromolecules 1995, 28, 4509–4515.
75. Qi, D.; Hinkley, J.; He, G. Model Simul Mater Sci Eng 2005, 13, 493–507.
76. Ewald, P. P. Ann Phys 1921, 64, 253–287.
77. Hammonds, K. D.; Ryckaert, J.-P. Comput Phys Commun 1991, 62, 336–351.
78. Frisch, M. J.; Trucks, G. W.; Schlegel, H. B.; Scuseria, G. E.; Robb, M. A.; Cheeseman, J. R.; Montgomery, J. A.; Vreven, J. T.; Kudin, K. N.; Burant, J. C.; Millam, J. M.; Iyengar, S. S.; Tomasi, J.; Barone, V.; Mennucci, B.; Cossi, M.; Scalmani, G.; Rega, N.; Petersson, G. A.; Nakatsuji, H.; Hada, M.; Ehara, M.; Toyota, K.; Fukuda, R.; Hasegawa, J.; Ishida, M.; Nakajima, T.; Honda, Y.; Kitao, O.; Nakai, H.; Klene, M.; Li, X.; Knox, J. E.; Hratchian, H. P.; Cross, J. B.; Bakken, V.; Adamo, C.; Jaramillo, J.; Gomperts, R.; Stratmann, R. E.; Yazyev, O.; Austin, A. J.; Cammi, R.; Pomelli, C.; Ochterski, J. W.; Ayala, P. Y.; Morokuma, K.; Voth, G. A.; Salvador, P.; Dannenberg, J. J.; Zakrzewski, V. G.; Dapprich, S.; Daniels, A. D.; Strain, M. C.; Farkas, O.; Malick, D. K.; Rabuck, A. D.; Raghavachari, K.; Foresman, J. B.; Ortiz, J. V.; Cui, Q.; Baboul, A. G.; Clifford, S.; Cioslowski, J.; Stefanov, B. B.; Liu, G.; Liashenko, A.; Piskorz, P.; Komaromi, I.; Martin, R. L.; Fox, D. J.; Keith, T.; Al-Laham, M. A.; Peng, C. Y.; Nanayakkara, A.; Challacombe, M. P.; Gill, M. W.; Johnson, B.; Chen, W.; Wong, M. W.; Gonzalez, C.; Pople, J. A. Gaussian 03; Gaussian Inc.: Wallingford, CT, 2004.
79. Chandra Singh, U.; Kollman, P. A. J Comput Chem 1984, 5, 129–145.
80. Allen, M. P.; Tildesley, D. J. Computer Simulations of Liquids; Clarendon Press: Oxford: England, 1987.
81. Flory, P. J. Statistical Mechanics of Chain Molecules; Hanser Publishers: New York, 1988.
82. Queyroy, S. Simulations Moléculaires Dynamiques De Surfaces De Polymère Amorphe: Cas De La Cellulose; Ph.D. thesis, University of Savoie: France,2004.
83. Coleman, M. R.; Koros, W. J. J Membr Sci 1990, 50, 285–297.
84. Shimazu, A.; Miyazaki, T.; Masatoshi, M.; Kenichi, I. J Polym Sci Part B: Polym Phys 2000, 38, 2525–2536.
85. Cornelius, C. J.; Marand, E.; Meakin, P.; Hill, A. J. In Advanced Materials for Membrane Separations; Pinnau, T.; Freeman, B. D., Eds., 2004; pp 234–252.
86. Fritsch, D.; Peinemann, K. V. J Membr Sci 1995, 99, 29–38.
87. Stupp, S. I.; Moore, J. S.; Martin, P. G. Macromolecules 1988, 21, 1228–1234.
88. Smith, W. Comput Phys Commun 1992, 67, 392–406.
89. Brown, D.; Neyertz, S. Mol Phys 1995, 84, 577–595.
90. Berendsen, H. J. C.; Postma, J. P. M.; van Gunsteren, W. F.; DiNola, A.; Haak, J. R. J Chem Phys 1984, 81, 3684–3690.
91. Brown, D.; Clarke, J. H. R.; Okuda, M.; Yamazaki, T. J Chem Phys 1996, 104, 2078–2082.
92. Auhl, R.; Everaers, R.; Grest, G. S.; Kremer, K.; Plimpton, S. J. J Chem Phys 2003, 119, 12718–12728.
93. Harmandaris, V. A.; Reith, D.; van der Vegt, N. F. A.; Kremer, K. Macromol Chem Phys 2007, 208, 2109–2120.
94. Mattice, W. L.; Helfer, C. A.; Sokolov, A. P. Macromolecules 2003, 36, 9924–9928.
95. Marque, G.; Neyertz, S.; Verdu, J.; Prunier, V.; Brown, D. Macromolecules 2008, 41, 3349–3362.
96. Pessan, L. A.; Koros, W. J. J Polym Sci Part B: Polym Phys 1993, 31, 1245–1252.
97. Langsam, M.; Burgoyne, W. F. J Polym Sci Part A: Polym Chem 1993, 31, 909–921.
98. Aitken, C. L.; Koros, W. J.; Paul, D. R. Macromolecules 1992, 25, 3424–3434.
99. Van Krevelen, D. W. Properties of Polymers; Elsevier Inc.: Amsterdam, 1990.
100. Boyd, R. H.; Pant, P. V. K. Macromolecules 1991, 24, 4078–4083.
101. Pant, P. V. K.; Boyd, R. H. Macromolecules 1993, 26, 679–686.
102. Lee, S.; Mattice, W. L. Comput Theor Polym Sci 1999, 9, 57–61.
103. Bondi, A. J Phys Chem 1954, 58, 929–939.
104. Neder, R. B.; Proffen, T. Diffuse Scattering & Defect Structure Simulations: A Cook Book Using the Program DISCUS; Oxford University Press: Oxford, 2009.
105. Hasegawa, M.; Horie, K. Prog Polym Sci 2001, 26, 259–335.

3.4. Preparation and validation of carbon dioxide molecular models

Several potential models for CO_2 have been reported in the literature.[228-231] Zhang and Duan compared the most popular fully-atomistic models, that is MSM,[229] EPM2,[230] TraPPE[231] and Errington[228] and proposed some optimized potential parameters (Table 13).[232] These different models predict accurately some properties and show deviations in other properties. For example, the MSM model has a remarkable accuracy in the estimation of the phase equilibrium, whereas the volumetric properties are predicted more accurately by the EPM2 model.

Model	$(\varepsilon_{C\text{-}C}/k_B)$ **(K)**	$\sigma_{C\text{-}C}$ **(Å)**	$(\varepsilon_{O\text{-}O}/k_B)$ **(K)**	$\sigma_{O\text{-}O}$ **(Å)**	α	q_C	$l_{C\text{-}O}$ **(Å)**
MSM[229]	29.0	2.785	83.1	3.014	...	0.5957	1.16
EPM2[230]	28.129	2.757	80.507	3.033	...	0.6512	1.149
Errington[228]	27.0	2.80	79	3.05	...	0.70	1.16
TraPPE[231]	29.07	2.753	83.20	3.029	14.0	0.6466	1.1433
Zhang and Duan[232]	28.845	2.7918	82.656	3.0	...	0.5888	1.163

Table 13. Potential model parameters for carbon dioxide. The optimized values of Zhang and Duan are given in the last row. ε and σ are the Van der Waals potential parameters, α is the exponential-6 potential parameter, q_C is the partial charge on the carbon atom and $l_{C\text{-}O}$ is the C-O bond length. q_O , the partial charge on an oxygen atom, is equal to minus half the magnitude of q_C to maintain electrical neutrality.

Many CO_2 transport studies use simpler united-atom models[67,69] which are easy to parameterize. However, they are less realistic and cannot provide any atomistic-level structural information. Consequently we preferred to use an all-atom potential model of CO_2 with three interaction centres and the parameters of Zhang and Duan[232] (Table 13) for our

studies. C-O bonds and the O-C-O bending angle of 180° were kept rigid with constraints in order to avoid non-equipartition of the kinetic energy.

Simulations of pure CO_2 with a system size of 512 molecules were first carried out to assess the *PVT* properties of the liquid-vapour coexistence curve based on the Zhang and Duan model.[232] Lennard-Jones (Eq. 41) interactions along with Ewald summation were used to calculate the non-bonded interactions with a cutoff distance R_c of 10 Å, a K_{max} of 18 and a value for α of 0.35. Long-range corrections to the energies were also added. Zhang and Duan[232] also used the same way to calculate the van der Waals and electrostatic interaction energies. However the exact parameters used in their calculations are not reported. In our studies, the saturated liquid and vapour systems were simulated under both constant-volume *NVT* and constant-pressure *NPT* conditions whereas Zhang and Duan[232] only used *NPT* simulation for *PVT* properties. In addition, their liquid-vapour coexistence curves were calculated using histogram-reweighting grand canonical Monte Carlo (*HRGCMC*) simulations under constant-chemical potential *NVE* conditions. All our simulations were run for at least 500 ps, out of which the final 400 ps were used to estimate the *PVT* properties. Our simulations are at least 5 to 10 times longer and our system sizes are twice the size of those reported by Zhang and Duan.[232]

Figure 30 shows the simulated coexistence properties of CO_2 as a function of the temperature. There is less than 1% deviation in the densities with respect to the values reported by Zhang and Duan[232] under *NPT* conditions. But the equilibrium pressures under *NVT* conditions (where the densities of the simulation boxes were fixed) exhibit deviations from the pressure values reported by Zhang and Duan.[232] This could be due to the incompressible nature of CO_2, a small difference in the density having a noticeable impact on

the pressure. It is also important to remember that the Zhang and Duan simulations were extremely short, and that there are likely to be statistical reasons for these small discrepancies.

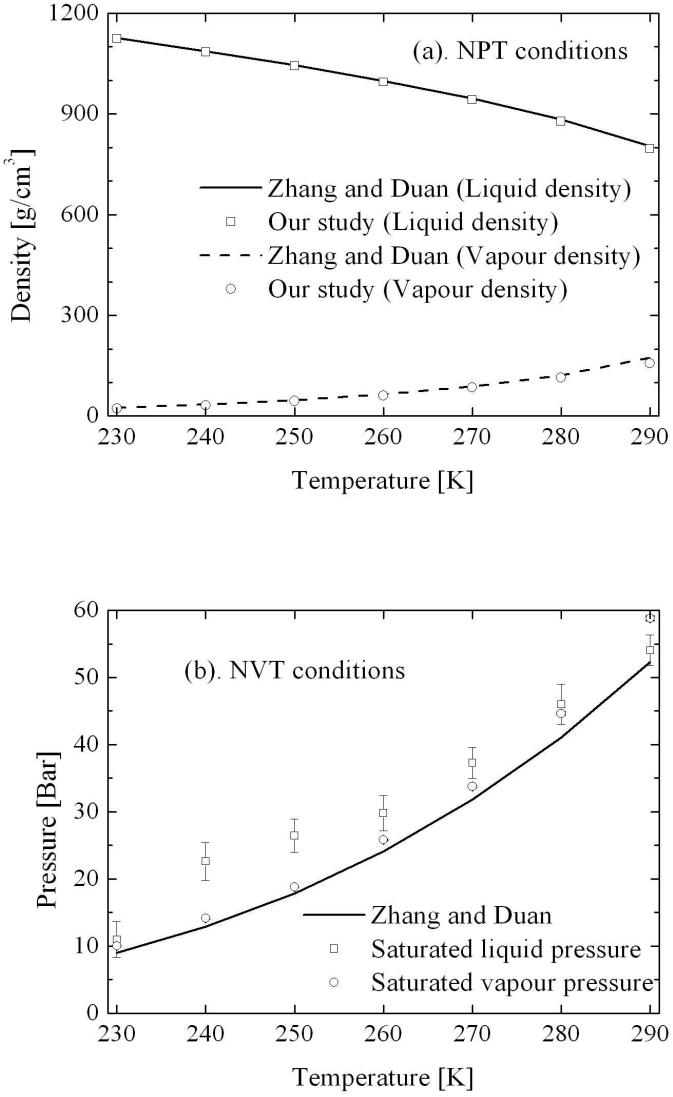

Figure 30. Liquid and vapour coexistence properties of our CO_2 model under constant-pressure *NPT* (a) and constant-volume *NVT* (b) conditions compared to those reported by Zhang and Duan.[232] Under *NPT* conditions (a), the densities are precisely reproduced while under *NVT* conditions (b), the pressures deviate slightly (open symbols) in both liquid and vapour states.

In order to check the results obtained from our NVT simulations, the same model of CO_2 was simulated using the GROMACS MD simulation package.[233] In GROMACS, a mass-

redistribution method[234] is adopted to keep rigid the CO_2 molecule instead of a vector constraint. The mass of CO_2 was redistributed between two virtual sites, with each mass being the combined mass of an oxygen + 1/2 mass of a carbon. However the point charges remained fixed to the positions of the respective atoms. The positions of virtual mass centres M were calculated using Eq.51:

$$\frac{d_{(C-M)}}{d_{(C-O)}} = \sqrt{\frac{m_O}{m_M}} \tag{51}$$

where d(C-M) is the distance between the carbon and a virtual mass centre, d(C-O) is the bond length between a carbon and an oxygen, mO is the mass of an oxygen and mM is the mass of a virtual mass site. Figure 31 illustrates the mass redistribution into virtual sites.

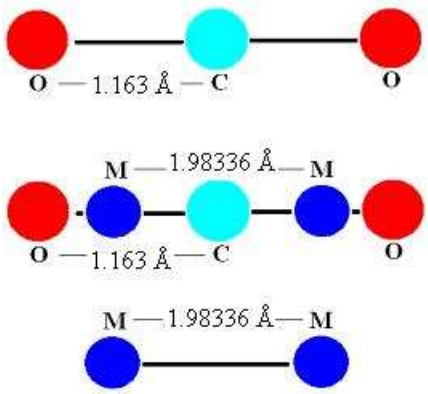

Figure 31. A schematic representation of the redistribution of masses in a CO_2 model used in GROMACS to keep the O-C-O bend rigid.[233]

In GROMACS, the simulations were 1000 ps long, in which the final 500 ps were considered for calculation of the equilibrium densities and pressures under both *NPT* and *NVT* conditions. A comparison of the results obtained is given in Table 14. The agreement in the pressure between *gmq* and GROMACS under NVT conditions is within statistical errors. Minor differences in the densities under NPT simulations were due to the selection of

inappropriate loose-coupling pressure parameters which led to long relaxation times for the density and were not considered of any consequence.

Saturated liquid density and pressure:

T /K	Z and D / kg m^{-3}	Density / kg m^{-3} (NPT, at pressure of Z and D)		Z and D / bar	Pressure / bar (NVT, at density of Z and D)	
		gmq	GROMACS		*gmq*	GROMACS
230	1125.83	1124.5±0.2	1119.2±0.2	8.97	11.0±2.7	17.0±4.2
240	1086.67	1084.8±0.2	1083.0±0.2	12.88	22.6±2.8	23.6±4.2
250	1044.54	1042.9±0.2	1039.6±0.2	17.88	26.4±2.5	29.3±4.4
260	998.13	995.2±0.2	993.5±0.3	24.13	29.8±2.7	31.5±4.3
270	945.89	942.2±0.3	938.3±0.2	31.79	37.3±2.3	38.4±4.1
280	883.84	877.0 ±0.2	877.5±0.2	41.08	46.0±3.0	49.1±4.5
290	804.7	796.0±0.3	793.4±0.4	52.33	54.1±2.3	60.8±4.1

Saturated vapour density and pressure :

Temp / K	Z and D / kg m^{-3}	Density / kg m^{-3} (NPT, at pressure of Z and D)		Z and D / bar	Pressure / bar (NVT, at density of Z and D)	
		gmq	GROMACS		*gmq*	GROMACS
230	24.65	23.34	24.11	8.97	10.0±0.1	9.6±0.1
240	34.74	32.21	33.51	12.88	14.1±0.1	13.9±0.1
250	47.98	45.13	46.15	17.88	18.8±0.1	19.2±0.1
260	65.29	61.61	66.54	24.13	25.8±0.1	25.9±0.1
270	88.36	85.366	88.82	31.79	33.8±0.1	34.1±0.1
280	121.52	114.86	118.89	41.08	44.6±0.2	44.7±0.1
290	174.22	157.93	156.93	52.33	58.8±0.3	58.6±0.2

Table 14. Comparison of saturated liquid and vapour densities and pressures between the reported values of Zhang and Duan ("Z and D"),[232] *gmq*, and GROMACS simulations.

Further validation of the CO_2 model was done by comparing the heat of vaporization (ΔH_{vap}) as a function of the temperature. ΔH_{vap} for a given temperature was estimated from the difference between the enthalpy of the gas phase and that of the liquid phase in both *gmq* and GROMACS.

$$\Delta H_{vap} = H_{vap} - H_{liq} \tag{52}$$

where ΔH_{vap} is the heat of vaporisation, H_{vap} is the heat of the vapour ($U_{vap} + P_{vap}V_{vap}$) and H_{liq} is the heat of the liquid ($U_{liq} + P_{liq}V_{liq}$).

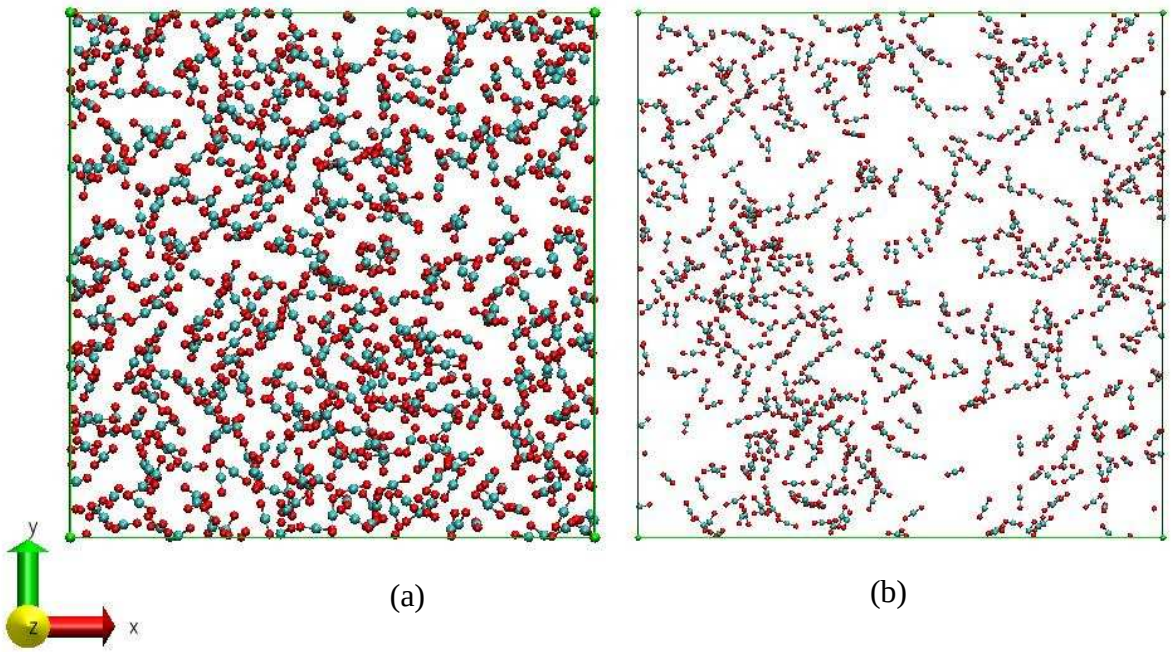

Figure 32. Equilibrated saturated liquid (a) and vapour (b) carbon dioxide molecular models at 290 K.

The calculated values of ΔH_{vap} are found to be in very good agreement with the experimental values reproduced by the Zhang and Duan model[232] (Figure 33).

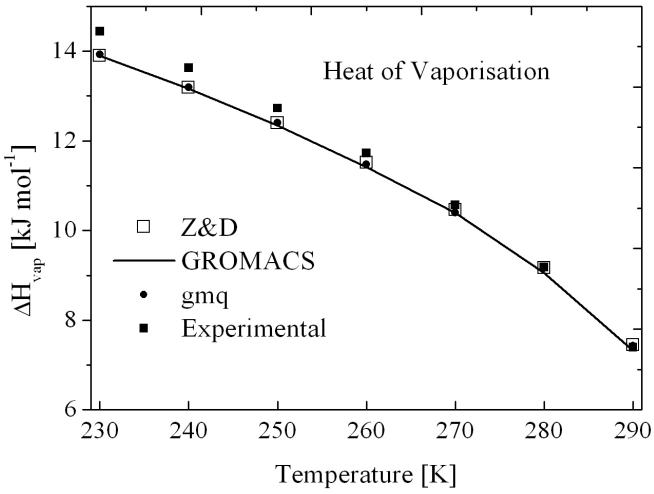

Figure 33. Comparison between experimental and simulated CO_2 heat of vaporisations

The polyimide bulk models and the optimized model of CO_2 prepared in this chapter were further used to study the CO_2 transport properties in the polymer matrices. The results of CO_2 sorption and sorption-induced volume dilation in polyimides along with the self-diffusion of CO_2 inside the polymer matrices will be presented in the next chapters.

Chapter 4.

Carbon dioxide solubility and volume-dilation studies

4.1. Introduction

The solubility of CO_2 in polymer models has been generally studied using test particle insertion methods and often only in the pure polymer models, *i.e.* at the infinite dilution limit. In such studies CO_2 has often been represented as a single spherical site. Such a united-atom approach is rather unsatisfactory as it can not explicitly include Coulombic interactions. Heuchel *et al.*[66,67,235] have attempted to study CO_2 solubility at different concentrations by using Grand Canonical Monte Carlo (GCMC) simulations on unswollen and artificially pre-swollen polymer models. Such simulations are, to us, not optimal as the GCMC simulations are performed on a single frozen snapshot configurations of the swollen and unswollen polymer and thus do not take into account the swelling process in a realistic manner. The resulting sorption isotherms can not be related to any physical experiment and only give some idea of limiting solubilities.

In our studies, we use a step-wise addition procedure to insert CO_2 molecules in to the bulk models of polyimides without any necessity for pre-swelling. The polymer models are then allowed to relax dynamically and the swelling process occurs naturally. An iterative procedure is used to establish the vapour pressure of CO_2 that would have to be applied in order for there to be an equilibrium with the amount of CO_2 inserted in the polymer models. This allows the full pressure vs. concentration isotherm to be calculated. Along with the solubility, the volume swelling induced by CO_2 was also calculated directly from the volumes of polymer models containing different concentrations of CO_2 for all the three polyimides under study. In order to understand the effect of exposure of high concentrations of CO_2 (*i.e.* conditioning effect) the desorption isotherms were also studied along with the respective volume contraction curves. To our knowledge, there are no other molecular simulations

studies of the sorption isotherm of CO_2 for the polyimides under study and this is the first time the iterative technique has been applied to obtain uptake curves in models of such complexity.

Full details of the techniques used and the results for the sorption and desorption isotherms, as well as a number of other analyses, are presented in the following article which is in preparation for submission to a peer-reviewed international journal.

Carbon dioxide solubility in three fluorinated polyimides studied by molecular dynamics simulations

Sudharsan Pandiyan[1&2], David Brown*[1], Sylvie Neyertz[1], & N. F. A. van der Vegt[2†]

[1]LMOPS-UMR CNRS 5041, University of Savoie, Bât IUT, 73376 Le Bourget-du-Lac Cedex, France

[2]Max-Planck-Institute for Polymer Research, Ackermannweg 10, 55128 Mainz, Germany

[†]Current address: Center of Smart Interfaces, Technical University of Darmstadt, Petersenstrasse 32, 64287 Darmstadt, Germany

ABSTRACT

Fluorinated polyimides are interesting polymer materials for gas separation applications because of their good mechanical, thermal and transport properties. We have performed molecular dynamics simulations (MD) of CO_2 sorption and desorption in three fluorinated polyimides:- 6FDA-6FpDA, 6FDA-6FmDA and 6FDA-DAM. These polyimides are known to vary significantly in their gas permeation properties. A stepwise procedure was used to insert CO_2 molecules in to the previously prepared polymer matrices in order to mimick the experimental procedure of progressive loading and to avoid the necessity of pre-swelling the samples. An iterative technique was then used to estimate the vapour pressure of CO_2 that would have to be applied in order to obtain the imposed uptake. The resulting sorption isotherms are found to have relatively good agreement with their respective experimental curves and the trend in solubility was reproduced (DAM>6FpDA>6FmDA). Desorption isotherms were also calculated starting from systems corresponding to an applied pressure of 60 bar. Changes in volume, void space, potential

energy etc. have been characterized and compared to experimental data and theories of gas sorption in glassy polymers.

1. Introduction

Carbon dioxide (CO_2) separation has become a challenging task in many industries. It is generally accepted that the increased emission of CO_2 to the atmosphere is an important reason for global warming.[1] There are different techniques to separate CO_2 from gas mixtures such as physical adsorption,[2-8] chemical adsorption,[6,9-16] low temperature distillation[17,18] and membrane separation.[19-28] The latter technique made the transition from the laboratory to commercial ventures in the early 1980s. Indeed, some dense glassy polymers have interesting features such as a fairly low cost, easy installation, high-selectivities for specific permeants and a high solubility for CO_2.[29]

The most basic requirements for polymer membranes to efficiently transport gas molecules are high permeation rates (or productivities) and selectivities (or separation efficiencies). Permeability P is the rate of transport for the penetrant through the membrane defined as the product of its solubility coefficient S and its diffusion coefficient D (Eq. 1):

$$P = S \times D \tag{1}$$

In Eq. 1, S is a thermodynamic parameter which can be obtained from the sorption isotherm (if C is the penetrant concentration and p is the partial pressure, then $S = C/p$). D is a kinetic parameter determined by chain packing and the mobility of the polymer chain segments as well as by the size and shape of the penetrant molecules. When applied to a gas mixture, the selectivity of the polymer membrane for gas A over gas B, $\alpha_{A/B}$ (also called permselectivity), is the ratio of their pure gas permeabilities (Eq. 2):

$$\alpha_{A/B} = \frac{P_A}{P_B} = \left(\frac{D_A}{D_B}\right) \times \left(\frac{S_A}{S_B}\right) \tag{2}$$

An important property of non-porous dense membranes is that permeants of similar sizes and diffusion coefficients can be separated if their solubilities differ to a large extent. This is especially

important for CO_2 separation applications as carbon dioxide exhibits much higher solubilities in dense polymers than other light gases.[30,31]

The transport of gases through polymer membranes can generally be described by a solution-diffusion mechanism.[32-36] Transport occurs when gas molecules in an upstream compartment enter the polymer matrix, diffuse across it and finally desorb on a downstream gas compartment.[37] However, it is well-known that CO_2 transport in glassy polymers often results in plasticization effects, and that the performance of the membrane can be significantly altered. For example, in CO_2/CH_4 gas separations, the polymer swells upon sorption of CO_2 accelerating the permeation of CH_4 and decreasing the permselectivity.[38]

Fluorinated polyimides are interesting polymer materials for gas separation applications because of their good mechanical, thermal and transport properties.[39-58] They also exhibit an acceptable resistance to plasticization.[41,42,59] In the present paper, we perform molecular dynamics (MD) simulations of CO_2 sorption and desorption in three fluorinated polyimides in order to characterize CO_2 solubility and plasticizing effects as a function of the polymer structure. The three polyimides under study are:- (a) poly{4,4'-(2,2,2-trifluoro-1-(trifluoromethyl)ethane-1,1-diyl)dianiline}-alt-{5,5'-(2,2,2-trifluoro-1-(trifluoromethyl) ethane-1,1-diyl)bis(isobenzofuran-1,3-dione)} (referred to hereafter as 6FDA-6FpDA), (b) poly({3,3'-(2,2,2-trifluoro-1-(trifluoromethyl)ethane-1,1-diyl)dianiline}-alt-{5,5'-(2,2,2-trifluoro-1-(trifluoromethyl) ethane-1,1-diyl)bis(isobenzofuran-1,3-dione)}) (6FDA-6FmDA) and (c) poly((2,4,6-trimethyl-m-phenylenediamine)-alt-{5,5'-(2,2,2-trifluoro-1-(trifluoromethyl)ethane-1,1-diyl) bis(isobenzofuran-1,3-dione)}) (6FDA-DAM). Their chemical formulae are shown in Fig. 1.

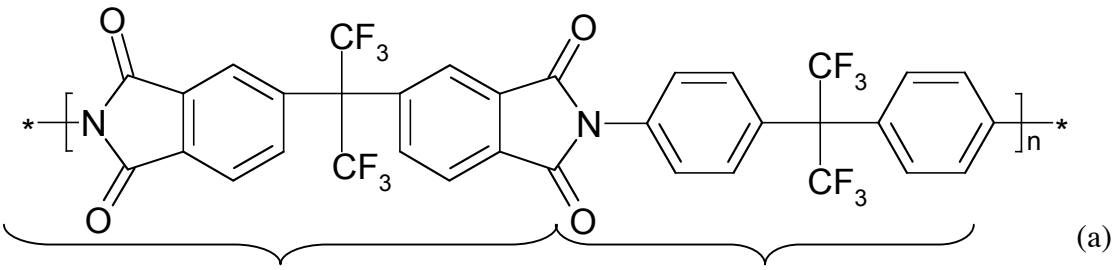

(a)

6FDA 6FpDA

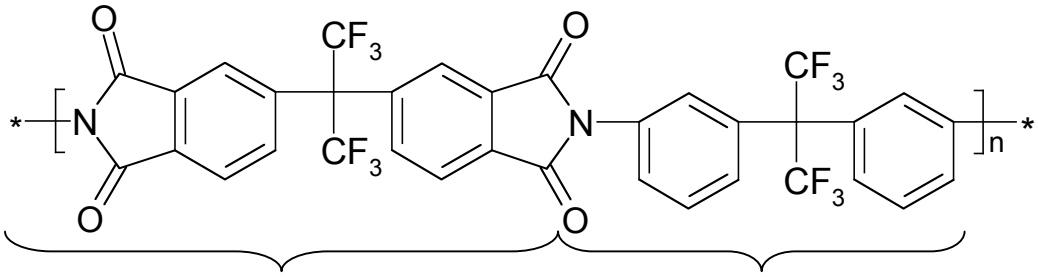

(b)

6FDA 6FmDA

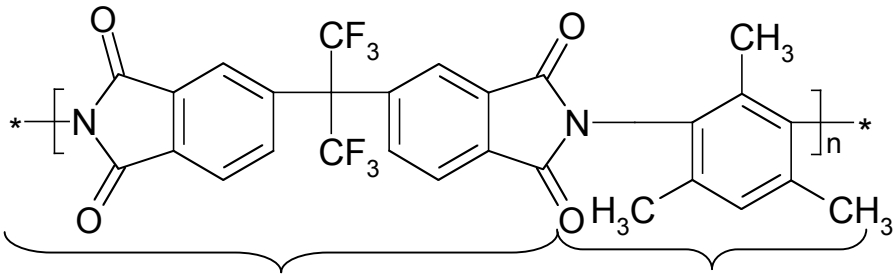

(c)

6FDA DAM

Figure 1. The chemical structures of (a) 6FDA-6FpDA, (b) 6FDA-6FmDA and (c) 6FDA-DAM polyimides

Note that 6FpDA is also sometimes referred to as BAAF,[39,60-63] 6FAP,[64,65] 4APF[66] or BAHF,[67] that DAM can be called TrMPD,[68-71] and 3MPDA,[55] and that 6FmDA corresponds to 3APF.[72] We have reported the results of a study of these three polyimides in the pure state in a recent paper[73] and they are known to significantly vary in their CO_2 permeation properties.[40-45,48,50,52,59,62,63,74-76] It is worth noting that

MD simulations of CO_2 transport in some of these systems have already been reported but they were either restricted to very short simulation times[77,78] (60 ps) or used low density approaches to create the models,[62,79] i.e. methods which are known to lead to a bias in the chain conformations.[80] These simulations also used a simple spherical representation for CO_2. However, we are not aware of any full sorption isotherms and CO_2-induced volume swelling studied by MD simulations for these three fluorinated polyimides.

On the other hand, quite a few experimental investigations have been dedicated to study CO_2 transport and the subsequent plasticization effects in these polymers. Coleman *et al.*[40-42] investigated the effect of high-pressure CO_2 exposure on permeability in 6FDA-6FpDA and 6FDA-6FmDA. Costello and Koros[81] reported the temperature dependence of gas transport in the same polymers and gave dual sorption parameters for CO_2. Singh-Ghosal and Koros[82] investigated mobility selectivity for 6FDA-6FpDA and 6FDA-6FmDA. Wang *et al.*[48] reported diffusivity, solubility and permeability for various gases in 6FDA-6FpDA. Fuhrman *et al.*[44] explained the thermal hysteresis of gas transport in 6FDA-6FpDA and 6FDA-6FmDA in terms of sub-T_g and T_g motions. Kim *et al.*[47,50-52] studied the effects of CO_2 exposure, physical aging and chemical crosslinking on the gas separation abilities of both 6FDA-6FpDA and 6FDA-DAM. Recio *et al.*[43] reported the effect of the solvent used for the preparation of 6FDA-6FpDA membranes on the transport properties. Various other studies on CO_2 transport and plasticization effects also include these polymers or closely related structures.[38,45,55-58,60,63,64,74-76,83-92] Consequently, there is a lot of available experimental evidence to confront to the MD simulations.

Details of the MD simulations are given in Section 2. They include the polymer models and the sample generation procedure, the choice of the CO_2 model, the addition of CO_2 into the pre-prepared polymer matrices and its subsequent removal. The results obtained for the pure CO_2 vapour are given in Section 3. In Section 4 the results of the CO_2 uptake simulations into the polyimides are presented and discussed. Finally, the results of the CO_2 unloading simulations are presented and discussed in Section 5.

2. Methods and Models

2.1 Iterative method for obtaining sorption isotherms

Our main aim in this work is to determine the full sorption isotherm of CO_2 in the model polyimides, i.e. the amount of CO_2 dissolved in the polymer as a function of the applied external pressure of carbon dioxide gas. In the laboratory this is a fairly routine experiment to perform by placing a polymer film in contact with the gas at a controlled pressure and measuring the mass change. Although this direct approach has also been mimicked in model systems [93] it poses serious problems with respect to the creation of realistic membrane models and the time and length scales of the MD simulations. In effect, to have a sufficient amount of bulk polymer material at the centre of the membrane implies a large membrane width (large system size), i.e. small surface area to volume ratio, but this inevitably leads to long simulation times as the attainment of equilibrium between the amount of gas in the gas phase and the amount of gas in the polymer phase is limited by the rate of diffusion of the gas in the polymer phase. In the case of CO_2 these diffusion rates are known from experiment to be too slow to render this approach feasible for a wide range of external gas pressures. An alternative approach is to first create models of the relaxed bulk polymers using standard 3D periodic boundary conditions. Such models have the advantage in that they do not contain any external surfaces so are purely bulk models. The disadvantage of these fully 3D periodic models is that the number of gas molecules in the polymer system and the pressure become *independent* variables, i.e. we can insert as much gas as we want and set the pressure to any value. However, a fairly simple iterative technique [94] can be used to find the external pressure of the gas corresponding to the number of gas molecules in the system and thus sorption isotherms can be calculated. The method is based on the fact that at equilibrium the total chemical potential of the gas in the polymer phase, μ^p, and the gas in the gas phase, μ^g, are equal. Thus, for a polymer containing a fixed number of penetrant gas molecules an NPT simulation is first made at some initial guess pressure, P_1. The resulting total chemical potential of the gas in the polymer phase evaluated from this first simulation,

$\mu^p(P_1)$, can then be used to obtain a second estimate of the pressure, P_2, from the (pre-calculated) total chemical potential of the gas in the gas phase as a function of pressure, i.e. by finding the pressure in the gas phase where $\mu^g(P_2) = \mu^p(P_1)$. A second NPT simulation of the gas in the polymer phase is then carried out at an applied pressure of P_2. This in turn gives a $\mu^p(P_2)$ which can again be used to obtain a third estimate $\mu^g(P_3) = \mu^p(P_2)$, and so on. In general the method converges rapidly as dense polymer matrices are relatively incompressible so modest changes in pressure do not provoke much change in density, and hence chemical potential.

In practice total chemical potentials are never actually calculated as certain simplifications can be made. In the case of a rigid gas molecule, as we will use for CO_2, the internal partition function is not dependent on the surrounding solvent so the equality of the total chemical potential can be shown to be equivalent to the following condition [95,96]

$$\Delta\mu_{ex} = \mu_{ex}^{p} - \mu_{ex}^{g} = kT \ln\frac{\rho^{g}}{\rho^{p}} \tag{3}$$

which relates the difference in *excess* (with respect to the ideal gas) chemical potentials of the permeant in the two phases to their different densities in the two phases. A convenient statistical mechanical approximation for the excess chemical potential in the NPT ensemble is given by the following equation[97]

$$\mu_{ex} = -kT \ln\frac{\left\langle V \exp\left(\frac{-\Delta\Phi}{kT}\right)\right\rangle}{\langle V \rangle} \tag{4}$$

where $\Delta\Phi$ is the energy of interaction resulting from the ***virtual*** introduction of an extra test particle into an equilibrium distribution of the system in question; details of the specific test particle insertion method that has been used here and checks on its reliability are given below. In practice then μ_{ex}^{g} and ρ^{g} have first to be calculated as a function of pressure for the pure gas system at the temperature required. μ_{ex}^{p} can

then be calculated at a certain mass fraction of CO_2 in the polymer from a simulation conducted at the initial guess pressure, P_1. The quantities $\mu_{ex}^{p}(P_1) - \mu_{ex}^{g}(P)$ and $kT \ln \frac{\rho^{g}(P)}{\rho^{p}(P_1)}$ can then be plotted separately as a function of pressure and the the point of intersection of the two curves gives the second approximation, P_2. A further simulation of the gas in the polymer has then to be conducted at P_2 and the procedure iterated to convergence.

We note also that the relationship between the excess chemical potentials and the solubilities then follows directly from Eq. 3

$$\frac{\rho^{g}}{\rho^{p}} = \exp\left(\frac{\Delta\mu_{ex}}{kT}\right) = \frac{\exp\left(-\frac{\mu_{ex}^{g}}{kT}\right)}{\exp\left(-\frac{\mu_{ex}^{p}}{kT}\right)} = \frac{S^{g}}{S^{p}} \tag{5}$$

thus we can define a scale of (dimensionless) solubility using

$$S = \exp\left(-\frac{\mu_{ex}}{kT}\right) = \exp\left(\frac{kT \ln \frac{\left\langle V \exp\left(\frac{-\Delta\Phi}{kT}\right)\right\rangle}{\langle V \rangle}}{kT}\right) = \frac{\left\langle V \exp\left(\frac{-\Delta\Phi}{kT}\right)\right\rangle}{\langle V \rangle} \tag{6}$$

where a solubility of 1 corresponds to that of an ideal gas.

2.2 MD simulations

All MD simulations were performed using the scalar and parallel versions of the general purpose *gmq* program.[98] The parameters for the models of the polyimides were taken from the TRIPOS 5.2 force field.[99] The partial charges, q_i, on the atoms were calculated using *Gaussian 03*,[100] at the B3LYP/6-31G** level, on representative three- or five-fragment structures of the polyimides under study by. For CO_2 the interaction parameters, including partial charges, were taken from optimized values reported by Zhang and Duan.[101] This is a rigid three-centre model with a C-O bond length of 1.163 Å, a partial charge on the

carbon atom of q_C=0.5888e (and neutralising charges on the oxygens of q_O=-q_C/2), and Lennard-Jones 12-6 interaction sites situated at the carbon and oxygen centres with $\sigma_{C\text{-}C}$=2.7918 Å, $\varepsilon_{C\text{-}C}/k_B$=28.845 K, $\sigma_{O\text{-}O}$=3.0 Å, and $\varepsilon_{O\text{-}O}/k_B$=82.656 K.

The equations of motion were integrated using using 1 fs integration time step. The SHAKE algorithm[102] was used to constrain all bond lengths. In addition to simple bond constraints, a special vector constraint was used to keep the bond angle of CO_2 (O-C-O) fixed at 180°.[103] The CO_2 molecule is thus completely rigid and just has five degrees of freedom; three translations and two rotations. We think it is important to point out that, without the bond angle constraint, the (flexible angle) model would acquire two extra degrees of freedom, an angle bend *and* a rotation around the long O-C-O axis. This latter degree of freedom has a vanishingly small moment of inertia associated with it and thus couples very poorly to the other degrees of freedom. This leads almost inevitably to a non-equipartition of kinetic energy in a classical MD simulation. Although this point has been known about for over 25 years, it has tended to be forgotten in recent times.[104-106]

The loose-coupling procedure was used to maintain the temperature and pressure close to the required value.[107,108] A loose coupling relaxation time of 0.1ps was used for temperature and 5 ps for the pressure. The Ewald summation method[109] was used to calculate the electrostatic interactions. In all cases the three parameters controlling the convergence of the Ewald sum: R_c, the real space cutoff, K_{max}, the maximum integer defining the range of the reciprocal space sum, and α, the separation parameter, were optimized in order to give an agreement of less than 1 bar between the direct and indirect calculations of the Fourier space contribution to the pressure.[98,110]

The Lennard-Jones 12-6 form was used to represent all the Van der Waals interactions with the Lorentz-Berthelot combining rule for unlike atom types; $\sigma_{AB} = \frac{\sigma_{AA} + \sigma_{BB}}{2}$ and $\varepsilon_{AB} = \sqrt{\varepsilon_{AA}\varepsilon_{BB}}$. The same real space truncation radius was used as optimized for the real space part of the Ewald sum. In all cases R_c exceeded 10 Å. Standard long range corrections were made systematically to the Lennard-Jones 12-6

potential contributions to the energy and pressure by assuming that the radial distribution functions were unity for distances greater than R_c.

2.3 Pure polyimides

Most details of the preparation of the relaxed models of the pure polymers have already been reported elsewhere[73] so only a brief outline will be presented here. The hybrid pivot Monte Carlo – molecular dynamics (PMC-MD) single-chain sampling technique was used to generate the initial conformations of the different types of polymer chains at temperatures just above their respective glass transition (T_g), i.e. 700 K for 6FDA-6FpDA and 6FDA-DAM and 600 K for 6FDA-6FmDA. Each chain contained 50 repeat units. Two different sizes of polymer matrices, 3-chain (~10,000 atoms) and 6-chain (~20,000 atoms), were prepared for each type of polymer by inserting the required number of independently-generated chains into a periodic MD box of a size corresponding to the experimental density at 298 K. Excluded volume was then introduced gradually. The simulation boxes with the complete potential switched on were then allowed to relax under NVT (constant number of atoms, constant volume, and controlled temperature) conditions for 500 ps and then cooled down to 298 K at the rate of 1 K/ps. After a short NVT relaxation at 298 K the simulation boxes were allowed to relax under NPT (constant number of atoms, controlled pressure and temperature) conditions for 3 ns. These relaxed samples at 298 K were the subject of precedent article.[73] All three polymers had good agreement with the available experimental density. Their X-ray diffractograms, fractional free volumes and Hildebrand solubility parameters were also calculated and validated against available experimental results. The intermolecular and intramolecular interactions and void space distributions were also analysed.

In general, experimental sorption studies of carbon dioxide in to polymers are performed above the critical temperature of CO_2 (~304 K). For this reason the configurations at the end of the MD simulations at 298 K were first heated to 308 K, at the rate of 1 K/ps, and then the simulations were continued under NPT conditions for a further 4ns. The resulting relaxed samples at 308 K were then used as the starting points for all subsequent sorption studies.

2.4 Pure carbon dioxide

The optimized all-atom potential parameters reported by Zhang and Duan[101] were utilized to simulate CO_2. This potential is reported to reproduce the liquid-vapour coexistence properties of carbon dioxide over a wide range of temperatures and pressures and predicts a critical temperature in good agreement with the experimental value of 304 K. As explained above, in this work it is required to know for this model of CO_2 the equilibrium pressure, density and excess chemical potential of the vapour along the 308 K isotherm. This is effectively the vapour phase which we consider to be in equilibrium with the gas sorbed in the polymers. MD simulations on systems of 512 molecules were carried out for 4 ns under NVT conditions using volumes determined by interpolation from the experimental data of Span and Wagner.[111] The last 3 ns of these simulations were used to obtain the corresponding average properties including the pressure.

2.5 Carbon dioxide uptake into polyimides

The calculation of the sorption isotherms were started with pure polyimide matrices at 308 K and as a first guess the equilibrium pressures were set to 1 bar. Random insertion of CO_2 molecules into systems containing the polyimides can lead to large overlaps and even ring spearings. In order to avoid this, an equilibrated dense system of CO_2 at approximately 1000 kg /m^3 was prepared in a box of the same size as the polyimide-containing simulation boxes; these could be either pure or systems already containing polyimide and CO_2. The CO_2 and polyimide containing simulation boxes were superimposed and the CO_2 molecules were ranked by order of the least number of overlaps with the atoms already present. The desired number of CO_2 molecules were then inserted into the polyimide containing systems from those that overlapped the least. After the insertion of CO_2, a short minimization is required to remove the remaining small overlaps and then the systems were equilibrated under NVT conditions for 50 ps then switched to NPT conditions for the production run. Most simulations were initially run for 4000 ps under NPT conditions at the initial guess pressure of 1 bar of which the final 3000 ps were used to

calculate the averages including the excess chemical potential. An estimation of the pressure of CO_2 vapour that has to be applied to obtain the imposed uptake was then obtained using the technique described in Section 2.1. If this pressure exceeded 10 bar, i.e. sufficently different in MD terms to the initial pressure, then this pressure was applied in a second NPT simulation of 3 ns, starting from the end of the first production run. The average excess chemical potential from this second run was then used to check for convergence of the iterative method. Within errors the left and right hand sides of Eq. 3 were the same for all these systems after just one iteration. In effect, the first estimate of the equilibrium vapour pressure obtained from the simulations at 1 bar was already quite reasonable.

To mimick the experimental approach, and to avoid the necessity of pre-swelling the polyimide containing systems, CO_2 loading was carried out in a progressive way. Pure polyimide samples were initially loaded with an amount of CO_2 corresponding to ~1% of the mass of the pure polyimide systems; in the ~10000 atoms systems, this corresponds to 25 molecules in the case of 6FDA-6FpDA and 6FDA-6FmDA and 19 molecules in the case of 6FDA-DAM. To obtain higher loadings copies of configurations at the preceding loading were made after 500 ps of the corresponding NPT simulation, a time sufficient to allow most of the volume swelling to occur. These copies were then used to start off simulations at higher loadings by adding a further ~2% by mass of CO_2, i.e. 50 molecules in the case of 6FDA-6FpDA and 6FDA-6FmDA and 38 molecules in the case of 6FDA-DAM for the ~10000 atoms systems. This procedure of adding 2% by mass was continued up until 25% of CO_2 had been added. Note that the simulations at 9% and 13% of CO_2 were not systematically extended for all systems beyond the 500 ps necessary to relax the systems for the next addition of 2%. Given the relatively small changes in pressure in this region the simulations at 9% and 13% were considered superfluous. Results for each type of polyimide were averaged over three independent systems.

2.6 Carbon dioxide unloading from polyimides

As hysteresis has been seen when performing desorption experiments after conditioning samples,[41,42,44,45,81] it was considered interesting to obtain the unloading curves from the model systems. In

real experiments the applied vapour pressure of CO_2 is the controlled variable and data exist for desorption curves startingfrom systems held at 60 bar.[41] For the 6FDA-DAM systems further loading, in 2% increments, up to ~31% was first required so as to attain a pressure of ~60 bar. The number of CO_2 molecules in the samples was then adjusted, on the basis of the sorption curves, in order to have an amount that corresponded to a pressure of ~60 bar. In terms of the mass of the pure polyimide systems, this was about 24.3%, 23.1% and 31.1% of CO_2 for 6FpDA, 6FmDA and 6FDA-DAM, respectively. As for the insertions, removal of CO_2 was also done in a progresive stepwise procedure. As for the loading curves, copies of the configurations obtained after 500 ps of NPT simulation were taken, a further 2% of the CO_2 was removed, and the resulting configurations were used as the initial configuration at the lower amount. The removal was continued all the way back down to the pure polymer matrices. Most of these simulations were carried out for 4 ns with averages obtained from the last 3 ns. The pressure in these desorption simulations was set to 1 bar so as to have direct comparisons with the uptake simulations. Given the results for the uptake curve, the corresponding equilibrium vapour pressures of the gas for the desorption were mostly obtained from the first estimate. Checks made on some systems again confirmed that this was in agreement with the converged values. The results presented are for just one sample for each type of polyimide.

2.7 Test particle insertion using excluded volume map sampling

In this work a test particle insertion (TPI) method employing a variant of the excluded volume map sampling (EVMS) approach [112,113] was used to calculate the excess chemical potentials of CO_2 in the pure polymer, polymer plus CO_2, and pure CO_2 systems. In the EVMS technique a large amount of the occupied space is pre-eliminated before particle insertions are attempted in order to improve the efficiency compared to purely random insertions. The details of this approach have been documented elsewhere [98] hence only a short description is presented here.

In the method, the MD box is first divided up into a number of subcells on the basis of an input subcell width, d_{grid}. As the MD box is not necessarily cubic and the number of subcells in each direction

has to be an integer, the subcells are constructed internally on the basis of this subcell width. In a second step, each atom in the system is visited and all subcells that fall entirely within a critical radius, w_{cut}, of the atom are mapped out, i.e. w_{cut} represents the "excluded" volume of an atom. Particle insertions are then made by randomly choosing one of the "mapped-in" subcells and then randomly placing and orientating a probe molecule within the chosen subcell. In this way occupied space can be pre-eliminated whilst preserving the advantages of a Monte Carlo sampling of space. The actual amount of space mapped out depends on w_{cut} and the d_{grid} parameters. A finer grid will pre-eliminate more space at the cost of a larger overhead in terms of memory and CPU time required to set up the map for each configuration. As the EVMS method performs a biased sampling of the space the results have to be corrected for the bias. This is done by simply assuming that $exp(-\Delta\Phi/kT)$ in the mapped-out cells is zero in which case true averages are approximated by multiplying by the ratio of the number of mapped-in cells to the total number of cells.

The difficulty with this EVMS method is knowing *a priori* what an appropriate value of w_{cut} should be for a particular system. For this reason different values of w_{cut} have to be first tested in a mode where trial insertions are made into the "mapped-out" cells, *i.e.* those nominally occupied by the particles present in the system. If the value of w_{cut} is appropriate then insertions into mapped-out cells should always give large positive (unfavourable) energy changes. However, should a favourable insertion be made ($\Delta\Phi \leq 0$) then the test has failed and a smaller value of w_{cut} has to be tried. In this way w_{cut} can be optimized, so as to pre-eliminate as much space as possible, without allowing favourable insertions in the mapped-out subcells. In this work many tests were made and appropriate values were found to be $w_{cut} = 2$ Å and $d_{grid} = 0.5$ Å for the case of CO_2 in the polyimides.

At best an EVMS method can improve the efficiency of a particle insertion approach by a factor of the total volume divided by the mapped-in volume, *e.g.* a factor of 20 if 95% of the space is considered occupied; in practice the overheads associated with pre-eliminating 95% of the space are not negligible.

Claims to factors of improvement of EVMS over conventional particle insertion greater than 20[113] should probably be treated with some skepticism.

In the case of a charge neutral probe molecule, like carbon dioxide, there is a subtle point to consider concerning the calculation of the energy difference. In principle the energy difference we require is just the interaction of the test particle with the real particles already present. If the Ewald summation is used to obtain the Coulombic part of this energy difference, using $\Delta\Phi_c = \Phi_c(N+1) - \Phi_c(N)$, there is a problem in that intrinsically the Ewald sum contains contributions from probe molecule interactions with *images* of itself and interactions of real particles with *images* of the probe molecule. The interaction energy of the probe with images of itself are removed in our code by performing the Ewald sum on the probe molecule alone in the MD box. However, this does not remove interactions of real particles with images of the probe so the energy difference does not strictly correspond to that of the interaction of one probe with an infinite array of real particles. As the probe molecules are relatively small in size and charge neutral this term is probably not of any importance in practice.

Although the EVMS method has been verified against the standard random insertion approach in the case of the Lennard-Jones fluid, it was considered prudent to first make a check in the case of carbon dioxide, in particular given the significant partial charges on the atoms of these molecules. The system chosen to make the test was pure liquid CO_2 at 290 K at a density of 804.722 kg m^{-3}, i.e. close to the liquid-vapour coexistence curve. This represents a reasonably stiff test of the EVMS method as although a significant amount of CO_2 can be absorbed by the polymers in question at 308 K, it is unlikely that the local density of CO_2 exceeds that of the pure liquid at 290 K. A system of 512 molecules of CO_2 were, thus, equilibrated in a cubic MD box at a density of 804.722 kg m^{-3} at 290 K. Configurations from an NVT production run of 300 ps were stored every 1 ps and these were then used to make the EVMS particle insertion tests. For the case of pure carbon dioxide at 290 K it was found that a $w_{cut} = 2.4$ Å could be used. A value of $d_{grid} = 0.1$ Å was also used and this led to about 77% of the space being mapped out.

With a required density of test particle insertions of 10 $Å^3$ this resulted in just over 100000 test insertions per configuration. The validation of the EVMS method was first made by comparing the Boltzmann factor weighted radial distribution functions accumulated during the test particle insertions, to those obtained from the production simulation itself. Figure 2 shows the comparison in the case of carbon-carbon interactions. Although not shown, similar excellent agreement was obtained for the carbon-oxygen and oxygen-oxygen interactions.

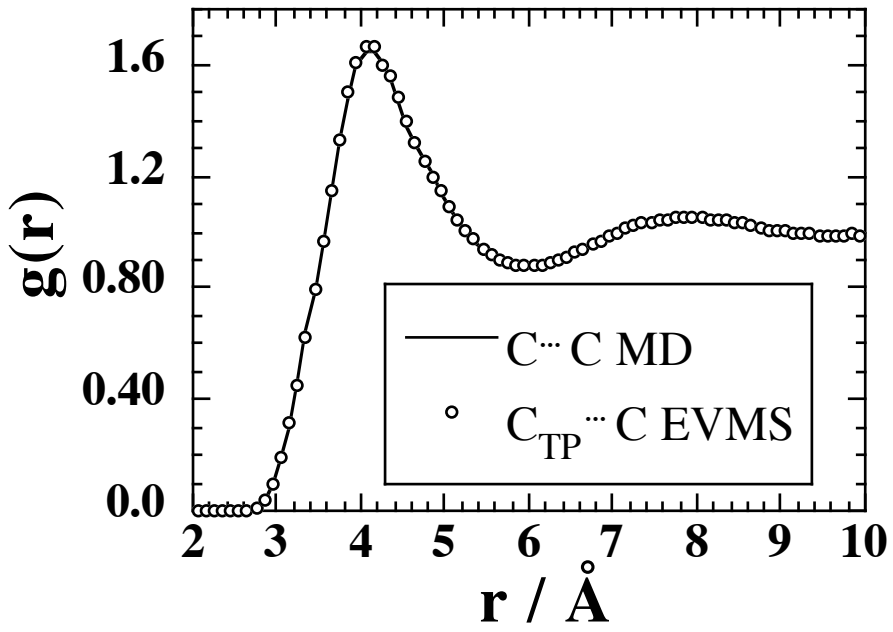

Figure 2. Intermolecular radial distribution functions, g(r), obtained for actual C···C interactions from stored configurations (solid line) from the MD simulation of pure liquid CO_2 at 290 K compared to those obtained by Boltzmann factor weighting test particle – actual particle interactions (C_{TP}···C) during the EVMS particle insertion tests (circles) on the same set of configurations.

As a confirmation of the results for the radial distribution functions, the Boltzmann weighted average insertion energy of the CO_2 test particle, $\langle \Delta\Phi exp(-\Delta\Phi/kT)\rangle / \langle exp(-\Delta\Phi/kT)\rangle$ = -17.06±0.03 kJ mol^{-1} (of

CO_2), compared well to that inferred from the average total potential intermolecular energy in the MD simulation, -17.02±0.02 kJ mol^{-1} (of CO_2). It is thus reasonable to conclude that the EVMS test particle insertion technique is reliable for CO_2.

3. Pure carbon dioxide vapour at 308 K

From the MD simulations on systems of pure CO_2 in the vapour phase, the excess chemical potential was extracted using the EVMS test particle insertion method from the configurations stored over the last 3 ns of the corresponding simulations. The results obtained are plotted as a function of the average pressure, obtained from the same simulations, in Figure 3. The excess chemical potentials calculated directly from test particle insertions were compared with the values obtained from the following equation, based on a knowledge of the equation of state (see Annex),

$$\mu_{ex} = -kT \ln\left[\frac{\rho(P',T)}{\rho^{ig}(P',T)}\right] + \frac{1}{N}\int_{P_{low}}^{P'}(V(P,T) - V^{ig}(P,T))dp \qquad (7)$$

where ρ^{ig} and V^{ig} are the density and volume of the corresponding ideal gas. In Eq. 7 it is assumed that there exists a sufficiently low pressure, P_{low}, that the gas behaves in an ideal manner and thus thedifference in the actual and ideal volumes disappears in the integral. For the model of CO_2 used here, even at the lowest pressures simulated, there existed some deviations from ideality. As volume is (roughly) inversely proportional to pressure the difference in volume at low pressures rapidly become very significant, thus rendering the use of Eq. 7 subject to a certain degree of error. This problem manifests itself in an offset of the curve at low pressure which is obviously present at all higher pressures. Nevertheless the comparison shown in Figure 3 is reasonably consistent. For all subsequent calculations involving the excess chemical potential of the vapour phase we stress that the values obtained directly from the test particle insertion approach will be used.

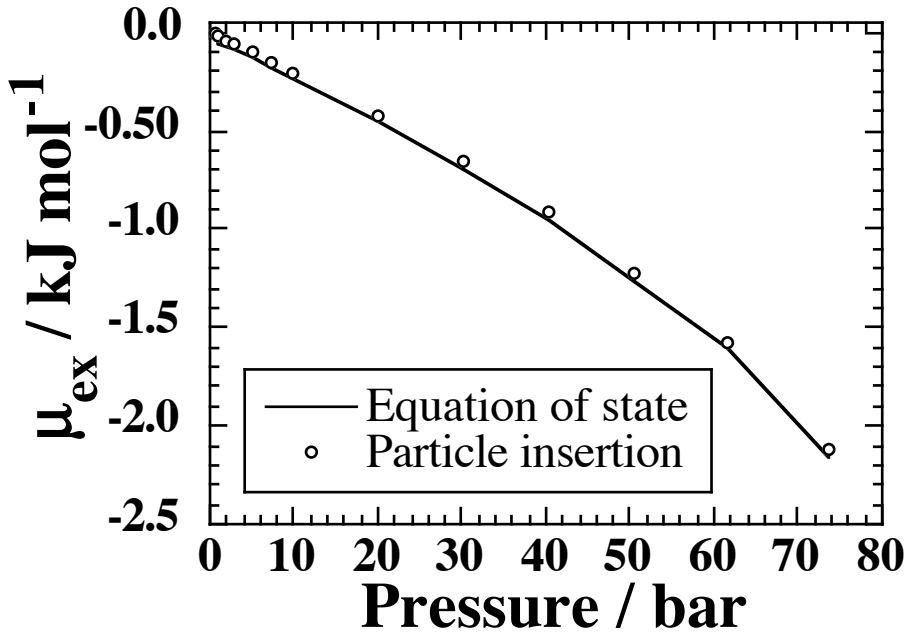

Figure 3. The excess chemical potential of carbon dioxide in the pure vapour phase at 308 K. Results for the direct evaluation of the excess chemical potential using the EVMS test particle insertion method (circles) are compared to the results obtained using the equation of state approximation given in Eq. 7 (line).

4 Carbon dioxide uptake into polyimides

In this section we present and discuss the results of the simulations described in Section 2.5 in which carbon dioxide is progressively loaded into the three types of polyimides and the equilibrium pressure of CO_2 corresponding to the imposed quantity of CO_2 is obtained through the iterative technique described in Section 2.1. All results in this section are averaged over three independent systems for each of the three types of polyimides.

4.1 Sorption isotherms

The results obtained using the iterative method described above for the equilibrium external gas pressure corresponding to the numbers of CO_2 molecules inserted into the different polymers are shown in Tables 1, 2, and 3. The true concentrations of gas in the polymer have been expressed as the ratio of the "volume" of gas absorbed by a certain volume of polymer

$$C(P) = \frac{V_p^{STP}(P)}{V(P)} = \frac{n_p(P)\, k_B\, T^{STP}}{V(P) P^{STP}} \tag{8}$$

The volume V_p^{STP} is the volume that the $n_p(P)$ molecules of gas absorbed in the polymer would occupy if the gas were ideal and at the standard temperature and pressure (T^{STP}=273.15 K; P^{STP}=1.01325 bar) conditions and $V(P)$ is the true volume of the polymer. However, in order to compare with the usual experimental practice, the nominal concentrations of the gas in the polymer at the different pressures, $C_0(P)$, have also been calculated using the following definition

$$C_0(P) = \frac{V_p^{STP}(P)}{V_0} = \frac{n_p(P)\, k_B\, T^{STP}}{V_0 P^{STP}} \tag{9}$$

where V_0 is the corresponding volume of the *pure* polymer, i.e. before any gas has been absorbed. In reality the true volume of the polymer, $V(P)$, changes as a function of the applied gas pressure as it absorbs more and more gas but most experiments do not measure simultaneously the volume of the polymer and the gas uptake. For completeness both the true and nominal concentrations are given in the tables. From the converged value of the pressure, P, the corresponding true and nominal solubility coefficients can be defined as, $S(P)=C(P)/P$ and $S_0(P)=C_0(P)/P$, respectively. These values are also given in the tables. Finally, to check the consistency of the iterative approach, the solubility coefficient as obtained from the test particle insertion method has also been calculated, $S^{TPI}(P)$. Using Eqs. 5 and 8 we can write

$$\frac{C(P)}{P} = \frac{n_p(P)\, k_B\, T^{STP}}{V(P) P P^{STP}} = \frac{\rho^p(P)\, k_B\, T^{STP}}{P P^{STP}} = \frac{S^p(P) \rho^g(P)\, k_B\, T^{STP}}{S^g(P) P P^{STP}} \equiv S^{TPI}(P) \tag{10}$$

thus eliminating the explicit appearance of the concentration of gas in the polymer from the expression for the solubility coefficient. In the limit that P tends to zero the ideal gas law can be invoked in which case the number density in the gas phase can be replaced by $\rho^g(P)=P/k_BT$ and the solubility in the gas phase becomes unity, $S^g(P)=1$, so Eq. 10 becomes

$$\lim_{P\to 0} S^{TPI}(P) = \frac{S^p(P) \dfrac{P}{k_B\, T}\, k_B\, T^{STP}}{S^g(P) P P^{STP}} = \frac{S^p(P)\, T^{STP}}{T P^{STP}} \tag{11}$$

TPI derived estimations of the solubility coefficients are also given in the tables. For all non-zero pressures Eq. 10 was used and estimates at zero pressure were from Eq. 11.

Table 1. Average results of the sorption isotherm MD simulations at 308 K on 6FDA-6FpDA. The averages are taken from three independent systems. The approximate mass percentages of CO_2 are given as obtained from the actual number of molecules inserted into the polymers. The corresponding true and nominal concentrations of gas in the polymer are shown in units of cm^3(STP) cm^{-3} of polymer (true or pure polymer volume). The pressure given is that estimated to be the equilibrium external vapour pressure of CO_2 which would have to be applied to give the imposed concentrations of CO_2 in the polymer. The true and nominal solubility coefficients are given as well as the solubility coefficient estimated from the EVMS test particle insertion analysis (Eq. 10 or 11) in units of cm^3(STP) cm^{-3} bar^{-1}. Error bars are the standard errors over the three independent systems.

~% CO_2	Number of CO_2	True Concn. $\frac{V_g^{STP}(P)}{V(P)}$	Nominal Concn. $\frac{V_g^{STP}(P)}{V_0}$	P / bar	True Solubility $\frac{C(P)}{P}$	Nominal Solubility $\frac{C_0(P)}{P}$	TPI Solubility
0	0	0.00	0.00	0	-	-	124±4
1	25	7.52±0.02	7.51±0.02	0.08±0.01	98±8	98±8	102±2
3	76	22.8±0.1	22.8±0.04	0.23±0.06	117±37	117±37	77±2
5	127	38.1±0.1	38.11±0.06	0.68±0.03	56±3	56±3	56±3
7	177	52.7±0.2	53.11±0.09	1.5±0.1	37±2	37±2	37±2
11	278	81.5±0.3	83.5±0.2	5.2±1.0	17±4	18±4	17±4
15	380	108.4±0.5	114.1±0.2	12±2	9.7±1.6	10.2±1.7	9.4±1.9
17	430	120.5±0.3	129±0.2	29±2	4.2±0.2	4.5±0.3	4.2±0.2
19	481	132±1	144±0.3	38±5	3.6±0.4	3.9±0.4	3.5±0.4
21	531	143±1	159±0.3	41±14	4.3±1.2	4.8±1.3	4.2±1.2
23	582	154±1	175±0.4	41±9	4.1±0.9	4.7±1.1	4.2±1.1
25	633	164±1	190±0.4	76±15	2.3±0.4	2.7±0.5	2.2±0.4

Table 2. As Table 1 for 6FDA-6FmDA.

~% CO_2	Number of CO_2	True Concn. $\frac{V_g^{STP}(P)}{V(P)}$	Nominal Concn. $\frac{V_g^{STP}(P)}{V_0}$	P / bar	True Solubility $\frac{C(P)}{P}$	Nominal Solubility $\frac{C_0(P)}{P}$	TPI Solubility
0	0	0.00	0.00	0	-	-	116±10
1	25	7.55±0.01	7.59±0.02	0.08±0.01	100±18	100±18	101±11
3	76	22.9±0.01	23.1±0.1	0.21±0.04	120±30	121±30	82±5
5	127	38.2±0.1	38.5±0.1	0.69±0.06	56±5	57±5	54±4
7	177	52.9±0.2	53.7±0.1	1.39±0.15	39±4	39±4	39±4
11	278	81.4±0.2	84.4±0.2	4.9±1.1	18.7±5.1	19.4±5.2	19±5
15	380	107.9±0.3	115.3±0.2	11.4±3.2	10.8±2.4	11.6±2.6	11±2
17	430	120.1±0.3	130.5±0.3	16.4±3.1	8.0±1.8	8.7±2	8.2±1.8
19	481	132.0±0.5	145.9±0.3	32±7.5	4.7±1.3	5.2±1.5	4.7±1.0
21	531	143±1	161.1±0.3	58±5.5	2.5±0.3	2.9±0.3	2.6±0.3
23	582	155±1	176.6±0.4	59±2.5	2.6±0.1	3.0±0.1	2.5±0.1
25	633	165±1	192.0±0.4	100±0.6	1.65±0.01	1.92±0.01	1.7±0.2

Table 3. As Table 1 for 6FDA-DAM.

~% CO_2	Number of CO_2	True Concn. $\frac{V_g^{STP}(P)}{V(P)}$	Nominal Concn. $\frac{V_g^{STP}(P)}{V_0}$	P / bar	True Solubility $\frac{C(P)}{P}$	Nominal Solubility $\frac{C_0(P)}{P}$	TPI Solubility
0	0	0.00	0.00	0	-	-	121±9
1	19	6.71±0.02	6.70±0.03	0.07±0.01	92±9	92±9	106±10
3	57	20.07±0.06	19.74±0.08	0.20±0.05	124±43	122±43	81±3
5	95	33.43±0.09	33.5±0.1	0.54±0.01	62±1	62±1	64±4
7	133	46.6±0.1	46.5±0.2	0.92±0.07	51±4	51±4	49±3
11	209	72.4±0.2	73.7±0.3	3.0±0.4	25±4	25±3	25±3
15	285	96.6±0.3	100.5±0.4	10.4±2.4	10.1±1.9	11±2	10.2±1.6
17	323	107.7±0.3	113.9±0.4	11.8±1.1	9.3±1.0	9.8±1.0	9.5±0.7
19	361	118.3±0.5	127.3±0.5	13.8±2.6	9.2±1.6	9.9±1.8	9.4±1.4
21	399	128.8±0.4	140.7±0.6	28.9±4.9	4.7±0.7	5.2±0.8	6.7±1.2
23	437	139.3±0.2	154.1±0.6	26.9±3.1	5.3±0.7	5.9±0.7	5.1±0.1
25	475	149.1±0.3	167.4±0.7	40±5	3.9±0.6	4.3±0.7	3.6±0.4
27	513	158.1±0.5	180.8±0.7	46±3	3.5±0.2	4.0±0.3	3.6±0.2
29	551	166.0±0.3	194.2±0.8	41±5	4.2±0.6	4.9±0.7	4.0±0.6
31	589	175.4±0.5	207.6±0.8	57±11	3.3±0.5	3.9±0.6	3.1±0.3

The results shown in Tables 1-3 demonstrate the robustness of the iterative technique. In general the equilibrium pressure is found to increase smoothly with loading, as one would expect. Slight variations in the average trend result from statistical noise. The reduction in the difference in the slopes of

the quantities $\mu_{ex}^{p}(P_1) - \mu_{ex}^{g}(P)$ and $kT \ln \frac{\rho^{g}(P)}{\rho^{p}(P_1)}$ at the higher pressures also leads to less precision on the point of intersection. At the lowest imposed concentrations of gas in the polymers, the equilibrium pressures were below the ~0.5 bar lower limit of the explicit simulations of the pure gas. In these cases linear interpolations have been used to obtain the excess chemical potential and the density of the gas phase on the basis that the excess chemical potential and the density of the gas phase both tend to zero as the pressure tends to zero.

Figure 4 shows the average sorption isotherms of the three polyimides in terms of the nominal concentration, $C_0(P)$. The smooth curves plotted through the data are non-linear least squares regression fits to the dual mode sorption (DMS) model

$$C_0(P) = k_D\, P + C_H^{'} \frac{bP}{(1 + b\, P)} \;\Rightarrow S_0(P) = \frac{C_0(P)}{P} = k_D + C_H^{'} \frac{b}{(1 + b\, P)} \qquad (12)$$

The DMS model is still a popular way of fitting such data even though careful analyses of experimental data obtained over increasing pressure ranges show clearly that the "constant" parameters (k_D , C'_H and b) are not at all constant but vary systematically with the pressure range used.[114] Also shown in Figure 4 are some corresponding experimental data taken from the literature. In general the experimental data obtained for the greatest range of pressure has been chosen to make the comparison. In the case of 6FDA-6FpDA this was the data of Coleman & Koros[41] which was found to be in good agreement with the data of Wang *et al.*[48] and Hibshman *et al.*[59] For 6FDA-6FmDA the data was again taken from the work of Coleman & Koros[41] which was again consistent with later work published by the same authors.[42] For 6FDA-DAM the only experimental data that was found at a range of pressures was that of Wind *et al.*[115] Hölck *et al.* have performed a single sorption measurement of CO_2 in 6FDA-DAM at a pressure of 10 bar and at 308 K.[79] Their reported nominal concentration of 81.4 cm^3(STP) cm^{-3} at 10 bar is somewhat higher than that also found experimentally by Wind *et al.*[115] and lower, by about the same amount, than our simulation result.

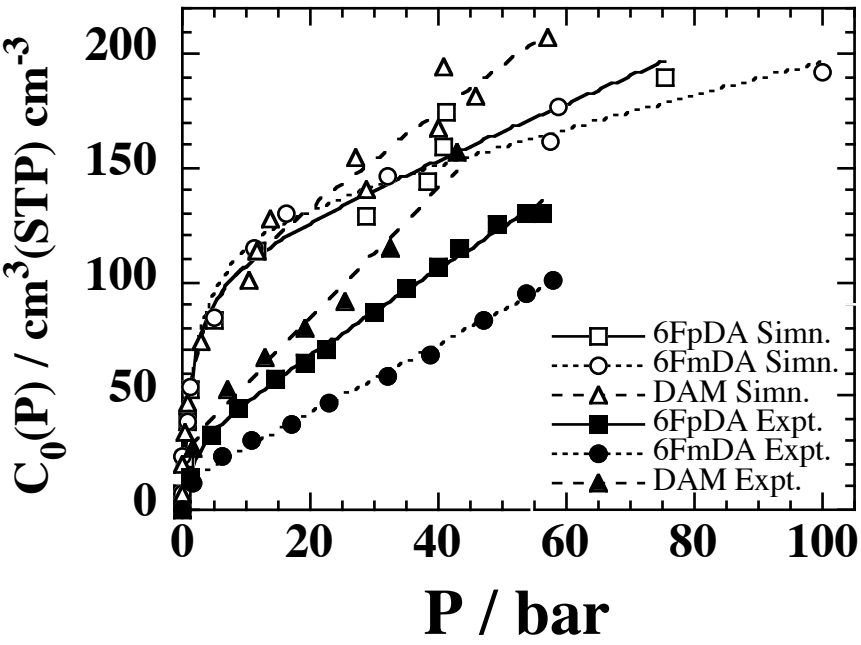

Figure 4. A comparison of CO_2 sorption isotherms of 6FDA-6FpDA, 6FDA-6FmDA and 6FDA-DAM at 308 K as obtained from the simulations reported here and experimental data taken from the papers of Coleman & Koros[41] (6FDA-6FpDA and 6FDA-6FmDA) and Wind *et al.*[115] (6FDA-DAM). The nominal concentrations (Eq. 9) are plotted as a function of the partial pressure of carbon dioxide. Smooth lines through the data are non-linear least-squares regression fits to the concentration form of the dual mode sorption model (Eq. 12). For clarity error bars on the pressure in the simulation data have been omitted.

There is a marked contrast in the behaviour of the concentration with pressure between simulation and experiment. The simulation data all show a very rapid and very similar increase in concentration at low pressures whereas the experimental data increase at a much slower rate and differences between the polymers are evident at much lower pressures. At higher pressures the faster rate of increase of the concentration of CO_2 in 6FDA-DAM is clear to see in the simulation data although a difference between 6FDA-6FpDA and 6FDA-6FmDA is not evident until above 60 bar. The models thus predict the same trends as experiment but the two isomers behave in a more similar way than actually found.

The notably more rapid increase in concentration with pressure implies higher solubilities in the models. This is apparent in Figure 5 where the corresponding nominal solubilities have been plotted.

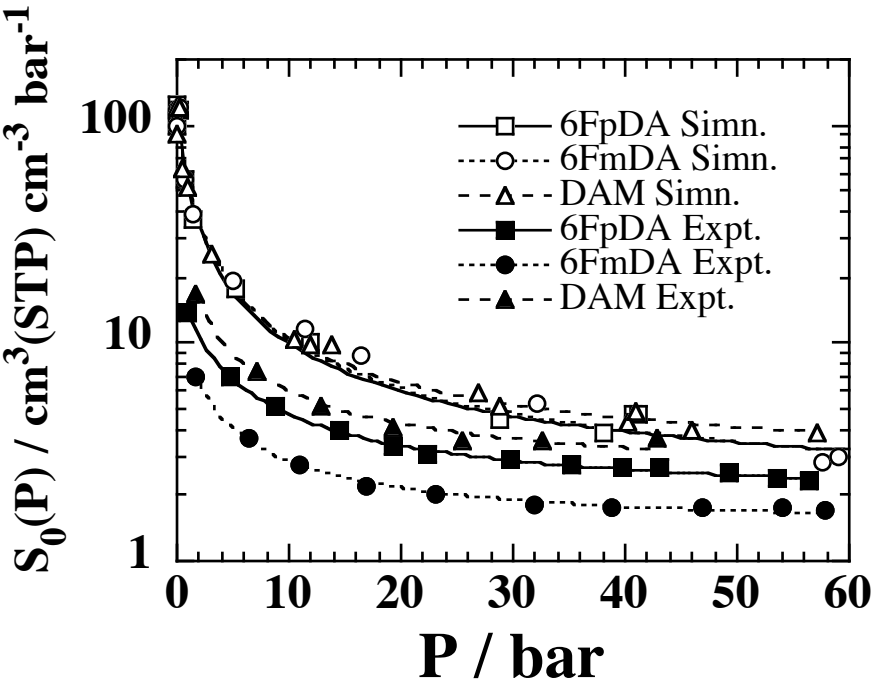

Figure 5. As Figure 4 for the nominal solubilities. Note the logarithmic scale on the y axis. Smooth lines through the data are non-linear least-squares regression to the solubility form of the dual mode sorption model (Eq. 12); we note in passing that the best fit DMS parameters depend on whether solubility or concentration curves are fitted. For clarity error bars on the pressure in the simulation data have again been omitted.

The limiting zero pressure solubilities in the model systems are all high and quite close (120±10 cm^3(STP) cm^{-3} bar^{-1}) compared to the experimental results:- ~21 for 6FDA-6FpDA, ~14 for 6FDA-6FmDA, and ~36 for 6FDA-DAM, as estimated from the best fit DMS parameters ($S_0(P \to 0) = k_D + C_H' b$). Model solubilities drop very sharply in the 0-20 bar pressure range and thus approach progressively the experimental values. For 6FDA-DAM the agreement is especially good with both model and experiment having limiting high pressure nominal solubilities of ~4 cm^3(STP) cm^{-3} bar^{-1}.

In the cases of 6FDA-6FpDA and 6FDA-6FmDA the model solubilities remain higher but only by a factor of about 2. It would thus seem that the models predict better the limiting (Henry's law) sorption but rather overestimate the initial (Langmuir-like) uptake. In the rest of this section we investigate and speculate on some of the reasons that may lie behind these discrepancies in the infinite dilution limit.

First of all, it is not unusual for empirical force field based molecular simulations to overestimate solubilities of gases in polymers or, more specifically, CO_2 in polyimides. Heuchel *et al*. have published estimates of limiting low-pressure solubilities of a single interaction centre model of CO_2 in a number of polyimides.[62] These are consistently higher than the quoted (partial pressure of CO_2 unspecified) experimental values. For example for 6FDA-6FpDA a model solubility of 106±18 cm^3(STP) cm^{-3} bar^{-1} is obtained, i.e. within errors the same as that found here, and for 6FDA-DAM a value somewhat lower of 68±5 cm^3(STP) cm^{-3} bar^{-1} was found.Unfortunately the details of the cross interactions between the single Lennard-Jones 12-6 site model of CO_2 and atoms in the polyimides are not specified. The pure polyimide being modelled using the COMPASS force field, i.e. with Lennard-Jones 9-6 potentials, it is not at all obvious what combining rule has been used. Nevertheless, to assess the effect of changing from an all-atom model of CO_2 with partial charges to a single neutral spherical representation, the solubilities of a single Lennard-Jones site model (σ=4Å, ε/k_B=226.23 K)[62] in our pure PI systems have been calculated using the TPI method. The resulting average solubility coefficients were:- 450±40, 382±13, and 354±22 cm^3(STP) cm^{-3} bar^{-1}, for 6FDA-6FpDA, 6FDA-6FmDA, and 6FDA-DAM, respectively. The considerably higher solubilities obtained suggest that the spherical representation of CO_2 is poorly adapted for such studies. Further tests using the single LJ site potential parameters optimized for supercritical CO_2 of Iwai *et al.*[116](σ=3.72Å, ε/k_B=236.1 K) gave the resulting average solubility coefficients:- 253±7, 220±5, and 198±6 cm^3(STP) cm^{-3} bar^{-1}, for 6FDA-6FpDA, 6FDA-6FmDA, and 6FDA-DAM, respectively. Again these are rather high.

A persistent concern in empirical force field based simulations is the parametrization of the Van der Waals part of the cross interactions, in particular in this case between the gas and the polymer. In general the force fields for the pure systems, polymer or gas, are developed independently with little or no attention paid to optimizing the gas-polymer interactions. Empirical mixing rules, such as the Lorentz-Berthelot ones used here, are known to have their limitations even for mixtures of rare gases.[117] Previous molecular level simulations of Helium in polyimides have investigated the effect of the cross-interactions by comparing different combining rules and concluded that this can influence solubilities and diffusion.[118] In order to estimate the degree of such effects in the case of carbon dioxide, the TPI calculations on the pure polymer systems have been repeated using the Waldmann-Hagler[117] combination rules:-

$\sigma_{AB} = \left(\frac{\sigma_{AA}^6 + \sigma_{BB}^6}{2} \right)^{\frac{1}{6}}$ and $\varepsilon_{AB} = \sqrt{\varepsilon_{AA}\varepsilon_{BB}} \left(\frac{2\sigma_{AA}^3 \sigma_{BB}^3}{\sigma_{AA}^6 + \sigma_{BB}^6} \right)$, for just the CO_2-polymer interactions. The resulting TPI solubility coefficients were:- 97±3, 88±7, and 92±6 cm^3(STP) cm^{-3} bar^{-1}, for 6FDA-6FpDA, 6FDA-6FmDA, and 6FDA-DAM, respectively. Compared to the corresponding values obtained using the Lorentz-Berthelot combination rules (Tables 1-3) these are between 20-25% lower, which is significant but still somewhat higher than the experimental values.

A further concern in the case of the three site model of carbon dioxide is the value chosen for the partial charge on the carbon atom; which by electroneutrality sets the value for the oxygens, $q_O=-q_C/2$. This value is optimized to best represent the properties of pure carbon dioxide.[101] It is not obvious, however, whether the same value should be used in the case of infinite dilution where the CO_2 molecule is only surrounded by polymer. Although it might be feasible to perform *ab initio* calculations to estimate the influence of the local environment on the charge distribution, an idea of the dependence of the solubility on this parameter can be obtained by simply scaling down the partial charges on the CO_2 molecule used as the test particle in the TPI calculations on the pure polymers. The results of some tests on just one system of a relaxed 6FDA-6FpDA system at 308 K are shown in Table 4. Scaling down the charges naturally reduces the interactions with the polymer atoms and leads to lower solubilities.

However, even if the partial charges are set to zero the solubility is still overestimated. Considering that experimental measurements of the quadrupole moment of CO_2 in the gas phase lead to even higher estimates of the partial charge on the oxygen atoms of -0.32 e,[119] it seems unlikely that this can be the prime cause.

Table 4. Influence of the partial charge distribution in the three site model of carbon dioxide on the solubility coefficient. The results of EVMS TPI calculations on just one pure relaxed system of 6FDA-6FpDA at 308 K are shown.

Charge scaling factor %	q_C / e	q_O / e	TPI Solubility / cm^3(STP) cm^{-3} bar^{-1}
100	0.58880	-0.29440	122
90	0.52992	-0.26496	102
80	0.47104	-0.23552	89
70	0.41216	-0.20608	79
0	0	0	55

Experimentally it is largely accepted that the solubility of gas molecules in polymer membranes is governed by the hole-filling mechanism at low gas pressures.[41,42,120] The amount of fractional free volume (FFV) available for gas sorption is the principle factor determining the solubility at low pressures.[41,42] In molecular models we can be certain that the FFV is completely available for CO_2 sorption. In experiments, however, it is possible that residual solvent molecules, or other contaminants, are present inside the membrane and these ultimately reduce the amount of CO_2 sorption.[121-123] Other experimental factors such as aging of the polymers, preparation method and solvent used to cast polymer membranes also have an impact on FFV and hence on solubility.[43] The thermal hysteresis also has a noticeable impact

on gas transport; there are chances of excess FFV get trapped within the polymer matrices because of the thermal treatments close to T_g.[44,81]

Physical aging of polymers generally leads to densification as the non-equilibrium free volume is gradually reduced.[124] Experimentally, the consequences of this have been measured in terms of the drop in solubility of CO_2 in aged samples of, for example, 6FDA-durene polyimide[125] and polycarbonate[126] and correlated to the reduction of the Langmuir component of the solubility. In these cases changes in solubility are at least of the order of 10% over aging periods ranging from hundreds of hours to hundreds of days. It is not obvious, however, to determine from these results the effects physical aging has on going from the MD simulation timescale of a few nanoseconds to a real experimental timescale of a few hours or days. Attempts to address this issue have been made using molecular simulations by generating polymer models at different densities corresponding to the known age-dependent experimental densities.[127] However, the correspondence between generating samples at different densities and then simulating them under constant volume conditions in order to maintain the initial density, i.e. at different pressures, and true physical aging, i.e. samples held at constant pressure for long periods, is not at all obvious. Such studies are more equivalent to studying the pressure dependence of solubility on freshly generated samples. The structural changes that lead to the densification that occurs with aging at constant pressure are not necessarily the same as those that occur under compression. Until this problem is tackled in a more satisfactory way it will remain difficult to quantify the effect aging from the nanosecond to experimental timescales has on solubility of gases in amorphous polymers. In this respect physical aging remains a factor that could well explain, at least in part, the discrepancies in the limiting low concentration solubilities.

4.2 Volume swelling

Penetrant-induced volume dilation is known to occur in the case of carbon dioxide sorption in glassy polymers.[128] Dilation experiments are often performed using a different apparatus than the sorption experiments so measuring volume changes with respect to gas concentration is inevitably subject to some

added uncertainty.[38,85,129] However, Wang *et al.*[130-132] have made concurrent measurements of sorption, dilation, and diffusion of CO_2 in polysulfone and polybenzylmethacrylate and Hölck *et al.* have performed a concurrent sorption and dilation measurement of CO_2 in 6FDA-DAM at 308 K at a pressure of 10 bar.[79]

In simulations carried out in periodic boundary conditions the dilation can be measured as a function of mass uptake directly. The volume swelling induced by CO_2 is directly measured from the differences in volumes of the polymer matrices containing different concentration of CO_2 with respect to pure polyimide matrices.

$$\%\,\text{Volume Swelling} = \frac{(V(P) - V_0)}{V_0} \times 100 = \frac{\Delta V(P)}{V_0} \times 100 \tag{13}$$

Figure 6a shows the relative volume swelling during loading of the different systems as a function of the nominal concentration of CO_2.

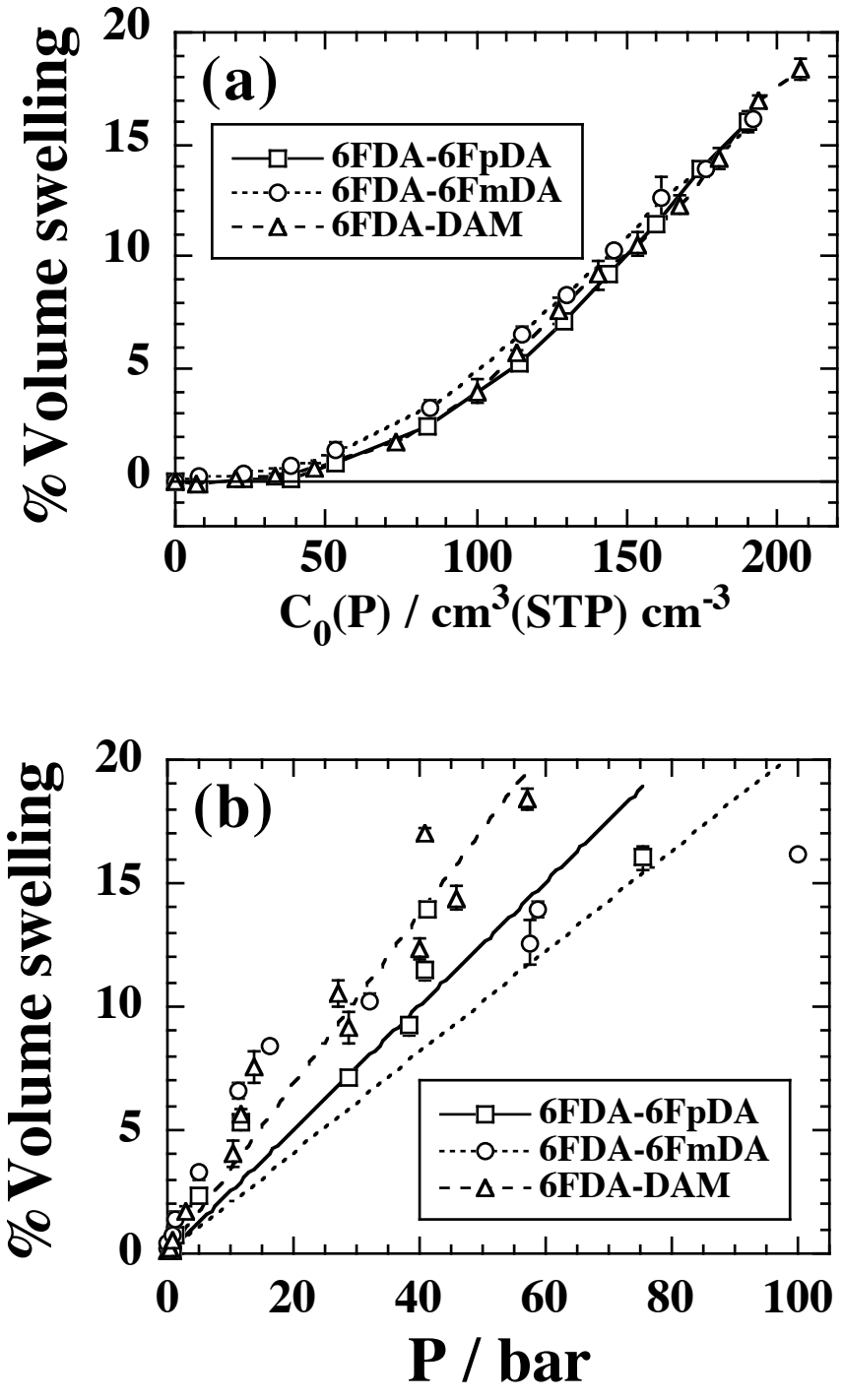

Figure 6. Average volume swelling induced at 308 K in the models of 6FDA-6FpDA, 6FDA-6FmDA and 6FDA-DAM by sorption of CO_2 plotted as a function of:- (a) the (pressure-dependent) nominal concentration of CO_2 and (b) the pressure. The lines in (b) are linear least-squares fits to the form of Eq. 15. For clarity the error bars on the pressure have been omitted from (b).

In general the swelling behaviour as a function of the gas concentration in these model polyimides is one in which the initial gas uptake causes little volume expansion. Thereafter there is a gradual transition to an almost linear increase in volume at higher concentrations. The slight differences between the model polymers in the volume swelling vs. concentration curves can be attributed to the differences in their FFV.[73,120] The denser packing and lower FFV (0.167) of the 6FDA-6FmDA polyimide leads to a slightly higher volume dilation in the low and intermediate CO_2 concentration range. With a higher FFV (0.176) 6FDA-6FpDA dilates less than the 6FDA-6FmDA isomer in the same concentration range. In 6FDA-DAM the packing is disrupted by the methyl substituents in the diamine part that give rise to the highest FFV (0.178) of the three but this is only marginally higher than that of 6FDA-6FpDA and does not lead to significant differences in volume swelling. At the higher concentrations the volume swelling behaviour seems to converge. The limiting slopes at high concentration can be related to the partial molar volume of CO_2

$$\frac{\partial V(n)}{\partial n} = \frac{\partial\left(\frac{\Delta V}{V_0}\right)}{\partial C}\frac{RT^{STP}}{P^{STP}} \tag{14}$$

and within errors these are all about 30±2 $cm^3\ mol^{-1}$ in the three polyimides. This value is somewhat lower than the average partial molar volume of CO_2 in a number of organic solvents of 46 $cm^3\ mol^{-1}$.[133] However, it is very similar to the range of values (27-31 $cm^3\ mol^{-1}$) reported for 6FDA-DAM-based cross-linked copolymers[45] and compares well also to the values found at short times for the dilation of polysulfone and polyethersulfone.[129]

To our knowledge the only published experimental data concerning the CO_2-induced volume dilation of any of the three particular polyimides studied here is the one concurrent sorption and dilation measurement made on 6FDA-DAM by Hölck *et al.* at a pressure of 10 bar and at a temperature of 308 K.[79] Their result of 6.13% volume dilation compares to our value of ~4% at a pressure of ~10 bar. However, if the comparison is made at the same nominal concentration of CO_2 instead (~80 cm^3(STP) cm^{-}

^{3}) then our result is somewhat lower at ~2%. The greater amount of swelling seen in experiment is consistent with other findings. Wessling *et al*. have carried out separate dilation and sorption experiments on related 6FDA-based polyimides.[85] Unlike our results, they find that dilation starts at very low nominal concentrations, ~10 cm^3(STP) cm^{-3} based on an extrapolation to zero dilation of the data given in Figure 5c of Ref.[85], reaching values of ~3% at a nominal concentration of ~50 cm^3(STP) cm^{-3}; compared to about 80-90 cm^3(STP) cm^{-3} in the model systems (Figure 6a). It is not possible to say whether the fact that the sorption and dilation experiments were done separately, with a different pressure loading protocol, influenced the results. Concurrent measurements of sorption and dilation of CO_2 by polysulfone and polybenzylmethacrylate indicate that dilation occurs immediately.[130-132] There are fundamental differences, however, between the experiments and the simulations in the way the loading is performed. In the experiments the CO_2 enters the membrane from the exterior and has to diffuse through the macroscopic sample whereas in the simulations the CO_2 is inserted directly at the most favourable sites. Once inserted though, the CO_2 molecules are free to, and do, diffuse, thus diminishing the importanceof where they are initially inserted. Another factor that can't be discounted is the different timescales involved. These are inevitably short in simulations with respect to experiments for which it is known that penetrant-induced volume relaxation can be extremely slow.[85,129]

It has previously been argued that if the Langmuir sorption term in the DMS model corresponds to a true hole-filling process then its effect on the volume dilation of the polymer should be negligible.[133] Volume dilation can then be attributed just to the number of moles of gas truly "dissolved" in the polymer matrix;from Eq. 12 this is simply proportional to $k_D P$. Assuming that the partial molar volume of CO_2, V_{CO_2}, is independent of pressure, this gives the following prediction for the volume dilation[133]

$$\frac{\Delta V}{V_0} = \frac{k_D P}{(RT^{STP} / P^{STP})} V_{CO_2} = \frac{k_D P}{(22414 cm^3)} V_{CO_2} \qquad (15)$$

Eq. 15 has been found to predict reasonably well the CO_2-induced volume dilation of polycarbonate using a value of V_{CO_2} = 46 cm^3 mol^{-1}.[133] For this reason the data for volume swelling has also been plotted as a function of the pressure in Figure 6b. The data for 6FDA-6FpDA and 6FDA-DAM show some scatter about the best fit lines to the form of Eq. 15, but it is clear that 6FDA-6FmDA shows a systematic deviation. Despite this the resulting linear least-squares best fit values for V_{CO_2} were 47±9, 65±13, and 38±4 cm^3 mol^{-1}, for 6FDA-6FpDA, 6FDA-6FmDA, and 6FDA-DAM, respectively. These don't compare particularly well to the common value of 30±2 cm^3 mol^{-1} determined directly from the volume swelling vs. nominal concentration curve. In addition, non-linear behaviour of the volume swelling with CO_2 vapour pressure has been found in 6FDA-DAM-based cross-linked copolymers[45], 6FDA-based polyimides,[85] and in polysulfone and polyethersulfone.[129] Such non-linear behaviour has led to the development of more elaborate models to describe swelling based on a continuous distribution of hole sizes.[134,135]

From Figure 6a it is clear that the effective volume dilation starts above a nominal concentration of ~40 cm^3(STP) cm^{-3}. The plasticization pressure of glassy polymers is defined as the point where the permeability passes through a minimum, thus the point at which the increasing diffusivity compensates for the decreasing solubility of the penetrant. Bos *et al.*[38] studied eleven different glassy polyimides and reported that all the polymers are plasticized at the same critical (nominal) concentration of 36±7 cm^3(STP) cm^{-3}. It may be a coincidence but this critical concentration corresponds to the point at which the slope of the volume dilation curves change to a higher value.

4.3 Void space

The void space analysis of the polyimides as a function of CO_2 concentration was carried out using a simple geometric technique and the probe accessible volume (PAV) was calculated. This method is similar to various other phantom sphere approaches commonly found in atomistic simulations and the

details of this specific method can be found elsewhere.[98] In brief, the PAV was obtained from repeated random insertions of a virtual probe of radius of 1.8 Å into the MD simulation boxes having different loadings of CO_2. The PAV was calculated in two ways by taking into account or not the actual CO_2 molecules present in the system. In the case where CO_2 molecules were excluded, all polymer atoms in the simulation boxes were treated as hard spheres with standard Van der Waals radii (1.20 Å for H, 1.47 Å for F, 1.50 Å for O, 1.55 for N and 1.70 Å for C) whereas the carbon dioxide molecules present were ignored. A random trial insertion was then "accepted" if the probe sphere did not overlap with any of the polymer atoms in the simulation box. The PAV is then calculated simply as the fraction of "accepted" insertions with respect to the total number of trials multiplied by the volume of the box. It is important to point out that, as such, the PAV is just the volume accessible to the *centres* of the virtual probes. This method does not make any attempt to calculate the total volume accessible to the virtual probe and is just intended to give relative comparisons between similar systems. In the case where the CO_2 molecules actually present in the system were considered the C and O atoms were given the same standard hard sphere radii as given above. These two calculations of the PAV give different information about the space available.

An illustration of the typical results obtained is shown in Figure 7 where the PAV is shown as a function of the nominal CO_2 concentration for just one system of the 6FDA-6FpDA polyimide; all systems were qualitatively similar in their behaviour. At nominal concentrations of CO_2 less than ~50 cm^3(STP) cm^{-3} the CO_2-excluded PAV hardly changes whereas the CO_2-included PAV gradually diminishes as holes are filled up. Above this critical concentration the CO_2-included PAV remains very small whereas the CO_2-excluded PAV reflects the same behaviour as the volume swelling curve (Figure 6a).

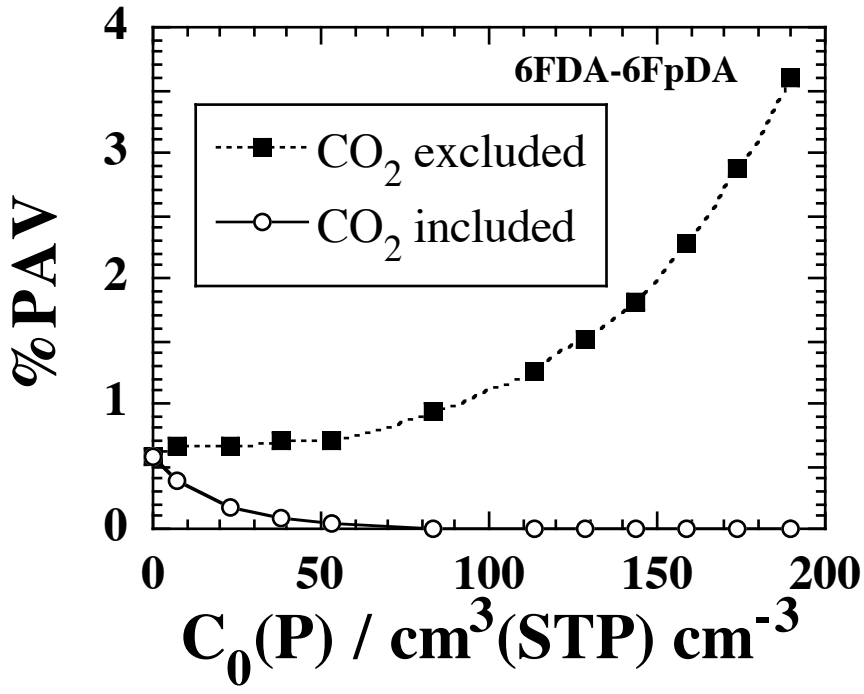

Figure 7 The probe accessible volume (PAV) expressed as a percentage of the pure polymer volume for one system of 6FDA-6FpDA at 308 K. The PAV has been obtained by both including and excluding the CO_2 molecules present in the system.

The distributions of PAV hole sizes were also analysed by using a cut-off distance of 0.5 Å to identify all accepted probe centres falling into the same hole. Although not shown here, the CO_2-excluded PAV hole size distributions remain similar below the critical concentration of CO_2. This also clearly indicates the domination of hole-filling sorption at low concentrations, there being no new holes formed in this regime. Above the critical concentration of CO_2, the percentage of smaller holes is diminished and the percentage of larer holes is increased.

4.4 Energy and Entropy

The changes in the average total potential energy, $\Delta\Phi$, of the different CO_2-containing systems, relative to the pure polymers, have been calculated and resolved into their component parts. Figure 8 shows these various contributions to the $\Delta\Phi$ as a function of the nominal CO_2 concentration in the case of

6FDA-6FpDA. The results for 6FDA-6FmDA are quantitatively very similar to 6FDA-6FpDA and although 6FDA-DAM shows slight differences qualitatively the trends are the same. The change in total potential energy is negative, i.e. exothermic, as reported in the literature.[82] At low concentrations $\Delta\Phi$ decreases almost linearly with the major contribution being the polymer-CO_2 interactions. The onset of volume swelling, above C_0~50 cm^3 (STP) cm^{-3}, coincides with a less steep decrease in the polymer-CO_2 contribution and changes in the polymer-polymer interactions. The intermolecular polymer-polymer contribution becomes less cohesive, as chains become further apart, whilst a slight decrease in the polymer-polymer intramolecular contribution counterbalances this. The gradual change in the CO_2-CO_2 contribution also nullifies the loss in the polymer-polymer cohesive energy.

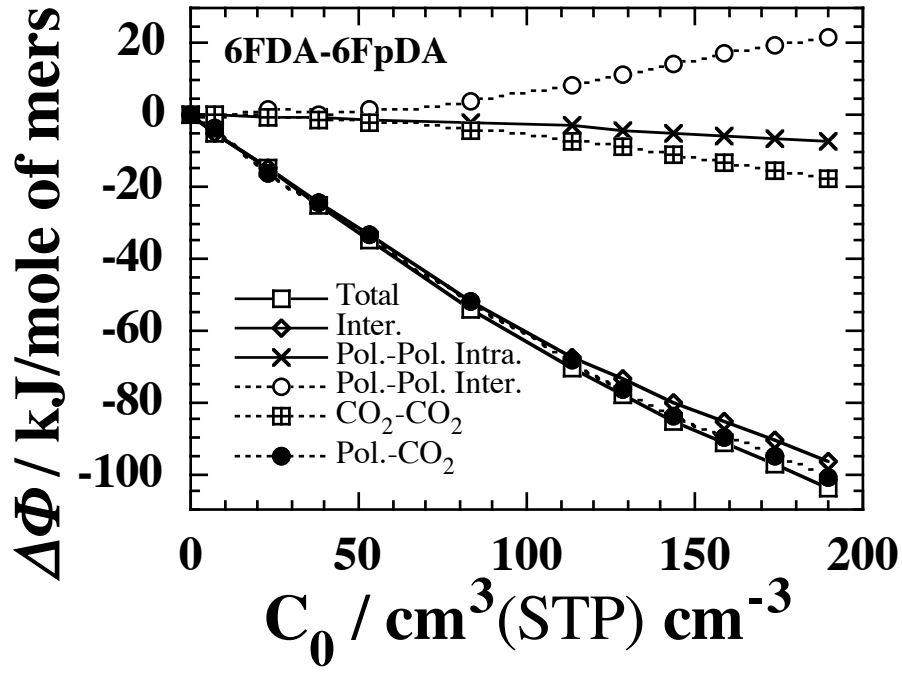

Figure 8. Changes in the total potential energy, and its resolution into the different contributions, with respect to the pure polymer as a function of the nominal concentration of CO_2 at 308 K for 6FDA-6FpDA. Energy changes are quoted in kJ/mole of mers.

The two contributions to the excess chemical potential, i.e. the excess molar enthalpy (h_{ex}) and the excess molar entropy (s_{ex}) were also estimated. To obtain estimates of h_{ex} the average values of $\Phi+PV$, i.e. total enthalpy minus the kinetic energy contribution, from the simulations carried out at 1 bar were plotted as a function of the number (n) of added CO_2 molecules. The resulting curves were then fitted to a combination of two linear functions

$$H(n) = (a + bn)(1 - S(n)) + (C + dn)S(n) \tag{16}$$

where a, b, c, and d are constants and $S(n)$ is a switching function which goes from 1 to 0 in a controllable interval either side of a critical number of added CO_2 molecules, n_c. In this work the following form for $S(n)$ has been chosen

$$S(n) = \frac{1}{2}\left(1 + \frac{n - n_c}{\omega + |n - n_c|}\right) \tag{17}$$

where ω is a variable parameter controlling the sharpness of the switching function; ω=0 being the standard Heaviside function. It seems reasonable to assume that the initial addition of CO_2 leads to a linear change in the enthalpy, the volume swelling being small initially this is effectively confirmed by Figure 8, and at high CO_2 concentration it should become linear again too as it tends towards a pure CO_2 system. The resulting smooth curves (not shown) gave excellent fits to the data and the excess molar enthalpies were then obtained from the analytical derivation of Eq. 16 and the best fit coefficients. The estimation of the derivatives in this way were consistent with numerical estimates using simple difference equations but were much smoother. Once the h_{ex} have been obtained the excess molar entropies can be estimated indirectly using the following equation

$$Ts_{ex} = h_{ex} - \mu_{ex} \tag{18}$$

All three excess molar properties are plotted for all three systems in Figure 9 as a function of the nominal CO_2 concentration.

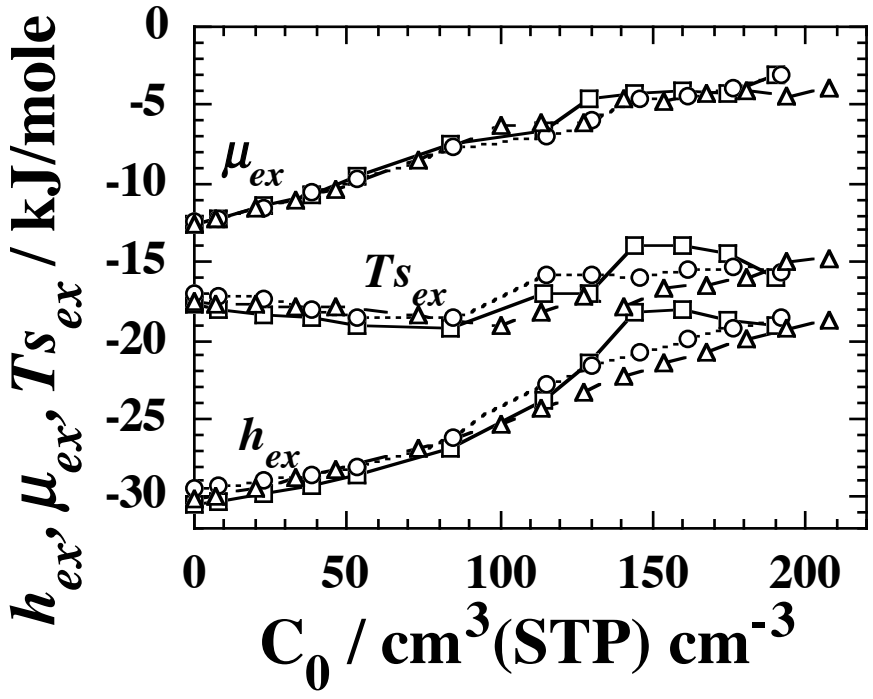

Figure 9 The excess molar enthalpy (h_{ex}). excess molar entropy (s_{ex}) and the excess chemical potential (μ_{ex}) plotted as a function of the nominal CO_2 concentration in the respective polymer matrices. Squares represent 6FDA-6FpDA, circles 6FDA-6FmDA, and triangles 6FDA-DAM.

The excess molar enthalpies gradually decrease from an initial value of about -30 kJ/mole to a value of about -20 kJ/mole as CO_2 concentration increases. This latter value is still relatively high compared to those typical of pure liquid CO_2, e.g. about -17 kJ/mole at 290 K as seen in Section 2.7, confirming the predominance of polymer-CO_2 interactions (see Figure 8) in the regime of concentrations studied. The behaviour of the excess molar chemical potential seems to mirror that of h_{ex} initially but at higher concentrations there are signs of a plateau at $\mu_{ex}\approx$-4 kJ/mole. This figure is already slightly above that for dense pure liquid CO_2 of -6 kJ/mole, albeit at a lower temperature of 290 K. This can be

explained by the behaviour of the Ts_{ex} term which we interpret as being consistent with the behaviour of the partial molar volume of added CO_2. Initial hole filling leads first to a slight descent to more negative values in the entropic contribution but once the volume swelling starts to accelerate this trend is reversed and Ts_{ex} begins to rise as each CO_2 has to create its own space in the system. The values of Ts_{ex} are still some way off that of about -11 kJ/mole typical of pure liquid CO_2 at 290 K but this is consistent with the partial molar volume still being less than that in pure CO_2 too.

According to the site-distribution model of Kirchheim[134-138] the sorbed gas molecules fill the low energy microvoids initially and then the polymer has to adjust itself to adopt more gas molecules. Gas insertion energies thus increase with the increasing concentration of gas molecules. This hypothesis can be tested to a certain extent by analysing the distribution of CO_2 insertion energies obtained from the TPI calculations carried out at different concentrations of CO_2 in the polymer matrices. The probability density distribution of insertion energies that results from TPI, $\rho(\Delta\Phi)$, necessarily contains information concerning those trial insertions which are of high energy, thus of low probability. To obtain a distribution more representative of the energy of likely sites of adsorption this distribution is weighted by the associated Boltzmann factor, i.e. $\rho_w(\Delta\Phi) = \rho(\Delta\Phi)*exp(-\Delta\Phi/kT)$. Examples of these weighted probability density functions are shown in Figure 10 in the case of 6FDA-6FpDA at a range of CO_2 concentrations.

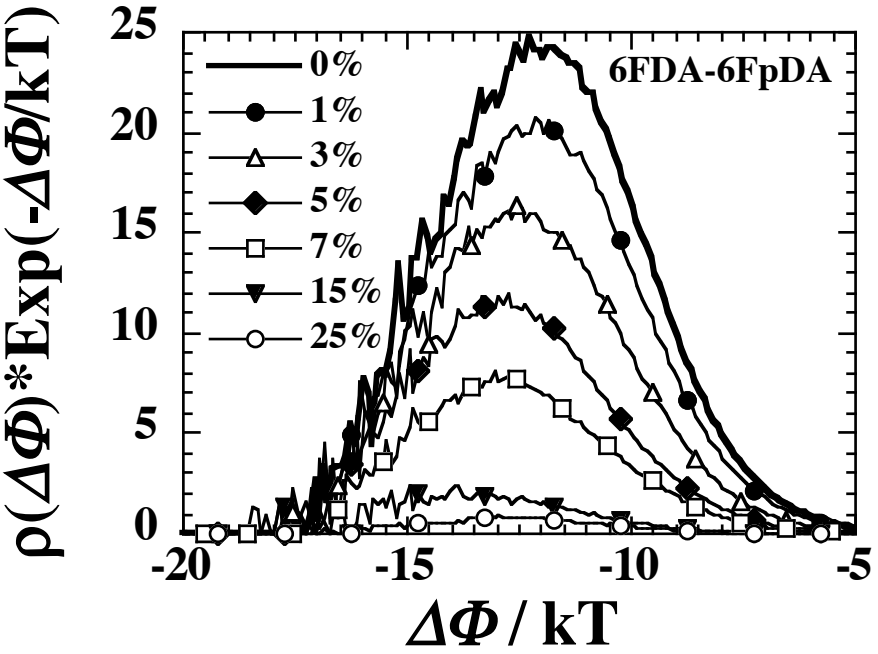

Figure 10. Boltzmann-factor-weighted probability density distributions for the insertion energy of a virtual probe CO_2 molecule in the 6FDA-6FpDA systems containing different concentrations of CO_2.

The resulting weighted insertion energy distributions are smooth and single-Gaussian like with no signs of a binodal distribution. They thus support the site-distribution model rather than the dual-sorption model. However, the weighted distributions also show a fairly homogeneous and progressive reduction in the number of sites available for adsorption. There is no obvious indication that the lower energy sites are being filled in preference. Indeed the peak in the distributions moves, if anything, towards lower energies in the range from 0% to 5%. This we attribute to the increasing quantity of CO_2 in the system in the phase before volume swelling becomes important. If the rubbery state had been attained, where Henry's law is obeyed, no further shift in $\rho_w(\Delta\Phi)$ would be expected at the higher loadings. The difference between 15% and 25% suggests that we have not yet reached this limit.

4.5 Cluster analysis

The possibility of formation of CO_2 clusters was analysed. Two molecules were deemed to be in the same cluster if the distance between the carbon atom of one molecule was within a distance of 3 Å of an oxygen atom of the other molecule. This distance was obtained by trial and error but roughly corresponds to the first peak in the radial distribution function. The average results obtained for the distribution of cluster sizes from the MD simulations of 25% CO_2 in 6FDA-6FpDA system are displayed in Figure 11.

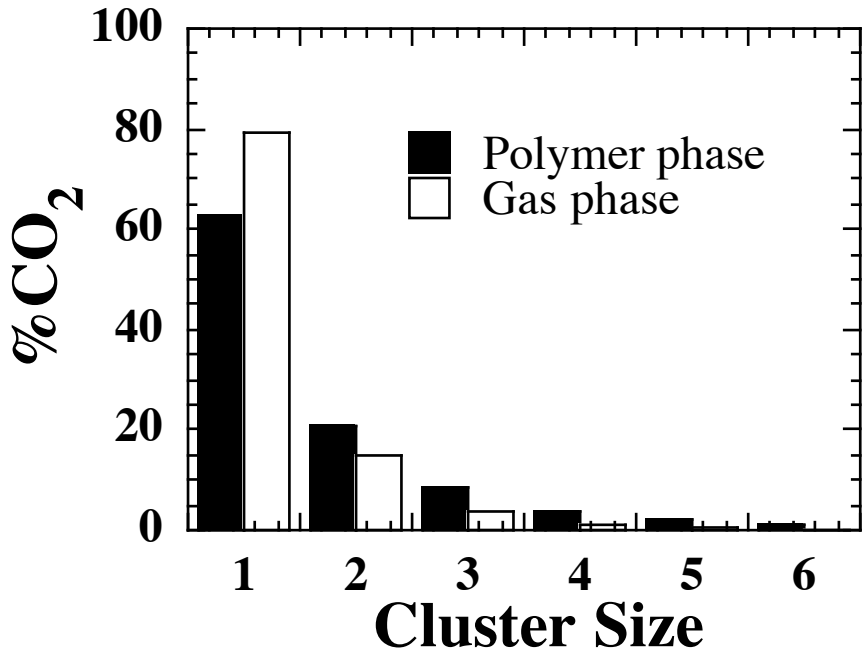

Figure 11. The percentage of CO_2 molecules in clusters of a given size in the 6FDA-6FpDA system containing ~25% of CO_2 compared to the distribution obtained from simulation of a pure gas phase CO_2 system at the same CO_2 density (see text for details).

For comparison the distribution obtained in the pure gas phase at same density of CO_2 (322.33 kg m^{-3}), i.e. from simulations using the same size of MD box as the 25% CO_2 in 6FDA-6FpDA system having first removed the polymer. As might be expected from the restricted space available to the CO_2 molecules in

the polymer plus CO_2 system, the percentage of single CO_2 molecules in the polymer phase is less than that in the gas phase. However, there is no obvious formation of large clusters which suggests that the CO_2 molecules tend to rest apart even in the polymer phase. Similar cluster distributions were found in other two polyimides under study. This also supported by the results for the potential energy which show a fairly feeble contribution of CO_2···CO_2 interactions to the total potential energy.

5 Carbon dioxide unloading from polyimides

The effect of penetrant-induced hysteresis (conditioning) under various CO_2 feed pressures has been reported in the literature for the 6FDA-6FpDA and 6FDA-6FmDA polyimides.[41,42] In these real experiments the conditioning was carried out at different gas pressures, upto ~60 bar, and for times of 2-3 weeks; such long times being necessary to attain "steady state" where permeabilities changed less than 0.5% per day. The experiments reveal that the significant increases in permeability after conditioning are due to increases in solubility and diffusivity, with the latter being the major cause due to enhancements caused by the volume relaxations and polymer chain mobilities.[41,42] Even though it is impossible to study the effects of such a long term conditioning, given current limitations of MD simulations, it is still nevertheless interesting to check the immediate effect of exposure to high concentrations of CO_2 in polymers. As explained in Section 2.6, unloading curves were produced in a similar manner to the loading curves this time by stepwise removal of the CO_2 molecules from systems exposed to a pressure of ~60 bar. Just one system for each type of polyimide was studied in this way.

Tables 5-7 show the nominal and true solubility of CO_2 calculated from the iterative and TPI procedures. The comparable values obtained between iterative and TPI solubilities once again confirms the reliability of the former procedure. Figure 12 shows a comparison of the nominal solubility vs. pressure curves for the sorption and desorption isotherms in the case of 6FDA-DAM. On the log-log scale of Figure 12 only a slight tendency for an increase in solubility is observed during desorption. The trend is the same in the other two polyimides (plots not shown) but differences are even less. This is not to say that there are no immediate conditioning effects when the polymer membrane is exposed to high pressure

of CO_2. There are compensating changes taking place which mean that the nominal solubility vs. pressure curves are not the best way to reveal them. To demonstrate this the volume contractions during desorption were also calculated directly from the volume of the MD simulation boxes. Figure 13 shows the volume dilations and contractions relative to the original pure polyimide systems, i.e. prior to any sorption of CO_2, as a function of nominal concentration of CO_2. The differences between dilation and contraction curves can be explained by the volume relaxations induced by the higher concentrations of CO_2.[79,135]. From Figure 13 it is clear that the 6FDA-DAM has the least amount of volume contraction as it shows almost 7% volume change at the end of complete desorption of CO_2, whereas the 6FDA-6FpDA and 6FDA-6FmDA exhibit close to 2.5 and 4% induced volume changes, respectively.

Table 5. Desorption isotherm MD simulations at 308 K on 6FDA-6FpDA. The approximate mass percentages of CO_2 are given as obtained from the actual number of molecules inserted into the polymers. The corresponding true and nominal concentrations of gas in the polymer are shown in units of cm^3(STP) cm^{-3} of polymer (true or pure polymer volume). The pressure given is that estimated to be the equilibrium external vapour pressure of CO_2 which would have to be applied to give the imposed concentrations of CO_2 in the polymer. The true and nominal solubility coefficients are given as well as the solubility coefficient estimated from the EVMS test particle insertion analysis (Eq. 10 or 11) in units of cm^3(STP) cm^{-3} bar^{-1}.

~% CO_2	Number of CO_2	True Concn. $\frac{V_g^{STP}(P)}{V(P)}$	Nominal Concn. $\frac{V_g^{STP}(P)}{V_0}$	P / bar	True Solubility $\frac{C(P)}{P}$	Nominal Solubility $\frac{C_0(P)}{P}$	TPI Solubility
24.33	616	184.23	163.22	45.70	3.57	4.03	3.36
23	582	174.07	153.12	37.20	4.12	4.68	3.99
21	531	158.81	142.41	23.75	6.00	6.69	5.85
19	481	143.86	131.64	17.20	7.65	8.36	7.68
17	430	128.60	119.91	11.40	10.52	11.28	10.62
15	380	113.65	107.41	6.15	17.46	18.48	17.01
11	278	83.14	80.88	2.75	29.41	30.23	27.95
7	177	52.94	52.34	1.20	43.61	44.11	46.17
5	127	37.98	37.86	0.60	63.11	63.31	64.31
3	76	22.73	22.68	0.23	98.63	98.83	95.69
1	25	7.48	7.48	0.07	115.04	115.03	117.32
0	0	0.00	0.00	-	-	-	137.63

Table 6. As Table 5 for 6FDA-6FmDA.

~% CO_2	Number of CO_2	True Concn. $\frac{V_g^{STP}(P)}{V(P)}$	Nominal Concn. $\frac{V_g^{STP}(P)}{V_0}$	P / bar	True Solubility $\frac{C(P)}{P}$	Nominal Solubility $\frac{C_0(P)}{P}$	TPI Solubility
23	582	176.00	153.63	42.00	3.66	4.19	4.33
21	531	160.58	140.31	38.90	3.61	4.13	4.79
19	481	145.46	131.65	25.80	5.10	5.64	5.61
17	430	130.03	119.52	16.10	7.42	8.08	8.08
15	380	114.91	107.30	10.25	10.47	11.21	10.81
11	278	84.07	81.06	3.30	24.56	25.48	24.51
7	177	53.53	52.74	1.15	45.86	46.54	44.56
5	127	38.41	38.05	0.55	69.18	69.83	70.02
3	76	22.98	22.92	0.26	88.17	88.39	84.53
1	25	7.56	7.53	0.07	109.19	109.57	109.93
0	0	0.00	0.00	-	-	-	127.68

Table 7 As Table 5 for 6FDA-DAM.

~% CO_2	Number of CO_2	True Concn. $\frac{V_g^{STP}(P)}{V(P)}$	Nominal Concn. $\frac{V_g^{STP}(P)}{V_0}$	P / bar	True Solubility $\frac{C(P)}{P}$	Nominal Solubility $\frac{C_0(P)}{P}$	TPI Solubility
31	589	209.27	176.15	74.15	2.38	2.82	1.36
29	551	195.77	165.99	43.80	3.79	4.47	2.85
27	513	182.27	155.57	31.00	5.02	5.88	5.72
25	475	168.76	145.82	21.95	6.64	7.69	5.84
23	437	155.26	135.73	12.28	11.05	12.64	10.52
21	399	141.76	124.90	9.95	12.55	14.25	11.63
19	361	128.26	113.36	5.39	21.03	23.80	19.58
17	323	114.76	102.81	5.01	20.52	22.91	19.10
15	285	101.26	92.56	4.20	22.06	24.14	20.69
11	209	74.26	68.48	1.93	35.48	38.47	33.20
7	133	46.90	44.25	0.74	60.21	63.81	51.22
5	95	33.75	31.62	0.43	73.54	78.49	69.01
3	57	19.90	18.97	0.20	96.81	101.51	90.52
1	19	6.75	6.33	0.05	126.55	135.01	123.26
0	0	0.00	0.00	-0	-	-	147.59

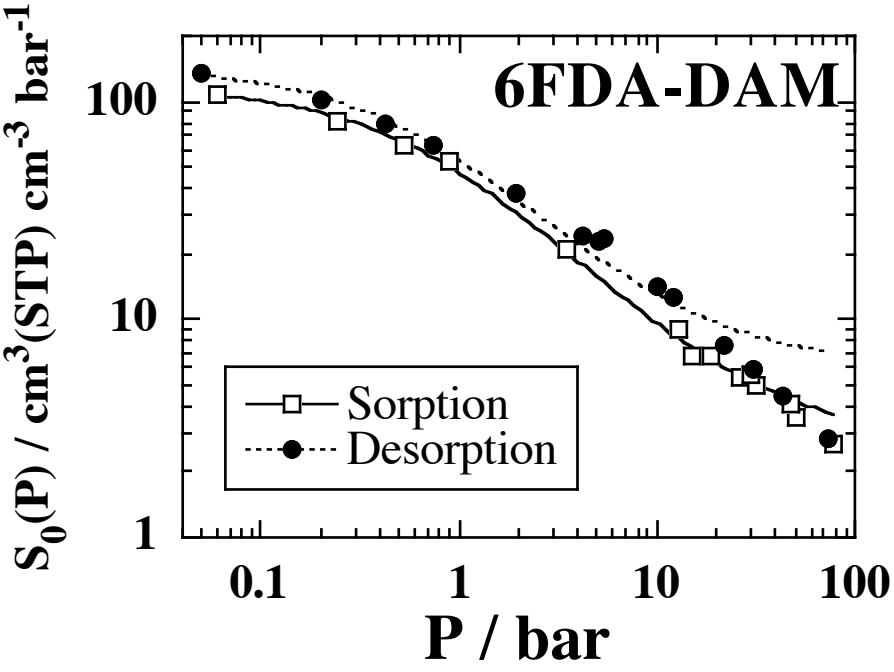

Figure 12 A comparison of CO_2 sorption and desorption isotherms obtained from just one sample of 6FDA-DAM at 308 K. The solubility coefficients are plotted as a function of nominal concentrations of carbon dioxide (Eq. 9) on a log-log scale. Lines are non-linear least squares regression fits to the solubility form of the dual mode sorption model (Eq. 12).

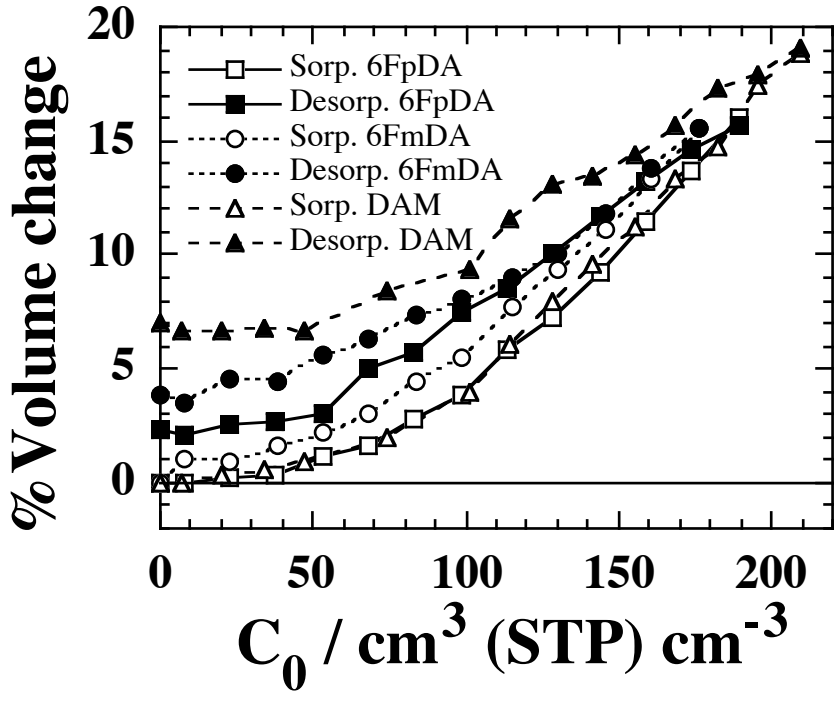

Figure 13 A comparison of volume swelling during sorption (open symbols) and volume contraction during desorption (filled symbols) for all three polyimides at 308 K as obtained from the simulations reported here. The percentage volume change relative to the original pure polyimide systems prior to the sorption of CO_2 are plotted as a function of nominal concentrations of carbon dioxide (Eq. 9).

Conclusion

MD simulation techniques have been successfully used to obtain sorption isotherms of CO_2 in three different polyimides:- 6FDA-6FpDA, 6FDA-6FmDA and 6FDA-DAM. For the first time, a simple iterative technique to obtain the sorption isotherm[94] has been applied to realistic models of polyimides. The method is robust and converges rapidly and both CO_2 loading and unloading curves were obtained. An excluded volume map sampling test particle insertion technique was found to be an efficient method to calculate the excess chemical potentials required for the iterative approach.

Although the solubilities in the infinite dilution limit predicted from the simulations were found to be significantly higher than those extrapolated to zero pressure from experimental data, at pressures of 10 bar the predicted solubilities are within a factor of 2 of the experimental results. The simulations also reproduce the experimental order in the solubilities of the three polyimides but the two structural isomers, 6FDA-6FpDA and 6FDA-6FmDA, are closer in behaviour than is found in reality. Explanations for the overestimation of infinite dilution solubilities in terms of the details of the potential models were sought but none of those tested could account for the discrepancies. In particular, the considerably higher solubilities obtained using a united-atom models of CO_2 suggest that this purely spherical representation of CO_2 is poorly adapted for such studies.

All three polyimides swell significantly and homogeneously during CO_2 sorption. There is no evidence to suggest that large clusters of CO_2 form even at the highest concentrations. Initial gas uptake causes little volume expansion, i.e. consistent with a hole-filling mechanism, but thereafter there is a gradual transition to an almost linear increase in volume at higher concentrations. These results were consistent with the determinations of the probe accessible volumes. Where comparisons with swelling in experimental systems were available, significant swelling in the models started at higher concentrations and so was less consequent when comapred at same concentration of CO_2.

Analysis of the changes in the contributions to the total potential energy reveal that the interactions between the polymer and the carbon dioxide are largely responsible for the change. Other contributions exist but tend to cancel out. The excess molar enthalpies and excess molar chemical potentials show trends with increased concentration consistent with a progression from a pure polyimide system to a pure dense CO_2 system. The associated excess molar enthalpy also shows trends consistent with an initial hole-filling behaviour followed by increased volume swelling. The Boltzmann factor weighted probability density distributions for the trial insertion energies show a single-Gaussian like peak. Although this could be thought to be supportive of the site-distribution model, rather than the dual

sorption model, there is no evidence to suggest that the lower energy microvoids are filled preferentially. Indeed the weighted distributions remain Gaussian-like and diminish homogeneously with concentration.

Immediate desorption following sorption leads to relatively small increases in the solubilities compared to those obtained in the laboratory through very long conditioning protocols. However, the models do predict significant changes in volume of the pure polymers following complete outgassing of the samples.

Acknowledgments

The CCRT, IDRIS and CINES national supercomputing centres in France, the MUST cluster at the University of Savoie (France) and the MPIP (Germany) are acknowledged for their generous provision of computer time. SP is deeply grateful to the *Assemblée des Pays de Savoie* and to the MPIP for the award of a doctoral research grant as well as to the *Région Rhône-Alpes* for the award of a travel grant.

Annex

The chemical potential at a certain higher pressure, P', can always be obtained by integration along an isotherm[95]

$$\mu(P',T) = \mu(P_{low},T) + \int_{P_{low}}^{P'} \left(\frac{\partial \mu}{\partial P}\right)_T dP \tag{A1}$$

where P_{low} is some reference "low" pressure and $\mu(P_{low},T)$ the corresponding chemical potential. The partial derivative of the chemical potential with respect to pressure at constant temperature is just $1/\rho = V/N$.[95] So we can write

$$\mu(P',T) = \mu(P_{low},T) + \int_{P_{low}}^{P'} \frac{V(P,T)}{N} dP \tag{A2}$$

Adding and subtracting a term kT/P, corresponding to the volume of the ideal gas divided by N, to the integral gives

$$\begin{aligned}
\mu(P',T) &= \mu(P_{low},T) + \int_{P_{low}}^{P'} \frac{V(P,T)}{N} - \frac{kT}{P} + \frac{kT}{P} dP \\
&= \mu(P_{low},T) + \int_{P_{low}}^{P'} \frac{V(P,T)}{N} - \frac{V^{ig}(P,T)}{N} dP + \int_{P_{low}}^{P'} \frac{kT}{P} dP \\
&= \mu(P_{low},T) + \int_{P_{low}}^{P'} \frac{V(P,T)}{N} - \frac{V^{ig}(P,T)}{N} dP + kT\left[\ln P\right]_{P_{low}}^{P'} \\
&= \mu(P_{low},T) + kT \ln \frac{P'}{P_{low}} + \frac{1}{N} \int_{P_{low}}^{P'} V(P,T) - V^{ig}(P,T)\, dP
\end{aligned} \tag{A3}$$

To obtain the chemical potential at the low pressure we use the standard statistical mechanics expression for the total chemical potential in the NPT ensemble[95,97]

$$\mu = kT \ln \frac{\rho \Lambda^3}{q} - kT \ln \frac{\left\langle V \exp\left(\frac{-\Delta U}{kT}\right)\right\rangle}{\langle V \rangle} = \mu_{id} + \mu_{ex} \tag{A4}$$

where q is the partition function for internal degrees of freedom and Λ is the de Broglie wavelength defined as:

$$\Lambda = \left(\frac{h^2}{2\pi m k_B T} \right)^{\frac{1}{2}} \tag{A5}$$

with h being Planck's constant and where it is understood that the number density $\rho = \frac{N}{\langle V \rangle} \approx \frac{N+1}{\langle V \rangle}$ is that corresponding to the applied conditions of P and T, i.e. ρ=ρ(P,T). Now for the reference state we choose a pressure *sufficiently low* that the ideal gas law holds then the chemical potential is well approximated by the first term in Eq. A4 and thus

$$\mu(P_{low},T) \approx kT \ln\left[\frac{\rho(P_{low},T)\Lambda^3}{q} \right] \approx kT \ln\left[\frac{P_{low}\Lambda^3}{qkT} \right] \tag{A6}$$

Eq. A3 can then be written as

$$\begin{aligned} \mu(P',T) &= kT \ln\left[\frac{P_{low}\Lambda^3}{qkT} \right] + kT \ln \frac{P'}{P_{low}} + \frac{1}{N} \int_{P_{low}}^{P'} V(P,T) - V^{ig}(P,T)\, dP \\ &= kT \ln\left[\frac{P_{low}\Lambda^3}{qkT} \right] + kT \ln \frac{P'}{P_{low}} + \frac{1}{N} \int_{P_{low}}^{P'} V(P,T) - V^{ig}(P,T)\, dP \\ &= kT \ln\left[\frac{P'\Lambda^3}{qkT} \right] + \frac{1}{N} \int_{P_{low}}^{P'} V(P,T) - V^{ig}(P,T)\, dP \\ &= kT \ln\left[\frac{\rho^{ig}(P',T)\Lambda^3}{q} \right] + \frac{1}{N} \int_{P_{low}}^{P'} V(P,T) - V^{ig}(P,T)\, dP \end{aligned} \tag{A7}$$

where we recognize that the term $\frac{P'}{kT}$ is just the number density of the ideal gas, $\rho^{ig}(P',T)$. Now adding and subtracting a term of $kT \ln \rho(P',T)$ gives

$$\begin{aligned} \mu(P',T) &= kT \ln\left[\frac{\rho^{ig}(P',T)\Lambda^3}{q} \right] - kT \ln \rho(P',T) + kT \ln \rho(P',T) + \frac{1}{N} \int_{P_{low}}^{P'} V(P,T) - V^{ig}(P,T)\, dP \\ &= kT \ln\left[\frac{\rho(P',T)\Lambda^3}{q} \right] - kT \ln\left[\frac{\rho(P',T)}{\rho^{ig}(P',T)} \right] + \frac{1}{N} \int_{P_{low}}^{P'} V(P,T) - V^{ig}(P,T)\, dP \end{aligned} \tag{A8}$$

It follows then that the excess chemical potential, *as defined by Eq. A4*, is given by

$$\mu_{ex} = -kT \ln\left[\frac{\rho(P',T)}{\rho^{ig}(P',T)}\right] + \frac{1}{N}\int_{P_{low}}^{P'} V(P,T) - V^{ig}(P,T)\, dP \qquad \text{(A9)}$$

References

(1) Forster, P.; Ramaswamy, V.; Artaxo, P.; Berntsen, T.; Betts, R.; Fahey, D. W.; Haywood, J.; Lean, J.; Lowe, D. C.; Myhre, G.; Nganga, J.; Prinn, R.; Raga, G.; Schulz, M.; Van Dorland, R., *Changes in Atmospheric Constituents and in Radiative Forcing. In: Climate Change 2007: The Physical Science Basis. Contribution of Working Group I to the Fourth Assessment Report of the Intergovernmental Panel on climate Change*. Cambridge University Press: Cambridge, United Kingdom and New York, NY, USA, 2007.

(2) Sarkar, S. C.; Bose, A. *Energy Conversion and Management* **1997,** 38 (*Supplement 1*), S105-S110.

(3) Ishibashi, M.; Ota, H.; Akutsu, N.; Umeda, S.; Tajika, M.; Izumi, J.; Yasutake, A.; Kabata, T.; Kageyama, Y. *Energy Conversion and Management* **1996,** 37 (*6-8*), 929-933.

(4) Kikkinides, E. S.; Yang, R. T.; Cho, S. H. *Industrial & Engineering Chemistry Research* **1993,** 32 (*11*), 2714-2720.

(5) Cavenati, S.; Grande, C. A.; Rodrigues, A. E. *Energy & Fuels* **2006,** 20 (*6*), 2648-2659.

(6) Ohta, H.; Umeda, S.; Tajika, M.; Nishimura, M.; Yamada, M.; Yasutake, A.; Izumi, J. *International Journal of Global Energy Issues* **1998,** 11 (*1*), 203-210.

(7) Gray, P. G. *Gas Separation & Purification* **1993,** 7 (*4*), 213-224.

(8) Knoblauch, K. *Gas Separation & Purification* **1993,** 7 (*4*), 195-196.

(9) Al-Marzouqi, M.; El-Naas, M.; Marzouk, S.; Abdullatif, N. *Separation and Purification Technology* **2008,** 62 (*3*), 499-506.

(10) Satyapal, S.; Filburn, T.; Trela, J.; Strange, J. *Energy & Fuels* **2001,** 15 (*2*), 250-255.

(11) Chakma, A. *Energy Conversion and Management* **1997,** 38 (*Supplement 1*), S205-S209.

(12) Lackner, K. S.; Butt, D. P.; Wendt, C. H. *Energy Conversion and Management* **1997,** 38 (*Supplement 1*), S259-S264.

(13) Gottlicher, G.; Pruschek, R. *Energy Conversion and Management* **1997,** 38 (*Supplement 1*), S173-S178.

(14) Gaudernack, B.; Lynum, S. *Energy Conversion and Management* **1997,** 38 (*Supplement 1*), S165-S172.

(15) Meratla, Z. *Energy Conversion and Management* **1997,** 38 (*Supplement 1*), S147-S152.

(16) Jody, B. J.; Daniels, E. J.; Wolsky, A. M. *Energy Conversion and Management* **1997,** 38 (*Supplement 1*), S135-S140.

(17) Pino, J. A.; Garcia, J.; Martinez, M. A. *Journal of Essential Oil Research* **1996,** 8 (*4*), 373.

(18) Gadalla, M.; Olujie, Z.; De Rijke, A.; Jansens, P. J. *Energy Oxford* **2006,** 31 (*13*), 2073.

(19) Nakabayashi, M.; Okabe, K.; Fujisawa, E.; Hirayama, Y.; Kazama, S.; Matsumiya, N.; Takagi, K.; Mano, H.; Haraya, K.; Kamizawa, C. *Energy Conversion and Management* **1995,** 36 (*6-9*), 419-422.

(20) Hiarayama, Y.; Kazama, S.; Fujisawa, E.; Nakabayashi, M.; Matsumiya, N.; Takagi, K.; Okabe, K.; Mano, H.; Haraya, K.; Kamizawa, C. *Energy Conversion and Management* **1995,** 36 (*6-9*), 435-438.

(21) Okabe, K.; Matsumiya, N.; Mano, H. *Separation and Purification Technology* **2007,** 57 (*2*), 242-249.

(22) Chung, S. J.; Park, J. H.; Li, D.; Ida, J. I.; Kumakiri, I.; Lin, J. Y. S. *Industrial & Engineering Chemistry Research* **2005,** 44 (*21*), 7999-8006.

(23) Xomeritakis, G.; Tsai, C.-Y.; Brinker, C. J. *Separation and Purification Technology* **2005,** 42 (*3*), 249-257.

(24) Sada, E.; Kumazawa, H.; Wang, J. S.; Koizumi, M. *Journal of Applied Polymer Science* **1992,** 45 (*12*), 2181-2186.

(25) Sridhar, S.; Veerapur, R. S.; Patil, M. B.; Gudasi, K. B.; Aminabhavi, T. M. *Journal of Applied Polymer Science* **2007,** 106 (*3*), 1585-1594.

(26) Rhim, J.-W.; Chowdhury, G.; Takeshi, M. *Journal of Applied Polymer Science* **2000,** 76 (*5*), 735-742.

(27) Hillock, A. M. W.; Koros, W. J. *Macromolecules* **2007,** 40 (*3*), 583-587.

(28) Pesiri, D. R.; Jorgensen, B.; Dye, R. C. *Journal of Membrane Science* **2003,** 218 (*1-2*), 11-18.

(29) Baker, R. W. *Industrial & Engineering Chemistry Research* **2002,** 41 (*6*), 1393-1411.

(30) Pandey, P.; Chauhan, R. S. *Progress in Polymer Science* **2001,** 26 (*6*), 853-893.

(31) Tanaka, K.; Okamoto, K.-I., Structure and Transport Properties of Polyimides as Materials for Gas and Vapor Membrane Separation. In *Materials Science of Membranes for Gas and Vapour Separation*, Yampolskii, Y. P.; Pinnau, I.; Freeman, B. D., Eds. John Wiley & Sons Ltd.: Hoboken, N.J., USA, 2006; p 445.

(32) Favre, E. *Journal of Membrane Science* **2004,** 229 (*1-2*), 241-242.

(33) Wijmans, J. G.; Baker, R. W. *Journal of Membrane Science* **1995,** 107 (*1-2*), 1-21.

(34) Paul, D. R. *Separation & Purification Reviews* **1976,** 5 (*1*), 33 - 50.

(35) Lonsdale, H. K. *Journal of Membrane Science* **1982,** 10 (*2-3*), 81-181.

(36) Koros, W. J.; Fleming, G. K. *Journal of Membrane Science* **1993,** 83 (*1*), 1-80.

(37) Koros, W. J.; Mahajan, R. *Journal of Membrane Science* **2000,** 175 (*2*), 181-196.

(38) Bos, A.; Pünt, I. G. M.; Wessling, M.; Strathmann, H. *Journal of Membrane Science* **1999,** 155 (*1*), 67-78.

(39) Shimazu, A.; Tukasa, M.; Shigeru, K.; Yasuo, I. *Journal of Polymer Science Part B: Polymer Physics* **2003,** 41 (*3*), 308-318.

(40) Coleman, M. R.; Koros, W. J. *Journal of Polymer Science Part B: Polymer Physics* **1994,** 32 (*11*), 1915-1926.

(41) Coleman, M. R.; Koros, W. J. *Macromolecules* **1997,** 30 (*22*), 6899-6905.

(42) Coleman, M. R.; Koros, W. J. *Macromolecules* **1999,** 32 (*9*), 3106-3113.

(43) Recio, R.; Palacio, L.; Pradanos, P.; Hernandez, A.; Lozano, A. E.; Marcos, A.; de la Campa, J. G.; de Abajo, J. *Journal of Membrane Science* **2007,** 293 (*1-2*), 22-28.

(44) Fuhrman, C.; Nutt, M.; Vichtovonga, K.; Coleman, M. R. *Journal of Applied Polymer Science* **2004,** 91 (*2*), 1174-1182.

(45) Wind, J. D.; Sirard, S. M.; Paul, D. R.; Green, P. F.; Johnston, K. P.; Koros, W. J. *Macromolecules* **2003,** 36 (*17*), 6433-6441.

(46) Pfromm, P. H.; Koros, W. J. *Polymer* **1995,** 36 (*12*), 2379-2387.

(47) Kim, J. H.; Koros, W. J.; Paul, D. R. *Polymer* **2006,** 47 (*9*), 3104-3111.

(48) Wang, R.; Cao, C.; Chung, T.-S. *Journal of Membrane Science* **2002,** 198 (*2*), 259-271.

(49) Kim, K. J.; So, W.-W.; Moon, S. J., *Preparation of 6FDA-based polyimide membranes for CO2 gas separation*. 2004; Vol. 153, p 531-534.

(50) Kim, J. H.; Koros, W. J.; Paul, D. R. *Journal of Membrane Science* **2006,** 282 (*1-2*), 21-31.

(51) Kim, J. H.; Koros, W. J.; Paul, D. R. *Journal of Membrane Science* **2006,** 282 (*1-2*), 32-43.

(52) Kim, J. H.; Koros, W. J.; Paul, D. R. *Polymer* **2006,** 47 (*9*), 3094-3103.

(53) Kim, K. J.; Park, S.-H.; So, W.-W.; Ahn, D.-J.; Moon, S.-J. *Journal of Membrane Science* **2003,** 211 (*1*), 41-49.

(54) Kim, T.-H.; Koros, W. J.; Husk, G. R. *Separation Science and Technology* **1988,** 23 (*12*), 1611 - 1626.

(55) Ye, L.; Pan, C.; Ding, M.; Xu, J. *Polymer International* **1999,** 48 (*9*), 832-836.

(56) Staudt-Bickel, C.; Koros, W. J. *Journal of Membrane Science* **1999,** 155 (*1*), 145-154.

(57) Staudt-Bickel, C.; Koros, W. J. *Journal of Membrane Science* **2000,** 170 (*2*), 205-214.

(58) Wind, J. D.; Paul, D. R.; Koros, W. J. *Journal of Membrane Science* **2004,** 228 (*2*), 227-236.

(59) Hibshman, C.; Mager, M.; Marand, E. *Journal of Membrane Science* **2004,** 229 (*1-2*), 73-80.

(60) Yoshino, M.; Nakamura, S.; Kita, H.; Okamoto, K.-I.; Tanihara, N.; Kusuki, Y. *Journal of Membrane Science* **2003,** 212 (*1-2*), 13-27.

(61) Shimazu, A.; Miyazaki, T.; Ikeda, K. *Journal of Membrane Science* **2000,** 166 (*1*), 113-118.

(62) Heuchel, M.; Hofmann, D.; Pullumbi, P. *Macromolecules* **2004,** 37 (*1*), 201-214.

(63) Tanaka, K.; Kawai, T.; Kita, H.; Okamoto, K.-I.; Ito, Y. *Macromolecules* **2000,** 33 (*15*), 5513-5517.

(64) Kawakami, H.; Nakajima, K.; Shimizu, H.; Nagaoka, S. *Journal of Membrane Science* **2003,** 212 (*1-2*), 195-203.

(65) Iwase, M.; Sannomiya, A.; Nagaoka, S.; Suzuki, Y.; Iwaki, M.; Kawakami, H. *Macromolecules* **2004,** 37 (*18*), 6892-6897.

(66) Koron, A. *Kobunshi Ronchibunshu* **1994,** 51 (*4*), 251-257.

(67) Fried, J. R.; Hu, N. *Polymer* **2003,** 44 (*15*), 4363-4372.

(68) Tanaka, K.; Taguchi, A.; Hao, J.; Kita, H.; Okamoto, K.-I. *Journal of Membrane Science* **1996,** 121 (*2*), 197-207.

(69) Matsui, S.; Sato, H.; Nakagawa, T. *Journal of Membrane Science* **1998,** 141 (*1*), 31-43.

(70) Islam, M. N.; Zhou, W.; Honda, T.; Tanaka, K.; Kita, H.; Okamoto, K.-I. *Journal of Membrane Science* **2005,** 261 (*1-2*), 17-26.

(71) Tanaka, K.; Masaaki, O.; Hiroyuki, T.; Hidetoshi, K.; Okamoto, K.-I. *Journal of Polymer Science Part B: Polymer Physics* **1992,** 30 (*8*), 907-914.

(72) Brown, D.; Clarke, J. H. R.; Okuda, M.; Yamazaki, T. *The Journal of Chemical Physics* **1994,** 100 (*8*), 6011-6018.

(73) Pandiyan, S.; Brown, D.; van der Vegt, N. F. A.; Neyertz, S. *Journal of Polymer Science Part B: Polymer Physics* **2009,** 47 (*12*), 1166-1180.

(74) Tanaka, K.; Kita, H.; Okamoto, K.-I. *Journal of Polymer Science Part B: Polymer Physics* **1993,** 31 (*9*), 1127-1133.

(75) Cornelius, C. J.; Marand, E. *Journal of Membrane Science* **2002,** 202 (*1-2*), 97-118.

(76) Matsumoto, K.; Xu, P.; Nishikimi, T. *Journal of Membrane Science* **1993,** 81 (*1-2*), 15-22.

(77) in `t Veld, P. J.; Stone, M. T.; Truskett, T. M.; Sanchez, I. C. *The Journal of Physical Chemistry B* **2000,** 104 (*50*), 12028-12034.

(78) Wang, X.-Y.; in 't Veld, P. J.; Lu, Y.; Freeman, B. D.; Sanchez, I. C. *Polymer* **2005,** 46 (*21*), 9155-9161.

(79) Hölck, O.; Heuchel, M.; Böhning, M.; Hofmann, D. *Journal of Polymer Science Part B: Polymer Physics* **2008,** 46 (*1*), 59-71.

(80) McKechnie, J. I.; Brown, D.; Clarke, J. H. R. *Macromolecules* **1992,** 25 (*5*), 1562-1567.

(81) Costello, L. M.; Koros, W. J. *Journal of Polymer Science Part B: Polymer Physics* **1995,** 33 (*1*), 135-146.

(82) Singh-Ghosal, A.; Koros, W. J. *Industrial & Engineering Chemistry Research* **1999,** 38 (*10*), 3647-3654.

(83) Hibshman, C.; Cornelius, C. J.; Marand, E. *Journal of Membrane Science* **2003,** 211 (*1*), 25-40.

(84) Pechar, T. W.; Kim, S.; Vaughan, B.; Marand, E.; Tsapatsis, M.; Jeong, H. K.; Cornelius, C. J. *Journal of Membrane Science* **2006,** 277 (*1-2*), 195-202.

(85) Wessling, M.; Huisman, I.; Boomgaard, T. v. d.; Smolders, C. A. *Journal of Polymer Science Part B: Polymer Physics* **1995,** 33 (*9*), 1371-1384.

(86) Duthie, X.; Kentish, S.; Powell, C.; Nagai, K.; Qiao, G.; Stevens, G. *Journal of Membrane Science* **2007,** 294 (*1-2*), 40-49.

(87) Thundyil, M. J.; Jois, Y. H.; Koros, W. J. *Journal of Membrane Science* **1999,** 152 (*1*), 29-40.

(88) Chung, T. S.; Cao, C.; Wang, R. *Journal of Polymer Science Part B: Polymer Physics* **2004,** 42 (*2*), 354-364.

(89) Pechar, T. W.; Kim, S.; Vaughan, B.; Marand, E.; Baranauskas, V.; Riffle, J.; Jeong, H. K.; Tsapatsis, M. *Journal of Membrane Science* **2006,** 277 (*1-2*), 210-218.

(90) Niwa, M.; Kawakami, H.; Kanamori, T.; Shinbo, T.; Kaito, A.; Nagaoka, S. *Macromolecules* **2001,** 34 (*26*), 9039-9044.

(91) Yeom, C. K.; Lee, J. M.; Hong, Y. T.; Choi, K. Y.; Kim, S. C. *Journal of Membrane Science* **2000,** 166 (*1*), 71-83.

(92) Shimazu, A.; Tsukasa, M.; Masatoshi, M.; Kenichi, I. *Journal of Polymer Science Part B: Polymer Physics* **2000,** 38 (*19*), 2525-2536.

(93) Neyertz, S.; Douanne, A.; Brown, D. *Journal of Membrane Science* **2006,** 280 (*1-2*), 517-529.

(94) van der Vegt, N. F. A.; Briels, W. J.; Wessling, M.; Strathmann, H. *The Journal of Chemical Physics* **1999,** 110 (*22*), 11061-11069.

(95) Ben-Naim, A., *Molecular Theory of Solutions*. Oxford University Press: Oxford, UK, 2006; p 400.

(96) Ben-Naim, A.; Marcus, Y. *The Journal of Chemical Physics* **1984,** 81 (*4*), 2016-2027.

(97) Frenkel, D.; Smit, B., *Understanding molecular simulation: from algorithms to applications*. Academic Press Inc.: San Diego, 1996.

(98) Brown, D. *The gmq User Manual Version 4*, 2008. Available at http://www.lmops.univ-savoie.fr/brown/gmq.html

(99) Clark, M.; Cramer III, R. D.; van Opdenbosch, N. *Journal of Computational Chemistry* **1989,** 10 (*8*), 982-1012.

(100) Frisch, M. J.; Trucks, G. W.; Schlegel, H. B.; Scuseria, G. E.; Robb, M. A.; Cheeseman, J. R.; Montgomery, J. A.; Vreven, J., T. ; Kudin, K. N.; Burant, J. C.; Millam, J. M.; Iyengar, S. S.; Tomasi, J.; Barone, V.; Mennucci, B.; Cossi, M.; Scalmani, G.; Rega, N.; Petersson, G. A.; Nakatsuji, H.; Hada, M.; Ehara, M.; Toyota, K.; Fukuda, R.; Hasegawa, J.; Ishida, M.; Nakajima, T.; Honda, Y.; Kitao, O.; Nakai, H.; Klene, M.; Li, X.; Knox, J. E.; Hratchian, H. P.; Cross, J. B.; Bakken, V.; Adamo, C.; Jaramillo, J.; Gomperts, R.; Stratmann, R. E.; Yazyev, O.; Austin, A. J.; Cammi, R.; Pomelli, C.; Ochterski, J. W.; Ayala, P. Y.; Morokuma, K.; Voth, G. A.; Salvador, P.; Dannenberg, J. J.; Zakrzewski, V. G.; Dapprich, S.; Daniels, A. D.; Strain, M. C.; Farkas, O.; Malick, D. K.; Rabuck, A. D.; Raghavachari, K.; Foresman, J. B.; Ortiz, J. V.; Cui, Q.; Baboul, A. G.; Clifford, S.; Cioslowski, J.; Stefanov, B. B.; Liu, G.; Liashenko, A.; Piskorz, P.; Komaromi, I.; Martin, R. L.; Fox, D. J.; Keith, T.; Al-Laham, M. A.; Peng, C. Y.; Nanayakkara, A.; Challacombe, M. P.; Gill, M. W.; Johnson, B.; Chen, W.; Wong, M. W.; Gonzalez, C.; Pople, J. A. *Gaussian 03*, Gaussian Inc.: Wallingford CT, 2004. Gaussian Inc., Wallingford CT

(101) Zhang, Z.; Duan, Z. *The Journal of Chemical Physics* **2005,** 122 (*21*), 214507.

(102) Hammonds, K. D.; Ryckaert, J.-P. *Computer Physics Communications* **1991,** 62 (*2-3*), 336-351.

(103) Ciccotti, G.; Ferrario, M.; Ryckaert, J. P. *Molecular Physics* **1982,** 47 (*6*), 1253 - 1264.

(104) Babarao, R.; Jiang, J. *Langmuir* **2008,** 24 (*10*), 5474-5484.

(105) Milano, G.; Guerra, G.; Müller-Plathe, F. *Chemistry of Materials* **2002,** 14 (*7*), 2977-2982.

(106) Müller-Plathe, F. *The Journal of Chemical Physics* **1995,** 103 (*10*), 4346-4351.

(107) Brown, D.; Clarke, J. H. R. *Computer Physics Communications* **1991,** 62 (*2-3*), 360-369.

(108) Berendsen, H. J. C.; Postma, J. P. M.; van Gunsteren, W. F.; DiNola, A.; Haak, J. R. *The Journal of Chemical Physics* **1984,** 81 (*8*), 3684-3690.

(109) Ewald, P. P. *Annal of Physics* **1921,** 64, 253-287.

(110) Brown, D.; Neyertz, S. *Mol. Phys.* **1995,** 84 (*3*), 577-595.

(111) Span, R.; Wagner, W. *J. Phys. Chem. Ref. Data* **1996,** 25, 1509-1596.

(112) Deitrick, G. L.; Scriven, L. E.; Davis, H. T. *The Journal of Chemical Physics* **1989,** 90 (*4*), 2370-2385.

(113) Domotor, G.; Hentschke, R. *The Journal of Physical Chemistry B* **2004,** 108 (*7*), 2413-2417.

(114) Bondar, V. I.; Kamiya, Y.; Yampolskii, Y. P. *J. Polym. Sci.: Part B: Polym. Phys.* **1996,** 34, 369-378.

(115) Wind, J. D.; Staudt-Bickel, C.; Paul, D. R.; Koros, W. J. *Macromolecules* **2003,** 36 (*6*), 1882-1888.

(116) Iwai, Y.; Higashi, H.; Uchida, H.; Arai, Y. *Fluid Phase Equilibria* **1997,** 127 (*1-2*), 251-261.

(117) Waldman, M.; Hagler, A. T. *Journal of Computational Chemistry* **1993,** 14 (*9*), 1077-1084.

(118) Neyertz, S. *Macromolecular Theory & Simulation* **2007,** 16 (*5*), 513–524.

(119) Buckingham, A. D.; Disch, R. L. *Proceedings of the Royal Society of London. Series A, Mathematical and Physical Sciences* **1963,** 273 (*1353*), 275-289.

(120) Stannet, V. T.; Koros, W. J.; Paul, D. R.; Lonsdale, H. K.; Baker, R. W. *Advances in Polymer Science* **1979,** 32, 69.

(121) Joly, C.; Le Cerf, D.; Chappey, C.; Langevin, D.; Muller, G. *Separation and Purification Technology* **1999,** 16 (*1*), 47-54.

(122) Chang, K.-S.; Hsiung, C.-C.; Lin, C.-C.; Tung, K.-L. *The Journal of Physical Chemistry B* **2009**.

(123) Fu, Y.-J.; Hu, C.-C.; Qui, H.-Z.; Lee, K.-R.; Lai, J.-Y. *Separation and Purification Technology* **2008,** 62 (*1*), 175-182.

(124) Pfromm, P. H., The Impact of Physical Aging of Amorphous Glassy Polymers on Gas Separation Membranes. In *Materials Science of Membranes for Gas and Vapour Separation*, Yampolskii, Y. P.; Pinnau, I.; Freeman, B. D., Eds. John Wiley & Sons Ltd.: Hoboken, N.J., USA, 2006.

(125) Lin, W. H.; Chung, T.-S. *Journal of Membrane Science* **2001,** 186 (*2*), 183-193.

(126) Chan, A. H.; Paul, D. R. *Polymer Engineering and Science* **1980,** 20 (*1*), 87-94.

(127) Wang, X.-Y.; Willmore, F. T.; Raharjo, R. D.; Wang, X.; Freeman, B. D.; Hill, A. J.; Sanchez, I. C. *J. Phys. Chem. B* **2006,** 110 (*33*), 16685–16693.

(128) Ismail, A. F.; Lorna, W. *Separation and Purification Technology* **2002,** 27 (*3*), 173-194.

(129) Böhning, M.; Springer, J. *Polymer* **1998,** 39 (*21*), 5183-5195.

(130) Wang, J.-S.; Kamiya, Y. *Journal of Membrane Science* **1995,** 98 (*1-2*), 69-76.

(131) Wang, J.-S.; Naito, Y.; Kamiya, Y. *Journal of Polymer Science: Part B: Polymer Physics* **1996,** 34 (*12*), 2027-2033.

(132) Wang, J.-S.; Kamiya, Y.; Naito, Y. *Journal of Polymer Science: Part B: Polymer Physics* **1998,** 36 (*10*), 1695-1702.

(133) Fleming, G. K.; Koros, W. J. *Macromolecules* **1986,** 19 (*8*), 2285-2291.

(134) Kirchheim, R. *Macromolecules* **1992,** 25 (*25*), 6952-6960.

(135) Kirchheim, R. *Journal of Polymer Science Part B: Polymer Physics* **1993,** 31 (*10*), 1373-1382.

(136) Ponitsch, M.; Gotthardt, P.; Gruger, A.; Brion, H. G.; Kirchheim, R. *Journal of Polymer Science Part B: Polymer Physics* **1997,** 35 (*15*), 2397-2408.

(137) Gruger, A.; Gotthardt, P.; Ponitsch, M.; Brion, H. G.; Kirchheim, R. *Journal of Polymer Science Part B: Polymer Physics* **1998,** 36 (*3*), 483-494.

(138) Gotthardt, P.; Gruger, A.; Brion, H. G.; Plaetschke, R.; Kirchheim, R. *Macromolecules* **1997,** 30 (*25*), 8058-8065.

Chapter 5.

Carbon dioxide diffusion studies

5.1 Production runs

In MD simulations, the self-diffusion coefficients *D* for gas molecules are generally calculated using Einstein's equation (Eq. 13). As mentioned in Section 1.3, this equation is only valid when the penetrants undergo a random walk, *i.e.* when they are in the Fickian regime. In order to reach this regime, sufficient simulation times are required.[107] The typical CO_2 diffusion coefficients for the polyimides under study are known to be in the range of 10^{-7} to 10^{-8} cm^2/s (Table 3 and Table 6) and the Fickian diffusion regime simply cannot be reached within the MD timescales of several nanoseconds at 308 K.

There are some earlier attempts based on the Gusev-Suter TST method to calculate the diffusion coefficients of gas molecules in dense glassy polymer models.[66-68] This method assumes that the polymer atoms are only influenced by the elastic thermal vibrations and that the insertions of gas molecules do not induce any structural relaxations. This is clearly not true for a penetrant such as CO_2, which leads to volume relaxations above a critical concentration. In addition, these studies use an unrealistic united-atom approximation, treating the linear CO_2 molecule as a spherical ball with a radius of 4 Å. [66-68] The large size of the "CO_2 sphere" artificially slows down diffusion, which leads to coefficients being close to the experimental values. Indeed, the most-often encountered case for more realistic penetrant models is that simulated diffusion coefficients are a bit larger than experimental ones, which can also be quite dependent on processing parameters. [236,237]

In our calculations, a polymer matrix of ~10000 atoms was equilibrated under *NPT* conditions at a temperature of 308 K with different CO_2 loadings for each polymer (1 to 25% with an increase of 2% per step for 6FDA-6FpDA and 6FDA-6FmDA, 1 to 31% for 6FDA-

DAM). Considering the current computational limitations, our simulations were 5500 ps long for each CO_2 loading, in which the final 5000 ps were considered as the production run. Even though this is not sufficient to reach the Fickian regime, these simulations should give us a basic idea of the CO_2 concentration dependence for the diffusion coefficient.

5.2. Mean square displacements (MSDs)

The average CO_2 MSD, $\left\langle \left| \mathbf{R}_i(t+t_0) - \mathbf{R}_i(t_0) \right|^2 \right\rangle$, calculated over a time-interval of 5000 ps during the sorption procedure are shown as a function of CO_2 concentration in Figure 34(a). In all three polyimides, the MSD decrease initially and increase above the critical concentration. At low pressures, the hole-filling sorption reduces the displacement of CO_2 molecules due to the tight packing of the gas molecules inside the voids. On the other hand, once the polyimide gets plasticized, the volume available to CO_2 molecules increases and the penetrants start to move more easily, which results in MSDs increasing at high CO_2 concentrations. The less dense 6FDA-DAM polyimide exhibit comparatively faster displacements over most of the concentration range, while the differences between 6FDA-6FpDA and 6FDA-6FmDA remain fairly small. The log-log plots of MSD *vs* time also reveal that the Fickian regime can be reached faster in highly-plasticized systems, when compared to systems with low CO_2 loadings. Their limiting slope is displayed in Figure 34 (b) and gets closer to one. This behaviour in glassy polymers is comparable to what is found experimentally and is generally explained by the combined effects of increased chain mobility and CO_2-induced volume relaxations.[27,28]

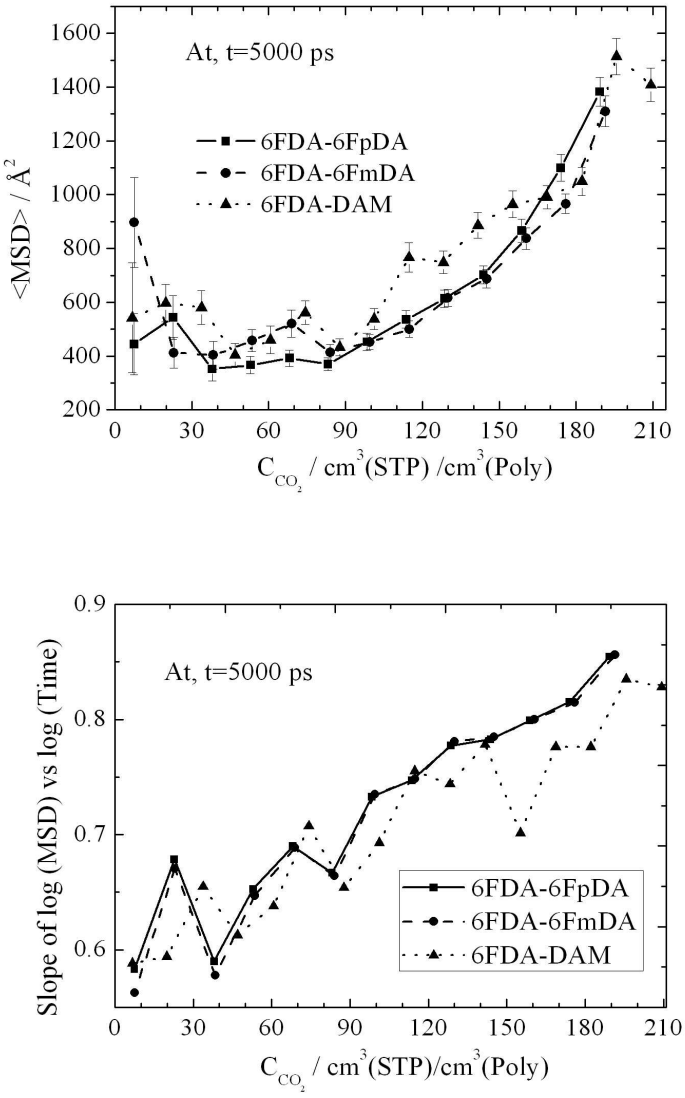

Figure 34. (a) the average mean square displacements for CO_2 molecules at a time interval of 5000 ps and (b) the limiting slopes of the corresponding *log(MSD)* vs *log(time)* plots shown as a function of CO_2 concentration for the three polyimides.

5.3. Factors affecting CO_2 diffusion

5.3.1. Polymer chain mobility

The displacement of the polymer chains as a function of CO_2 concentration can be calculated using the polymer atoms average MSD (Figure 35). As expected, the relative mobility of the polymer atoms increases at higher CO_2 concentrations, even if the actual MSD remain fairly small. Krause *et al.*[238,239] studied the glass transition temperature as a function of CO_2 concentration in polysulfone and they found a decrease in the T_g of approximately 2.5 K per cm^3(STP)/cm^3(polymer). Although the atom MSD are still too small and the 5000 ps timescale is too short to know whether this is the case for our polyimides, it is interesting that such large-scale chain properties can be associated to the penetrant concentration. It is clear that the systems with the highest loadings have an increased mobility. However, finding the actual T_g would require running each of these systems as a function of temperature, which is beyond the scope of the present work. In addition, T_g obtained through molecular simulations are usually higher than the experimental values because of the rate of change of temperature (in K/ps), which is much higher those used under experimental conditions.

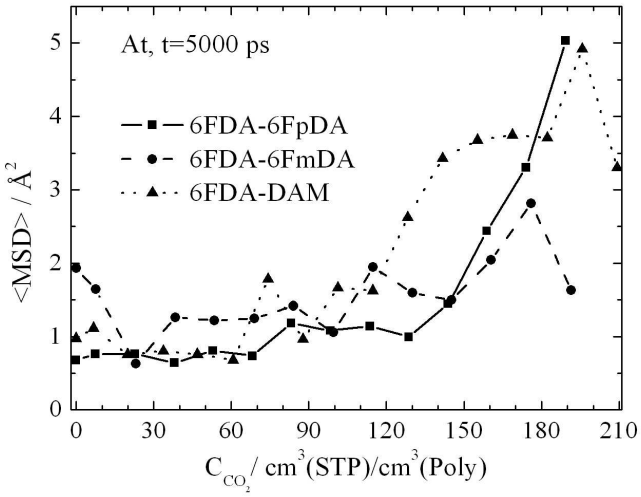

Figure 35. Average mean square displacements for the polymer atoms as a function of CO_2 concentration at 308 K over a time-interval of 5000 ps.

5.3.2. Polymer density

Polymer packing density is one of the many factors affecting the diffusion of gas molecules inside polymer membranes.[240,241] Our pure polyimide models have been carefully prepared and validated with respect to their respective experimental densities. However during the sorption phase, CO_2-induced volume swelling eventually decreases the density of the polymer. Figure 36 shows the density of the polymer calculated from the mass of the polymer chain and the final volume of MD box after the volume swelling at different loadings, it is clear that the increase in gas displacements at high concentrations is correlated to a decrease in the packing density of the polymer.

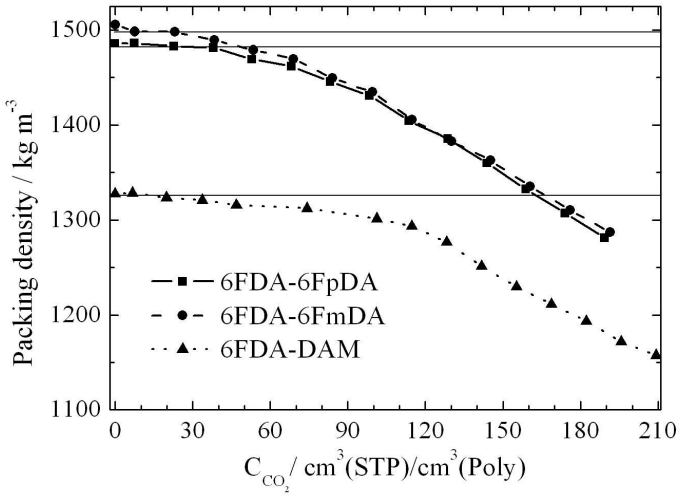

Figure 36. Polymer packing density calculated using the final swollen volume and the mass of the polymer chain as a function of CO2 concentration. The horizontal lines indicate the respective pure polymer experimental average density values (From top: 6FDA-6FmDA (1493 kg m-3), 6FDA-6FpDA (1477 kg m-3) and 6FDA-DAM (1330 kg m-3)) [27-29,31,32,35,36,38,39,42,45,49,52,54,56,57,61,63,70,118,145,156]

5.4. Effect of exposure to high-concentration CO_2 (conditioning effect)

As discussed in chapter 4, the exposure of polymers to high CO_2-concentrations has an impact on their structure, even on the very brief timescales available to MD simulations. Consequently it is interesting to study whether CO_2 conditioning has any effect on CO_2 mobility over the desorption phase. For this purpose, penetrant MSD were calculated in systems which have been previously exposed to high CO_2 concentrations. The MSD curves for the same loading are found to be larger in the desorption than in the sorption simulations, as can be seen seen for 6FDA-DAM in Figure 37. At high CO_2 concentrations (29%), the volume is already dilated in the sorption step-by-step simulations, and there are little differences in the desorption MSD curve vs the sorption ones However, for systems with low CO_2 concentrations (5%), the displacement is much higher during desorption when compared

to sorption because of the irreversible volume relaxations. A similar behaviour is found in the other two polyimides. It is clear that the exposure of polymer membranes to high concentrations of CO_2, even for short times, also has a huge impact on gas diffusion.

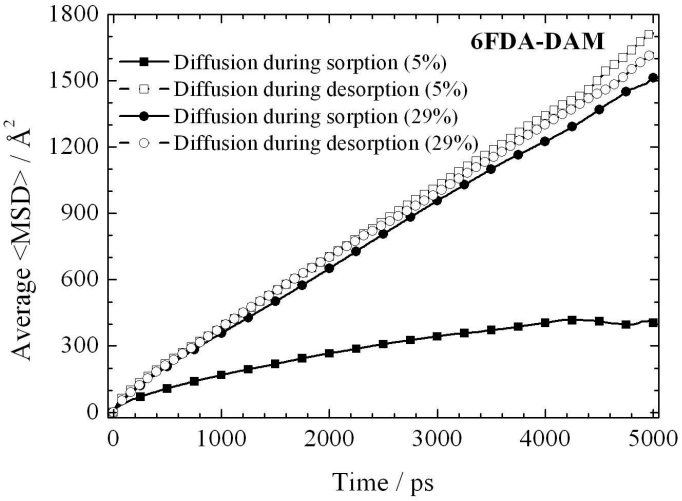

Figure 37. CO_2 average mean square displacement during sorption (solid lines with filled symbols) and desorption (dashed lines with open symbols) in 6FDA-DAM. The curves shown are for the systems containing ~5% and ~29% CO_2 both for the sorption and desorption isotherms.

Carbon dioxide diffusivity in fluorinated polyimides

S. Neyertz*[1], S. Pandiyan[1&2], N.F.A. van der Vegt[2†] and D. Brown[1]

[1]LMOPS-UMR CNRS 5041, University of Savoie, Bât IUT, 73376 Le Bourget-du-Lac Cedex, France

[2]Max-Planck-Institute for Polymer Research, Ackermannweg 10, 55128 Mainz, Germany

[†]Current address: Center of Smart Interfaces, Technical University of Darmstadt, Petersenstrasse 32, 64287 Darmstadt, Germany

* Corresponding author

Current version on 25 september 2009

1. Introduction

The transport of gases through dense polymer membranes is generally described by the so-called solution-diffusion mechanism.[1, 2, 3-5] Gas molecules contained in an upstream compartment enter the polymer matrix, diffuse across it and desorb onto a downstream gas compartment. The rate of transport for the penetrant through the membrane is referred to as its permeability *P*. If the upstream gas pressure is much larger than the downstream pressure, the permeability *P* can simply be expressed as the product of a solubility coefficient *S* and a diffusion coefficient *D* (Eq. 1):

$$P = S \times D \tag{1}$$

In Eq. 1, *S* is a thermodynamic term associated with the number of gas molecules sorbing at the surface and inside the polymer matrix, while *D* is a kinetic parameter which characterizes the mobility of the penetrant in this specific matrix. Interestingly, high permeabilities coefficients can either be obtained through large *D* values, through large *S* values or through both these effects combined.[5] The ratio of permeabilities of gas "A" and "B" under mixed gas feed conditions, P_A/P_B, defines the permselectivity

$\alpha_{A/B}$ of the membrane. $\alpha_{A/B}$ can itself be broken into two parts, *i.e.* the diffusivity selectivity D_A/D_B multiplied by the solubility selectivity S_A/S_B .[6]

Fluorinated polyimides are interesting membrane materials for gas separation applications because of their good mechanical, chemical and thermal properties[7] combined with relatively high permeabilities and permselectivities. With respect to non-fluorinated polyimides, the introduction of -$C(CF_3)_2$- groups in the polymer chain tends to reduce interchain interactions, increase the free-volume and decrease the ability of charge transfer complexes between dianhydride and diamines.[8, 9] This leads to greater solubilities for penetrants such as carbon dioxide CO_2[10] but the differences in permeabilities are thought to be mostly related to diffusivities and diffusivity selectivities.[6, 9]

We have earlier carried out molecular dynamics (MD) simulations of three fluorinated polyimides in their pure state[11] based on the 4,4'-(hexafluoroisopropylidene)diphtalic dianhydride (6FDA), which are known to vary notably in their permeation properties with respect to CO_2. [10, 12-18] These polyimides, *i.e.* the structural isomers 6FDA-6FpDA and 6FDA-6FmDA along with 6FDA-DAM, differ simply in the structure of their diamine. Their chemical formulae are shown in Fig. 1. It should be noted that in the literature, 6FDA-6FpDA can be referred to as 6FDA-BAHF,[13] 6FDA-BAAF[8, 9], while 6FDA-DAM is sometimes called 6FDA-mTrMPD[14].

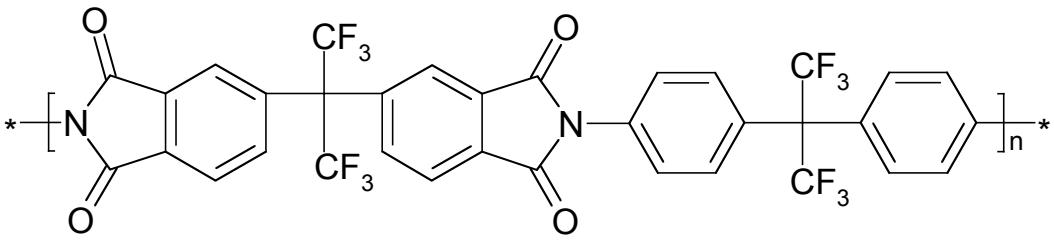

(a)

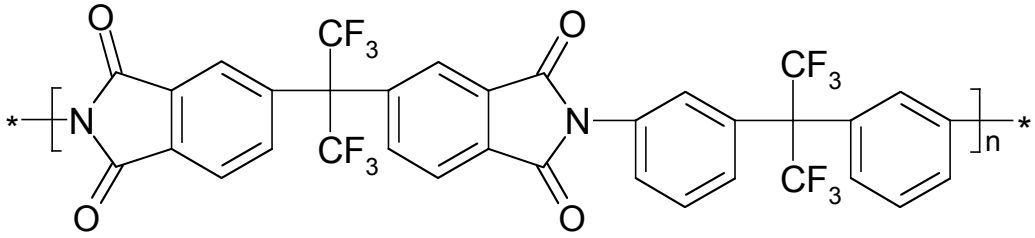

(b)

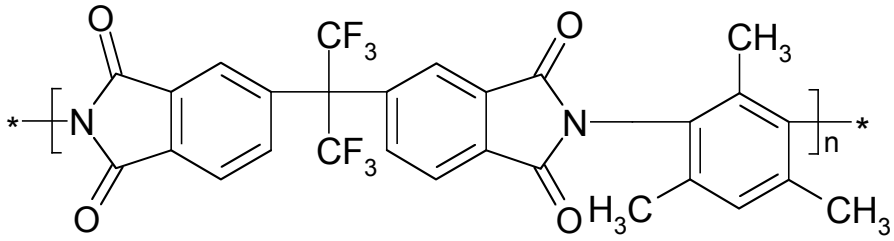

(c)

Figure 1 The chemical structures of (a) 6FDA-6FpDA, (b) 6FDA-6FmDA and (c) 6FDA-DAM polyimides

Experimentally, it has been reported that the effect of changing the bond location of the trifluoromethyl central moiety on the diamine from *para* (6FDA-6FpDA) to *meta* (6FDA-6FmDA) leads to a decrease in CO_2 permeability by a factor of ~12 at near-ambiant conditions.[12] This was attributed by Coleman et al. to differences in diffusivities, which were of the order of ~7.5, while solubility only varied by ~1.6.[12] However, this could hardly be explained by the small differences in densities (1.466 for the *para*-isomer and 1.493 for the *meta*-isomer reported in that specific study),[12] intersegmental packing and fractional free volumes.[11, 12] The third polyimide under study, 6FDA-DAM, is characterized by a lower

density (~1.35) and bulky nonplanar structures, which make chain packing less efficient.[11, 14] Consequently, it exhibits very high CO_2 permeabilities and diffusion coefficients.[14] In addition to these structural considerations, it is well-known that CO_2 transport in glassy polymers often results in volume-swelling and plasticization effects of the matrix, which lead to even higher diffusivities and lower diffusivity selectivities. Conditioning is defined as the hysteretic change in properties following exposure to such penetrants at high activities.[19, 20]

We have carried out extensive molecular dynamics (MD) simulations of 6FDA-6FpDA, 6FDA-6FmDA and 6FDA-DAM polyimides with CO_2 weight percentages ranging from 1% to ~30%, that is covering the entire 0 to 60 atm pressure range. Unlike what has been done elsewhere,[21] the models were loaded progressively with CO_2 in increments of 2% in order to avoid artificially pre-swelling the simulation boxes. For each polyimide under study, the sorption phase was followed by a progressive desorption phase in decrements of 2%. This allowed us to study the conditioning effect associated to high CO_2 concentrations on the limited timescale available to MD simulations. The different parameters associated with solubility such as the CO_2 sorption and desorption isotherms and the associated volume swellings and contractions are being reported elsewhere.[22] In the present paper, we concentrate rather on penetrant mobility and diffusion, which is studied here as a function of both the polymer matrix and the CO_2 concentration. The simulation details are given in Sec. 2., while the penetrant trajectories and diffusivities are analysed in Sec. 3.

2. Simulation Models

All calculations were performed using the MD code of the gmq package[23] in its parallel form. The preparation procedures for the pure polyimide matrices[11] and for the polyimide+CO_2 models[22] have already been described in detail. Consequently, only their main features will be summarized here.

The parameters for the polyimides were taken from the freely available TRIPOS 5.2 force-field,[24] with the partial charges[11] being calculated using the *ab initio* Gaussian 03 code.[25] The bonds were kept rigid with the SHAKE algorithm[26] in order to use a time-step of 10^{-15} s in the integration algorithm. The

other "bonded" interactions were described with angle-bending, torsional and out-of-plane potentials. In addition, "nonbonded" excluded-volume Lennard-Jones LJ 12-6 and electrostatic potentials were applied to all atom pairs separated by more than two bonds on the same chain or belonging to different chains. All parameters for CO_2 were taken from the optimized values reported by Zhang and Duan.[27] CO_2 is modelled here as a rigid three-site molecule with each atom carrying a partial charge and LJ 12-6 parameters. Both C-O bonds are fixed to 1.163 Å and the O-C-O angle is kept at 180°. For the latter, a special vector constraint had to be used.[28] This is very important as a flexible model for CO_2 will have two extra degrees of freedom, *i.e.* an angle bend and a rotation around the long O-C-O axis, in addition to its three translations and two rotations. The rotation around the O-C-O axis couples very poorly with the other degrees of freedom and leads to non-equipartition of the kinetic energy, an artifact which is quite visible in simulations of pure CO_2. As such, the O-C-O angle should remain fixed. Lorentz-Berthelot combining rules[29] were used for all unlike-atom LJ interactions and electrostatic interactions were evaluated using the Ewald summation method.[30, 31] The truncation radii used for both real-space electrostatic and Van der Waals contributions were set to 9 Å, and an optimal convergence of the Ewald sums[32] was obtained for (α, K_{max}) parameters equal to (0.27, 13) for 6FDA-6FpDA, (0.28, 13) for 6FDA-6FpDA and (0.28, 14) for 6FDA-DAM. Long-range corrections to the energy and the pressure were added using the approximation that the radial distribution functions are equal to unity beyond the cutoff.[29] The temperature T was maintained at 308 K by loose-coupling to a heat bath[33] with a constant equal to 0.1 ps. The pressure P was also maintained by loose-coupling with a constant equal to 5 ps.[34]

Initial configurations for the fluorinated macromolecules were obtained using the well-documented hybrid pivot Monte Carlo-molecular dynamics (PMC-MD) single-chain sampling technique.[11, 35] The polymer matrices used for the diffusion studies contained three polyimide chains of length 50 monomers each, which amounted to a total of ~10000 atoms per simulation box. The pure models were in agreement within ~1% with the experimental densities and with available wide-angle X-ray scattering data. This is unlike the smaller packing models for 6FDA-DAM reported by Hofmann and

co-workers. where their average densities differ by about 6% from the experimental data.[36] Comparative analyses of our pure matrices, including cohesive energies, Hildebrand solubility parameters, fractional free volumes, void space distributions and intermolecular as well as intramolecular interactions have been reported elsewhere.[11] In the present work, all MD runs were carried out at 308 K (35°C), that is above the critical temperature of CO_2 of ~31°C as in experiment,[12] and under *NPT* conditions (controlled number of atoms, controlled pressure, controlled temperature).

Gas molecules were introduced into the polymer matrices by preparing equilibrated dense boxes of CO_2 at approximately 1000 $kg.m^{-3}$, and superimposing polyimide-containing boxes with CO_2 boxes of the same size. The required number of CO_2 (see later) was added by selecting those which overlapped least with the polymer atoms. This reduces initial high overlap energies, but in practice, this method is equivalent to a completely random insertion for mobile penetrants. To be consistent with the experimental approach and to avoid the necessity of artificially pre-swelling[21, 36] the polyimide-containing systems, CO_2 loading was carried out in a very progressive way. Pure polyimide samples were initially loaded with an amount of CO_2 corresponding to ~1% in mass of the pure polymers. *NPT* simulations were run for 500 ps, which was found to be enough for the box volume to settle, and a further 2% by mass of CO_2 was subsequently added to the systems to obtain 3% CO_2 simulation boxes. This procedure of adding 2% by mass was continued up at least until 25% of CO_2 had been added. Thirteen simulations boxes with increasing percentages of CO_2 (1% to 25% in increments of 2%) were thus obtained for the 6FDA-6FpDA+CO_2 and 6FDA-6FmDA+CO_2 systems. In the case of 6FDA-DAM+CO_2, loading was extended up to 31% in order to attain a CO_2 concentration corresponding to a pressure of ~60 bar,[22] which has been used experimentally for conditioning of fluorinated polyimides.[19] This amounted to sixteen simulation boxes for the latter, and a total of forty-two corresponding to sorption for the three polyimides. As hysteresis has been reported upon desorption following conditioning of the samples,[19, 20] removal of CO_2 starting from the highest concentrations was carried out in decrements of 2% in the same progressive way as that described above for sorption. At the end of the desorption phase, systems were also run with 0%

CO_2 to assess the effect of conditioning on the volume of the pure polymer. This desorption procedure thus added forty-two more systems to the study. As all simulations were run for at least 5500 ps, only one pure matrix for each polyimide could be used for these diffusion studies. This is unlike our work on the pure matrices[11] and on CO_2 solubility in these systems,[22] where results were averaged over several systems for each polyimide and for each CO_2 percentage. Some specific values such as the volume expansion reported in the present paper will thus differ very slightly from the averaged values reported in the other papers.

The true CO_2 concentration $C_{true}(CO_2)$ corresponding to a specific number of gas molecules n_{gas} in a given polymer is simply the ratio between the volume of the gas, V_{gas}, and that of the penetrant-containing polymer, V_{pol}. $C_{true}(CO_2)$ expressed in cm^3(STP)/(cm^3 polymer), a unit which is usually written as cm^3(STP) cm^{-3} is given by Eq. 2:

$$C_{true}(CO_2) = \frac{V_{gas}^{STP}}{V_{pol}} = \frac{n_{gas}\ k_B\ T^{STP}}{P^{STP}\ V_{pol}} \tag{2}$$

where V_{gas}^{STP} is the volume of the ideal gas at standard temperature and pressure conditions (T^{STP}=273.15 K; P^{STP}=1.013 bar), and k_B is Boltzmann constant. However, the usual experimental practice is to consider the volume of the pure polymer $V_{pol\text{-}pure}$ rather than that of the penetrant-containing polymer V_{pol} which is rather difficult to follow upon sorption.[19] This nominal concentration, referred hereafter as $C_{nom}(CO_2)$, can be obtained using Eq. 3:

$$C_{nom}(CO_2) = \frac{V_{gas}^{STP}}{V_{pol\_pure}} = \frac{n_{gas}\ k_B\ T^{STP}}{P^{STP}\ V_{pol\_pure}} \tag{3}$$

It is clear that $C_{nom}(CO_2) = C_{true}(CO_2)$ if the polymer does not undergo any swelling upon sorption, which is the case for low loadings. They will only be different if the volume changes, and in the systems under study, a maximum difference of 15% between $C_{true}(CO_2)$ and $C_{nom}(CO_2)$ was found at the highest percentages.[22] These concentrations are also related to a vapour pressure P_{CO2}, which has to be applied

experimentally to maintain this amount of gas in the polymer. In the models under study, P_{CO2} has been established using an iterative procedure[37] and extensive details are reported elsewhere.[22] The number of CO_2 molecules n_{gas} inserted into the polymer as well as the corresponding mass percentages and nominal concentrations $C_{nom}(CO_2)$ are given in Table 1 for all systems under study.

~% CO_2	6FDA-6FpDA		6FDA-6FmDA		6FDA-DAM	
	n_{gas}	$C_{nom}(CO_2)$	n_{gas}	$C_{nom}(CO_2)$	n_{gas}	$C_{nom}(CO_2)$
1	25	7	25	8	19	7
3	76	23	76	23	57	20
5	127	38	127	39	95	34
7	177	53	177	54	133	47
9	228	68	228	70	171	61
11	278	83	278	85	209	74
13	329	98	329	100	247	88
15	380	114	380	116	285	101
17	430	129	430	131	323	115
19	481	144	481	147	361	128
21	531	159	531	162	399	142
23	582	174	582	178	437	155
25	633	189	633	193	475	169
27	-	-	-	-	513	182
29	-	-	-	-	551	196
31	-	-	-	-	589	209

Table 1 Number of CO_2 molecules (n_{gas}) inserted into the polymer systems, approximate mass percentages (obtained from the ratio between the mass of CO_2 and the mass of the polymer) and nominal concentrations $C_{nom}(CO_2)$ calculated using Eq. 3. The latter are expressed in cm^3(STP)/(cm^3 polymer), also referred to as cm^3(STP) cm^{-3}. The number of atoms of the pure polymers are 9906 for 6FDA-6FpDA and 6FDA-6FmDA, and 8406 for 6FDA-DAM.

Two schematic representations of the 6FDA-6FpDA system containing 15% CO_2, which is the loading closest to P_{CO2} ~10 bar (*i.e.* the pressure at which most permeation experiments are carried out)[12, 13] are displayed in Fig. 2 using the VMD 1.8.2 visualization software.[38] Fig. 2a shows the entire simulation box at time t = 5000 ps with the unfolded coordinates for the polyimide and the folded ones

for CO_2, while Fig. 2b gives a close-up of Fig. 2a with all coordinates folded back into the primary box. Periodic boundary conditions were applied in the three dimensions in order to remove edge-effects.

(a) **(b)**

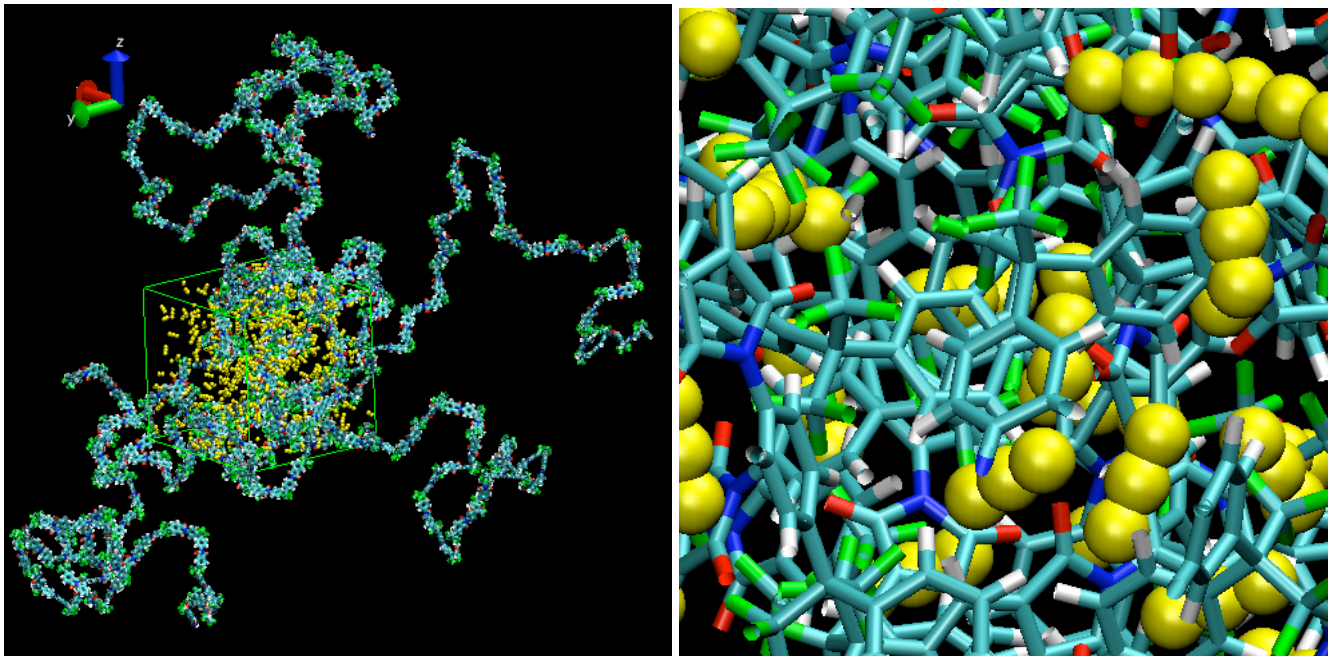

Figure 2 The 6FDA-6FpDA system loaded with 15% CO_2 at t = 5000 ps (a) The entire simulation box of size ~50 $Å^3$ and (b) a 13×13 $Å^2$ close-up of (a). The color code is the following: cyan = polyimide C, red = polyimide O, blue = polyimide N, white = polyimide H, green = polyimide F, yellow = penetrant O and C. These schematic representations are displayed using the VMD 1.8.2 software.[38]

The complexity of such systems is well illustrated by Fig. 2, where the polyimide is displayed with bonds only and the penetrants with hard spheres. Over the course of the simulations, configurations were stored every 10 ps, the first 500 ps of each run were discarded and all analyses were carried out on production intervals of at least 5000 ps.

3. CO_2 DIFFUSIVITY IN FLUORINATED POLYIMIDES

The main purpose of this work is to study the different parameters associated with CO_2 diffusivity in three 6FDA-based polyimides as a function of the progressive CO_2 loading, both upon sorption and desorption. It should be noted that no evidence of crystallinity has been reported experimentally for these materials,[39] so the amorphous models should be consistent with the real systems.

3.1. CO_2 trajectories

The mechanisms underlying small gas motion in glassy dense matrices are known to be based on combinations of oscillations within available free volumes and occasional jumping events.[40-42] Diffusion proceeds by hopping between different voids, which is made possible by the temporary opening of channels within the polymer matrix.[40, 41, 43] The behaviour of CO_2 in the three polyimides under study is indeed found to be similar to that of smaller and less-soluble penetrants.[35, 44-46] Figure 3a displays some individual square displacements, $(r_i(t)-r_i(0))^2$, for CO_2 molecules belonging to the 6FDA-6FpDA and 6FDA-6FmDA 1% systems ($C_{nom}(CO_2) \approx 8$ cm^3(STP) cm^{-3}), which were run up to 10000 ps. In Figure 3b, the actual trajectories of the CO_2 carbons in the 6FDA-DAM systems at 3% and 15% are visualized using VMD.

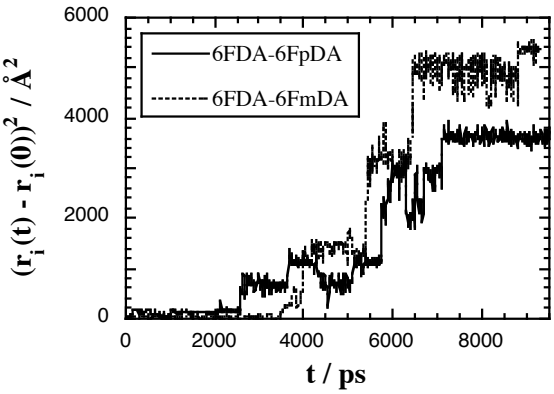

(a)

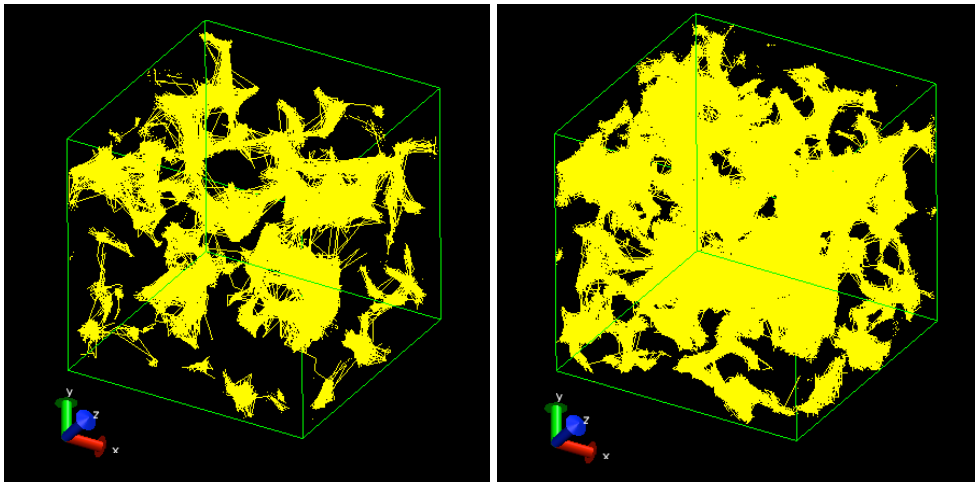

(b)

Figure 3 **(a)** Individual displacements of CO_2 molecules belonging either to the 6FDA-6FpDA or to the 6FDA-6FmDA systems, both being loaded with 1% CO_2 **(b)** Schematic representations of CO_2 trajectories over 5000 ps displayed using VMD in the 6FDA-DAM systems loaded with 3% (left) and 15% (right) CO_2. Configurations have been accumulated every 10 ps so that each segment actually spans that time-interval.

The jump mechanism is well visible in Fig. 3a. Even if the individual molecules can oscillate within the same site for typically several hundred picoseconds (with an amplitude usually < 5-10 Å), they also jump back and forth between different sites. They occasionnally get temporarily "trapped" in a dead-end but always eventually reach a position which allows them to take another path. Close examinations of

individual trajectories reveal that the behaviour pattern can differ at lot between the penetrants in terms of time-of-residences and jump efficiencies. These motion mechanisms are thus very representative of the heterogeneity of microvoids in such glassy polymer matrices. Fig. 3b shows that diffusivity is isotropic in our bulk polymer models. It is clear that the more penetrants in the matrix, the more likely they are to sample the available void space, and indeed, in similar pictures with higher loadings, it becomes increasingly difficult to display unaffected regions of the matrix, others than on the scale of few Å. The mobility of the polymers, which undergo natural fluctuations of that order of magnitude, allows for a temporary passage of the gas molecules. It is worth nothing that, as noted before, the 15% CO_2 loading (right in Fig. 3b) is the closest to P_{CO2} ~10 atm for all three polyimides.

In our models, the effective volume dilation starts above a nominal concentration of ~40 cm^3(STP) cm^{-3},[22] which corresponds to ~5-7% CO_2 depending on the polyimide under study. This is in excellent agreement with the experimental study of Bos *et al.*[47] who studied eleven different glassy polyimides and reported that all the polymers are getting plasticized at the same critical (nominal) concentration of 36±7 cm^3(STP) cm^{-3}. Despite volume dilation, the basic jump mechanism is still found to be present at higher CO_2 loading. This is clearly shown by Fig. 4a, where several CO_2 trajectories were extracted from some 5000 ps 6FDA-DAM simulations under different loading conditions. Molecules diffuse at lot faster in the more concentrated systems (with a maximum volume swelling of 19% for 6FDA-DAM),[22] jumps show larger amplitudes and time-of-residences get shorter. However, they do not yet really display the very smooth paths characteristic of liquid-like diffusion. This suggests that we are still in a transition stage between the hopping-type and the liquid-like regimes, and that plasticization in the experimental pressure range is not likely to result readily in a change of mechanism for CO_2 motion. Fig. 4b gives the distributions for the magnitudes r of the CO_2 displacement vectors as a function of CO_2 loading in 6FDA-6FpDA. These distributions have been averaged over all time-origins and over all gas molecules for a time-interval of 4000 ps. In Fig. 4b, the characteristic shoulder pattern of the van Hove correlation functions in the non-Fickian regime is still visible.[44] There is a weak peak at very low distances which is

associated to the CO_2 molecules which remain or return to the near vicinity of their position at the time-origin, while the larger peak is related to those molecules which manage escaping from their initial environment. As CO_2 loading increases, the first peak tends to disappear in favour of the second diffusive one, a behaviour which is fully consistent with the trajectories displayed in Fig. 4a. However, even if the first peak is very attenuated, it is still present at the highest concentrations.

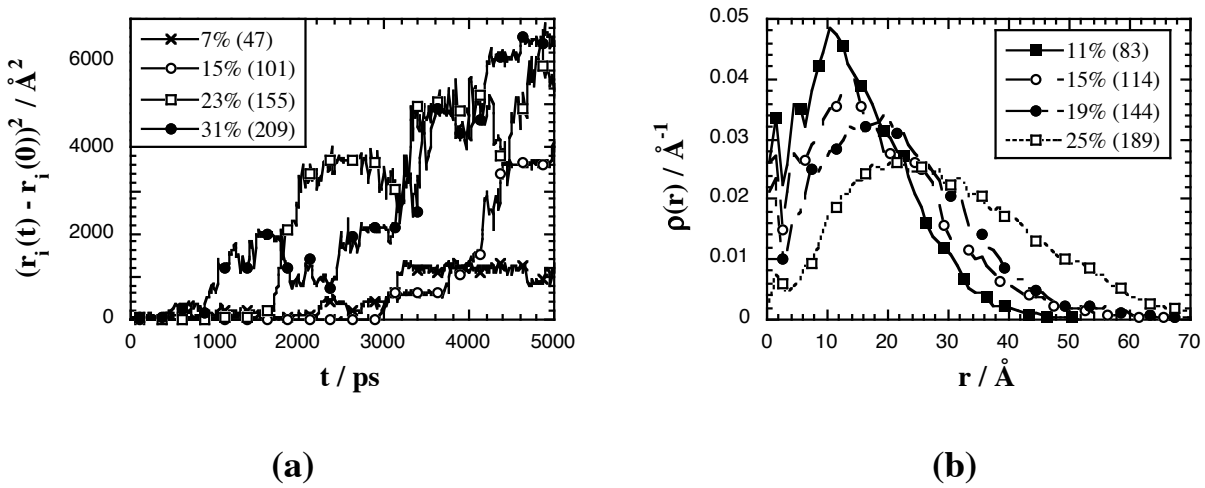

Figure 4 **(a)** Individual displacements of CO_2 molecules in 6FDA-DAM with different CO_2 loadings **(b)** Normalized distributions of the magnitudes *r* of the displacement vectors over a time-interval of 4000 ps in 6FDA-6FpDA with different CO_2 loadings. The $\rho(r)$ have been averaged over all time-origins and over all gas molecules. The figures in parentheses in the legends are the nominal concentrations $C_{nom}(CO_2)$ in cm^3(STP) cm^{-3}.

3.2. The different diffusion regimes for CO_2 at 308 K

In MD simulations, diffusion coefficients are usually obtained from the penetrant mean-square displacements, MSDs = $\langle (r_i(t+t_0)-r_i(t_0))^2 \rangle$, averaged over all penetrants and all possible t_0 time origins of the production runs. The MSDs can then be used to evaluate the self-diffusion coefficients *D* using Einstein's equation:

$$D = \lim_{t\to\infty} \frac{1}{6t} <\left(r_i\left(t+t_0\right) - r_i\left(t_0\right)\right)^2> \qquad (4)$$

However, Eq. 4 is only valid under the assumption that the gas molecules follow a random walk. In dense polymers, where penetrant motion is strongly restricted by the immediate environment, the random-walk condition is obtained within the framework of a long-time Fickian diffusive limit, *i.e.* when the MSDs are proportional to t. In the intervening time, with the exception of a short-time ballistic regime at the very start, the MSD curves are usually found to be proportional to t^n with $n < 1$, which characterizes the so-called anomalous diffusion regime.[40, 41, 44, 48] The actual diffusion regime can identified from log(MSD)-log(t) plots, [40, 41] where the transition from the anomalous to the Fickian regime is characterized by a slope tending to one.[49]

The penetrant MSDs in 6FDA-6FpDA are given in Figure 5. Fig. 5a displays the MSDs obtained at low loadings which decrease while %CO_2 increases. Fig. 5b gives the MSDs at higher loading which increase with %CO_2. The lowest MSD obtained for 11% ($C_{nom}(CO_2)$ ≈ 80 cm^3(STP) cm^{-3}) is shown in both graphs.

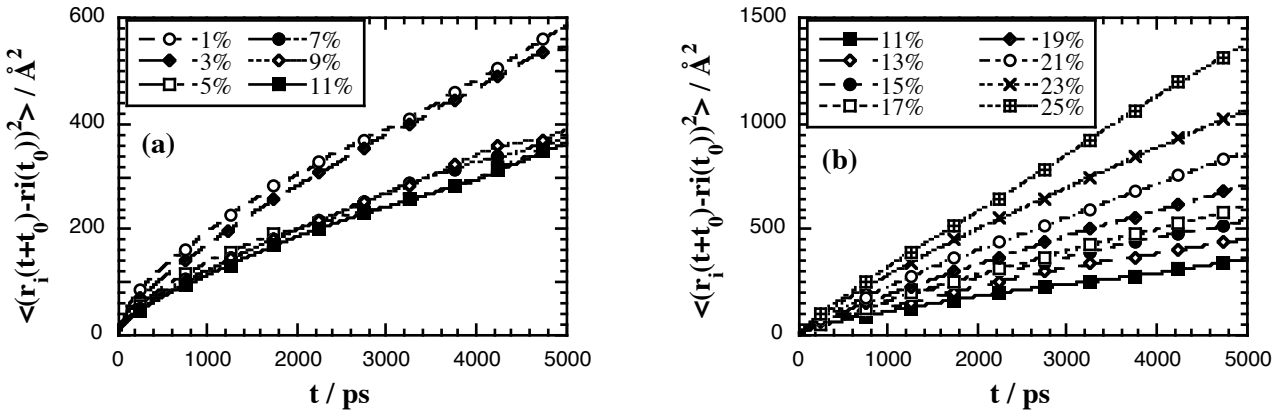

Figure 5 CO_2 mean-square displacements (MSDs) in 6FDA-6FpDA *vs* time plots for **(a)** 1 to 11% CO_2 **(b)** 11 to 25% CO_2. The MSDs have been averaged over all penetrants in a system and all possible time-origins t_0

Similar plots are obtained for 6FDA-6FmDA and 6FDA-DAM. It is not possible to extract true diffusion coefficients as the slopes obtained from the corresponding long-time limits of the *log(MSD)-log(t)* plots fall within the range 0.6 to 0.9. As expected, those associated to the highest CO_2 concentrations tend to approach a slope of one faster than the lower loading systems, which is consistent with an increased mobility in the former (Fig. 5b).

The values of the CO_2 MSD in 6FDA-6FpDA obtained for a time-interval $(t\text{-}t_0) = 4000$ ps, both over the sorption and the desorption phases, are displayed in Fig. 6 as a function of the nominal CO_2 concentration. The percentage of volume change defined as:

$$Volume\ change = \frac{(V(C_{nom}) - V_0)}{V_0} \times 100 = \frac{\Delta V}{V_0} \times 100 \qquad (5)$$

where V_0 is the volume of the pure polymer prior to any CO_2 insertion and $V(C_{nom})$ is the volume of the simulation box corresponding to a specific loading is also indicated on Fig. 6.

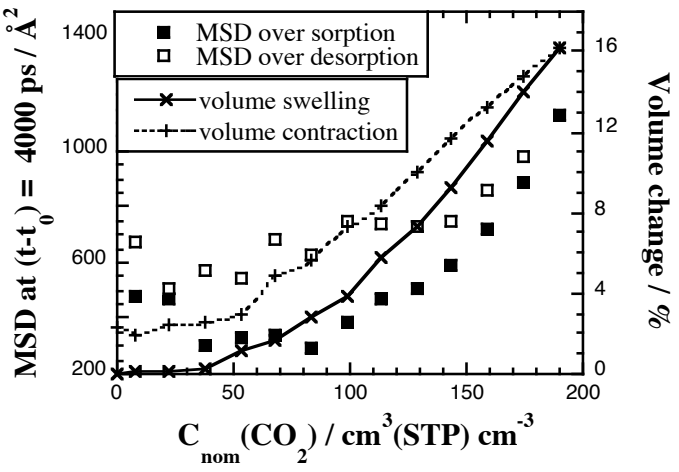

Figure 6 Left axis: CO_2 MSD values in 6FDA-6FpDA simulations averaged over all time-origins and all penetrants over a time-interval of 4000 ps. The black squares refer to MSD obtained over the progressive loading sorption phase and the white squares to the progressive desorption phase. Right axis: the corresponding percentages of volume swelling over sorption and volume contraction over desorption (Eq. 5).

In our 6FDA-6FpDA model, volume swelling starts at ~40 cm^3(STP) cm^{-3} and goes up to ~16% at ~200 cm^3(STP) cm^{-3}. Following exposure to this concentration, the simulation box volume decreases when CO_2 molecules are progressively removed, but never returns to the values of the volume found in the sorption phase. Indeed, this specific conditioning eventually results in a volume increase of ~2.5% for the pure polymer. Penetrant-induced hysteresis thus clearly occurs in glassy polymer even over the few nanoseconds timescale available to MD simulations.

As far as the sorption MSDs (black squares in Fig. 6) are concerned, they tend to slightly decrease up to $C_{nom}(CO_2) \approx 80$ cm^3(STP) cm^{-3} (volume swelling of ~3%), as can be seen from Fig. 5a. This can linked to the limited volume change associated with the increase in the number of penetrants, which leads to available sites for diffusion being occupied by other CO_2 molecules. However, within the available statistical resolution and with the exception of very low loadings, the penetrant MSD in that concentration range are actually rather similar. This is consistent with the observation that, unlike penetrants such as H_2O,[50] CO_2 does not tend to form any CO_2...CO_2 clusters inside the polyimide matrix.[22] The mobility of one penetrant is thus unlikely to be affected by that of another penetrant, except for purely space-occupying considerations. At higher concentrations, plasticization results in a constant increase in volume, and thus in more space available for the penetrants to move. The same behaviour has been reported experimentally by Coleman and Koros for CO_2 pressures greater than 10 atm,[19] which in our model correspond to nominal concentrations above ~100 cm^3(STP) cm^{-3}. These authors showed that the increase in diffusivity in plasticized films offsets the decrease in the solubility and leads for 6FDA-6FpDA to an overall increase in permeability of ~7 at 60 atm compared to that at 10 atm in unconditioned films. They also described the permeability as increasing significantly over the first 2 days following exposure to CO_2, a stage which is followed by a slow creep to the steady-state permeability over a 2-3 week period.[19] It is clear that such timescales can never be directly accessed using MD simulations, and in the CO_2 MSD averaged over a time-interval of 4000 ps (Fig. 6), the increase in diffusivity between 100 and 200 cm^3(STP) cm^{-3} is only ~2.5. While it is difficult from a statistical point-of-view to use a higher

time-interval when production runs are 5000 ps long, the same ratio is found to be ~2.0 if the analyses are carried out over a time-interval of 1000 ps, ~2.1 over 2000 ps and ~2.3 for 3000 ps. It is thus likely that this ratio will keep on increasing with time up to when the Fickian diffusion regime is attained.

The hysteresis found in the volumetric analyses[22] is also evident in the diffusivities (white squares in Fig. 6), with the CO_2 MSD analysed over the same time-interval being quite a bit higher in desorption than in sorption. Interestingly the largest differences are seen for the low CO_2 loadings, *i.e.* systems with an initially limited volume swelling. This can be directly associated to chain motion, which is enhanced in the most-swollen systems as the packing density of the polymer decreases. Similar penetrant MSD *vs* loading plots are obtained for 6FDA-6FmDA and 6FDA-DAM.

While their comparative volumetric properties have been reported elsewhere,[22] it is possible to compare their permeation properties by multiplying the MSD over a given time-interval by the corresponding experimental nominal solubility S_0.[19, 51] This "pseudo-permeability", that is the product of solubility by diffusivity (Eq. 1), is displayed in Fig. 7 for all three polyimides under study. The order in "pseudo-permeabilities" is 6FDA-6FmDA < 6FDA-6FpDA < 6FDA-DAM, which is fully consistent with experimental results.[10, 12-18] For 6FDA-DAM, both the sorption and the desorption values have been indicated in Fig. 7.

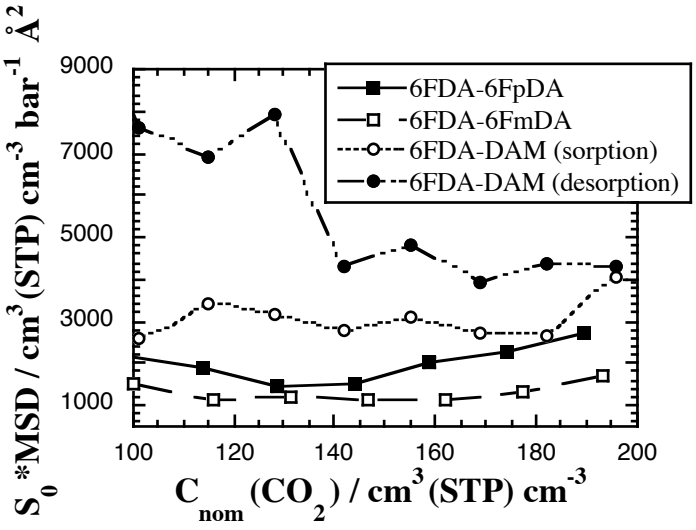

Figure 7 "Pseudo-permeabilities" obtained from the product of the experimental nominal solubilities S_0 [19, 51] by the CO_2 MSD values averaged over all time-origins and all penetrants for a time-interval $(t\text{-}t_0)$ = 4000 ps. The data shown are extracted from the sorption phase, except for 6FDA-DAM for which both the sorption and the desorption data are displayed.

If one compares the symmetric 6FDA-6FpDA and asymmetric 6FDA-6FmDA isomers, their density difference is known to be rather small both from an experimental and from a modelling point of view, *i.e.* about 1%.[11] It has been noted in an experimental study that, although this could reflect small variations in intersegmental packing and void spaces, such a limited difference in density is not enough to fully explain the respective gas transport properties.[12] Indeed, the permeability of CO_2 in the *para* isomer has been reported to be about 12 times higher than that in the *meta* isomer.[12] On the other hand, both isomers have been shown to differ notably in glass-transition T_g and sub-T_g temperatures, and hence in dynamic properties.[39] 6FDA-6FpDA displays a T_g at 593 K and three secondary transitions, among which an intense one at 391.5 K. In the case of 6FDA-6FmDA, the T_g is at 527 K, with a sub-T_g transition at 422 K which is more difficult to distinguish as it appears as a shoulder to the T_g. While the T_g of 6FDA-6FmDA is lower than that of 6FDA-6FpDA, there is an obvious change in the slope of CO_2 permeability *vs* T at the sub-T_g temperature of 391.5 K, which is only found in 6FDA-6FpDA.[39] The subtle chain

motions that begin near 391.5 K in the *para*-isomer are thus associated with gas transport. On the other hand, the lack of a similar high-intensity sub-T_g transition situated far enough from the large fluctuations of the T_g in 6FDA-6FmDA is attributed to an increased intersegmental and intrasegmental steric resistance in the nonsymmetric *meta* unit, which does not allow such an energetically favored motion as that of the symmetric *para* linkage.[19, 39] This is supported by our MD simulations for the pure polymers, where probability density distributions for distances between C_1 (the central carbon in the 6FDA dianhydride) and C_2 (the central carbon in the diamine) were found to exhibit two peaks for 6FDA-6FmDA and a single peak situated at larger distances for the symmetric 6FDA-6FpDA isomer. Both peaks in 6FDA-6FmDA were attributed to the two different positions of the C_2 atom with respect to C_1 that result from a rotation through 180° of the diamine ring around the N-C bond linking it to the dianhydride. These two peaks were also apparent in the $C_1 \cdots C_2 \cdots C_1$ angle distributions in 6FDA-6FmDA. In contrast, the $C_1 \cdots C_2 \cdots C_1$ angles in 6FDA-6FpDA were all close to 110°, as expected from the symmetry of the *para*-substitution. *para*-linked aromatic rings, which are separated by larger distances than their the *meta* isomer, can move more freely and this affects properties such as diffusivities.[11] The restricted mobility of *meta*-linked phenylene rings permits more efficient packing and, as a consequence, 6FDA-6FmDA is more densely packed than 6FDA-6FpDA.[11] This is confirmed by experimentally-determined densities, d-spacings and fractional free volumes (FFV).[39]

Interestingly, the trend of the *meta*-connected polyimide having lower permeabilities than the *para*-connected ones is a general one. In their comparison of gas permeabilities in fluorinated and non-fluorinated polyimides,[13] the nineteen systems studied by Tanaka et al. included *meta*-linked PMDA-mp'ODA and *para*-linked PMDA-pp'ODA as well as *meta*-linked 6FDA-mp'ODA and *para*-linked 6FDA-pp'ODA. Although the diamine is not the same as the one under study here, the *meta*-linked systems systematically have a slightly higher density and lower fractional free volume. Although differences in densities are quite small (0.011 $g.cm^{-3}$ between MDA-mp'ODA and PMDA-pp'ODA, and 0.006 $g.cm^{-3}$ between 6FDA-mp'ODA and 6FDA-pp'ODA), the permeability for CO_2 is found to ~3

times larger in both *para* isomers compared to their *meta* counterparts. This ratio is mostly due to the differences in diffusion coefficients which are also of the order of ~2-3. In the same vein, the 6FDA-ODA *para* isomer has been reported as having a CO_2 permeability which is twice that of the *meta* isomer by Stern et al. [52] while Matsumoto et al. report a difference of 3.8 for exactly the same polymers.[8, 9] They also studied other (*para-meta*) pairs, which lead to differences in P_{CO2} of ~2.4 for 6FDA-TPE and of ~3.5 for 6FDA-BAPS.[8, 9] In all cases, the *para*-connected polyimides exhibit higher gas permeabilities and lower permselectivities than the *meta*-connected polyimides because of their larger amount of free volume and lower interchain interactions, which mean that the gas can permeate more easily. Such an order of magnitude between *para*- and *meta*-connected structures is more in agreement with the results of our models, where similarly low differences in densities and associated CO_2 pseudo-permeabilities (Fig. 6) are found, rather than the factor of 12 reported by Coleman et al.[12] As we are not aware of any other experimental data on CO_2 permeability in 6FDA-6FmDA, it is difficult to assess the reproducibility of the experimental measurements and their dependence upon the processing parameters. In addition, there is no mention either of the number of films used in the permeation studies, nor of the reproductibility of the measurements.[12] Our models thus display the *para*- vs *meta*- trend found elsewhere, but not up to the surprisingly high value given for the two isomers in the literature.

In 6FDA-DAM, the bulkiness of the methyl groups make chain packing inefficient. It has long been reported that key factors in controlling the diffusion coefficient and selectivity for glassy polymers are the packing density associated to the local mobility of polymer chains. The high fraction of large holes created by packing irregularities when methyl substituents are added to the diamine motive was identified by Tanaka et al. as being an important feature in the large increase of diffusivities associated to much lower CO_2/CH_4 selectivities.[14] This is clearly the case here both over the sorption phase and over the desorption phase. Interestingly, the model reproduces even over such limited timescales the qualitative features of the conditioning loop found experimentally with permeabilities getting even higher at lower loadings over the desorption phase.[19, 20] Examination of the model data reveal that, while the desorption

MSD are always higher than the sorption ones, there is little variation as a function of CO_2 concentration over this range. The main factor affecting the "pseudo-permeabilities" are the higher solubilities S_0 at lower loadings. There is thus an interplay between diffusion and solubility which results in such a shape for the permeability over desorption.

3.3. Temperature dependence of D

As temperature increases, the mechanism of penetrant motion is expected to gradually change from the successions of oscillations within voids and jumping events to a more homogeneous liquid-like scattering process.[53, 54] However, the temperature dependence of the diffusion coefficient remains Arrhenius in nature as long as the mechanism is still largely in the low-temperature hopping regime,[39] which happens even over the glass transition region in glassy polymers.[54] This is the case at 700 K, which lies above the T_g of all three polyimides (reported from various experimental studies as being in the range 575-605 K for 6FDA-6FpDA, 640-670 K for 6FDA-DAM and ~530 K for 6FDA-6FmDA)[11], as can be seen in Fig 8:

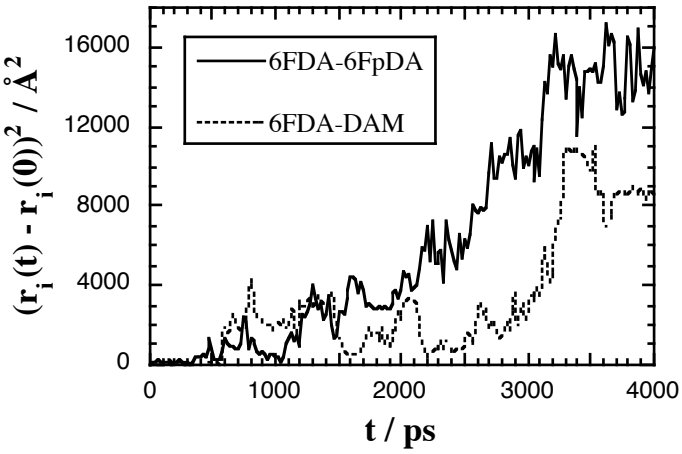

Figure 8 Individual displacements of CO_2 molecules belonging either to the 6FDA-6FpDA or to the 6FDA-DAM systems at 700 K, both being loaded with 3% CO_2

If one compares Fig. 3a at 308 K and Fig. 8 at 700 K, it is clear that at higher temperatures, the jumps are more frequent and the time of residence in voids is much shorter. The oscillations are also larger that those found for higher concentrations at 308 K (Fig. 4a). However, the basic mechanism still remains that of hopping-type rather than liquid-like diffusion. 700 K was the highest temperature considered for both 6FDA-6FmDA and 6FDA-DAM. 6FDA-6FpDA was actually studied over a larger (400 K-900 K) temperature range, but the trajectories at 900 K are qualitatively similar to those at 700 K. It is thus possible to write the Arrhenius equation for the diffusion coefficient as a function of temperature, *D(T),* (Eq. 6):

$$D(T) = D_0 \ \exp\left(\frac{-E_d}{RT}\right) \qquad (6)$$

where D_0 is a prefactor, E_a is the activation energy for diffusion and R is the gas constant. Additional simulations for all three polyimides under study were run at various temperatures T ranging from 400 K to 900 K and the corresponding diffusion coefficients *D(T)* were extracted from the Fickian regime parts of the CO_2 MSDs *vs* time curves, identified by a slope of one in the *log(MSD)-log(time)* plots. Figure 9a shows the natural logarithm of *D(T)* as a function of the reciprocal temperature for three different CO_2 loadings in the 6FDA-6FpDA polyimide. Fairly low loadings (1%, 3% and 15%) were selected in order to account for the well-known decrease in solubility as temperature increases.[39] The actual simulation points are displayed with symbols only (circles and white squares) while the lines are the extrapolations of the MD results down to the experimental temperature range. The black squares are the extrapolated model values at 308 K and the crosses are a series of experimental CO_2 diffusion coefficients at 308 K which can be found in the literature.[12, 13, 15, 17, 18]

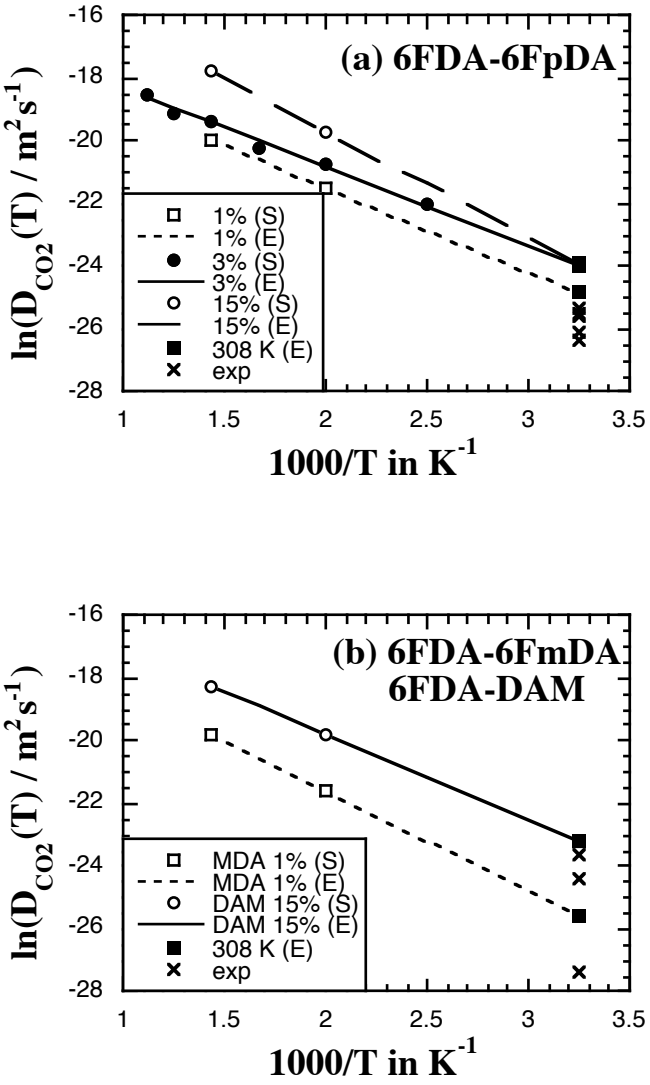

Figure 9 Logarithm of the CO_2 diffusion coefficient as a function of reciprocal temperature in **(a)** 6FDA-6FpDA loaded with 1%, 3% and 15% CO_2 and **(b)** 6FDA-6FmDA loaded with 1% CO_2 and 6FDA-DAM loaded with 15% CO_2. The simulated data (S) obtained at $T > 400$ K are indicated by circles and white squares. The lines are extrapolations (E) to the simulated data, the black squares are the extrapolated model values at 308 K and the crosses are experimental data available in the literature (see text for details)

The linear Arrhenius extrapolation holds well for all 6FDA-6FpDA loadings under study. This is especially obvious for the 3% system, where data were obtained at 100 K intervals, but the other loadings

basically lead to similar diffusion coefficients at 308 K. The agreement with experimental data is good, even if there is a fair amount of scatter in the latter. This is not surprising considering the large amount of processing factors that affect permeation in glassy systems,[55] such as molecular weight,[56] film thickness,[57] residual solvent,[58] heating cycle,[59, 60] casting conditions.[60] and more specifically for CO_2, the strong impact of conditioning.[19, 20] The simulated extrapolated D_{CO2} for 6FDA-6FpDA at 308 K is of the order of ~2 10^{-7} cm^2s^{-1}, while Coleman et al. [12] report 1.3 10^{-7} cm^2s^{-1} and Wang et al. [18] 1.7 10^{-7} cm^2s^{-1}. This order of magnitude would have been difficult to obtain on the MD timescale by using the MSD vs time curves at 308 K only. Results for the other two polyimides under study are given in Fig. 9b. There are a lot less available experimental data [12, 14, 16] and their reproductibility is difficult to assess. However the model is found to agree very well for DAM (D_{CO2} for 6FDA-DAM at 308 K is ~8 10^{-7} cm^2s^{-1} while Tanaka et al.[10, 14] give 5.4 10^{-7} cm^2s^{-1}). On the other hand, it appears to overestimate the diffusion coefficient for 6FDA-6FmDAwhich is ~8 10^{-8} cm^2s^{-1}, that is larger than the only experimental value available by Coleman et al., ~1.34 10^{-8} cm^2s^{-1} (lower cross on Fig. 9b).[12] In simulations, an agreement within a factor 2-3 for the diffusion coefficient is usually considered as very good,[40] taking into account both the simplified nature of the modelling and the many experimental factors. It is clear that 6FDA-6FpDA and 6FDA-DAM fall well within this range. In the case of 6FDA-6FmDA, we only have one experimental value to compare to, and as noted before, the model difference of ~2.5 between *para-* and *meta-* is quite consistent with other *para-vs-meta* studies. Another point to consider is that, in experimental studies, *D* is usually obtained indirectly by dividing permeability, measured using a gas permeation equipment by solubility, which is determined by a sorption cell.[12-14] Tanaka et al. give as an estimation of the uncertainties as being ±3% for *P* and ±3×10^{-4} cm^3(STP) cm^{-3} $cmHg^{-1}$ for *S* in their studies.[13, 14]

The activation energies for the diffusion E_d can be obtained from the Arrhenius extrapolations of the high-temperature data displayed in Fig. 9. E_d is found to be approximately equal to ~

6.6 kcal mol^{-1} for 6FDA-6FpDA, ~6.3 kcal mol^{-1} for 6FDA-6FmDA and ~5.4 kcal mol^{-1} for 6FDA-DAM. Although we are not aware of any experimental high-temperature data for the latter,

Costello et al.[39] have measured gas permeabilities for several penetrants, among which CO_2, at temperatures up to 600 K for 6FDA-6FpDA and to 550 K for 6FDA-6FmDA. Gas solubilities were obtained at temperatures up to 473 K. Diffusion coefficients were again obtained indirectly. In 6FDA-6FpDA, the activation energy for permeation E_p is found to be consistently higher above the sub-T_g temperature of 391.5 K than that below this temperature. The authors thus report two values for E_p, one below ~391.5 K and one above, attributing the difference to an enhanced segmental and vibrational motion above this secondary transition. The corresponding E_d are 7.4 kcal mol^{-1} above 391.5 K and 4.4 kcal mol^{-1} below. Considering the differences in conditions and timescales between experiment and modelling, the model value of E_d = 6.6 kcal mol^{-1} for 6FDA-6FpDA obtained over a 400 K-900 K temperature range compares rather favourably with the experimental value of 7.4 kcal mol^{-1}. There is an even better agreement for 6FDA-6FmDA with the model value of E_d = 6.3 kcal mol^{-1} falling very close to the experimental value of 6.6 kcal mol^{-1}.[39] The diffusion coefficients and activation energies of the model system are thus clearly validated by available experimental data.

Acknowledgments

The CCRT, IDRIS and CINES national supercomputing centres in France, the MUST cluster at the University of Savoie (France) and the MPIP (Germany) are acknowledged for their generous provision of computer time.

References

1. Paul, D. R. *Sep. Purif. Reviews* 1976, 5, (1), 33 - 50.
2. Lonsdale, H. K. *J. Membr. Sci.* 1982, 10, (2-3), 81-181.
3. Wijmans, J. G.; Baker, R. W. *J. Membr. Sci.* 1995, 107, (1-2), 1-21.
4. Koros, W. J.; Mahajan, R. *J. Membr. Sci.* 2000, 175, 181-196.
5. Yampolskii, Y.; Pinnau, I.; Freeman, B. D., *Materials Science of Membranes*. John Wiley & Sons Ltd.: Chichester, U.K., 2006.
6. Kim, T. H.; Koros, W. J.; Husk, G. R. *Separation Science and Technology* 1988, 23, 1611-1626.

7. Ghosh, M. K.; Mittal, K. L., *Polyimides: fundamentals and applications*. Marcel Dekker, Inc.: New York, 1996.
8. Matsumoto, K.; Xu, P.; Nishikimi, T. *J. Membr. Sci*. 1993, 81, 15-22.
9. Matsumoto, K.; Xu, P. *J. Memb. Sci*. 1993, 81, 23-30.
10. Tanaka, K.; Kita, H.; Okamoto, K.-I. *J. Polym. Sci., Part B: Polym. Phys*. 1993, 31, 1127-1133.
11. Pandiyan, S.; Brown, D.; Van der Vegt, N. F. A.; Neyertz, S. *J. Polym. Sci., Part B: Polym. Phys*. 2009, 47, (12), 1166-1180.
12. Coleman, M. R.; Koros, W. J. *J. Memb. Sci*. 1990, 50, 285-297.
13. Tanaka, K.; Kita, H.; Okano, M.; Okamoto, K. I. *Polymer* 1992, 33, 585-592.
14. Tanaka, K.; Okano, M.; Toshino, H.; Kita, H.; Okamoto, K.-I. *J. Polym. Sci., Part B: Polym. Phys*. 1992, 30, 907-914.
15. Mikawa, M.; Nagaoka, S.; Kawakami, H. *J. Memb. Sci*. 1999, 163, 167-176.
16. Yeom, C. K.; Lee, J. M.; Hong, Y. T.; Choi, K. Y.; Kim, S. C. *J. Memb. Sci*. 2000, 166, 71-83.
17. Tanaka, K.; Kawai, T.; Kita, H.; Okamoto, K.-I.; Ito, Y. *Macromolecules* 2000, 33, (15), 5513-5517.
18. Wang, R.; Cao, C.; Chung, T.-S. *J. Memb. Sci*. 2002, 198, 259-271.
19. Coleman, M. R.; Koros, W. J. *Macromolecules* 1997, 30, (22), 6899-6905.
20. Coleman, M. R.; Koros, W. J. *Macromolecules* 1999, 32, (9), 3106-3113.
21. Hölck, O.; Siegert, M. R.; Heuchel, M.; Böhning, M. *Macromolecules* 2006, 39, (26), 9590-9604.
22. Pandiyan, S.; Neyertz, S.; Van der Vegt, N. F. A.; Brown, D. *To be submitted in Macromolecules* 2009.
23. Brown, D. *The gmq User Manual Version 4: available at http://www.lmops.univ-savoie.fr/brown/gmq.html* 2008.
24. Clark, M.; Cramer III, R. D.; Van Opdenbosch, N. *J. Comp. Chem*. 1989, 10, (8), 982-1012.
25. Frisch, M. J.; Trucks, G. W.; Schlegel, H. B.; Scuseria, G. E.; Robb, M. A.; Cheeseman, J. R.; Montgomery, J. A.; Vreven, J., T. ; Kudin, K. N.; Burant, J. C.; Millam, J. M.; Iyengar, S. S.; Tomasi, J.; Barone, V.; Mennucci, B.; Cossi, M.; Scalmani, G.; Rega, N.; Petersson, G. A.; Nakatsuji, H.; Hada, M.; Ehara, M.; Toyota, K.; Fukuda, R.; Hasegawa, J.; Ishida, M.; Nakajima, T.; Honda, Y.; Kitao, O.; Nakai, H.; Klene, M.; Li, X.; Knox, J. E.; Hratchian, H. P.; Cross, J. B.; Bakken, V.; Adamo, C.; Jaramillo, J.; Gomperts, R.; Stratmann, R. E.; Yazyev, O.; Austin, A. J.; Cammi, R.; Pomelli, C.; Ochterski, J. W.; Ayala, P. Y.; Morokuma, K.; Voth, G. A.; Salvador, P.; Dannenberg, J. J.; Zakrzewski, V. G.; Dapprich, S.; Daniels, A. D.; Strain, M. C.; Farkas, O.; Malick, D. K.; Rabuck, A. D.; Raghavachari, K.; Foresman, J. B.; Ortiz, J. V.; Cui, Q.; Baboul, A. G.; Clifford, S.; Cioslowski, J.; Stefanov, B. B.; Liu, G.; Liashenko, A.; Piskorz, P.; Komaromi, I.;

Martin, R. L.; Fox, D. J.; Keith, T.; Al-Laham, M. A.; Peng, C. Y.; Nanayakkara, A.; Challacombe, M. P.; Gill, M. W.; Johnson, B.; Chen, W.; Wong, M. W.; Gonzalez, C.; Pople, J. A. *Gaussian 03*, Gaussian Inc.: Wallingford CT, 2004.

26. Hammonds, K. D.; Ryckaert, J.-P. *Comp. Phys. Commun.* 1991, 62, 336-351.
27. Zhang, Z.; Duan, Z. *J. Chem. Phys.* 2005, 122, 214507-1- 214507-15.
28. Ciccotti, G.; Ferrario, M.; Ryckaert, J. P. *Molecular Physics* 1982, 47, (6), 1253 - 1264.
29. Allen, M. P.; Tildesley, D. J., *Computer Simulation of Liquids*. Clarendon Press: Oxford, England, 1987.
30. Ewald, P. P. *Ann. Phys.* 1921, 64, 253-287.
31. Smith, W. *Comp. Phys. Commun.* 1992, 67, 392.
32. Fincham, D. *Mol. Simul.* 1994, 13, 1-19.
33. Berendsen, H. J. C.; Postma, J. P. M.; Van Gunsteren, W. F.; DiNola, A.; Haak, J. R. *J. Chem. Phys.* 1984, 81, 3684-3690.
34. Brown, D.; Clarke, J. H. R. *Comp. Phys. Commun.* 1991, 62, 360-369.
35. Neyertz, S. *Soft Mater.* 2007, 4, (1), 15-83.
36. Hölck, O.; Heuchel, M.; Böhning, M.; Hofmann, D. *J. Polym. Sci., Part B: Polym. Phys.* 2007, 46, (59-71).
37. Van der Vegt, N. F. A.; Briels, W. J.; Wessling, M.; Strathmann, H. *J. Chem. Phys.* 1999, 110, (22), 11061-11069.
38. Humphrey, W.; Dalke, A.; Schulten, K. *J. Mol. Graphics* 1996, 14, (1), 33-38.
39. Costello, L. M.; Koros, W. J. *J. Polym. Sci.: Part B. Polym. Phys.* 1995, 33, 135-146.
40. Müller-Plathe, F. *Acta Polym.* 1994, 45, 259-293.
41. Gusev, A. A.; Müller-Plathe, F.; Van Gunsteren, W. F.; Suter, U. W. *Adv. Polym. Sci.* 1994, 116, 207-247.
42. Gusev, A. A.; Suter, U. W.; Moll, D. J. *Macromolecules* 1995, 28, 2582-2584.
43. Greenfield, M. L.; Theodorou, D. N. *Macromolecules* 1998, 31, (20), 7068-7090.
44. Neyertz, S.; Brown, D. *Macromolecules* 2004, 37, (26), 10109-10122.
45. Neyertz, S. *Macromol. Theory Simul.* 2007, 16, 513-524.
46. Neyertz, S.; Brown, D. *Macromolecules* 2008, 41, (7), 2711-2721.
47. Bos, A.; Pünt, I. G. M.; Wessling, M.; Strathmann, H. *J. Membr. Sci.* 1999, 155, 67-78.
48. Müller-Plathe, F.; Rogers, S. C.; Van Gunsteren, W. F. *Chemical physics letters* 1992, 199, (3-4), 237-243.
49. Cuthbert, T. R.; Wagner, N. J.; Paulaitis, M. E.; Murgia, G.; D'Aguanno, B. *Macromolecules* 1999, 32, 5017-5028.

50. Marque, G.; Neyertz, S.; Verdu, J.; Prunier, V.; Brown, D. *Macromolecules* 2008, 41, (9), 3349-3362.
51. Wind, J. D.; Sirard, S. M.; Paul, D. R.; Green, P. F.; Johnston, K. P.; Koros, W. J. *Macromolecules* 2003, 36, (17), 6433-6441.
52. Stern, S. A.; Mi, Y.; Yamamoto, H. *J. Polym. Sci., Part B: Polym. Phys.* 1989, 27, 1887-1909.
53. Pant, P. V. K.; Boyd, R. H. *Macromolecules* 1993, 26, (4), 679-686.
54. Bharadwaj, R. K.; Boyd, R. H. *Polymer* 1999, 40, 4229-4236.
55. Pandey, P.; Chauhan, R. S. *Prog. Polym. Sci.* 2001, 26, 853-893.
56. Eastmond, G. C.; Page, P. C. B.; Paprotny, J.; Richards, R. E.; Shaunak, R. *Polymer* 1993, 34, (3), 667-670.
57. Mensitieri, G.; Del Nobile, M. A.; Monetta, T.; Nicodemo, L.; Bellucci, F. *J. Memb. Sci.* 1994, 89, 131-141.
58. Joly, C.; Le Cerf, D.; Chappey, C.; Langevin, D.; Muller, G. *Sep. Purif. Technol.* 1999, 16, 47-54.
59. Kawakami, H.; Mikawa, M.; Nagaoka, S. *J. Memb. Sci.* 1996, 118, 223-230.
60. O'Brien, K. C.; Koros, W. J.; Husk, G. R. *Polymer Engineering and Science* 1987, 27, (3), 211-217.

Conclusions

Conclusions

This research project started with a detailed literature search for polymers with high CO_2 permeability. Fluorinated polyimides were found to be an attractive option, because of their very good mechanical, chemical resistance and gas transport properties. Among the various fluorinated polyimides, 6FDA-dianhydride-based polyimides are very popular, because of their applications in a wide range of industries ranging from gas filtration to aeronautics. There is also a large amount of experimental data available in the literature. We selected three 6FDA-based polyimides for our study, namely 6FDA-6FpDA, 6FDA-6FmDA and 6FDA-DAM.

6FDA-6FpDA and 6FDA-6FmDA are structural *para* and *meta* isomers. Their static properties such as the density, the FFV, the Hildebrand solubility parameter are quite comparable (see section 3.3). However, their gas transport properties are different, with the *para*-isomer exhibiting a diffusion approximately 10 times faster and a solubility for CO_2 approximately twice as large compared to its *meta*-isomer.[27,28,118] It is important to note that while there are many studies related to the *para*-isomer in the literature, there is actually very little on the *meta*-isomer.[27,28,32,33,40,42,54,56,118,130] There are some explanations for the differences in their gas transport properties based on their T_g and sub-T_g temperatures,[70,118] but there is no clear insight. This is the reason while we selected these two polyimides for our studies. The third polyimide, 6FDA-DAM, differs only in the diamine structure, but it has a considerably larger permeability for CO_2 when compared to the other two polyimides. There is also a range of CO_2 diffusion and solubility data available in the literature for this polyimide.[30,32,49,59,144,156]

Molecular dynamics simulations of all-atom bulk models for the three selected polyimides were carried out in the first stage. The well documented PMC-MD technique[169-177,169-177,225] was adopted to prepare the initial chain configurations with an n-local value of 4. In total, thirty individual models were simulated in two different sizes (~10000 atoms and ~20000 atoms). All the simulations were 3000 ps long and the final 2000 ps were considered as the production runs. The relaxed densities of all our bulk models were in very good agreement with the average experimental densities of the respective polyimides.[27-29,31,32,35,36,38,39,42,45,49,52,54,56,57,61,63,70,118,145,156] The FFV calculated using Bondi's group contribution method, the model wide-angle X-ray scattering (WAXS) data used to calculate the d-spacing were also found to be in good agreement with the literature data.[44,144] In addition, potential energies and Hildebrand solubility parameters were calculated and found to be close to the values for similar types of polymers.[169,170,175] This work allowed us to analyse the structural properties and void spaces with respect to the gas transport properties.

Following the preparation of the pure polymer models, a 3-site rigid carbon dioxide molecular model, using the the optimized parameters reported by Zhang and Duan,[232] was validated by comparing the liquid-vapour coexistence properties and the experimental heat of vaporisation to the known values.[232]

In the second stage of this project, the CO_2 sorption isotherms were calculated using the all-atom bulk models of the selected polyimides and the site-site CO_2 molecular models prepared previously. A systematic and realistic step-wise insertion procedure was adopted to insert CO_2 molecules to the bulk models of polyimides. The polyimide models were allowed to relax naturally without imposing any pre-swelling.

In molecular dynamics simulations, the pressure and the CO_2 concentration inside the bulk models are independent of the external pressure. In order to calculate the external pressure which is in equilibrium with the concentration of CO_2 inside the polymer model, an iterative procedure, based on the fact that the total chemical potential of the gas in the gas phase and the gas in the polymer phase is equal, was used.[242] This method predicts the concave shape of the mass uptake curve. While the solubilities calculated at low pressures are comparatively high with respect to the experimental values, they tend to converge above pressures of 10 atm. At this pressure, model solubilities are around twice the experimental solubilities, which is quite good considering the approximations used in the models and the many factors affecting the experimental measurements. From a simulation point-of-view, the deviations between model and experimental solubilities could possibly be explained by factors such as the selection of mixing rules for Van der Waals cross terms for calculating non-bonded interactions[243] or the partial charges used in the site-site CO_2 models. However, we found a limited dependence, since after testing a range of these parameters, model solubilities were still higher than the experimental values. From an experimental point of view, these discrepancies could be attributed to factors affecting the fractional free volumes and their distributions such as ageing of glassy polymers, thermal history, solvents used to cast films or drying conditions.[31-33,40,56,57,118] For example, since the solubility at low pressures is highly dominated by the hole-filling sorption, the plasticization or anti-plasticization effects induced by residual solvent can affect it.[244-246]

CO_2-induced volume swelling upon sorption was analysed as a function of CO_2 concentration. The polymer models were allowed to relax on their own and volume dilations were calculated directly from the equilibrium volumes of the models with different CO_2 loadings. At low loadings, the differences in volume swelling between different polyimides

can be explained by the differences in their FFV. The lower FFV (0.167) of 6FDA-6FmDA leads to dilations at lower CO_2 concentrations than 6FDA-6FpDA and 6FDA-DAM which have slightly higher FFV (0.176 and 0.178 respectively).[247] The partial molar volume of CO_2 calculated at high concentrations, where each and every incoming CO_2 molecule contributes to volume swelling, is 30±2 cm^3 mol^{-1} in all three polyimides, which is very much within the range of experimental values found in the literature.[124] There are no direct experimental curves to compare to our model volume dilation data for all these polyimides. However the only data available for 6FDA-DAM[69] shows that the volume swelling predicted by our models is a bit smaller than the experimental value. This can be explained by the relatively slow dynamics of volume dilation[135] and other factors such as ageing. Interestingly, in all three polyimides, the slope of the volume swelling curve shifts towards a higher value above the critical concentration of ~40 cm^3(STP)/cm^3(polymer) of CO_2 and experimentally Bos *et al*. found a critical concentration of 36±7 cm^3(STP)/cm^3(polymer) for 11 different glassy polymers.[132] The probe accessible void volume (PAV) analyses support the theory that hole-filling sorption is the dominant mechanism at low concentrations of CO_2, while the effective volume swelling starts above the critical concentration of CO_2.

The experiments by Krause *et al.*,[238,239] which concluded that there is a dependence of the glass transition temperature on the concentration of CO_2 of 2.5 K/cm^3(STP)/cm^3(polymer) for polysulfone are very interesting with respect to the behaviour of our models. Although it is unlikely that a glass-to-rubber transition occurs over the timescale of the MD simulations, the polymer chain mean-square displacements are indeed enhanced at high CO_2 concentrations.

The radial distribution functions show that the shortest polymer-penetrant distances associated to CO_2 are found with be those with the carbonyl oxygens and the fluorines on the

polyimide chains. This is likely to be related to the fact that these specific atoms "stick out" of chain and are thus closer to the penetrant. However, cluster analyses of CO_2 in the polymer matrices reveal that CO_2 molecules behave in a way similar to their gaseous state. There is no formation of large CO_2 clusters, thus implying homogeneous swelling of the polymer.

In general, the exposure of glassy polymer membranes to high CO_2 concentration leads to a conditioning effect.[27,28,32,33] In experiments, this conditioning is studied after exposing the polymer membranes to high CO_2 pressures for 2-3 weeks in order to obtain stable permeation conditions.[27,28] However, it is not possible to address such timescales in MD simulations, and thus the conditioning effect is studied here on very short timescales. In the present work, we obtained desorption isotherms and volume contraction curves, starting from the highest-concentration systems at 60 bar pressure for all three polyimides. Interestingly, the immediate exposure of polymer models to 60 bar does have an effect on solubilities and on volume relaxations. The volume changes in the pure polymer systems induced by sorption and subsequent desorption of CO_2 were greater for 6FDA-DAM (6.5%) than 6FDA-6FmDA (4%) and 6FDA-6FpDA (2.5%). These relaxations can be explained by the structural transformations of these polymers at high CO_2 concentrations.

In order to calculate diffusion coefficients for CO_2 in these polymers, models would have to be simulated for sufficient times (typically hundred of ns) in order to reach the Fickian regime. This would require a huge amount of computational time. Consequently, we used shorter simulations (5000 ps) to study the CO_2-concentration dependence of the mean square displacements. As expected, the displacement of CO_2 molecules decreases up to the critical concentration and increases at higher concentrations, due to volume swelling. The underlying key factors are polymer chain mobility and packing density.

This project could be further carried out by analysing the mixed-gas transport properties in these polyimide models, such as CO_2/CH_4. It would also be interesting to build chemically cross-linked polymer models in order to address their effect on gas transport and volume swelling.

Annexes

All bond, bending and torsional angle, out-of-plane and Van der Waals parameters taken from TRIPOS 5.2[168] (Table 9) and the converted values to the analytical forms used in *gmq* are presented here. The equations (Eq. 46) used for conversion are given in section 3.1.

Bonds	Bond type	Bond Length [Å]
1—2	C_1—C_{F1}	1.540
1—3	C_1—C_{ar1}	1.525
2—7	C_{F1}—F_1	1.360
3—3	C_{ar1}—C_{ar1}	1.395
3—4	C_{ar1}—C_{ket}	1.510
3—13	C_{ar1}—H	1.084
4—5	C_{ket}—O_{ket}	1.220
4—6	C_{ket}—N	1.345
6—8	N—C_{ar2}	1.416
6—15	N—H	1.000
8—8	C_{ar2}—C_{ar2}	1.395
8—9	C_{ar2}—C_2	1.525
8—12	C_{ar2}—C_{CH3}	1.540
8—13	C_{ar2}—H	1.084
8—15	C_{ar2}—H	1.084
9—10	C_2—C_{F2}	1.540
10—11	C_{F2}—F_2	1.360
12—14	C_{CH3}—H	1.100

Table 15. Bond lengths.

Bending type	Atom type	θ_0	$k_{i,j,k}$ [kcal mol^{-1} deg^{-2}]	k_θ [kJ mol^{-1}]
2—1—2	C_{F1}—C_1—C_{F1}	109.5	0.024	741.968
2—1—3	C_{ar1}—C_1—C_{F1}	109.5	0.024	741.968
3—1—3	C_{ar1}—C_1—C_{ar1}	109.5	0.018	556.476
1—2—7	F_1—C_{F1}—C_1	109.5	0.020	618.307
7—2—7	F_1—C_{F1}—F_1	109.5	0.040	1236.61
1—3—3	C_{ar1}—C_{ar1}—C_1	120	0.024	879.057
3—3—3	C_{ar1}—C_{ar1}—C_{ar1}	120	0.024	879.057
4—3—3	C_{ket}—C_{ar1}—C_{ar1}	120	0.024	879.057
3—3—13	C_{ar1}—C_{ar1}—H	120	0.024	879.057
3—4—5	C_{ar1}—C_{ket}—O_{ket}	120	0.026	952.311
3—4—6	C_{ar1}—C_{ket}—N	120	0.040	1465.09
5—4—6	N—C_{ket}—O_{ket}	123	0.030	1171.67
4—6—4	C_{ket}—N—C_{ket}	120	0.018	659.239
4—6—8	C_{ket}—N—C_{ar2}	120	0.052	1904.62
4—6—15	C_{ket}—N—H_{term}	119	0.016	574.577
6—8—8	C_{ar2}—C_{ar2}—N	120	0.062	2270.897
8—8—8	C_{ar2}—C_{ar2}—C_{ar2}	120	0.024	879.057
8—8—9	C_{ar2}—C_{ar2}—C_2	120	0.024	879.057
8—8—12	C_{CH3}—C_{ar2}—C_{ar2}	120	0.024	879.057
8—8—13	C_{ar2}—C_{ar2}—H	120	0.024	879.057
8—8—15	C_{ar2}—C_{ar2}—H	120	0.024	879.057
8—9—8	C_{ar2}—C_2—C_{ar2}	109.5	0.018	556.476
8—9—10	C_{F2}—C_2—C_{ar2}	109.5	0.024	741.968
10—9—10	C_{F2}—C_2—C_{F2}	109.5	0.024	741.968
9—10—11	F_2—C_{F2}—C_2	109.5	0.020	618.307
11—10—11	F_2—C_{F2}—F_2	109.5	0.040	1236.61
8—12—14	C_{ar2}—C_{CH3}—H	109.5	0.016	494.645
14—12—14	H—C_{CH3}—H	109.5	0.024	741.968

Table 16. Bending angle parameters in TRIPOS 5.2 (kcal mol^{-1} deg^{-2}) and converted values in *gmq* (kJ mol^{-1})

Torsion	Symbol	Bond type	*k* [kcal mol^{-1} deg^{-2}]	*s*	C_1	C_2	C_3	C_4	C_5	C_6
2-1-2-7	C_{F1}-C_1-C_{F1}-F_1	1	0.2	3	836.8	2510.4	0	-3347.2	0	0
3-1-2-7	C_{ar1}-C_1-C_{F1}-F_1	1	0.2	3	836.8	2510.4	0	-3347.2	0	0
2-1-3-3	C_{F1}-C_1-C_{ar1}-C_{ar1}	1	0.12	-3	502.08	-1506.24	0	2008.32	0	0
3-1-3-3	C_{ar1}-C_1-C_{ar1}-C_{ar1}	1	0.12	-3	502.08	-1506.24	0	2008.32	0	0
1-3-3-3	C_1- C_{ar1}- C_{ar1}-C_{ar1}	ar	2	-2	16736	0	-16736	0	0	0
1-3-3-13	C_1- C_{ar1}- C_{ar1}-H	ar	2	-2	16736	0	-16736	0	0	0
3-3-3-3	C_{ar1}-C_{ar1}-C_{ar1}-C_{ar1}	ar	2	-2	16736	0	-16736	0	0	0
3-3-3-4	C_{ar1}-C_{ar1}-C_{ar1}-C_{ket}	ar	2	-2	16736	0	-16736	0	0	0
3-3-3-13	C_{ar1}- C_{ar1}- C_{ar1}-H	ar	2	-2	16736	0	-16736	0	0	0
4-3-3-4	C_{ket}- C_{ar1}- C_{ar1}-C_{ket}	ar	2	-2	16736	0	-16736	0	0	0
4-3-3-13	C_{ket} - C_{ar1}- C_{ar1}-H	ar	2	-2	16736	0	-16736	0	0	0
13-3-3-13	H- C_{ar1}- C_{ar1}- H	ar	2	-2	16736	0	-16736	0	0	0
3-3-4-5	C_{ar1}-C_{ar1}-C_{ket}-O_{ket}	1	1.6	-2	13388.8	0	-13388.8	0	0	0
3-3-4-6	C_{ar1}-C_{ar1}-C_{ket}-N	1	1.6	-2	13388.8	0	-13388.8	0	0	0
3-4-6-4	C_{ar1}-C_{ket}-N-C_{ket}	am	6.46	-2	54057.28	0	-54057.28	0	0	0
3-4-6-8	C_{ar1}- C_{ket} -N-C_{ar2}	1	6.46	-2	54057.28	0	-54057.28	0	0	0
3-4-6-15	C_{ar1}-C_{ket}-N-H	1	6.46	-2	54057.28	0	-54057.28	0	0	0
5-4-6-4	O_{ket}- C_{ket} –N- C_{ket}	1	6.46	-2	54057.28	0	-54057.28	0	0	0
5-4-6-8	O_{ket}- C_{ket} -N-C_{ar2}	1	6.46	-2	54057.28	0	-54057.28	0	0	0
5-4-6-15	Oket-C_{ket}-N-H	1	6.46	-2	54057.28	0	-54057.28	0	0	0
4-6-8-8	C_{ket} -N-C_{ar2}- C_{ar2}	1	1.6	-2	13388.8	0	-13388.8	0	0	0
6-8-8-12	N- C_{ar2}- C_{ar2}-C_{CH3}	ar	2	-2	16736	0	-16736	0	0	0
6-8-8-13	N- C_{ar2}- C_{ar2}-H	ar	2	-2	16736	0	-16736	0	0	0
8-8-8-8	C_{ar2}- C_{ar2}- C_{ar2}- C_{ar2}	ar	2	-2	16736	0	-16736	0	0	0
8-8-8-9	C_{ar2}- C_{ar2}- C_{ar2}-C_2	ar	2	-2	16736	0	-16736	0	0	0
8-8-8-12	C_{ar2}- C_{ar2}- C_{ar2}-C_{CH3}	ar	2	-2	16736	0	-16736	0	0	0
8-8-8-13	C_{ar2}- C_{ar}2- C_{ar2}-H	ar	2	-2	16736	0	-16736	0	0	0

9-8-8-13	C_2- C_{ar2}- C_{ar2}-H	ar	2	-2	16736	0	-16736	0	0	0
12-8-8-13	C_{CH3}- C_{ar2}- C_{ar2}-H	ar	2	-2	16736	0	-16736	0	0	0
13-8-8-13	H- C_{ar2}- C_{ar2}-H	ar	2	-2	16736	0	-16736	0	0	0
13-8-8-15	H- C_{ar2}- C_{ar2}-H_{term}	ar	2	-2	16736	0	-16736	0	0	0
2-1-2-7	C_{F1}-C_1-C_{F1}-F_1	1	0.2	3	502.08	-1506.24	0	2008.32	0	0
3-1-2-7	C_{ar1}-C_1-C_{F1}-F_1	1	0.2	3	502.08	-1506.24	0	2008.32	0	0
2-1-3-3	C_{F1}-C_1-C_{ar1}-C_{ar1}	1	0.12	-3	502.08	-1506.24	0	2008.32	0	0
3-1-3-3	C_{ar1}-C_1-C_{ar1}-C_{ar1}	1	0.12	-3	836.8	2510.4	0	-3347.2	0	0
1-3-3-3	C_1- C_{ar1}- C_{ar1}-C_{ar1}	ar	2	-2	836.8	2510.4	0	-3347.2	0	0
1-3-3-13	C_1- C_{ar1}- C_{ar1}-H	ar	2	-2	836.8	2510.4	0	-3347.2	0	0
3-3-3-3	C_{ar1}-C_{ar1}-C_{ar1}-C_{ar1}	ar	2	-2	836.8	2510.4	0	-3347.2	0	0
3-3-3-4	C_{ar1}-C_{ar1}-C_{ar1}-C_{ket}	ar	2	-2	502.08	-1506.24	0	2008.32	0	0

Table 17. Torsional angles and parameters in TRIPOS 5.2 [kcal mol^{-1} deg^{-2}] and the torsional coefficients (C_m) [J mol^{-1}] in *gmq*.

Out-of-Plane	Symbol	k [kcal mol^{-1} $angstrom^{-2}$]	k_{oop} [kg s^{-2}]
3; 1-3-3	C_{ar1}; C_1-C_{ar1}-C_{ar1}	480	666.9792
3; 3-3-4	C_{ar1}; C_{ar1}-C_{ar1}-C_{ket}	480	666.9792
3; 3-3-13	C_{ar1}; C_{ar1}-C_{ar1}-H	480	666.9792
4; 3-5-6	C_{ket}; C_{ar1}-O_{ket}-N	480	666.9792
6; 4-4-8	N; C_{ket}-C_{ket}-C_{ar2}	120	166.7486
6; 4-4-15	N; C_{ket}-C_{ket}-H_{term}	120	166.7486
8; 6-8-8	C_{ar2}; N-C_{ar2}-C_{ar2}	480	666.9792
8; 8-8-9	C_{ar2}; C_{ar2}-C_{ar2}-C_2	480	666.9792
8; 8-8-12	C_{ar2}; C_{ar2}-C_{ar2}-C_{CH3}	480	666.9792
8; 8-8-13	C_{ar2}; C_{ar2}-C_{ar2}-H	480	666.9792
8; 8-8-15	C_{ar2}; C_{ar2}-C_{ar2}-H_{term}	480	666.9792

Table 18. Out-of-plane potential parameters in TRIPOS 5.2 and *gmq* in the units of kcal mol^{-1} $angstrom^{-2}$ and kg s^{-2}, respectively.

Symbol	r_{ij} [Å]	$k_{i,j}$ [kcal mol^{-1}]	σ [Å]	ε [K^{-1}]
C	1.7	0.107	3.029	53.844
O	1.52	0.116	2.708	58.373
N	1.55	0.095	2.762	47.806
F	1.47	0.109	2.619	54.851
H	1.5	0.042	2.673	21.135

Table 19. Van der Waals potential parameters in TRIPOS 5.2 and gmq in the units of kcal mol^{-1} and K^{-1}, respectively.

References

References :

1. Sroog, C. E.; Endrey, A. L.; Abramo, S. V.; Berr, C. E.; Edwards, W. M.; Olivier, K. L. *Journal of Polymer Science Part A: General Papers* **1965,** 3, (4), 1373-1390.
2. Blodgett, J., A.J. *Scientific American* **1983,** 249, 86.
3. Ghosh, M. K.; Mittal, K. L., *Polyimides: Fundamentals and applications*. Marcel Dekker Inc.: New York, 1996.
4. Barrer, R. M., *Diffusion In and Through Solids*. Cambridge University Press: London, 1951.
5. Stern, S. A. In *Industrial Applications of Membrane Processes: The Separation of Gas Mixtures*, in Membrane Processes for Industry, Proceedings of the Symposium, Southern Research Institute, Birmingham, AL,, 1966; Southern Research Institute, Birmingham, AL,, 1966.
6. Meares, P. *Journal of the American Chemical Society* **2002,** 76, (13), 3415-3422.
7. Baker, R. W. *Industrial & Engineering Chemistry Research* **2002,** 41, (6), 1393-1411.
8. Koros, W. J.; Fleming, G. K. *Journal of Membrane Science* **1993,** 83, (1), 1-80.
9. Herzog, H., *Greenhouse gas Control and Technologies*. Elsevier Science Ltd., : Oxford, UK, 1999; p 101-106.
10. Sarkar, S. C.; Bose, A. *Energy Conversion and Management* **1997,** 38, (Supplement 1), S105-S110.
11. Ishibashi, M.; Ota, H.; Akutsu, N.; Umeda, S.; Tajika, M.; Izumi, J.; Yasutake, A.; Kabata, T.; Kageyama, Y. *Energy Conversion and Management* **1996,** 37, (6-8), 929-933.
12. Kikkinides, E. S.; Yang, R. T.; Cho, S. H. *Industrial & Engineering Chemistry Research* **1993,** 32, (11), 2714-2720.

13. Cavenati, S.; Grande, C. A.; Rodrigues, A. E. *Energy & Fuels* **2006,** 20, (6), 2648-2659.

14. Ohta, H.; Umeda, S.; Tajika, M.; Nishimura, M.; Yamada, M.; Yasutake, A.; Izumi, J. *International Journal of Global Energy Issues* **1998,** 11, (1), 203-210.

15. Gray, P. G. *Gas Separation & Purification* **1993,** 7, (4), 213-224.

16. Knoblauch, K. *Gas Separation & Purification* **1993,** 7, (4), 195-196.

17. Al-Marzouqi, M.; El-Naas, M.; Marzouk, S.; Abdullatif, N. *Separation and Purification Technology* **2008,** 62, (3), 499-506.

18. Satyapal, S.; Filburn, T.; Trela, J.; Strange, J. *Energy & Fuels* **2001,** 15, (2), 250-255.

19. Chakma, A. *Energy Conversion and Management* **1997,** 38, (Supplement 1), S205-S209.

20. Lackner, K. S.; Butt, D. P.; Wendt, C. H. *Energy Conversion and Management* **1997,** 38, (Supplement 1), S259-S264.

21. Gottlicher, G.; Pruschek, R. *Energy Conversion and Management* **1997,** 38, (Supplement 1), S173-S178.

22. Gaudernack, B.; Lynum, S. *Energy Conversion and Management* **1997,** 38, (Supplement 1), S165-S172.

23. Meratla, Z. *Energy Conversion and Management* **1997,** 38, (Supplement 1), S147-S152.

24. Jody, B. J.; Daniels, E. J.; Wolsky, A. M. *Energy Conversion and Management* **1997,** 38, (Supplement 1), S135-S140.

25. Pino, J. A.; Garcia, J.; Martinez, M. A. *Journal of Essential Oil Research* **1996,** 8, (4), 373.

26. Gadalla, M.; Olujie, Z.; De Rijke, A.; Jansens, P. J. *Energy Oxford* **2006,** 31, (13), 2073.

27. Coleman, M. R.; Koros, W. J. *Macromolecules* **1997,** 30, (22), 6899-6905.

28. Coleman, M. R.; Koros, W. J. *Macromolecules* **1999,** 32, (9), 3106-3113.

29. Tanaka, K.; Kawai, T.; Kita, H.; Okamoto, K.; Ito, Y. *Macromolecules* **2000,** 33, (15), 5513-5517.

30. Tanaka, K.; Masaaki, O.; Hiroyuki, T.; Hidetoshi, K.; Okamoto, K. *Journal of Polymer Science Part B: Polymer Physics* **1992,** 30, (8), 907-914.

31. Fuhrman, C.; Nutt, M.; Vichtovonga, K.; Coleman, M. R. *Journal of Applied Polymer Science* **2004,** 91, (2), 1174-1182.

32. Kim, J. H.; Koros, W. J.; Paul, D. R. *Journal of Membrane Science* **2006,** 282, (1-2), 21-31.

33. Kim, J. H.; Koros, W. J.; Paul, D. R. *Journal of Membrane Science* **2006,** 282, (1-2), 32-43.

34. Hibshman, C.; Mager, M.; Marand, E. *Journal of Membrane Science* **2004,** 229, (1-2), 73-80.

35. Liu, Y.; Pan, C.; Ding, M.; Xu, J. *Polymer International* **1999,** 48, (9), 832-836.

36. Matsumoto, K.; Xu, P.; Nishikimi, T. *Journal of Membrane Science* **1993,** 81, (1-2), 15-22.

37. Iwase, M.; Sannomiya, A.; Nagaoka, S.; Suzuki, Y.; Iwaki, M.; Kawakami, H. *Macromolecules* **2004,** 37, (18), 6892-6897.

38. Kawakami, H.; Nakajima, K.; Shimizu, H.; Nagaoka, S. *Journal of Membrane Science* **2003,** 212, (1-2), 195-203.

39. Hibshman, C.; Cornelius, C. J.; Marand, E. *Journal of Membrane Science* **2003,** 211, (1), 25-40.

40. Recio, R.; Palacio, L.; Pradanos, P.; Hernandez, A.; Lozano, A. E.; Marcos, A.; de la Campa, J. G.; de Abajo, J. *Journal of Membrane Science* **2007,** 293, (1-2), 22-28.

41. Ayala, D.; Lozano, A. E.; de Abajo, J.; García-Perez, C.; de la Campa, J. G.; Peinemann, K. V.; Freeman, B. D.; Prabhakar, R. *Journal of Membrane Science* **2003,** 215, (1-2), 61-73.

42. Cornelius, C. J.; Marand, E. *Journal of Membrane Science* **2002,** 202, (1-2), 97-118.

43. Wind, J. D. Improving Polyimide Membrane Resistance to Carbon Dioxide Plasticization in Natural Gas Separations The University of Texas at Austin, 2002.

44. Shimazu, A.; Miyazaki, T.; Ikeda, K. *Journal of Membrane Science* **2000,** 166, (1), 113-118.

45. Coleman, M. R.; Koros, W. J. *Journal of Membrane Science* **1990,** 50, (3), 285-297.

46. Fried, J. R.; Hu, N. *Polymer* **2003,** 44, (15), 4363-4372.

47. Pavel, D.; Shanks, R. *Polymer* **2003,** 44, (21), 6713-6724.

48. Wang, W.; Griffiths, R. M. T.; Giles, M. R.; Williams, P.; Howdle, S. M. *European Polymer Journal* **2003,** 39, (3), 423-428.

49. Fritsch, D.; Peinemann, K. V. *Journal of Membrane Science* **1995,** 99, (1), 29-38.

50. Hiarayama, Y.; Kazama, S.; Fujisawa, E.; Nakabayashi, M.; Matsumiya, N.; Takagi, K.; Okabe, K.; Mano, H.; Haraya, K.; Kamizawa, C. *Energy Conversion and Management* **1995,** 36, (6-9), 435-438.

51. Zhao, X.; Liu, J.; Yang, H.; Fan, L.; Yang, S. *European Polymer Journal* **2008,** 44, (3), 808-820.

52. Staudt-Bickel, C.; Koros, W. J. *Journal of Membrane Science* **2000,** 170, (2), 205-214.

53. Yoshino, M.; Nakamura, S.; Kita, H.; Okamoto, K.; Tanihara, N.; Kusuki, Y. *Journal of Membrane Science* **2003,** 212, (1-2), 13-27.

54. Tanaka, K.; Kita, H.; Okano, M.; Okamoto, K. *Polymer* **1992,** 33, (3), 585-592.

55. Shimazu, A.; Miyazaki, T.; Shigeru, K.; Yasuo, I. *Journal of Polymer Science Part B: Polymer Physics* **2003,** 41, (3), 308-318.

56. Kim, J. H.; Koros, W. J.; Paul, D. R. *Polymer* **2006,** 47, (9), 3094-3103.

57. Kim, J. H.; Koros, W. J.; Paul, D. R. *Polymer* **2006,** 47, (9), 3104-3111.

58. Cooper, A. I.; DeSimone, J. M. *Current Opinion in Solid State and Materials Science* **1996,** 1, (6), 761-768.

59. Islam, M. N.; Zhou, W.; Honda, T.; Tanaka, K.; Kita, H.; Okamoto, K. *Journal of Membrane Science* **2005,** 261, (1-2), 17-26.

60. Chung, T. S.; Cao, C.; Wang, R. *Journal of Polymer Science Part B: Polymer Physics* **2004,** 42, (2), 354-364.

61. Shimazu, A.; Miyazaki, T.; Masatoshi, M.; Kenichi, I. *Journal of Polymer Science Part B: Polymer Physics* **2000,** 38, (19), 2525-2536.

62. Kirchheim, R. *Macromolecules* **1992,** 25, (25), 6952-6960.

63. Tanaka, K.; Kita, H.; Okamoto, K. *Journal of Polymer Science Part B: Polymer Physics* **1993,** 31, (9), 1127-1133.

64. Gruger, A.; Gotthardt, P.; Ponitsch, M.; Brion, H. G.; Kirchheim, R. *Journal of Polymer Science Part B: Polymer Physics* **1998,** 36, (3), 483-494.

65. Coleman, M. R.; Koros, W. J. *Journal of Polymer Science Part B: Polymer Physics* **1994,** 32, (11), 1915-1926.

66. Heuchel, M.; Hofmann, D. *Desalination* **2002,** 144, (1-3), 67-72.

67. Heuchel, M.; Hofmann, D.; Pullumbi, P. *Macromolecules* **2004,** 37, (1), 201-214.

68. Hofmann, D.; Fritz, L.; Ulbrich, J.; Paul, D. *Computational and Theoretical Polymer Science* **2000,** 10, (5), 419-436.

69. Hölck, O.; Heuchel, M.; Böhning, M.; Hofmann, D. *Journal of Polymer Science Part B: Polymer Physics* **2008,** 46, (1), 59-71.

70. Wang, X.-Y.; in 't Veld, P. J.; Lu, Y.; Freeman, B. D.; Sanchez, I. C. *Polymer* **2005,** 46, (21), 9155-9161.

71. *Carbon Dioxide Capture and Storage*; Cambridge University Press, Cambridge: New York, 2005.

72. Neftel, A.; Moor, E.; Oeschger, H.; Stauffer, B. *Nature* **1985,** 315, (6014), 45-47.

73. Saha, A. K.; Bandyopadhyay, S. S.; Biswas, A. K. *Chemical Engineering Science* **1995,** 50, (22), 3587-3598.

74. Belmabkhout, Y.; Serna-Guerrero, R.; Sayari, A. *Chemical Engineering Science* 64, (17), 3721.

75. Grande, C. A.; Rodrigues, A. E. *International Journal of Greenhouse Gas Control* **2008,** 2, (2), 194-202.

76. Zhang, J.; Webley, P. A.; Xiao, P. *Energy Conversion and Management* **2008,** 49, (2), 346-356.

77. Chaffee, A. L.; Knowles, G. P.; Liang, Z.; Zhang, J.; Xiao, P.; Webley, P. A. *International Journal of Greenhouse Gas Control* **2007,** 1, (1), 11-18.

78. Moon, S.-H.; Shim, J.-W. *Journal of Colloid and Interface Science* **2006,** 298, (2), 523-528.

79. Bonnot, K.; Tondeur, D.; Luo, L. A. *Chemical Engineering Research and Design* **2006,** 84, (3), 192-208.

80. Mansoori, S. A.; Iglauer, S.; Pentland, C. H.; Bijeljic, B.; Blunt, M. J. *Energy Procedia* **2009,** 1, (1), 3173-3180.

81. Morrison III, W. H.; Holser, R.; Akin, D. E. *Industrial Crops and Products* **2006,** 24, (2), 119-122.

82. Ochiai, B.; Endo, T. *Progress in Polymer Science* **2005,** 30, (2), 183-215.

83. Cui, Z. D.; Wu, S. L.; Li, C. F.; Zhu, S. L.; Yang, X. J. *Materials Letters* **2004,** 58, (6), 1035-1040.

84. Purnell, P.; Seneviratne, A. M. G.; Short, N. R.; Page, C. L. *Composites Part A: Applied Science and Manufacturing* **2003,** 34, (11), 1105-1112.

85. Campanari, S. *Journal of Power Sources* **2002,** 112, (1), 273-289.

86. Dean, J. R.; Khundker, S. *Journal of Pharmaceutical and Biomedical Analysis* **1997,** 15, (7), 875-886.

87. Beckman, E. J. *Environmental Science & Technology* **2003,** 37, (23), 5289-5296.

88. Muntó, M.; Ventosa, N.; Sala, S.; Veciana, J. *Journal of Supercritical Fluids* **2008,** 47, (2), 147-153.

89. Sala, S.; Danten, Y.; Ventosa, N.; Tassaing, T.; Besnard, M.; Veciana, J. *Journal of Supercritical Fluids* **2006,** 38, (3), 295-305.

90. Han, H.; Cao, W.; Zhang, J. *Process Biochemistry* **2005,** 40, (9), 3148-3151.

91. Kerler, B.; Robinson, R. E.; Borovik, A. S.; Subramaniam, B. *Applied Catalysis B: Environmental* **2004,** 49, (2), 91-98.

92. De Gioannis, B.; Gonzalez, A. V.; Subra, P. *Journal of Supercritical Fluids* **2004,** 29, (1-2), 49-57.

93. ZareNezhad, B.; Hosseinpour, N. *Energy Conversion and Management* **2009,** 50, (6), 1491-1496.

94. Ravagnani, A. T. F. S. G.; Ligero, E. L.; Suslick, S. B. *Journal of Petroleum Science and Engineering* **2009,** 65, (3-4), 129-138.

95. Ferguson, R. C.; Nichols, C.; Leeuwen, T. V.; Kuuskraa, V. A. *Energy Procedia* **2009,** 1, (1), 1989-1996.

96. van Bergen, F.; Gale, J.; Damen, K. J.; Wildenborg, A. F. B. *Energy* **2004,** 29, (9-10), 1611-1621.

97. deMontigny, D.; Kritpiphat, W.; Gelowitz, D.; Tontiwachwuthikul, P. *Energy Conversion and Management* **1997,** 38, (Supplement 1), S223-S228.

98. Rei, M.; Milke, E. C.; Gomes, R. M.; Schaeffer, L.; Souza, J. P. *Materials Letters* **2002,** 52, (4-5), 360-365.

99. Weitzner, G. *American Journal of Surgery* **1940,** 48, (3), 620-624.

100. Cuomo, R.; Sarnelli, G.; Savarese, M. F.; Buyckx, M. *Nutrition, Metabolism and Cardiovascular Diseases* **2009,** In Press, Corrected Proof.

101. Butterworth, G. J.; Dowling, P. D. *Journal of Electrostatics* **1981,** 11, (1), 43-55.

102. Byrne, C. M.; Allen, S. D.; Lobkovsky, E. B.; Coates, G. W. *Journal of the American Chemical Society* **2004,** 126, (37), 11404-11405.

103. Drake, B. G.; Gonzalez-Meler, M. A.; Long, S. P. *Annual Review of Plant Physiology and Plant Molecular Biology* **1997,** 48, (1), 609-639.

104. Jin, H.; Subramaniam, B. *Chemical Engineering Science* **2003,** 58, (9), 1897-1901.

105. Gusev, A. A.; Müller-Plathe, F.; van Gunsteren, W. F.; Suter, U. W. *Advances in Polymer Science* **1994,** 116, 207-247.

106. Graham, T. *Phil. Mag.* **1866,** 26, 402.

107. Müller-Plathe, F. *Acta Polymerica* **1994,** 45, (4), 259-293.

108. Babarao, R.; Jiang, J. *Langmuir* **2008,** 24, (10), 5474-5484.

109. Müller-Plathe, F. *Journal of Chemical Physics* **1995,** 103, (10), 4346-4351.

110. Milano, G.; Guerra, G.; Müller-Plathe, F. *Chemistry of Materials* **2002,** 14, (7), 2977-2982.

111. Leach, A. R., *Molecular Modelling - Principles and Applications*. Second Edition ed.; Pearson Education Limited: Harlown England, 2001.

112. Kirchheim, R. *Journal of Polymer Science Part B: Polymer Physics* **1993,** 31, (10), 1373-1382.

113. Ponitsch, M.; Gotthardt, P.; Gruger, A.; Brion, H. G.; Kirchheim, R. *Journal of Polymer Science Part B: Polymer Physics* **1997,** 35, (15), 2397-2408.

114. Gotthardt, P.; Gruger, A.; Brion, H. G.; Plaetschke, R.; Kirchheim, R. *Macromolecules* **1997,** 30, (25), 8058-8065.

115. Subramanian, S.; Heydweiller, J. C.; Stern, S. A. *Journal of Polymer Science Part B: Polymer Physics* **1989,** 27, (6), 1209-1220.

116. Wijmans, J. G.; Baker, R. W. *Journal of Membrane Science* **1995,** 107, (1-2), 1-21.

117. Bondar, V. I.; Kamiya, Y.; Yampolskii, Y., P. . *Journal of Polymer Science Part B: Polymer Physics* **1996,** 34, (2), 369-378.

118. Costello, L. M.; Koros, W. J. *Journal of Polymer Science Part B: Polymer Physics* **1995,** 33, (1), 135-146.

119. Kanehashi, S.; Nagai, K. *Journal of Membrane Science* **2005,** 253, (1-2), 117-138.

120. Kanehashi, S.; Nakagawa, T.; Nagai, K.; Duthie, X.; Kentish, S.; Stevens, G. *Journal of Membrane Science* **2007,** 298, (1-2), 147-155.

121. Sanchez, I. C.; Lacombe, R. H. *Macromolecules* **2002,** 11, (6), 1145-1156.

122. Doghieri, F.; Sarti, G. C. *Macromolecules* **1996,** 29, (24), 7885-7896.

123. Lipatov, Y. S. *Russian Chemical Reviews* **1978,** 47, 186-198.

124. Wind, J. D.; Sirard, S. M.; Paul, D. R.; Green, P. F.; Johnston, K. P.; Koros, W. J. *Macromolecules* **2003,** 36, (17), 6433-6441.

125. Hess, B.; Peter, C.; Ozal, T.; van der Vegt, N. F. A. *Macromolecules* **2008,** 41, (6), 2283-2289.

126. Torrie, G. M.; Valleau, J. P. *Journal of Computational Physics* **1977,** 23, (2), 187-199.

127. Ferrenberg, A. M.; Swendsen, R. H. *Physical Review Letters* **1989,** 63, (12), 1195.

128. Kumar, S.; Rosenberg, M. J.; Bouzida, D.; Swendsen, H. R.; Kollman, A. P. *Journal of Computational Chemistry* **1992,** 13, (8), 1011-1021.

129. Widom, B. *J. Chem. Phys.* **1963,** 39, 2808-2812.

130. Wang, R.; Cao, C.; Chung, T.-S. *Journal of Membrane Science* **2002,** 198, (2), 259-271.

131. Wang, D.; Jiang, W.; Gao, H.; Jiang, Z. *Journal of Membrane Science* **2006,** 281, (1-2), 203-210.

132. Bos, A.; Pünt, I. G. M.; Wessling, M.; Strathmann, H. *Journal of Membrane Science* **1999,** 155, (1), 67-78.

133. Rutherford, S. W.; Do, D. D. *Adsorption* **1997,** 3, (4), 283-312.

134. Ismail, A. F.; Lorna, W. *Separation and Purification Technology* **2002,** 27, (3), 173-194.

135. Wessling, M.; Huisman, I.; van den Boomgaard, T.; Smolders, C. A. *Journal of Polymer Science Part B: Polymer Physics* **1995,** 33, (9), 1371-1384.

136. Leon, S.; van der Vegt, N. F. A.; Delle Site, L.; Kremer, K. *Macromolecules* **2005,** 38, (19), 8078-8092.

137. Yang, C.-Y.; Hsu, S. L.-C.; Chen, J. S. *Journal of Applied Polymer Science* **2005,** 98, (5), 2064-2069.

138. Baek, S.; Kang, J.; Li, X.; Lee, M.; Kim, J. *Optical Letters* **2004,** 29, 301-303.

139. Jiang, W.; Wang, D.; Guan, S.; Gao, H.; Zhao, Y.; Jiang, Z.; Gao, W.; Zhang, D.; Zhang, D. *Journal of Photochemistry and Photobiology A: Chemistry* **2008,** 197, (2-3), 426-433.

140. Quaranta, A.; Vomiero, A.; Carturan, S.; Maggioni, G.; Della Mea, G. *Synthetic Metals* **2003,** 138, (1-2), 275-279.

141. Synowki, R. A.; Jeffrey, S. H.; Woollam, J. A. *Journal of Spacecraft and Rockets* **1993,** 30, (1), 116-119.

142. St. Clair, A. K.; St. Clair, T. L.; Shevket, K. I. *Polymer Material Science and Engineering* **1984,** 51, 62.

143. Koron, A. *Kobunshi Ronchibunshu* **1994,** 51, (4), 251-257.

144. Matsui, S.; Sato, H.; Nakagawa, T. *Journal of Membrane Science* **1998,** 141, (1), 31-43.

145. Cornelius, C. J.; Marand, E.; Meakin, P.; Hill, A. J. *ACS Symposium Series* **2004,** 876, 234-252.

146. Braun, D.; Cherdron, H.; Rehahn, M.; Ritter, H.; Voit, B., *Polymer Synthesis: Theory and Practice Fundamentals, Methods, Experiments*. 4th Edition ed.; Springer-Verlag Heidelberg, Germany, 2005.

147. Blackadder, A. D.; Keniry, S. J. *Die Makromolekulare Chemie* **1971,** 141, (1), 211-222.

148. Canada, D. C.; Laing, W. R. *Analytical Chemistry* **2002,** 39, (6), 691-692.

149. Moynihan, C. T.; Macedo, P. B. *Journal of Physical Chemistry* **2002,** 75, (21), 3379-3381.

150. Ree, M.; Shin, T. J.; Park, Y. H.; Lee, H.; Chang, T. *Korea Polymer Journal* **1999,** 7, (6), 360.

151. Chung, T. S.; Vora, R. H.; Jaffe, M. *Journal of Polymer Science, Part A: Polymer Chemistry* **1991,** 29, (8), 1207.

152. van Krevelen, D. W., *Properties of Polymers*. 3 ed.; Elsevier Inc.: Amsterdam, 1990.

153. McKechnie, J. I.; Brown, D.; Clarke, J. H. R. *Macromolecules* **1992,** 25, (5), 1562-1567.

154. in `t Veld, P. J.; Stone, M. T.; Truskett, T. M.; Sanchez, I. C. *Journal of Physical Chemistry B* **2000,** 104, (50), 12028-12034.

155. Husk, C. R.; Cassidy, P. E.; Gebert, K. L. *Macromolecules* **1988,** 21, (5), 1234.

156. Yeom, C. K.; Lee, J. M.; Hong, Y. T.; Choi, K. Y.; Kim, S. C. *Journal of Membrane Science* **2000,** 166, (1), 71-83.

157. Pfromm, H. P., The Impact of Physical Aging of Amorphous Glassy Polymers on Gas Separation Membranes. In *Materials Science of Membranes for Gas and Vapour Separation*, Yampolskii, Y. P.; Pinnau, I.; Freeman, B. D., Eds. John Wiley & Sons Ltd.: Hoboken, N.J., USA, 2006; p 445.

158. Smith, S. W.; Hall, C. K.; Freeman, B. D. *Journal of Computational Physics* **1997,** 134, (1), 16-30.

159. Frenkel, D.; Smit, B., *Understanding molecular simulation: from algorithms to applications*. Second Edition ed.; Academic Press Inc.: San Diego, 2002; p 638.

160. Hammonds, K. D.; Ryckaert, J.-P. *Computer Physics Communications* **1991,** 62, (2-3), 336-351.

161. Brown, D. *The gmq User Manual Version 4*, available at http://www.lmops.univ-savoie.fr/brown/gmq.html; 2008.

162. Brown, D.; Clarke, J. H. R. *Computer Physics Communications* **1991,** 62, (2-3), 360-369.

163. Allen, M. P.; Tildesley, D. J., *Computer Simulation of Liquids*. Clarendon Press: Oxford, England, 1987.

164. Berendsen, H. J. C.; Postma, J. P. M.; van Gunsteren, W. F.; DiNola, A.; Haak, J. R. *Journal of Chemical Physics* **1984,** 81, (8), 3684-3690.

165. Ciccotti, G.; Ferrario, M.; Ryckaert, J. P. *Molecular Physics* **1982,** 47, (6), 1253 - 1264.

166. Ewald, P. P. *Annal of Physics* **1921,** 64, 253-287.

167. Fincham, D. *Molecular Simulations* **1994,** 13, (1), 1--19.

168. Clark, M.; Cramer III, R. D.; Van Opdenbosch, N. *Journal of Computational Chemistry* **1989,** 10, (8), 982-1012.

169. Marque, G.; Neyertz, S.; Verdu, J.; Prunier, V.; Brown, D. *Macromolecules* **2008,** 41, (9), 3349-3362.

170. Pinel, E.; Brown, D.; Bas, C.; Mercier, R.; Alberola, N. D.; Neyertz, S. *Macromolecules* **2002,** 35, (27), 10198-10209.

171. Neyertz, S.; Brown, D. *Journal of Chemical Physics* **2001,** 115, (2), 708-717.

172. Neyertz, S.; Douanne, A.; Brown, D. *Journal of Membrane Science* **2006,** 280, (1-2), 517-529.

173. Neyertz, S.; Douanne, A.; Brown, D. *Macromolecules* **2005,** 38, (24), 10286-10298.

174. Neyertz, S.; Brown, D.; Clarke, J. H. R. *Journal of Chemical Physics* **1996,** 105, (5), 2076-2088.

175. Neyertz, S.; Brown, D. *Macromolecules* **2004,** 37, (26), 10109-10122.

176. Neyertz, S.; Brown, D. *Journal of Chemical Physics* **1996,** 104, (24), 10063-10063.

177. Neyertz, S.; Brown, D. *Journal of Chemical Physics* **1995,** 102, (24), 9725-9735.

178. Brown, D.; Clarke, J. H. R.; Okuda, M.; Yamazaki, T. *Journal of Chemical Physics* **1994,** 100, (8), 6011-6018.

179. Shih, J. H.; Chen, C. L. *Macromolecules* **2002,** 28, (13), 4509-4515.

180. Qi, D.; Hinkley, J.; He, G. *Modelling and Simulation in Materials Science and Engineering* **2005,** 13, (4), 493.

181. Chen, C. L.; Chen, H. L.; Lee, C. L.; Shih, J. H. *Macromolecules* **2002,** 27, (8), 2087-2091.

182. Chen, C. L.; Lee, C. L.; Chen, H. L.; Shih, J. H. *Macromolecules* **2002,** 27, (26), 7872-7876.

183. Ben-Naim, A., *Molecular Theory of Solutions*. Oxford University Press: Oxford, UK, 2006; p 400.

184. Frisch, M. J.; Trucks, G. W.; Schlegel, H. B.; Scuseria, G. E.; Robb, M. A.; Cheeseman, J. R.; Montgomery, J. A.; Vreven, J., T. ; Kudin, K. N.; Burant, J. C.; Millam, J. M.; Iyengar, S. S.; Tomasi, J.; Barone, V.; Mennucci, B.; Cossi, M.; Scalmani, G.; Rega, N.; Petersson, G. A.; Nakatsuji, H.; Hada, M.; Ehara, M.; Toyota, K.; Fukuda, R.; Hasegawa, J.; Ishida, M.; Nakajima, T.; Honda, Y.; Kitao, O.; Nakai, H.; Klene, M.; Li, X.; Knox, J. E.; Hratchian, H. P.; Cross, J. B.; Bakken, V.; Adamo, C.; Jaramillo, J.;

Gomperts, R.; Stratmann, R. E.; Yazyev, O.; Austin, A. J.; Cammi, R.; Pomelli, C.; Ochterski, J. W.; Ayala, P. Y.; Morokuma, K.; Voth, G. A.; Salvador, P.; Dannenberg, J. J.; Zakrzewski, V. G.; Dapprich, S.; Daniels, A. D.; Strain, M. C.; Farkas, O.; Malick, D. K.; Rabuck, A. D.; Raghavachari, K.; Foresman, J. B.; Ortiz, J. V.; Cui, Q.; Baboul, A. G.; Clifford, S.; Cioslowski, J.; Stefanov, B. B.; Liu, G.; Liashenko, A.; Piskorz, P.; Komaromi, I.; Martin, R. L.; Fox, D. J.; Keith, T.; Al-Laham, M. A.; Peng, C. Y.; Nanayakkara, A.; Challacombe, M. P.; Gill, M. W.; Johnson, B.; Chen, W.; Wong, M. W.; Gonzalez, C.; Pople, J. A. *Gaussian 03*, Gaussian Inc.: Wallingford CT, 2004.

185. Chandra Singh, U.; Kollman, P. A. *Journal of Computational Chemistry* **1984,** 5, (2), 129-145.
186. Ferry, J. D., *Viscoelastic Properties of Polymers*. 3rd Edition ed.; Wiley: New York, 1980; p 672.
187. Theodorou, D. N.; Suter, U. W. *Macromolecules* **2002,** 18, (7), 1467-1478.
188. Boyd, R. H.; Pant, P. V. K. *Macromolecules* **2002,** 24, (23), 6325-6331.
189. Greenfield, M. L.; Theodorou, D. N. *Macromolecules* **2001,** 34, (24), 8541-8553.
190. Ramos, J.; Vega, J. F.; Theodorou, D. N.; Martinez-Salazar, J. *Macromolecules* **2008,** 41, (8), 2959-2962.
191. Daoulas, K. C.; Terzis, A. F.; Mavrantzas, V. G. *Macromolecules* **2003,** 36, (17), 6674-6682.
192. Sok, R. M.; Berendsen, H. J. C.; van Gunsteren, W. F. *Journal of Chemical Physics* **1992,** 96, (6), 4699-4704.
193. Kotelyanskii, M.; Wagner, N. J.; Paulaitis, M. E. *Macromolecules* **1996,** 29, (26), 8497-8506.
194. Kremer, K.; Müller-Plathe, F. *Molecular Simulation* **2002,** 28, (8), 729 - 750.
195. Müller-Plathe, F. *ChemPhysChem* **2002,** 3, (9), 754-769.

196. Praprotnik, M.; Delle Site, L.; Kremer, K. *Annual Review of Physical Chemistry* **2008,** 59, (1), 545-571.

197. Strauch, T.; Yelash, L.; Paul, W. *Physical Chemistry Chemical Physics* **2009,** 11, (12), 1942-1948.

198. Delle Site, L.; Abrams, C. F.; Alavi, A.; Kremer, K. *Physical Review Letters* **2002,** 89, (15), 156103.

199. Peter, C.; Delle Site, L.; Kremer, K. *Soft Matter* **2008,** 4, (4), 859-869.

200. Alexiadis, O.; Harmandaris, V. A.; Mavrantzas, V. G.; Delle Site, L. *Journal of Physical Chemistry C* **2007,** 111, (17), 6380-6391.

201. Villa, A.; van der Vegt, N. F. A.; Peter, C. *Physical Chemistry Chemical Physics* **2009,** 11, (12), 2068-2076.

202. Villa, A.; Peter, C.; van der Vegt, N. F. A. *Physical Chemistry Chemical Physics* **2009,** 11, (12), 2077-2086.

203. Harmandaris, V. A.; Adhikari, N. P.; van der Vegt, N. F. A.; Kremer, K. *Macromolecules* **2006,** 39, (19), 6708-6719.

204. Ayton, G. S.; Noid, W. G.; Voth, G. A. *Current Opinion in Structural Biology* **2007,** 17, (2), 192-198.

205. Mulder, T.; Harmandaris, V. A.; Lyulin, A. V.; van der Vegt, N. F. A.; Kremer, K.; Michels, M. A. J. *Macromolecules* **2008,** 42, (1), 384-391.

206. Hess, B.; van der Vegt, N. F. A. *Macromolecules* **2008,** 41, (20), 7281-7283.

207. Mulder, T.; Harmandaris, V., A.; Lyulin, V. A.; van der Vegt, N. F. A.; Michels, M. A. J. *Macromolecular Theory and Simulations* **2008,** 17, (7-8), 393-402.

208. Mulder, T.; Harmandaris, V. A.; Lyulin, A. V.; van der Vegt, N. F. A.; Vorselaars, B.; Michels, M. A. J. *Macromolecular Theory and Simulations* **2008,** 17, (6), 290-300.

209. Harmandaris, V. A.; Adhikari, N. P.; van der Vegt, N. F. A.; Kremer, K.; Mann, B. A.; Voelkel, R.; Weiss, H.; Liew, C. *Macromolecules* **2007,** 40, (19), 7026-7035.

210. Harmandaris, V., A. ; Reith, D.; van der Vegt, N. F. A.; Kremer, K. *Macromolecular Chemistry and Physics* **2007,** 208, (19-20), 2109-2120.

211. Schravendijk, P.; Ghiringhelli, L. M.; Delle Site, L.; van der Vegt, N. F. A. *Journal of Physical Chemistry C* **2007,** 111, (6), 2631-2642.

212. Goudeau, S.; Charlot, M.; Müller-Plathe, F. *Journal of Physical Chemistry B* **2004,** 108, (48), 18779-18788.

213. van Zon, A.; Mos, B.; Verkerk, P.; de Leeuw, S. W. *Electrochimica Acta* **2001,** 46, (10-11), 1717-1721.

214. de Leeuw, S. W.; Van Zon, A.; Bel, G. J. *Electrochimica Acta* **2001,** 46, (10-11), 1419-1426.

215. Flory, P. J., *The Statistical Mechanics of Chain Molecules*. Hanser Publications: New York, 1988.

216. Lal, M. *Molecular Physics* **1969,** 17, (1), 57 - 64.

217. Baschnagel, J.; Qin, K.; Paul, W.; Binder, K. *Macromolecules* **2002,** 25, (12), 3117-3124.

218. Almarza, N. G.; Enciso, E.; Alonso, J.; Bermejo, F. J.; Alvarez, M. *Molecular Physics* **1990,** 70, (3), 485 - 504.

219. Metropolis, N.; Rosenbluth, A., W. ; Rosenbluth, M., N. ; Teller, A., H. ; Teller, E. *Journal of Chemical Physics* **1953,** 21, (6), 1087-1092.

220. Brown, D.; Clarke, J. H. R.; Okuda, M.; Yamazaki, T. *Journal of Chemical Physics* **1994,** 100, (2), 1684-1692.

221. Brown, D.; Clarke, J. H. R.; Okuda, M.; Yamazaki, T. *Journal of Chemical Physics* **1996,** 104, (5), 2078-2082.

222. Marque, G. Absorption d'eau par les polymères. Ph.D. Thesis, University of Savoie, Chambery, France, 2009.

223. Marceau, S. Architecture multiéchelle de nanocomposites. Ph.D. Thesis, University of Savoie, Chambery, France, 2003.

224. Queyroy, S. Simulations moléculaires dynamiques de surfaces de polymère amorphe: cas de la cellulose. Ph.D. Thesis, University of Savoie, Chambery, France, 2004.

225. Neyertz, S. *Soft Materials* **2006,** 4, (1), 15 - 83.

226. Auhl, R.; Everaers, R.; Grest, G. S.; Kremer, K.; Plimpton, S. J. *Journal of Chemical Physics* **2003,** 119, (24), 12718-12728.

227. Harmandaris, V. A.; Reith, D.; van der Vegt, N. F. A.; Kremer, K. *Macromolecular Chemistry and Physics* **2007,** 208, (19-20), 2109-2120.

228. Errington, J. R. Ph.D. Thesis, Cornell University, 1999.

229. Murthy, C. S.; Singer, K.; McDonald, I. R. *Molecular Physics* **1981,** 44, (1), 135.

230. Harris, J. G.; Yung, K. H. *Journal of Physical Chemistry* **2002,** 99, (31), 12021-12024.

231. Potoff, J., J. ; Siepmann, J. I. *AIChE Journal* **2001,** 47, (7), 1676-1682.

232. Zhang, Z.; Duan, Z. *Journal of Chemical Physics* **2005,** 122, (21), 214507.

233. Hess, B.; Kutzner, C.; van der Spoel, D.; Lindahl, E. *Journal of Chemical Theory and Computation* **2008,** 4, (3), 435-447.

234. Berendsen, H. J. C.; Van Gunsteren, W. F., *Molecular Liquids: Dynamics and Interactions (NATO Science Series C)*. Springer: Reidel Dordrecht, The Netherlands, 1984; p 600.

235. Heuchel, M.; Böhning, M.; Hölck, O.; Siegert, M. R.; Hofmann, D. *Journal of Polymer Science Part B: Polymer Physics* **2006,** 44, (13), 1874-1897.

236. Neyertz, S.; Brown, D. *Macromolecules* **2008,** 41, (7), 2711-2721.

237. Neyertz, S.; Brown, D. *Macromolecules* **2009**.

238. Krause, B.; Mettinkhof, R.; van der Vegt, N. F. A.; Wessling, M. *Macromolecules* **2001,** 34, (4), 874-884.

239. Krause, B.; Sijbesma, H. J. P.; Munuklu, P.; van der Vegt, N. F. A.; Wessling, M. *Macromolecules* **2001,** 34, (25), 8792-8801.

240. Takeuchi, H. *Journal of Chemical Physics* **1990,** 93, (6), 4490-4491.

241. Meunier, M. *Journal of Chemical Physics* **2005,** 123, (13), 134906.

242. van der Vegt, N. F. A.; Briels, W. J.; Wessling, M.; Strathmann, H. *Journal of Chemical Physics* **1999,** 110, (22), 11061-11069.

243. Neyertz, S. *Macromolecular Theory and Simulations* **2007,** 16, (5), 513-524.

244. Fu, Y.-J.; Hu, C.-C.; Qui, H.-z.; Lee, K.-R.; Lai, J.-Y. *Separation and Purification Technology* **2008,** 62, (1), 175-182.

245. Joly, C.; Le Cerf, D.; Chappey, C.; Langevin, D.; Muller, G. *Separation and Purification Technology* **1999,** 16, (1), 47-54.

246. Chang, K.-S.; Hsiung, C.-C.; Lin, C.-C.; Tung, K.-L. *Journal of Physical Chemistry B* 113, (30), 10159.

247. Pandiyan, S.; Brown, D.; van der Vegt, N. F. A.; Neyertz, S. *Journal of Polymer Science Part B: Polymer Physics* **2009,** 47, (12), 1166-1180.